Fluorescent Carbon Dots as Sensitizers for Nanostructured Solar Cells

Adam Marinovic

Supervisor: Prof Maria-Magdalena Titirici

A thesis submitted for the Degree of Doctor of Philosophy

School of Engineering and Materials Science

Queen Mary University of London

London, United Kingdom

September 2016

Statement of Originality

I, Adam Marinovic, confirm that the research included within this thesis is my own work or that where it has been carried out in collaboration with, or supported by others, that this is duly acknowledged below and my contribution indicated. Previously published material is also acknowledged below.

I attest that I have exercised reasonable care to ensure that the work is original, and does not to the best of my knowledge break any UK law, infringe any third party's copyright or other Intellectual Property Right, or contain any confidential material.

I accept that the College has the right to use plagiarism detection software to check the electronic version of the thesis.

I confirm that this thesis has not been previously submitted for the award of a degree by this or any other university.

The copyright of this thesis rests with the author and no quotation from it or information derived from it may be published without the prior written consent of the author.

Signature:

Date:

“Ignore the naysayers. Work like hell. Trust yourself. Break some rules and don’t be afraid to fail.

You are going to find naysayers at any turn you make. Don’t listen to them. Just visualize your goal and know exactly where you want to go. Trust yourself. Get out there and work like hell. Break some rules and never ever be afraid of failure.

You should go out there and be hungry for success. You should be hungry to make your mark. You should be hungry to be heard and seen, and to have an effect out there. What is the point of being on this world if all you want to do is being liked by everyone and avoid trouble? The only way to get to any place is by breaking some rules. When you are out there partying and messing around, someone at the same time is working hard. Someone is getting smarter and someone is winning. Just remember that.

If you want to coast through life don’t pay any attention to any of these rules, but if you want to win, there is absolutely no way around hard work. You can’t always win but don’t be afraid of making decisions. You can’t be paralyzed by the fear of failure or you will never push yourself. You keep pushing because you believe in yourself and in your vision. You know it is the right thing to do and success will come.

Just remember. You can’t climb the ladder of success with your hands in your pockets.”

A. S.

Dedicated to my mother Vesna, to my father Ivica, and to my sister Sofija.

I hope I didn’t disappoint.

Acknowledgements

Doing a PhD research has been a transformative experience for me. It was one of the most intense periods of my life, but also one of the richest. I have learned a lot about myself, pushed myself to the limits of my scientific capabilities, and developed myself both professionally and personally. There are a lot of people who have left a long lasting impression on me during this PhD research journey.

First of all, I would like to thank my supervisor Prof Magdalena Titirici for giving me the opportunity to do a PhD in her research group. She provided endless support and guidance throughout my PhD, and I admire her sharp attitude towards doing the scientific research. With great happiness I remember our visits to conferences in South Korea, China and Hong Kong. Those were the crazy days. Also, I have a huge respect for Magdalena for finishing two half-marathons in London together with me. That was a lot of sweat, and beers afterwards.

I am grateful to my amazing friend Dr Filoklis Pileidis for spending four years of research with me in the same laboratory, and teaching me the fundamentals of chemistry. Of course, we had to finish one half-marathon in his hometown of Thessaloniki. I would like to thank Dr Vasanth Kumar Kannuchamy for being an amazing colleague always ready to discuss latest research topics, and for being the honest academic researcher. My special thanks goes to my friends Dr Michal Lipka and Dr Yury Korolev for organizing unforgettable parties in a flat in Pimlico.

I am grateful to Prof Steve Dunn and Dr Joe Briscoe for their advice and discussions about the photovoltaic solar cells. I further would like to thank Dr Zofia Luklinska, Dr Nadja Tarakina, Dr Marta Sevilla, Dr Rory Wilson and Dr Krystelle Mafina for their help with the materials characterisation equipment and training. I would like to thank Jonathon Hills for his patience with resolving any PhD related issues.

I am grateful to my colleagues, Nikos, Kathrin, Mo and Servann, for creating a good atmosphere in the laboratory.

My final thanks goes to my family and to my darling Feng, who always kept me motivated during this journey.

Abstract

Fluorescent carbon dots are a new class of carbon nanomaterials that have emerged recently, and have created a lot of interest as a potential competitor to classical semiconductor quantum dots. Carbon dots possess low toxicity, biocompatibility, easy and low-cost synthesis, and good optical properties. They show huge potential as novel and versatile nanomaterials for a wide range of applications such as bioimaging, drug delivery, chemical sensing, photocatalysis, and as sensitizers for photovoltaic solar cells.

The main motivation for this research was the need to produce non-toxic, low-cost nanomaterials with good optical and electrical properties for the use in the fabrication of sustainable, inexpensive nanostructured solar cells with good efficiency.

The main aims and objectives of this PhD research were: to synthesize fluorescent carbon dots from biomass-derived precursors by using the hydrothermal synthesis method, to understand and explain structural and optical properties of the as-synthesized carbon dots, and to use the carbon dots as sensitizers for nanostructured solar cells.

Carbon dots (CDs) were synthesized using hydrothermal synthesis method from polysaccharides (chitosan and chitin), monosaccharide (D-glucose), amino acids (L-arginine and L-cysteine), and from real food waste in the form of lobster shells. Carbon dots were thoroughly characterized to obtain the information about their structural and optical properties. The as-synthesized carbon dots showed polydispersity and quasi-spherical morphology, with particle sizes ranging from 5-17 nm. Carbon dots showed predominantly amorphous nature, and the functional groups from the starting precursors were successfully incorporated into the as-synthesized carbon dots. Diluted solutions of carbon dots were transparent under daylight and showed blue-green photoluminescence emission under UV excitation. All carbon dots showed excitation-dependent photoluminescence emission which was more pronounced for excitation wavelengths larger than 320 nm. Chitosan CDs, L-cysteine CDs and lobster CDs also showed excitation-independent emission for excitation wavelength in the range of 200 - 320 nm. The highest fluorescence quantum yield of (43.3 ± 2.1) % was calculated for L-arginine CDs. It was concluded that the origin of light emission in carbon dots must be governed by the interplay between the absorption due to the carbon cores and the surface functional groups.

Considering the application of the as-synthesized carbon dots, two types of solar cells were fabricated. Carbon dots were used as sensitizers for ZnO-nanorod-based and for TiO_2-based nanostructured solar cells.

Three types of carbon dots (chitosan CDs, chitin CDs and D-glucose CDs) were used as sensitizers for ZnO-nanorod-based solar cells. ZnO nanorods were successfully coated with carbon dots, and the chitosan-CDs-sensitized solar cells showed the efficiency of 0.061 %. When using layer-by-layer coating method, solar cells with combination of chitosan- and chitin-CDs as sensitizers showed the efficiency of 0.077 %.

All six types of carbon dots (chitosan CDs, chitin CDs, D-glucose CDs, L-arginine CDs, L-cysteine CDs, and lobster CDs) were used as sensitizers for TiO_2-based nanostructured solar cells. TiO_2-based solar cells sensitized with carbon dots showed much higher efficiency compared to the ZnO-nanorod-based solar cells. L-arginine-CDs sensitized TiO_2-based solar cells showed the highest efficiency of (0.362 ± 0.007) %, which was the best efficiency of all fabricated solar cells.

By surveying a range of biomass-derived carbon dots, and demonstrating a clear link between functionalisation and solar cell performance, this PhD research project provides a guide to direct future development of low-cost, biomass-derived sensitizers for nanostructured solar cells.

Contents

Statement of Originality i

Acknowledgements iv

Abstract v

List of Abbreviations and Symbols ix

List of Figures xi

List of Tables xviii

Chapter 1 | Introduction 19

Chapter 2 | State of the Art 25

2.1 Introduction 25

2.2. Syntheses of Carbon Dots 26

2.3. Structural and Optical Properties of Carbon Dots 32

2.4. Applications of Carbon Dots 50

2.5. Solar Photovoltaics Technologies 53

2.6. Solar Cell Basics 55

2.7. Basic Working Principles of Carbon Dot Solar Cells 60

Chapter 3 | Structural and Optical Properties of Carbon Dots 65

3.1. Introduction 65

3.2. Morphology of Carbon Dots 69

3.3. Potential Formation Mechanism of Chitosan -, Chitin- and Glucose-derived Carbon Dots and Microspheres 78

3.4. Chemical Composition and Structural Features of Carbon Dots 84

3.5. The Optical Properties of Carbon Dots 99

3.6. Summary 108

Chapter 4 | Carbon Dot Sensitized Solar Cells 111

4.1. Introduction 111

4.2. Carbon Dots as Sensitizers for ZnO-based Solid State Nanostructured Solar Cells 112

4.3. Carbon Dots as Sensitizers for TiO_2-based Nanostructured Solar Cells 118

4.4. Summary 132

Chapter 5 | Conclusions and Perspectives 136

Chapter 6 | Experimental Section 144

6.1. Synthesis of Carbon Dots 144

6.2. Synthesis of ZnO Nanorods 145

6.3. Fabrication of Photovoltaic Devices Based on ZnO Nanorods Sensitized with Carbon Dots 146

6.4. Synthesis of Homemade TiO_2 Powder (QM-TiO_2) 146

6.5. Fabrication of Photovoltaic Devices Based on TiO_2 Sensitized with Carbon Dots 147

6.6. Current-Voltage Measurements of Solar Cell Devices 148

6.7. Structural and Optical Characterisation Methods 149

Chapter 7 | Appendix 152

7.1. List of Publications 152

7.2. List of International Oral Presentations 152

7.3. List of Poster Presentations 153

7.4. Awards and Honours 153

References 155

List of Abbreviations and Symbols

Key abbreviations and symbols used in this PhD thesis are defined here. Some less important ones are defined in the main body of the text.

BET	Brunauer-Emmett-Teller theory
CDs	Carbon Dots
CQDs	Carbon Quantum Dots
CuSCN	Copper (I) Thiocyanate
DI Water	Deionized Water
EA	Elemental Analysis
E_G	Energy Band Gap
FF	Fill Factor
FTIR	Fourier Transform Infrared Spectroscopy
FTO	Fluorine-doped Tin Oxide
FWHM	Full Width at Half Maximum
GQDs	Graphene Quantum Dots
HMF	Hydroxymethylfurfural
HOMO	Highest Occupied Molecular Orbital
HTC	Hydrothermal Carbonization
I-V	Current-Voltage
J_{SC}	Short Circuit Current Density
J-V	Current Density-Voltage
LbL	Layer-by-Layer
LHE	Light Harvesting Efficiency
LUMO	Lowes Unoccupied Molecular Orbital
M	Molar
η	Efficiency
PCE	Power Conversion Efficiency
PL	Photoluminescence
PLE	Photoluminescence Excitation
PV	Photovoltaic

QDs	Semiconductor Quantum Dots
QSDFT	Quenched Solid Density Functional Theory
QY	Quantum Yield
Raman	Raman Spectroscopy
R_S	Series Resistance
R_{SH}	Shunt Resistance
SEM	Scanning Electron Microscopy
SEM EDX	Scanning Electron Microscopy with Energy Dispersive X-ray Spectroscopy
Si	Silicon
TEM	Transmission Electron Microscopy
$TiCl_4$	Titanium Tetrachloride
TiO_2	Titanium Dioxide
UV-Vis	Ultraviolet-Visible
V_{OC}	Open Circuit Voltage
XPS	X-ray Photoelectron Spectroscopy
XRD	X-ray Diffraction
ZnO	Zinc Oxide
Φ	Quantum Yield

List of Figures

Figure 1. 1 Relationship between power conversion efficiency (%), module areal costs ($/m^2) and cost per peak watt (in $/W$_p$ and $/kWh). 22

Figure 2. 1 Picture of different fractions of fluorescent carbon under 365 nm excitation (A), and TEM images of short tubule carbon (B). 27

Figure 2. 2 (a) Aqueous solution of the PEG$_{1500N}$ - attached carbon dots excited at the indicated wavelengths and photographed directly. (b) The absorption (ABS) and luminescence emission spectra (with excitation wavelengths increasing in 20 nm increments) of carbon dots in an aqueous solution. 28

Figure 2. 3 (a) TEM image of the organophilic derivative with the inset showing an individual carbogenic nanoparticle with a hallo ring around its surface. (b) TEM micrograph of the aqueous-dispersible nanoparticles with the inset showing magnified single nanoparticle. The corresponding size histograms are given aside....................... 29

Figure 2. 4 (a) UV/Vis absorption (—), photoluminescence (PL) excitation (- - - -), and emission (•–•–) spectra of CDs in aqueous solutions. Insets show photographs of CDs in aqueous solution under visible (left) and UV (right) light. (b) Excitation-dependent PL of CDs. 30

Figure 2. 5 A synthetic route using citric acid and ethylenediamine. From ionization to condensation, polymerization, and carbonization. 31

Figure 2. 6 (a) Preparation of the CDs from three different phenylenediamine isomers (oPD, mPD and pPD). (b) Photographs of m-CDs, o-CDs, and p-CDs dispersed in ethanol in daylight (left), and under λ=365 nm UV irradiation (right). 31

Figure 2. 7 (a) TEM and (b) high-resolution TEM images of CDs. The inset shows the size distribution obtained from TEM images. (c) Schematic depicting the proposed structure of CDs. 33

Figure 2. 8 Carbon dots synthesized from candle soot and from graphite rods. 36

Figure 2. 9 Diagram showing the various kinds of electronic transitions that may occur in organic molecules. Reproduced from[85] 38

Figure 2. 10 Optimized geometries of CND model systems: (a) CND1, (b) CND2, (c) $CND1^{bilayer}$, (d) $CND1^{epoxy}$, (e) $CND1^{hydroxy}$, (f) $CND1^{pyridine}$. (g) Simulated absorption spectrum of CND1. 39

Figure 2. 11 (a) Normalized absorption of a PMMA film containing a blend of PAHs (blue) and of the CDs in aqueous solution (black dashed line). (b) PL spectra of the same samples excited at different wavelengths with the CD PL spectrum (black dashed line) as a reference. (c) PL peak wavelength as a function of the excitation wavelength (x-axis). 40

Figure 2. 12 Fluorescence spectra of C-dots1 (a) and C-dots2 (b) monitored at different excitation wavelengths in the range of 280–460 nm. C-dots1 are carboxyl-functionalized (C-dots/COOH) and C-dots2 are amine-functionalized (C-dots/NH2). . 41

Figure 2. 13 (A) TEM image and (B) size distribution of N-Cdots1. (C) TEM image and (D) size distribution of oxidized N-Cdots from carbonized L-DOPA (3-(3,4-dihydroxyphenyl)-L-alanine) obtained in HNO_3 after reflux and dialysis. HRTEM images of (E) N-Cdots1 extracted from carbonized L-DOPA and (F) oxidized N-Cdots from carbonized L-DOPA obtained in HNO_3 after reflux and dialysis (scale bar = 5 nm). HRTEM images show the graphite core with an amorphous shell in oxidized N-Cdots but mainly a graphite property in N-Cdots1. 42

Figure 2. 14 (a) Bulk PL spectrum of CNDs in water (spectrum 1) and exemplary PL spectra of single CNDs dispersed on the surface of a glass cover slide (spectra 2–5). Before plotting, the experimental data has been subjected to averaging over five data points. Inset shows two photographs of a cuvette containing CNDs in an aqueous solution under ambient light excitation (left) and upon excitation with a 488 nm laser (right)...43

Figure 2. 15 (a) Preparation of the RGB PL CDs from three different phenylenediamine isomers (oPD, mPD and pPD). (b) Photographs of *m*-CDs, *o*-CDs, and *p*-CDs dispersed in ethanol in daylight (left), and under λ=365 nm UV irradiation (right). (c–e) UV/Vis absorption spectra of mPD, oPD, and pPD (red line), m-CDs, o-CDs, and p-CDs (black line), and PL emission spectra of m-CDs, o-CDs, and p-CDs (blue and green lines). ... 44

Figure 2. 16 (a) PL and Abs spectra of IPCA, inset shows photographs of IPCA solution under visible and UV light. (b) A schematic of the relationship between different products in the one-pot hydrothermal system of citric acid (CA) and ethylenediamine (EDA). (c) A schematic of the CDs obtained at different hydrothermal temperatures... 46

Figure 2. 17 (a) Splitting of energy levels in semiconductor quantum dots (QDs) due to the quantum confinement effect. Band gap of QDs increases with the decrease in size of QDs. (b) Photoluminescence mechanism in QDs. 49

Figure 2. 18 Scheme of the different photoluminescence mechanisms in CDs: (a) when trap states are present and (b) when individual emitters are present.............................. 50

Figure 2. 19 Average module efficiencies and price per area from 2009-2013 are shown for commercial PV technologies in three conventional generations (G1 in red, G2 in green and G3 in blue). The single G3 data point corresponds to performance projections for a III-V MJ module (multijunction module)... 55

Figure 2. 20 Structure and electric properties of a *pn*-junction diode before and after diffusion of charge carriers across the junction interface. 56

Figure 2. 21 Energy band diagrams during operation of a *pn*-junction diode in the dark showing: (a) reverse bias, (b) equilibrium, and (c) forward bias conditions. Blue and orange arrows represent flux of electrons and holes, respectively................................. 57

Figure 2. 22 (a) Current-voltage (J-V) characteristics of a solar cell in the dark (blue curve) and under illumination (red curve). The short-circuit current density (J_{SC}), open-circuit voltage (V_{OC}), and fill factor (*FF*) are indicated on the graph. Since the current output of an illuminated solar cell is proportional to its illuminated surface area, the current density (J ; current divided by area) is normalized for different cell sizes. (b, c) Current and voltage are measured between the positive and negative terminals of the solar cell. 57

Figure 2. 23 Operation of a solar cell under illumination and interaction of photons with semiconductor material. 58

Figure 2. 24 Effects of the series resistance (R_S) and shunt resistance (R_{SH}) on the shape of an *I-V* curve.. 60

Figure 2. 25 Schematic representation of dye sensitized solar cell (DSSC)................... 61

Figure 2. 26 Photoinduced processes occurring during the photovoltaic energy conversion at the surface of the nanocrystalline TiO_2. 62

Figure 2. 27 Operating principle of a typical carbon dot sensitized solar cell (CDSSC). 63

Figure 3. 1 Structure of D-glucose in its open-chain form. 66

Figure 3. 2 Structure of α-D-glucopyranose and β-D-glucopyranose isomers. 67

Figure 3. 3 Structure of chitin (a) and chitosan (b). 68

Figure 3. 4 Structure of L-arginine (a) and L-cysteine (b). 69

Figure 3. 5 TEM images at 200 kV and corresponding size histograms of as-synthesized carbon dots derived from: a) chitosan, b) chitin, c) D-glucose, d) L-arginine, e) L-cysteine and f) lobster. 70

Figure 3. 6 a) High resolution TEM image at 200 kV of chitosan carbon dots and b) electron diffraction image of chitosan carbon dots. 72

Figure 3. 7 SEM images of: a) chitosan microspheres, b) chitin microspheres and c) glucose microspheres. 73

Figure 3. 8 TEM microtommed micrography of glucose microspheres at different magnifications. 74

Figure 3. 9 CO_2 adsorption isotherms (273 K) and pore size distributions (calculated using CO_2 adsorption data *via* the NLDFT kernel assuming carbon slit pores) of chitosan-, chitin- and glucose microspheres (continued from previous page). 76

Figure 3. 10 The proposed mechanism of TPA formation: (1) amide formation, (2) imide formation, (3) dehydration and (4) intramolecular condensation. 83

Figure 3. 11 FTIR spectra of: (a,b) carbon dots and (c, d, e) carbon microspheres. 86

Figure 3. 12 Deconvoluted C 1s and N 1s peaks of: (a, b) chitosan CDs, (c, d) chitin CDs, (e) glucose CDs, (f, g) L-arginine CDs, (h, i, j) L-cysteine CDs and (k, l) lobster CDs. 91

Figure 3. 13 Deconvoluted C 1s and N 1s peaks of: (a, b) chitosan microspheres, (c, d) chitin microspheres and (e) glucose microspheres. 94

Figure 3. 14 Raman spectra of: a) carbon dots and b) carbon microspheres. 96

Figure 3. 15 XRD profiles for: (a, b) carbon dots and c) carbon microspheres. 98

Figure 3. 16 Carbon dots under daylight (undiluted) and under UV excitation of 365 nm (diluted solutions). Row (a) from left to right: chitosan CDs, chitin CDs and D-glucose CDs. Row (b) from left to right: L-arginine CDs, L-cysteine CDs and lobster CDs. ... 100

Figure 3. 17 UV-Vis absorption spectra of as-synthesized carbon dots. 101

Figure 3. 18 Photoluminescence spectra and excitation-independent/dependent emission plots of the as-synthesized carbon dots (continued from previous pages): chitosan CDs (a, b, c); chitin CDs (d, e, f); glucose CDs (g, h, i); L-arginine CDs (j, k, l); L-cysteine CDs (m, n, o) and lobster CDs (p, q, r). 104

Figure 3. 19 Normalized absorption, photoluminescence excitation (PLE) and photoluminescence (PL) emission plots for all carbon dots (PL excitation wavelength is given in brackets): a) chitosan CDs, b) chitin CDs, c) D-glucose CDs, d) L-arginine CDs, e) L-cysteine CDs and f) lobster CDs. 105

Figure 3. 20 Schematic diagram of energy levels of carbon dots' core and surface states. Highest occupied molecular orbital (HOMO), lowest unoccupied molecular orbital (LUMO), excitation energy (E_{ex}), energy band-gap (E_G), and quantum yield (QY). ...107

Figure 4. 1 TEM images of ZnO nanorods coated with carbon dots: a) single coating of glucose CDs and b) four layers of chitosan CDs + glucose CDs. Clear texturing on the smooth crystalline ZnO surface indicated the coverage of ZnO nanorods with carbon dots (highlighted by the blue area to show the interface between the ZnO and CDs)..114

Figure 4. 2 UV/Vis transmission spectra for ZnO nanorods coated with carbon dots using single layer of carbon dots (a), and 4-layer layer-by-layer (LbL) coating (b). ...115

Figure 4. 3 Illuminated current-voltage plots for ZnO/CDs/CuSCN solar cells using single layer of carbon dots (a), and 4-layer layer-by-layer (LbL) coating (b). 115

Figure 4. 4 (a) Schematic overview of the TiO_2-based nanostructured solar cell sensitized with carbon dots, and (b) non-sensitized photoanodes consisting of TiO_2 paste coated onto FTO glass substrate. 119

Figure 4. 5 (a) Absorption spectra of TiO_2 (P25) sensitized with different carbon dots. (b) Images of non-sensitized TiO_2 (P25) photoanode (left) and sensitized TiO_2 (P25) photoanode with carbon dots (right). (c) As-fabricated complete nanostructured solar cell (2x2 cm) held together by paper clips (yellow) and consisting of: FTO / TiO_2 (P25) / CDs / electrolyte / Pt electrode. 120

Figure 4. 6 Illuminated current-voltage (J-V) data for solar cells composed of FTO / TiO_2 (P25) / CDs / (I_3^-/I^-) electrolyte / Pt electrode : a) chitosan CDs+P25, chitin CDs+P25 and D-glucose CDs+P25 ; b) L-arginine CDs+P25, L-cysteine CDs+P25 and lobster CDs+P25. Data is shown for the best solar cell devices of each type. 122

Figure 4. 7 Box plots of solar cell parameters using carbon dots derived from L-arginine (ARG), L-cysteine (CYS), lobster shells (LOB), chitosan (CS), chitin (CT) and glucose (GLU): (a) short-circuit current density (J_{sc}); (b) open-circuit voltage (V_{oc}); (c) fill factor (*FF*); (d) power conversion efficiency (*PCE*). Height of box plot represents standard error while whiskers represent min-max value. 123

Figure 4. 8 (a, b) TEM images of QM-TiO_2 powder, and (c) corresponding electron diffraction image. 127

Figure 4. 9 (a, b) TEM images of commercial TiO_2 (P25) powder, and (c) corresponding electron diffraction image. 128

Figure 4. 10 (a) Nitrogen adsorption-desorption isotherms and (b) pore size distribution plots for TiO_2 (P25) and QM-TiO_2 powders. Surface area was determined by applying the BET theory and the pore size distribution was obtained by fitting the isotherm to QSDFT adsorption kernel implemented in the NovaWin software. 128

Figure 4. 11 XRD plots for the as-synthesized TiO_2 (P25) powder (a) and QM-TiO_2 powder (b). (A=anatase, R=rutile). 129

Figure 4. 12 (a) Absorption spectra of QM-TiO_2 sensitized with carbon dots. (b) Illuminated current-voltage (J-V) curves for solar cells made from QM-TiO_2 sensitized with L-Arginine CDs and chitosan CDs. 130

Scheme 3. 1 Potential chemical reactions involved in the formation of carbon dots and carbon microspheres formed by hydrothermal carbonization of glucose: a) dehydration of glucose to HMF and potentially to levulinic and formic acid; b) self-condensation reaction of HMF; c) Diels-Alder condensation of HMF; d) reaction of acetone with HMF. 78

Scheme 3. 2 Potential chemical reactions involved in the formation of carbon dots from chitosan/chitin precursors: a) hydrolysis of chitosan/chitin to glucosamine; b) glucosamine dehydration / deamination to HMF and ammonia; c) reaction of HMF with ammonia. 80

Scheme 3. 3 Possible formation of carbon dots and their further growth into carbon microspheres, along with a schematic of their chemical structure when produced from glucose or chitosan/chitin precursors. 81

Scheme 4. 1 Preparation of carbon dot sensitized nanostructured solar cells by hydrothermal carbonization of biomass-derived precursors, and combination with chemically grown ZnO nanorods. 113

List of Tables

Table 3. 1 Concentration of carbon dots and synthesis mass yield of carbon microspheres, all after 6 h of HTC reaction at 200 °C. 77

Table 3. 2 Elemental composition of the as-synthesized carbon dots (CDs) and the selected examples of carbon microspheres. 85

Table 3. 3 Summary of FTIR results for as-synthesized carbon dots (CDs). 87

Table 3. 4 The summary of general XPS data of carbon dots and carbon microspheres. 89

Table 3. 5 Summary of XPS peak positions found for all CDs. 93

Table 3. 6 Summary of Raman analysis data for carbon dots and carbon microspheres. Data fitting has been carried out using Lorentzian peaks. The last column shows the ratio of D to G band intensity. 96

Table 3. 7 Position of the maximum excitation peaks, PL emission peaks, FWHM of maximum PL emission and fluorescence QY values, for all carbon dots. 107

Table 4. 1 Solar cell parameters for CDs-sensitized ZnO nanorod solar cells, obtained from J-V curves in Figure 4. 3. 116

Table 4. 2 Solar cell operational parameters for carbon dot sensitized TiO_2 (P25) solar cells. Averages and errors are taken from three devices per type and three measurements per device. 122

Table 4. 3 Light harvesting efficiency (LHE), power conversion efficiency (PCE) and average internal efficiency of as-fabricated solar cells with commercial TiO_2 (P25). 124

Table 4. 4 Solar-cell operational parameters for solar cells fabricated from QM-TiO_2 sensitized with L-Arginine CDs and chitosan CDs. Averages and errors are taken from three devices per type and three measurements per device. 130

Table 4. 5 Light harvesting efficiency (LHE), power conversion efficiency (PCE) and average internal efficiency of as-fabricated solar cells with QM-TiO_2 sensitized with L-arginine CDs and chitosan CDs. 131

Chapter 1 | Introduction

Population and income are the key drivers behind the growing demand for energy. The world's population is projected to reach nearly 8.8 billion people by the year 2035. Over the same period, GDP (gross domestic product) is expected to increase more than double where around one-fifth of that increase will come from the growth in population and four-fifths from the improvements in the productivity. The growth in the world economy means that more energy will be required and the energy consumption is predicted to increase by 34% between 2014 and 2035.[1] Fossil fuels remain the dominant source of energy today and accounted for 86% of the total energy supply in 2015 (projections suggest that fossil fuels will account for almost 80% of total energy supply in 2035).[1] In 2015 the total world oil consumption was 4331.3 millions of tonnes of oil which increased with 10.1% compared to the year 2005.[1] Burning fossil fuels generates huge amounts of CO_2 in the earth's atmosphere, extinguishing our ecosystem. Total world CO_2 emissions in 2015 were 33508.4 million tonnes of CO_2 which increased with 17.4% compared to the year 2005.[1]

To decrease our dependence on fossil fuels and reduce the risk of destroying the planet Earth, we must seek for novel sustainable technologies and renewable energy sources. New materials should be created without using rare elements, but by using precursors widely provided by nature.

Carbon is one of the most widespread elements in nature and is responsible for our existence. Carbon exists in nature in different allotrope forms such as diamond, graphene, graphite and amorphous carbon.[2] A large number of new carbon materials with well-defined nanostructures have been synthesized, such as fullerenes, carbon dots, carbon nanotubes, graphene, nanodiamonds, etc.[2] With regard to applications, carbon will continue to play an important role. Despite the fact that carbon is widespread in nature, it is still mainly synthesized from fossil-based precursors using energy-consuming processes which generate toxic gases and chemicals. Preparation of carbon nanomaterials from renewable resources is becoming a recognized area, specifically in terms of economic advantages and applications. Nature has developed the production of carbon from biomass by using the process of coal formation, so we only need to translate this process into a synthetic process.

Hydrothermal carbonization (HTC) is a novel technology able to produce carbon materials from biomass in water at low temperatures, mimicking the natural process of coal formation (which takes millions of years) in the laboratory in just few hours. The HTC technique is of significant importance and has been intensively researched over the last few years as a sustainable synthetic route for the production of carbon materials with a variety of applications.[3] This method was first described by Friedrich Bergius in 1913 as a synthetic route to mimic coal formation in few hours under self-generated pressures and mild temperatures (130-250 °C).[4] In 1931 Bergius was awarded the Nobel Prize for his studies on the production of synthetic coal as well as hydrogenation and high pressure reactions. A revival of this process started at the Max-Planck Institute of Colloids and Interfaces in Germany throughout the work of Titirici *et al.*[5] HTC process is currently considered as one of the most sustainable approaches for the production of functional carbon materials. The transformation mechanism and the chemical structure of HTC carbons have been understood, along with ways for their functionalization with organic groups as well as nanoparticles, and an important array of applications was demonstrated.[6,7] A prerequisite for the HTC process is the use of carbohydrates or carbohydrate-rich biomass as a precursor. These compounds are highly abundant and renewable.

In the HTC process, renewable biomass or biomass-derived precursors are used and are converted into carbonaceous materials using mild processing temperatures (< 200 °C) under self-generated pressure.[3] The HTC process relies on the dehydration of carbohydrates to hydroxymethylfurfural (HMF) followed by a reaction cascade consisting of ring-opening reactions, substitutions, cycloadditions and polycondensations to form the final carbon structure.[8,9] The HTC method is capable of producing carbon and carbon hybrid materials with controlled structure and morphologies in an energy-saving manner.[10]

Some important advantages of this new carbonization technique should be underlined: (i) carbonization temperatures are low (130-250 °C) ; (ii) carbonization takes place typically in water under self-generated pressure [11] ; (iii) spherical micro-sized particles are obtained [12] ; (iv) controlled porosity can be introduced by using natural templates, nanocasting procedures, activation procedures and thermal treatments [13,14] ; (v) resulting carbon particles have (polar) oxygenated groups on the surface which can be used in post-functionalization strategies [15] ; (vi) carbonaceous materials can be combined with inorganic nanoparticles to form composites with special properties [16] ;

(vii) electronic properties and surface chemistry can be controlled by additional thermal treatment, while the morphology and porosity are maintained ; (viii) synthesis can be described as “carbon negative”, which means that it has the potential to bind the CO_2 fixed by the original plant precursor [12].

Solar energy is one of the few low-carbon, renewable resources which possess the scalability and the technological maturity to meet the ever-growing global demand for electricity. Among solar energy technologies, solar photovoltaics (PV) are the most widely deployed and have provided 1.1% of the global power generation in 2015.[1] The global solar PV power generating capacity in 2015 was 231 GW (gigawatt), which represents an increase of 28.1% versus the year 2014.[1] In 2015, China’s cumulative installed capacity (43.5 GW) moved it ahead of Germany (39.7 GW), with Japan (35.4 GW) and the US (25.6 GW) following.[1]

The Sun continuously delivers about 174 000 TW (terawatt) of energy to the upper level of the Earth's atmosphere at an average power density of 1366 W m^{-2} (solar constant).[17] This value is reduced to around 1000 W m^{-2} by atmospheric absorption and scattering, and to 125 - 305 W m^{-2} (3 to 7.3 kWh per m^2 per day) by latitude-dependent incidence, seasonal variation, and daily variation.[18] Cloud cover and weather further reduce this value to 183 W m^{-2}, which is the global-average solar irradiance over land. This represents the starting point for all solar harvesting technologies.[19]

Nanostructured solar cells provide opportunities to revolutionize the conversion of solar energy by enabling highly efficient and low-cost solar cell devices. Nanostructured solar cells represent the next-generation solar cells (third generation solar cells) which include those that are based on nanostructures or nanostructured interfaces such as nanowires, mesoscopic, semiconductor quantum dot and carbon dot solar cells.[20,18] They hold great promise towards new approaches for converting solar energy into electricity.

The commercial and domestic adoption of photovoltaics as an energy source depends on the costs to consumers expressed in \$/kWh, and how this compares with the cost of conventional energy sources. The overall cost can be estimated from the rated cost per peak watt (in \$/W_p), which includes costs related to the operation of the solar module (“module costs”) and costs related to its installation (“balance of system costs”). “Module costs” strongly depend on the efficiency of a solar module to convert sunlight into electricity. With the current cost of photovoltaics approaching about 1 \$/W_p, the average cost to the consumer is ~ 0.10 \$/kWh.[21] This is comparable to the average cost of grid electricity in the US, and this situation is called grid parity. For widespread adoption of solar PVs, the costs of next-generation PVs should be reduced to 0.05 - 0.03 \$/kWh and these solar cells should show long-term stability of 10-15 years (**Figure 1. 1**).

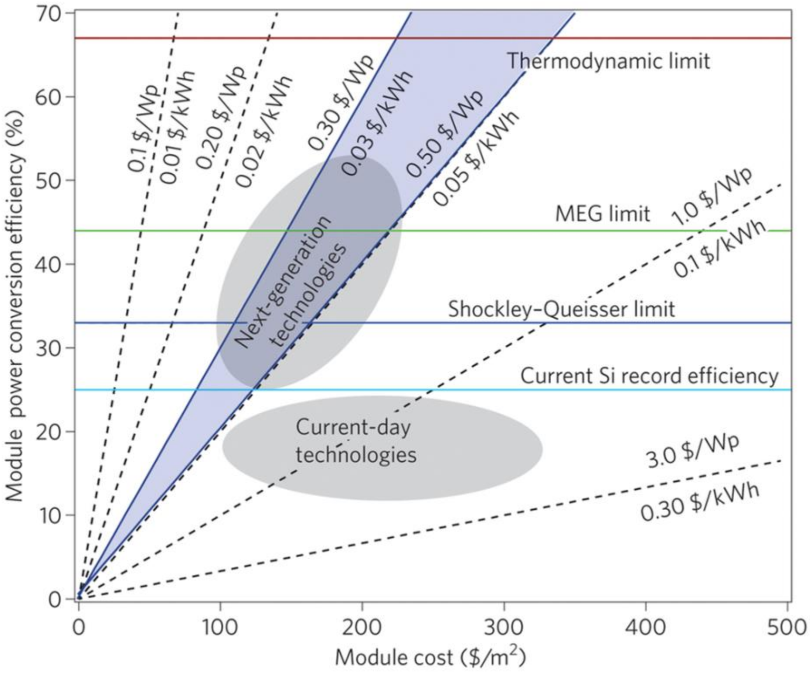

Figure 1. 1 Relationship between power conversion efficiency (%), module areal costs (\$/m^2) and cost per peak watt (in \$/W$_p$ and \$/kWh).

Blue horizontal line is the Shockley-Queisser limit [22,23] for single-junction solar cell devices (32.9 % efficiency). Third-generation PV devices could increase the limiting efficiency (multiexciton generation limit, MEG limit). The thermodynamic limit at 1 sun irradiation is shown as the red line at 67% and can be reached by an infinite stack of *p-n* junctions. Reproduced from Beard *et al.*[21], Copyright 2014 Macmillan Publishers Limited.

Nanoscale solar cell systems show different properties compared with bulk or thin film solar cells of the same compounds. The large surface-to-volume ratio of nanomaterials can provide various benefits, and objects with a size of 1-20 nm can also exhibit quantization effects which influence the energy band gap of a material. Two approaches based on nanostructures are being explored for photovoltaics: (i) significant reduction in material usage and reduction in final costs; (ii) photovoltaic devices with a higher limiting efficiency than the Shockley-Queisser limit [22,23] (32.9 % efficiency). Both approaches can lead to significantly lower costs per kWh of next-generation solar cell devices.

The main aims and objectives of this PhD research were: (i) to synthesize fluorescent carbon dots from renewable biomass-derived precursors by using hydrothermal synthesis method; (ii) to fully characterize and explain the structural and optical properties of the as-synthesized carbon dots; (iii) to try to explain the possible formation mechanism of fluorescent carbon dots; (iv) to use the as-synthesized carbon dots as sensitizers for ZnO-based and TiO_2-based nanostructured solar cells; (v) to measure and explain the operational parameters of as-fabricated solar cell devices.

This PhD thesis is composed of 7 chapters. Chapter 1 opens with a general introduction on the topic of the thesis. It gives an overview of fossil fuel consumption in the world, CO_2 generation, carbon nanomaterials and their synthesis, advantages of hydrothermal carbonization method, and a general overview of solar photovoltaics and nanostructured solar cells.

Chapter 2 describes the current state of the art on the synthesis of carbon dots, structural and optical properties of carbon dots, and different applications of carbon dots. Also, this chapter offers a primer on solar cell basics and the basic operating principles of carbon dot solar cells.

Chapter 3 is focused on the characterization and fundamental understanding of structural and optical properties of as-synthesized carbon dots. Also, this chapter offers an explanation for the possible formation mechanism of fluorescent carbon dots synthesized by hydrothermal methods.

Chapter 4 presents the applications of carbon dots in the next-generation solar photovoltaics. This chapter shows that carbon dots can be successfully used as sensitizers for ZnO-based and TiO_2-based nanostructured solar cells. Chapter 4 also describes the full characterization and measurements of operational parameters of as-fabricated solar cell devices.

Conclusions about the work done in this PhD thesis and future perspectives about the development of photoluminescent carbon nanomaterials are given in Chapter 5.

Chapter 6 describes the experimental procedures used in this PhD research for the synthesis and characterization of carbon dots, and also describes the fabrication and characterization of nanostructured solar cells.

The final chapter, Chapter 7, offers an overview of the PhD candidate’s accomplishments considering the publications, awards and honours, international oral talks, and poster presentations.

Chapter 2 | State of the Art

2.1 Introduction

Carbon is one of the most important and unique elements with a huge chemical diversity. Since carbon is the main building block of organic compounds, it is essential for all living organisms. Carbon and its chemical compounds are also important products in chemical and energy industry.[7,24] Pure carbon is an inorganic material which exists in multiple allotropes with variety of properties. Two best known crystalline allotropes of carbon are graphite (sp^2 hybridized carbon atoms) and diamond (sp^3 hybridized carbon atoms), and also amorphous carbon.[25] In bulk, graphite and diamond can be considered to consist of infinite carbon networks and they do not show photoluminescent properties. If the size of these carbon networks is reduced to nanometre scale, the resulting structural changes usually change electronic properties of the material, and thus its optical properties.

A large numbers of nanoscale allotropes of carbon have been discovered in the last thirty years, such as fullerenes[26], carbon nanotubes[27], graphene[28] and photoluminescent carbon nanoparticles[29]. Members of the family of carbon nanoparticles include: graphene quantum dots[30,31], carbon dots[32,33] and polymer dots[34]. Clear classification of these carbon nanoparticles is sometimes difficult. Graphene quantum dots (GQDs) are considered to consist of few layers of single-layer graphene sheets often functionalized with different functional groups at the surface/edges. GQDs are anisotropic with lateral dimensions greater than their height.[35] Polymer dots (PDs) are considered to be amorphous agglomerates of conjugated and cross-linked polymers. Properties of PDs are mostly determined by the constituting monomers, and the carbon core and connected polymer chains can self-assemble to form PDs.[35] Carbon dots (CDs) are spherical carbon nanoparticles with sizes usually bellow 20 nm in diameter, which can possess crystalline lattice or can be amorphous, and usually have different functional groups present on their surface.[35,36] If carbon dots possess crystalline features they are usually called carbon quantum dots (CQDs). Characteristic optical properties and structural features of carbon dots are largely determined by the specific synthesis methods used. Colloidal carbon dots synthesized by solution-based synthesis methods offer the greatest flexibility in introducing different heteroatoms and dopants.[37,38]

Carbon dots possess easy and cheap synthesis, low toxicity, biocompatibility, good optical properties with high fluorescence quantum yield and stability against photo-bleaching, making them promising materials for applications like bioimaging, photovoltaic solar cells, displays and solid state lighting.[39,40]

2.2. Syntheses of Carbon Dots

A large variety of synthetic techniques and starting precursors has been used to synthesize carbon dots (CDs). Generally speaking, the synthesis methods can be divided into top-down and bottom-up methods, all having certain advantages and disadvantages. Top-down methods involve physical or chemical disruption of bulk carbon precursor usually graphite or amorphous carbon. This can be achieved by laser ablation[41], arc discharge[29], electrochemical synthesis[42] and chemical oxidation in strong acids[43]. Bottom-up syntheses generally do not require any specific starting precursor because CDs can be prepared with bottom-up synthesis from any organic precursor that undergoes carbonization. Bottom-up syntheses offer simple and fast preparation of CDs with large number of surface functional groups, and allow easy introduction of dopants which significantly affect the photoluminescent properties of as-synthesized CDs. Bottom-up methods include solvothermal synthesis[44,45,33], microwave synthesis[46,47] and template supported synthesis[48].

In top-down methods starting materials are dispersed or cut into small fragments of nanometre sizes. Fluorescent carbon nanoparticles were firstly discovered in 2004 by Xu *et al.* as by-product in the synthesis of carbon nanotubes by arc-discharge method[29]. They were able to synthesize blue-green, yellow and orange fluorescent carbon nanoparticles (**Figure 2. 1**).

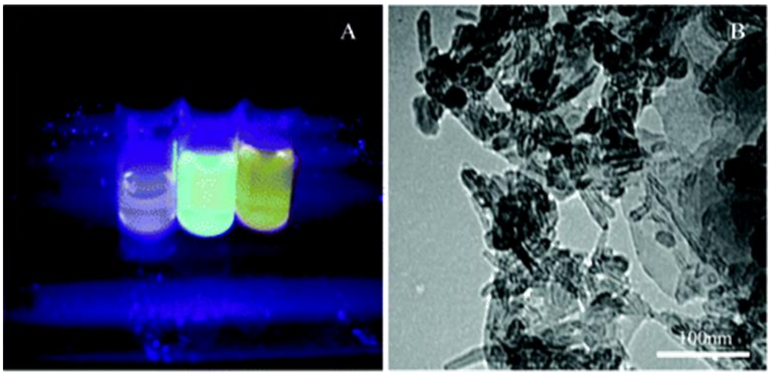

Figure 2. 1 Picture of different fractions of fluorescent carbon under 365 nm excitation (A), and TEM images of short tubule carbon (B).
Reproduced from Xu *et al.*[29], Copyright 2004 American Chemical Society.

In 2006 Sun *et al.* tried to directly synthesize fluorescent carbon nanoparticles by laser ablation of graphite. After the surface passivation with PEG $_{1500N}$ (diamine-terminated oligomeric poly-(ethylene glycol)) of as produced nanoparticles, they managed to obtain fluorescent carbon nanoparticles with photoluminescence quantum yield (QY) of 10 % (**Figure 2. 2**).[41] Put simply, photoluminescence QY is the ratio of photons absorbed to photons emitted through fluorescence by a certain material. QY gives the probability of the excited state being deactivated by fluorescence rather than by another, non-radiative mechanism.

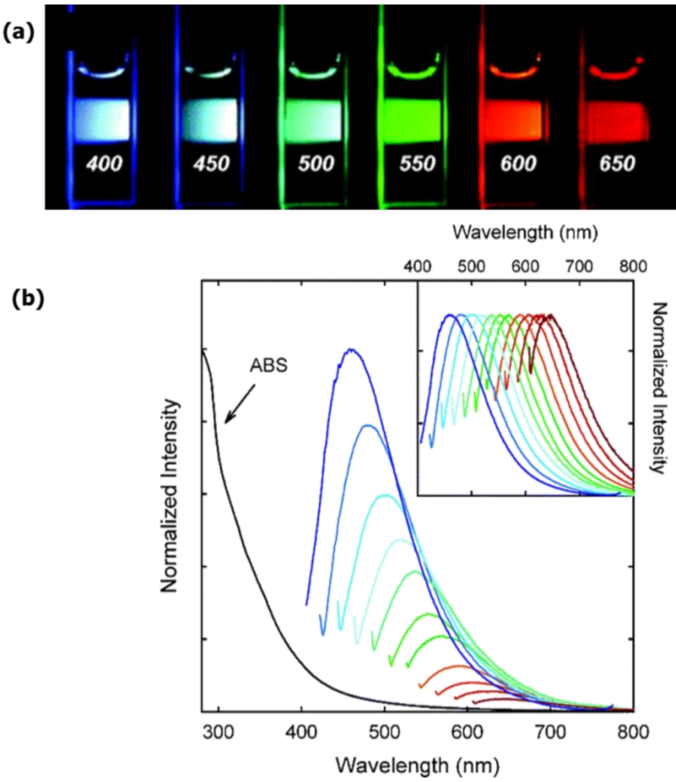

Figure 2. 2 (a) Aqueous solution of the PEG_{1500N} - attached carbon dots excited at the indicated wavelengths and photographed directly. (b) The absorption (ABS) and luminescence emission spectra (with excitation wavelengths increasing in 20 nm increments) of carbon dots in an aqueous solution.

Reproduced from Sun *et al.*[41], Copyright 2006 American Chemical Society.

Hu *et al.*[49] have developed one-step synthesis of fluorescent carbon nanoparticles by irradiating graphite with a 1064 nm pulsed laser. Their fluorescent CDs have shown photoluminescence QY of 8 %. In their further study they showed that the size of as-synthesized CDs can be tuned from 3 nm to 10 nm by changing the laser pulse width, and the maximum observed photoluminescence QY was 12 %.[50] Combustion soot from natural gas and burning candles has also been collected and further treated in harsh acidic environments to obtain fluorescent carbon nanoparticles.[43] In 2007 Zhou *et al.*[51] have synthesized fluorescent carbon nanoparticles by electrochemical etching from multiwalled carbon nanotubes, with photoluminescence QY of 6 %. Bao *et al.*[42] have synthesized fluorescent CDs by exfoliation from carbon fibres and they showed that optical properties of CDs changed significantly after further electrochemical surface oxidation. Top-down synthesis methods have led to the discovery of fluorescent carbon nanoparticles but further development in the area of fluorescent CDs is mostly related to the bottom-up synthesis methods.

Bottom-up synthesis methods offer the possibility to use wide variety of molecular precursors with different functional groups to synthesize fluorescent colloidal carbon nanoparticles. Some of the bottom-up synthesis methods include: solvothermal/hydrothermal synthesis[44,33,34,52], high temperature pyrolysis by using microwave heating[53] and thermal combustion of certain molecular precursors[54]. In 2008 Bourlinos *et al.*[44] have synthesized for the first time fluorescent CDs from organic molecular precursors (**Figure 2. 3**). They have obtained organophilic nanoparticles by using citric acid monohydrate and octadecylamine, and have also obtained hydrophilic nanoparticles by using hydrothermal synthesis of citric acid monohydrate and *N*-(2-hydroxyethyl)ethylenediamine.

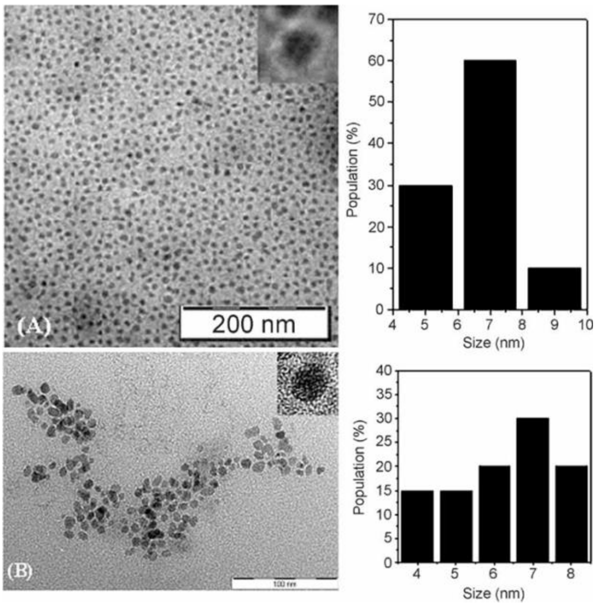

Figure 2. 3 (a) TEM image of the organophilic derivative with the inset showing an individual carbogenic nanoparticle with a hallo ring around its surface. (b) TEM micrograph of the aqueous-dispersible nanoparticles with the inset showing magnified single nanoparticle. The corresponding size histograms are given aside.
Reproduced from Bourlinos *et al.*[44], Copyright 2008 WILEY-VCH.

Carbon dots have also been synthesized from a vast variety of natural precursors such as grass[34], orange juice[52], soy milk[55], rice[56], coffee[57], etc. This points out to an important concept in synthesis of CDs where the thermal treatment of substances which contain carbon, hydrogen and oxygen will in most cases give fluorescent carbon nanoparticles. It was also observed that CDs containing nitrogen showed some favourable optical properties, where nitrogen was present on the surface of CDs [58,59].

Generally speaking, synthesis of CDs involves one molecular precursor which is the carbon source and another molecular precursor which contains other elements which will be incorporated into the final CD’s structure. Therefore, in the last few years the focus in synthesis of CDs has switched to controlled synthesis of CDs by using selected molecular precursors which contain specific heteroatoms such as nitrogen or sulphur. One of the most used combinations is citric acid as carbon source and ethylenediamine or urea as nitrogen source[33,60]. By reacting citric acid with ethylenediamine under hydrothermal conditions, Zhu *et al.*[33] have synthesized fluorescent CDs with high photoluminescence QY of 82 % (**Figure 2. 4**). The optical properties of the as-synthesized CDs were dependent on the synthesis temperature and the ration between the starting precursors.

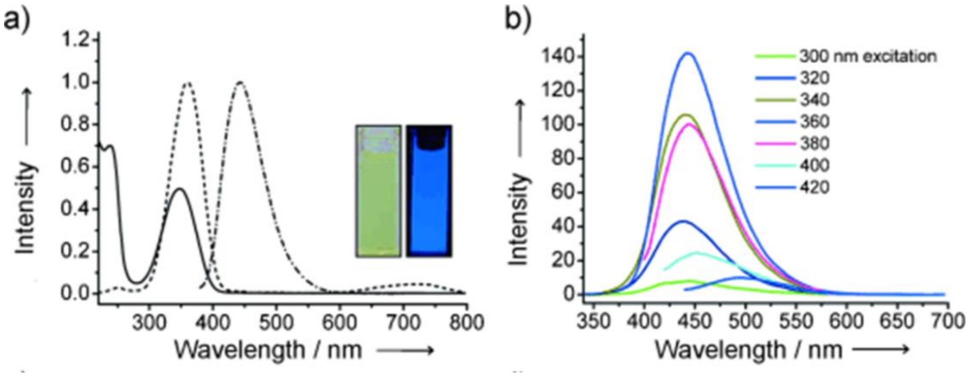

Figure 2. 4 (a) UV/Vis absorption (—), photoluminescence (PL) excitation (- - - -), and emission (•–•–) spectra of CDs in aqueous solutions. Insets show photographs of CDs in aqueous solution under visible (left) and UV (right) light. (b) Excitation-dependent PL of CDs. Reproduced from Zhu *et al.*[33], Copyright 2013 WILEY-VCH.

The authors have also proposed the possible CD’s formation mechanics where citric acid and ethylenediamine form a salt at elevated temperatures and then react to form a large network due to the functional groups present on the surface of precursor molecules. Polymerized network carbonizes at temperatures around 200 °C resulting in amorphous CDs with small sp^2 crystalline domains (**Figure 2. 5**).

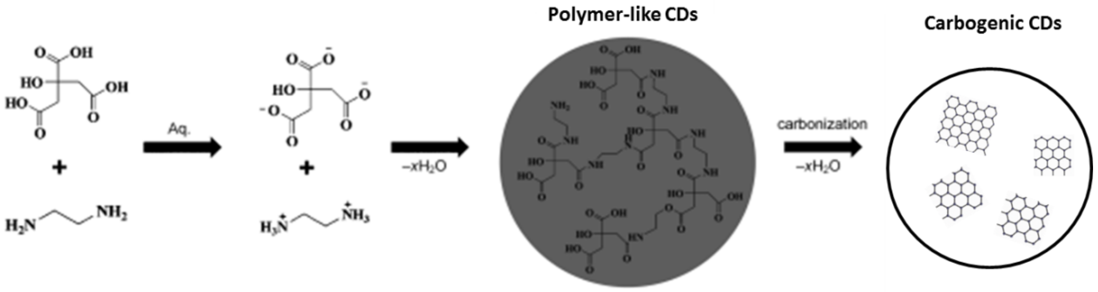

Figure 2. 5 A synthetic route using citric acid and ethylenediamine. From ionization to condensation, polymerization, and carbonization.

Reproduced from Zhu *et al.*[33], Copyright 2013 WILEY-VCH.

Jiang *et al.*[45] have synthesized N-doped, colour tunable CDs by using phenylenediamines which were solvothermally heated in ethanol (180 °C for 12 h). Since the starting precursors had different variation of the functional group configuration, it led to CDs with the photoluminescent emission from green, blue to red colour (**Figure 2. 6**).

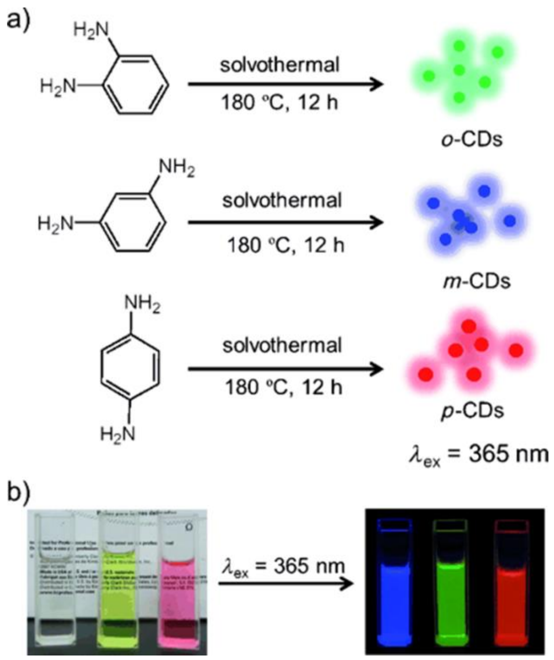

Figure 2. 6 (a) Preparation of the CDs from three different phenylenediamine isomers (oPD, mPD and pPD). (b) Photographs of m-CDs, o-CDs, and p-CDs dispersed in ethanol in daylight (left), and under λ=365 nm UV irradiation (right).

Reproduced from Jiang *et al.*[45], Copyright 2015 WILEY-VCH.

Another element which is often included in the structure of CDs is sulphur. Sulphur is mostly used in co-doping with nitrogen in order to improve the optical properties of CDs specifically photoluminescence QY [61,56]. Nitrogen and sulphur co-doped CDs were synthesized by Dong *et al.*[62] by using hydrothermal treatment of citric acid and L-cysteine. They have obtained CDs with high photoluminescence QY of 73 %. It is interesting to notice that Kasprzyk *et al.*[63] have also used citric acid and L-cysteine for the synthesis of carbon dots, and have pointed out to the formation of highly fluorescent molecular fluorophore 5-oxo-2,3-dihydro-5H-[1,3]thiazolo[3,2-a]pyridine-3,7-dicarboxylic acid (TPA).

Boron and phosphorus containing molecular precursors have also been used for the synthesis of CDs. Zhou *et al.*[64] have synthesized P-doped carbon quantum dots (PCQDs) by a solvent-thermal method using phosphorous tribromide and hydroquinone as precursors. The as-prepared PCQDs showed strong visible fluorescence with photoluminescence QY up to 25%. Shan *et al.*[65] have synthesized B-doped carbon quantum dots by using hydroquinone and boron tribromide as precursors in hydrothermal conditions at 200 °C. P-N and B-N co-doped CDs have been synthesized by Barman *et al.*[66] who used boric acid and ortho-phosphoric acid in combination with citric acid and diethylenetriamine, in hydrothermal treatment at 170 °C for 1 h.

There is still an open debate about whether and to which extend these dopants are being incorporated into the core of CDs during the synthesis procedure. It is hard to distinguish between the surface and the core of such small carbon nanoparticles by using currently available characterization techniques which don't provide sufficient spatial resolution.

2.3. Structural and Optical Properties of Carbon Dots

The structure of carbon dots differs a lot when using different synthesis methods and when incorporating different dopant elements. Generally speaking, CDs can be considered to consist of a carbon core and different functional groups attached to the surface. The carbon core consists of an amorphous carbon network which can contain crystalline domains with sp^2 hybridized carbon.[67] Both crystalline sp^2 domains and sp^3 domains are usually confirmed by Raman spectroscopy with the corresponding peaks at around 1560 cm^{-1} (G band) and around 1360 cm^{-1} (D band).[68,62] G band (crystalline) confirms the presence of the sp^2 hybridized (crystalline) core while the D band (disorder) accounts for defects and disordered carbon associated with amorphous carbon. If the intensity ratio (I_D/I_G) is small (~0.5) it shows that the as-synthesized CDs have high crystalline carbon core, while larger ratio indicates a growing disorder and amorphous carbon present in CDs. Dong *et al.*[62] have synthesized CDs from precursors containing only carbon and oxygen atoms ("undoped CDs" denoted O-CDs), nitrogen-doped CDs (N-CDs), and nitrogen and sulphur co-doped CDs (N,S-CDs). They showed that O-CDs had the largest I_D/I_G ratio of 0.8 while N-CDs had 0.6 and N,S-CDs had 0.5. They concluded that the O-CDs are characterized by the largest disorder.

Also, HRTEM images and corresponding electron diffraction images are used to confirm the presence of crystalline structure in CDs, showing lattice fringes and diffraction patterns in certain CDs (**Figure 2. 7**). Lattice fringes show the distance in the range of 0.21nm - 0.24 nm for the (001) lattice plane and 0.32 nm - 0.38 nm for the (002) lattice plane of graphite.[67,48] Large variation in the distance of (002) lattice planes is usually ascribed to the turbostratic disorder in multiple stacked sheets of carbon [69].

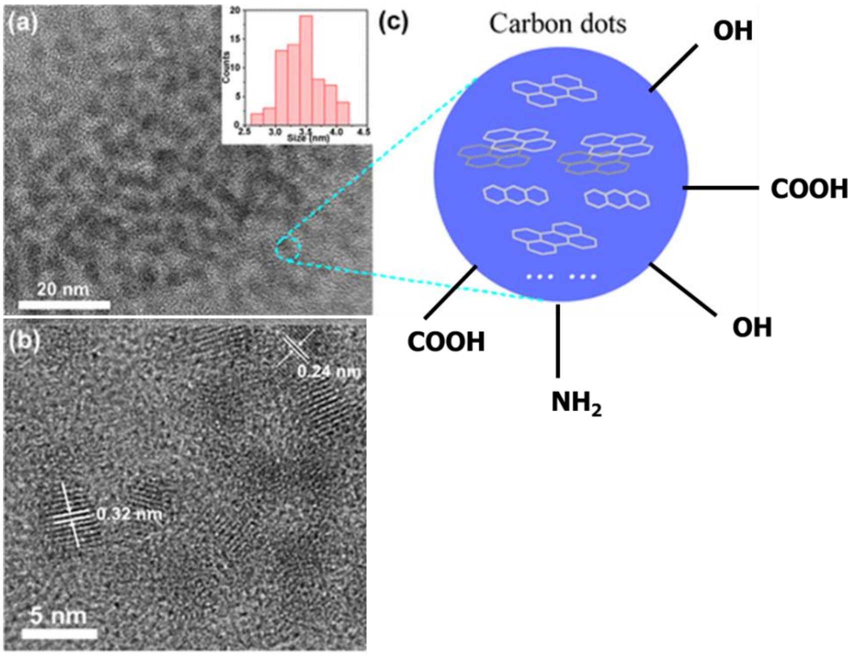

Figure 2. 7 (a) TEM and (b) high-resolution TEM images of CDs. The inset shows the size distribution obtained from TEM images. (c) Schematic depicting the proposed structure of CDs. Reproduced from Fu *et al.*[67], Copyright 2015 American Chemical Society.

X-ray diffraction (XRD) patterns of CDs usually show a broad peak centred at 2θ=25° which corresponds to (002) graphite planes with a lattice distance of 0.34 nm

[33,70]. The presence of broad XRD peak reflects the existence of amorphous framework in CDs.

As mentioned previously CDs have a carbogenic core with different carbon hybridizations (sp^2 and sp^3), but also CDs possess different functional groups present on the surface. Most common surface functional groups include alcohols, carboxylic acids and amine groups. Surface passivation of CDs with polymer-like surface ligands is also done in certain cases usually to prevent agglomeration of CDs and to increase the photoluminescence QY or to change the optical properties of CDs. [71,72]

Fourier transform infrared spectroscopy (FTIR) is used to identify the characteristic functional groups present on the surface of as-synthesized CDs. FTIR spectrum of CDs usually shows stretching vibrations of O-H, N-H and C-H bonds in the region of 3600 - 2700 cm^{-1}, C=O stretching mode at around 1635 cm^{-1}, N-H bending mode at around 1570 cm^{-1} and the presence of C-C and C-O bonds below 1500 cm^{-1} [33,73,45].

X-ray photoelectron spectroscopy (XPS) is usually used to analyse different chemical states of the elements and to estimate the absolute ratio between elements present on the surface of CDs. Characteristic C 1s peak is observed at 284-289 eV and can be deconvoluted into three different carbon species which are carbon bound to carbon at 284.7 eV, carbon bound to oxygen at 286.2 eV and carbon bound to nitrogen at 287.7 eV. The presence of other functional groups on the surface of CDs can also be confirmed by N 1s peak at 398-402 eV, O 1s peak at 531-534 eV, and S 2p peak at 163-165 eV.[74,73,45]

Photoluminescence (PL) of CDs is probably the most intriguing and incompletely understood property of CDs. The first discovery of CDs in 2004 by Xu *et al.*[29] was connected with the unexpected PL that revealed the presence of CDs. CDs also showed the broad PL emission covering the whole visible region of the spectrum, which was highlighted by Sun *et al.*[41] Using appropriate excitation wavelengths, different emission colours can be obtained from the solution of CDs. This multi-colour PL emission became a key indicator of the presence of CDs. Considering principles of PL, it can be concluded that the observed optical properties of CDs could only occur in a heterogeneous system. In CDs which show excitation-dependent PL emission, luminescence centers of specific energy levels are photoselected by the chosen excitation wavelength. By performing single particle measurements or by using separation techniques, optical heterogeneity of CDs' samples can be reduced or even eliminated. These techniques make it possible to isolate lone CDs or individual fractions of CDs that contribute to the multi-colour emission of the whole ensemble of CDs in a solution [75,76]. By using different excitation wavelengths, different fractions of CDs will show emission of different colours.

There is still an open debate about the origins of optical heterogeneity of CDs. One would expect that the optical properties of CDs would be determined by their size and the spatial confinement of the electron-hole pairs. However, several studies have shown that the position of PL emission maximum is independent of the particle size. For example, Vinci *et al.*[76] have used graphite nanofiber to synthesize CDs and then separate CDs into different size fractions by using HPLC method, and they found no clear relationship between particle size and PL emission. Liu *et al.*[43] have synthesized CDs from candle soot and found that different fractions of CDs with similar particle sizes had different PL emission colour (**Figure 2. 8 e**). In contrast to that, Yang *et al.*[77] have demonstrated size-dependent PL emission in different fractions of crystalline CDs. These CDs were obtained by hydrothermal synthesis from glucose in the presence of monopotassium phosphate. Also, Li *et al.*[78] have demonstrated size-dependent PL emission from CDs obtained electrochemically from graphite rods. In these two cases the PL emission became red-shifted as the size of the CDs increased, which is the same property observed in the semiconductor quantum dots [79] (**Figure 2. 8**).

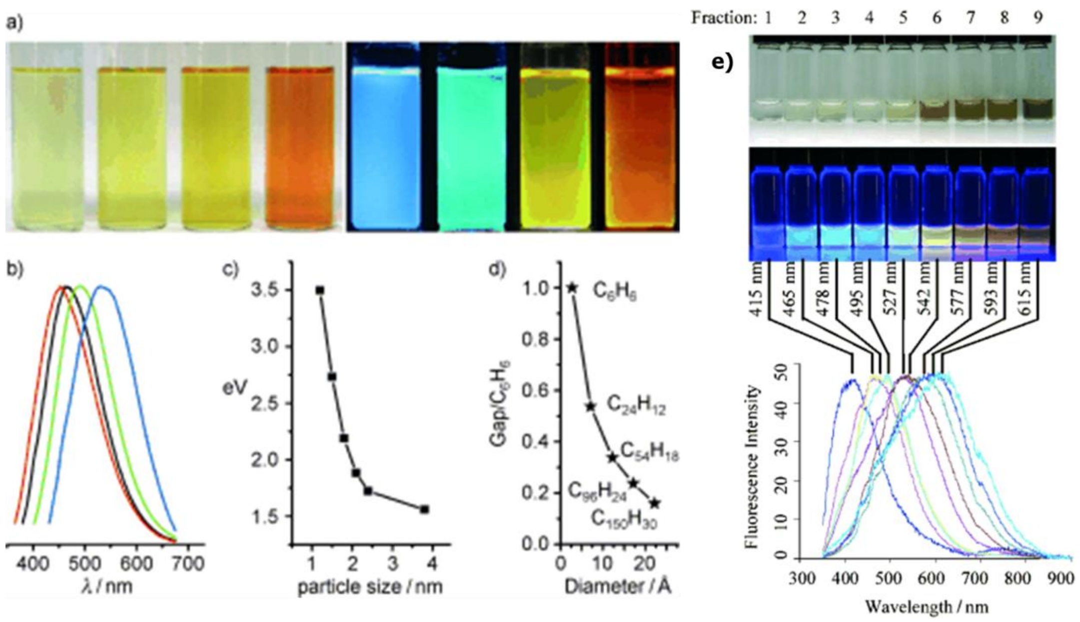

Figure 2. 8 Carbon dots synthesized from candle soot and from graphite rods.

(a) Typical sized carbon quantum dot (CQDs) optical images illuminated under white (left; daylight lamp) and UV light (right; 365 nm); (b) PL spectra of typical sized CQDs: the red, black, green, and blue lines are the PL spectra for blue-, green-, yellow-, and red-emission CQDs, respectively; (c) relationship between the CQDs size and the PL properties; (d) HOMO–LUMO gap dependence on the size of the graphitene fragments. Reproduced from Li *et al.*[78], Copyright 2010 WILEY-VCH. (e) Optical characterization of the purified carbon nanoparticles (CNPs). Optical images illuminated under white (top) and UV light (312 nm; center). Bottom: Fluorescence emission spectra (excitation at 315 nm) of the corresponding CNP solutions. The maximum emission wavelengths are indicated above the spectra. Reproduced from Liu *et al.*[43], Copyright 2007 WILEY-VCH.

Zhao *et al.*[80] suggested that the red-shifting of PL emission in CDs might be related to the system's degree of conjugation and thus would depend on the CDs' crystalline character and not their physical size. Fuyuno *et al.*[81] have used HPLC method to separate as-synthesized graphene nanodots (GNDs) and showed that the PL emission wavelengths of GNDs depend on the size of their sp^2 domains. The authors concluded that GNDs of different sizes contained different population of sp^2 domains, where larger GNDs had higher probability of containing larger sp^2 clusters and showed PL emission at higher wavelength. Structural disorder reduces the actual size of the conjugated system in a single carbon dot and can explain the size-independent PL emission observed for majority of CDs. CDs functionalized with oxygen- and nitrogen-containing functional groups (like OH, COOH, NH_2) can also show red-shifting of PL emission as a function of aromatic system size.[82]

Models of multilayer graphitic CDs functionalized with different oxygen-containing functional groups (like hydroxyl, epoxy, carboxyl) were studied by density functional theory (DFT) to clarify the effects of size and stacking of conjugate systems on the origin of PL emission in CDs. Sudolska *et al.*[83] have modelled absorption of oxygen-containing CDs (O-CDs) using a multilayer model of oxygen functionalized pyrene and coronene building blocks. Aromatic carbon rings formed a conjugated sp^2 system that overlapped when several building blocks were stacked up. They identified UV absorption band at 260 nm which corresponded to $\pi \rightarrow \pi^*$ transitions, and absorption band at 300 nm which corresponded to interlayer $\pi \rightarrow \pi^*$ charge transfer on high energy side (295 nm) and to $n \rightarrow \pi^*$ transitions on its low energy side (310 nm). They showed that for the absorption at 295 nm charge depletion happened in the middle layer while charge accumulation happened in the outer layer, which illustrated interlayer charge transfer. For the absorption at 310 nm, they found charge accumulation around the functional groups. The main conclusion was that $\pi \rightarrow \pi^*$ transitions originate from sp^2 hybridized carbon core and $n \rightarrow \pi^*$ transitions correspond to non-binding electron orbitals which were introduced by the oxygen functionalization at the edge of CDs. Also, there were few other computational studies which used bilayer structures as a model for CDs and they showed that excited-state coupling was weak and that stacking did not contribute to red-shifting of absorption.[84,82]

Just briefly about the electronic transitions. Ultraviolet light (190-380 nm) and visible light (380-750 nm) radiation can interact with matter, which causes electronic transitions (excitation of electrons from the ground state to a higher energy state). Generally speaking, the following electronic transitions are possible: $n \rightarrow \pi^*$, $\pi \rightarrow \pi^*$, $n \rightarrow \sigma^*$, $\pi \rightarrow \sigma^*$, $\sigma \rightarrow \pi^*$, and $\sigma \rightarrow \sigma^*$ (**Figure 2. 9**). Only the two lowest energy ones ($n \rightarrow \pi^*$ and $\pi \rightarrow \pi^*$) are achieved by the energies available in the 200-800 nm spectrum. The energies in the ultraviolet and visible region of light are sufficient to promote or excite an electron to a higher energy orbital. Energetically favoured electron promotion will be from the highest occupied molecular orbital (HOMO) to the lowest unoccupied molecular orbital (LUMO), and the resulting state is called an excited state.

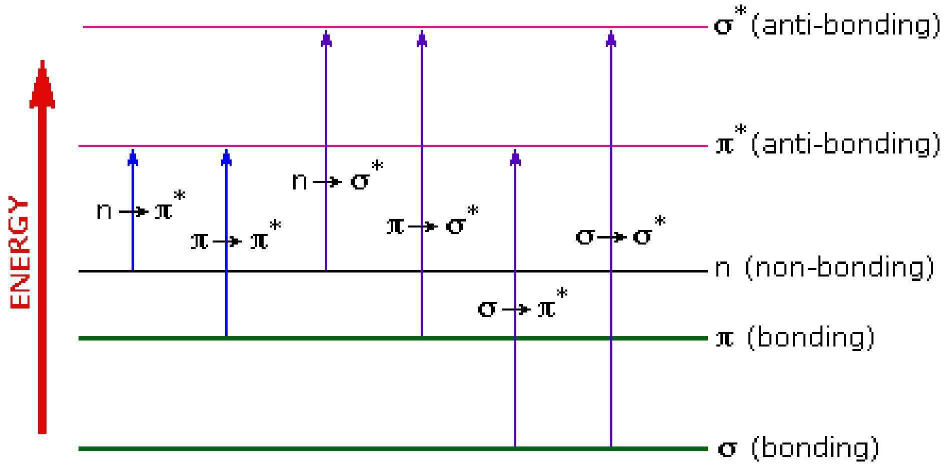

Figure 2. 9 Diagram showing the various kinds of electronic transitions that may occur in organic molecules. Reproduced from[85].

Majority of the computational studies have been performed on the well-defined carbon models but Margraf *et al.*[86] have examined wholly amorphous CDs. They used Monte Carlo simulation to generate amorphous CDs with sizes around 2 nm using periodic carbon structures containing only C and H, and also using structures containing varied quantities of O and N. Their calculations indicated that hybridization of the carbon atoms (sp^2/sp^3 carbon ratio) and heteroatoms both contributed little to the observed band-gap variations, but geometric factors (like topology of the sp^2 conjugated carbon framework) had a much stronger effect. They also observed that the excitation energies which corresponded to electronic transitions from the ground state to the first excited state of the model amorphous CDs decreased as the diameter of CDs increased. They also identified characteristic “band-gap” and “surface” states.

Strauss *et al.*[82] have modelled absorption and fluorescence spectra of carbon nanodots (CNDs) by using two single layer, amide capped graphene sheets and a bilayer model consisting of two stacked graphene sheets (**Figure 2. 10**). All the sheets were non-planar because functional groups caused out-of-plane distortions of sp^2 network. They showed that pyridinic nitrogen and epoxy-oxygen atoms caused a blueshift of spectral features, while stacking, larger sheet size and hydroxylation all caused a redshift of spectral features.

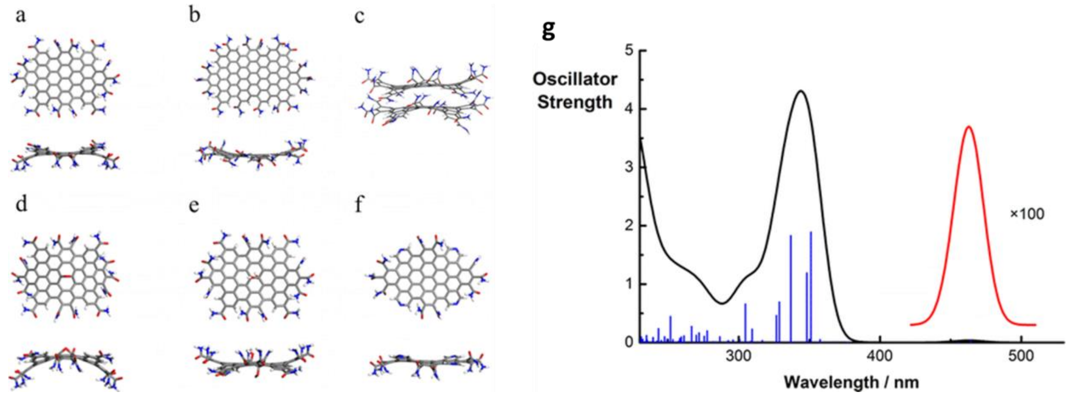

Figure 2. 10 Optimized geometries of CND model systems: (a) CND1, (b) CND2, (c) $CND1^{bilayer}$, (d) $CND1^{epoxy}$, (e) $CND1^{hydroxy}$, (f) $CND1^{pyridine}$. (g) Simulated absorption spectrum of CND1.

Reproduced from Strauss *et al.*[82], Copyright 2014 American Chemical Society.

Their model was successful in describing $\pi \rightarrow \pi^*$ character of all considered states but couldn't be used to describe processes at longer excitation and emission wavelengths. Their experimental data and simulated absorption and emission spectra were qualitatively similar. It is interesting to notice at this point that experimentally measured absorption spectra of oxygen-CDs (O-CDs) are usually unstructured and show no sharp peaks, while nitrogen-CDs (N-CDs) usually show well resolved peaks corresponding to $\pi \rightarrow \pi^*$ and $n \rightarrow \pi^*$ transitions.[33,87]

Fu *et al.*[67] have used model system based on polyaromatic hydrocarbons (PAHs; anthracene, pyrene, and perylene) in an amorphous matrix of poly(methyl methacrylate) (PMMA) in order to experimentally compare the optical properties of CDs with those of PAHs. Films which contained single PAH molecules exhibited absorption and fluorescence spectra like CDs (**Figure 2. 11**). Excitation wavelength-dependent PL emission was only observed in films which contained all three PAHs. They have proposed that CDs consist mostly of small sp^2 domains in an amorphous matrix of sp^3 carbon centers. They also concluded that functionalization of polyaromatic domains and surface defects in the amorphous matrix only had minor effects on the optical properties. These findings highlight that structural differences on a molecular level in CDs affect their optical properties.

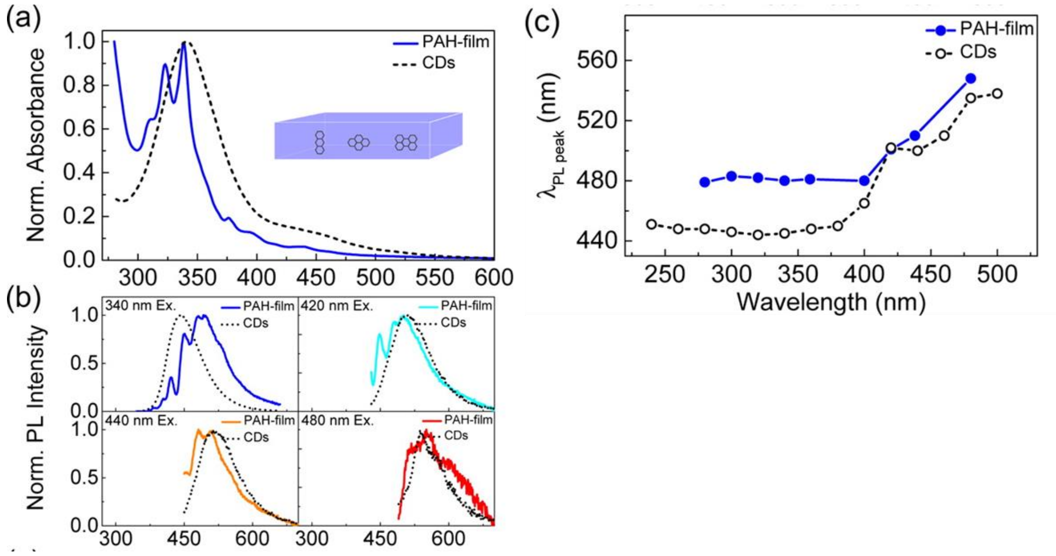

Figure 2. 11 (a) Normalized absorption of a PMMA film containing a blend of PAHs (blue) and of the CDs in aqueous solution (black dashed line). (b) PL spectra of the same samples excited at different wavelengths with the CD PL spectrum (black dashed line) as a reference. (c) PL peak wavelength as a function of the excitation wavelength (x-axis).
Reproduced from Fu *et al.*[67], Copyright 2015 American Chemical Society.

Results discussed above suggest that the PL emission from CDs should be attributed to the localized units within the CDs and not to the particle as a whole. Xu *et al.*[88] have observed emission of multiple photons after single laser pulse excitation of CDs, confirming the presence of multiple PL emission centers within individual CD.

Majority of the CDs show strong blue photoluminescence emission when excited within their low energy (high wavelength) UV absorption band. Absorption band located at 350 nm is commonly ascribed to $n\rightarrow\pi^*$ transitions in the literature [83]. The $n\rightarrow\pi^*$ transitions are important in CDs because they are related to doping and surface functionalization at the edge of carbon core. When CDs are excited within the high energy (low wavelength) $\pi\rightarrow\pi^*$ UV absorption band (corresponding to conjugated carbon rings in the carbon core), only weak photoluminescence is observed. When increasing excitation wavelength, CDs usually show excitation wavelength-dependent PL emission where the PL emission peak shifts to higher wavelengths (redshifts) and the PL emission intensity drops (**Figure 2. 12**).

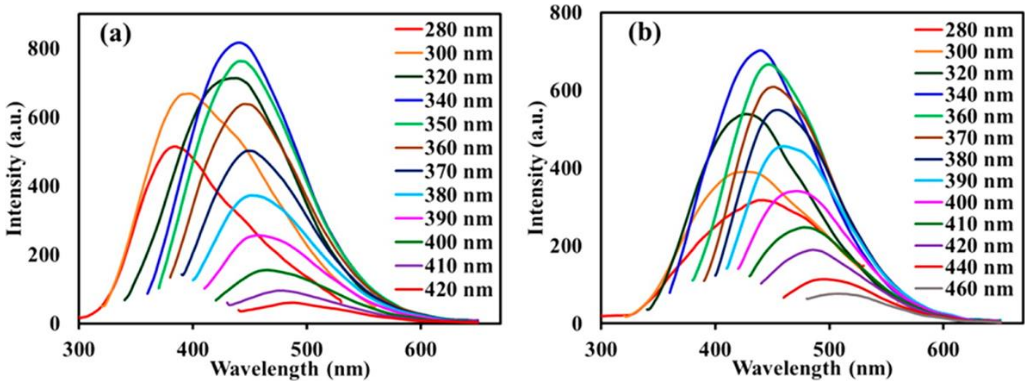

Figure 2. 12 Fluorescence spectra of C-dots1 (a) and C-dots2 (b) monitored at different excitation wavelengths in the range of 280–460 nm. C-dots1 are carboxyl-functionalized (C-dots/COOH) and C-dots2 are amine-functionalized (C-dots/NH2).

Reproduced from Dhenadhayalan *et al.*[70], Copyright 2015 American Chemical Society.

It is interesting to notice again **Figure 2. 11 c** which shows the position of the PL emission peak with an increasing excitation wavelength. PL emission stays constant until the excitation wavelength reaches around 375 nm. This correspond to the tail of the n→π^* transition in the absorption spectra (**Figure 2. 11 a**). When the excitation wavelength increases beyond 375 nm, surface states with low absorption strength (starting at around 400 nm) are excited and PL emission is strongly shifted to higher wavelengths (redshifted). This redshift of PL emission and lower PL emission intensity are often associated with surface states or defect states in the amorphous shell of CDs [89,90]. Functional groups on the surface of CDs are also related to defect states.

There is still a lot of misunderstanding in the literature considering the excitation-dependent PL emission and excitation-independent PL emission. CDs are often labelled as excitation-independent in the literature if CDs show no emission redshift upon excitation within the n→π^* band in the UV absorption. But excitation of low energy (high wavelength) surface states will lead to PL emission redshift. Dong *et al.*[62] have reported “excitation-independent” PL emission in nitrogen- and sulphur-doped CDs, but their PL emission still showed redshift at wavelengths higher than 400 nm, and also their CDs showed decrease in PL emission intensity.

The interplay between the amorphous sp^3 surface regions of N-CDs with the crystalline sp^2 core at different oxidation levels of CDs was studied by Xu *et al.*[58] They concluded that oxidation increases the sp^3 shell region and reduces the sp^2 core structure, and the majority of oxygen groups were located in the shell (**Figure 2. 13**). The authors proposed that nitrogen bound to the crystalline sp^2 core will disorder the hexagonal ring structure and will introduce emissive trap states within the core, which will lead to enhanced PL emission. They have also assigned CDs' core and amorphous shell as separate PL emission centers, and concluded that the dominating PL emission originated from the CD core structure.

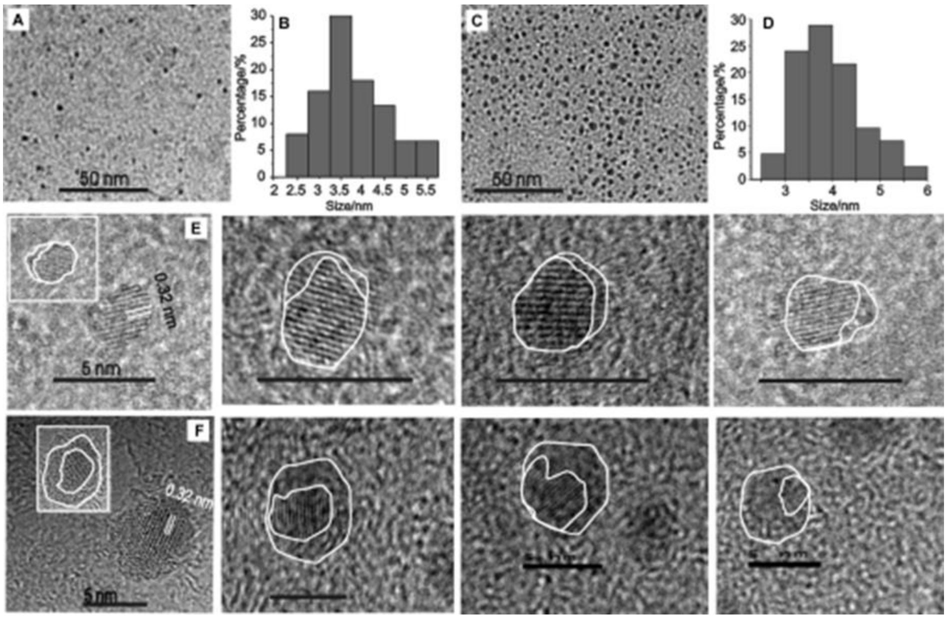

Figure 2. 13 (A) TEM image and (B) size distribution of N-Cdots1. (C) TEM image and (D) size distribution of oxidized N-Cdots from carbonized L-DOPA (3-(3,4-dihydroxyphenyl)-L-alanine) obtained in HNO$_3$ after reflux and dialysis. HRTEM images of (E) N-Cdots1 extracted from carbonized L-DOPA and (F) oxidized N-Cdots from carbonized L-DOPA obtained in HNO$_3$ after reflux and dialysis (scale bar = 5 nm). HRTEM images show the graphite core with an amorphous shell in oxidized N-Cdots but mainly a graphite property in N-Cdots1.
Reproduced from Xu *et al.*[58], Copyright 2013 WILEY-VCH.

Single CD particle luminescence measurements on oxygen-CDs (O-CDs) were conducted by Ghosh *et al.*[91] They synthesized CDs from sucrose by using microwave oven and have obtained two CD species with different sizes and crystallization patterns. They have excited CDs with 488 nm excitation and observed PL emission from green to orange. Authors have also found that the broad PL emission spectrum of ensemble of CDs was formed by the superposition of single CDs emission spectra (**Figure 2. 14**).

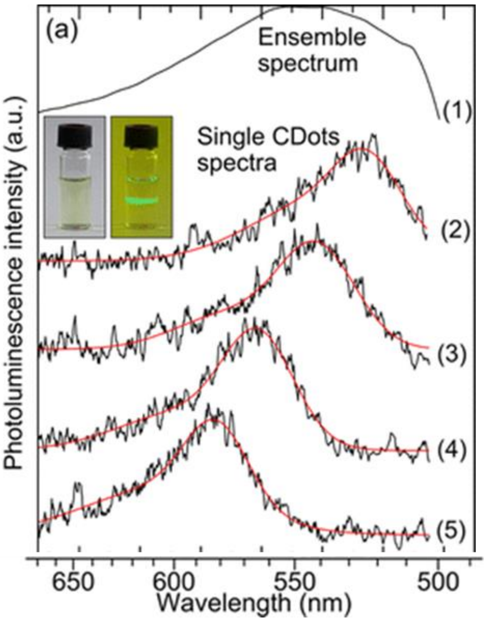

Figure 2. 14 (a) Bulk PL spectrum of CNDs in water (spectrum 1) and exemplary PL spectra of single CNDs dispersed on the surface of a glass cover slide (spectra 2–5). Before plotting, the experimental data has been subjected to averaging over five data points. Inset shows two photographs of a cuvette containing CNDs in an aqueous solution under ambient light excitation (left) and upon excitation with a 488 nm laser (right).
Reproduced from Ghosh *et al.*[91], Copyright 2014 American Chemical Society.

CDs with full-colour tuneable PL emission were synthesized by Jiang *et al.*[45], who have used phenylenediamine isomers as precursors in a solvothermal synthesis method in ethanol. The difference between phenylenediamine isomers was in the substitution pattern of the amine group: meta-substitution (m-CDs), ortho-substitution (o-CDs) and para-substitution (p-CDs). m-CDs showed blue PL emission, o-CDs showed green PL emission and p-CDs showed red PL emission (**Figure 2. 15**). Size of the as-synthesized CDs and nitrogen content in CDs varied between the samples so that m-CDs had size of 6 nm and 4 % nitrogen, o-CDs had size of 8 nm and 7 % of nitrogen and p-CDs had size of 10 nm and 16% nitrogen. The authors have observed redshift of PL emission as the size of CDs and nitrogen content increased. Maximum PL QY was 20 % for p-CDs.

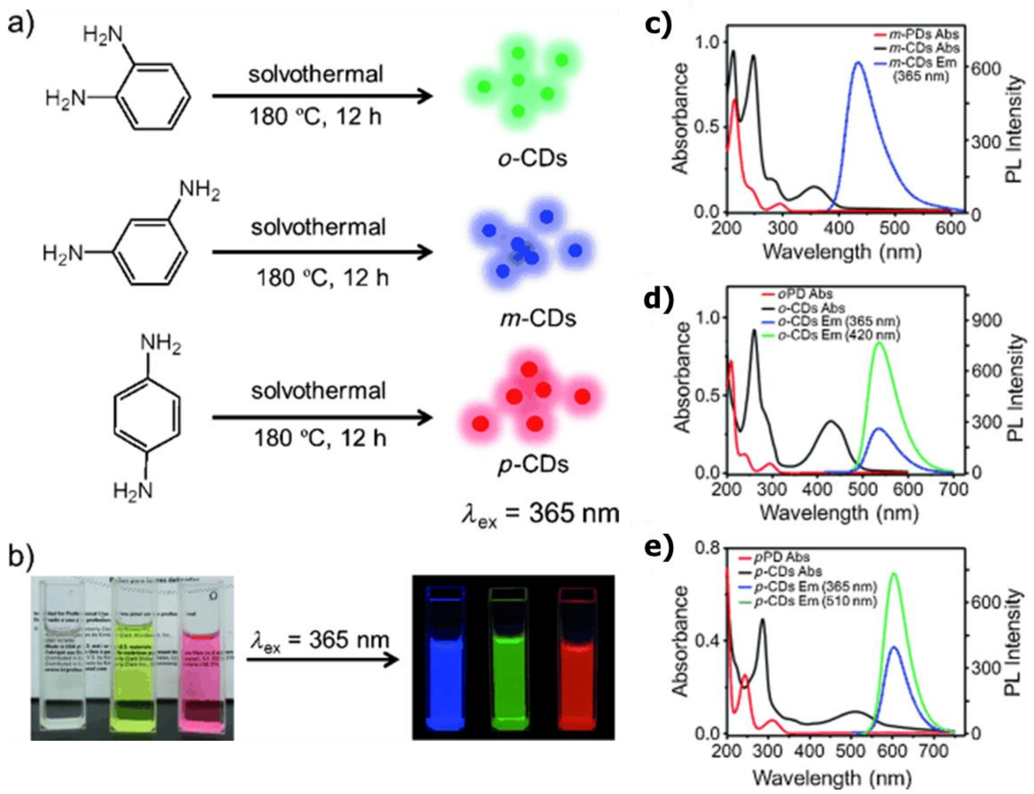

Figure 2. 15 (a) Preparation of the RGB PL CDs from three different phenylenediamine isomers (oPD, mPD and pPD). (b) Photographs of *m*-CDs, *o*-CDs, and *p*-CDs dispersed in ethanol in daylight (left), and under *λ*=365 nm UV irradiation (right). (c–e) UV/Vis absorption spectra of mPD, oPD, and pPD (red line), m-CDs, o-CDs, and p-CDs (black line), and PL emission spectra of m-CDs, o-CDs, and p-CDs (blue and green lines).

Reproduced from Jiang *et al.*[45], Copyright 2015 WILEY-VCH.

One of the most commonly used protocols to synthesize N-CDs is to use hydrothermal synthesis of citric acid and ethylenediamine, which was firstly developed in 2013 by Zhu *et al.*[33] They have obtained N-CDs with high PL QY of 80 %. Authors have also distinguished between crystalline, carbonized carbon core (produced at high temperature synthesis) and surface/molecule-state (at lower reaction temperatures) when CDs are polymerized but not fully carbonized. They concluded that excitation-dependent PL emission originated from molecular states on the surface of CDs.

Whether size effects (quantum confinement), or trap states or molecular states on the surface of CDs influence the excitation-dependent PL emission, is still a point of debate in the literature. Majority of publications, as mentioned previously, suggest that the size of CDs play negligible role for the PL emission of CDs.

Fluorescence mechanism of N-CDs synthesized by microwave heating from citric acid (carbon source) and urea (nitrogen source) was explained by Strauss *et al.*[82] One sample was synthesized under pressure of 15 bar (pCDs) and another one under atmospheric pressure (aCDs). Both samples pCDs and aCDs showed absorption peak at 350 nm, but aCDs also showed another absorption peak at 410 nm and a long absorption tail through the visible spectrum. Second absorption peak was related to the presence of another species of CDs formed during the synthesis under atmospheric pressure. Authors have performed computational modelling of these CDs and have succeeded to mimic the experimental absorption spectra and the blue emission of CDs. Their model showed a blueshift of spectral properties by pyridinic nitrogen at the edge of CDs and to lesser extent by epoxy-oxygen atoms, while hydroxylation caused a spectral redshift of PL properties.

Wang *et al.*[92] have used hydrothermal synthesis of citric acid with ethylenediamine (EDA), diethylenetriamine (DETA) and triethylenetriamine (TEPA), which allowed them to study the influence of increased nitrogen content and the chain length of the precursor. Nitrogen content (around 16 %) and the size of as-synthesized CDs (around 4 nm) didn’t change when using different nitrogen-containing precursors. Nitrogen atoms were incorporated into the heterocyclic carbon ring system around the core termination or core edge. Nitrogen species were in the form of pyrrolic and pyridinic nitrogen and amide group. Amount of nitrogen-carbon double bonds correlated with PL QY. Authors have concluded that the increased amount of cyclic imines enhanced the conjugated system in the carbon core and significantly improved the PL QY.

Identification of a strong blue emitting fluorophore IPCA (imidazo[1,2-a]pyridine-7-carboxylic acid, 1,2,3,5-tetrahydro-5-oxo-) was reported by Song *et al.*[93] who have used hydrothermal synthesis of citric acid and ethylenediamine (EDA) precursors. IPCA fluorophore showed biggest contribution to the fluorescence with overall PL QY of 86 %. Absorption and emission features of IPCA showed huge similarity to CDs. Authors have considered IPCA fluorophore as an important emissive centre of CDs which is attached to the surface of CDs or integrated into the carbogenic core. Authors have also concluded that CD cores possess their own intrinsic emission different to the emission of fluorophore IPCA. Different emissive states of CDs can be controlled by the reaction temperature where at low synthesis temperatures CDs with a dominant light emissive molecular state are formed, and at higher synthesis temperatures CDs with PL contribution from carbon core states are formed (**Figure 2. 16**). It was also shown that IPCA can be used as a single precursor for the hydrothermal synthesis of CDs, and IPCA can also be considered as a reaction intermediate on the way to full carbonization of the starting precursors.

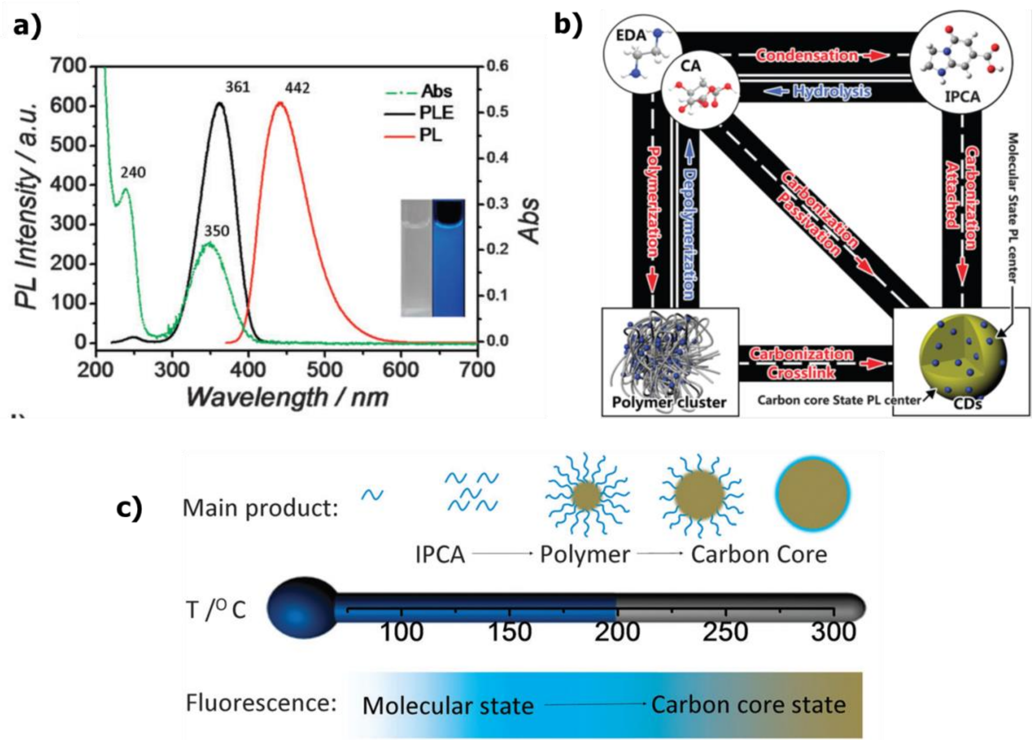

Figure 2. 16 (a) PL and Abs spectra of IPCA, inset shows photographs of IPCA solution under visible and UV light. (b) A schematic of the relationship between different products in the one-pot hydrothermal system of citric acid (CA) and ethylenediamine (EDA). (c) A schematic of the CDs obtained at different hydrothermal temperatures.

Reproduced from Song *et al.*[93], Copyright 2015 The Royal Society of Chemistry.

These fluorophore molecules show absorption and PL emission bands similar to those commonly observed in CDs. This makes it difficult to distinguish these two components and their contributions to absorption and PL emission. Organic fluorophores do not show excitation-dependent PL emission typically found for CDs. UV absorption band at 260 nm is usually assigned to $\pi\rightarrow\pi^*$ transitions of sp^2 carbons and absorption band at 350 nm is assigned to $n\rightarrow\pi^*$ transitions by non-bonding orbitals like C=O. For those cases in the literature where authors have claimed excitation-independent PL emission, it can be speculated that the PL emission originated from fluorophores rather than from CDs. Fluorophores can also be integrated into the amorphous shell of CDs and attached to the surface of CDs.

Other chemical elements, and not just nitrogen, have been used for doping CDs to enhance their PL QY or to change their PL emission properties. Dong *et al.*[62] have synthesized nitrogen and sulphur co-doped CDs (N,S-CDs) by using hydrothermal synthesis of citric acid (carbon source) and L-cysteine (both nitrogen and sulphur source). As-synthesized CDs showed blue luminescence, high PL QY of 78 % and low Raman I_D/I_G ratio of 0.5 indicating ordered crystalline structure in CDs. Authors have concluded that co-doping with sulphur enhanced the high energy luminescent states introduced by nitrogen, and also reduced broad, low energy states associated with oxygen. N,S-CDs are an example of CDs with high PL QY and weak excitation-dependent PL emission.

Xu *et al.*[94] have also prepared N,S-CDs by using hydrothermal synthesis of sodium citrate (carbon source) and sulfamide (nitrogen and sulphur source). Authors have found that nitrogen and sulphur were incorporated into the CD core by C-N and C-S bonds, and the PL QY correlated with the sulphate content and the amount of oxidized carbon atoms at the surface of CDs. They have also calculated theoretical density of states for a CD model consisting of 268 atoms, and have shown that impurities caused by solely N or S doping shifted the density of state peaks towards the LUMO level (lowest unoccupied molecular orbital), while impurities caused by N and S co-doping shifted the density of state peaks towards the HOMO level (highest occupied molecular orbital). Authors have concluded that dangling N- and S- bonds enhanced the electron transfer from the surface, while dangling S-N bonds increased the hole transfer from the surface. This once again shows that CDs are good electron and hole donors and acceptors, and also points out to importance of dopant atoms for the electronic properties of CDs.[95]

Co-doping CDs with other heteroatoms except S and N has also been done. Phosphor (P) and boron (B) co-doping has been done by Barman *et al.*[66] who have used hydrothermal synthesis method of citric acid (carbon source), diethylenetriamine (nitrogen source), boric acid (boron source) and orthophosphoric acid (phosphor source). Nitrogen, boron and phosphor were all successfully incorporated into the CD core. N,P-CDs showed the highest PL QY of 70 %. Absorption peak at 350 nm ($n \rightarrow \pi^*$ transitions) for N-CDs was blue-shifted for N,B-CDs and red-shifted for N,P-CDs. PL emission peak for all CDs was located in the blue region of spectrum. Authors have concluded that nitrogen and phosphor donate additional electrons into the $n \rightarrow \pi^*$ system, while boron changes electronic structure of the system and creates holes in CDs (enhancing non-radiative recombination).

Bhunia *et al.*[96] have synthesized N,S,P-CDs by using vitamin B_1 as carbon, nitrogen and sulphur source, and using phosphate salt as an additional co-doping source. By changing synthesis temperature, authors have managed to synthesize blue emitting CDs (at 90 °C in water) and green emitting CDs (at 130 °C in ethylene glycol). As synthesized N,S,P-CDs had the highest PL QY of 76 %.

Considering the different origins of photoluminescence in classical semiconductor quantum dots (QDs) and carbon dots (CDs), the following conclusions can be made.

The photoluminescence (PL) in QDs has the origin in the radiative band-edge recombination (electron-hole pair recombination). When a photon with energy greater than the bandgap energy E_G is absorbed, an electron from the valence band (VB) is promoted to the conduction band (CB) leaving a hole behind. The following recombination of electrons and holes results in the emission of a photon of light, giving rise to fluorescence (**Figure 2. 17**). This type of PL is usually called intrinsic bandgap fluorescence or HOMO - LUMO transition (highest occupied molecular orbital, HOMO, and the lowest unoccupied molecular orbital, LUMO). This is the mechanism of PL for the impurity-free QDs where no interstates within the bandgap exist. PL properties of QDs are entirely governed by the quantum confinement effect.[97,98] The PL emission band of QDs is generally very narrow with full-width-at-half-maximum (FWHM) less than 50 nm. Also, PL of QDs shows excitation-independent emission.

Just briefly about the basics of semiconductor quantum dots (QDs). QDs are nanocrystals of a semiconducting material with diameters in the range of 2-10 nm. They were first discovered in 1981 by Ekimov *et al.*[99] QDs show unique electronic properties which are intermediate between those of bulk semiconductors and discrete molecules. QDs can emit distinctive colours determined by the size of the particles.

Due to the small size of QDs, the electrons in QDs are confined in a small space (quantum box), and when the radii of the semiconductor nanocrystal is smaller than the exciton Bohr radius (average distance between the electron in the conduction band and the hole in the valence band), there is a quantization of the energy levels. (**Figure 2. 17**).[100] These discrete, quantized energy levels of QDs relate them more closely to atoms than bulk materials. As the size of the QDs decreases, the difference in energy band gap between the highest valence band and the lowest conduction band increases.

Thus more energy is then needed to excite the electron, and more energy is released when the electron returns to its ground state. This results in a colour shift from red to blue in the emitted light. As a result of this phenomenon, QDs can emit any colour of light simply by changing the size of QDs.

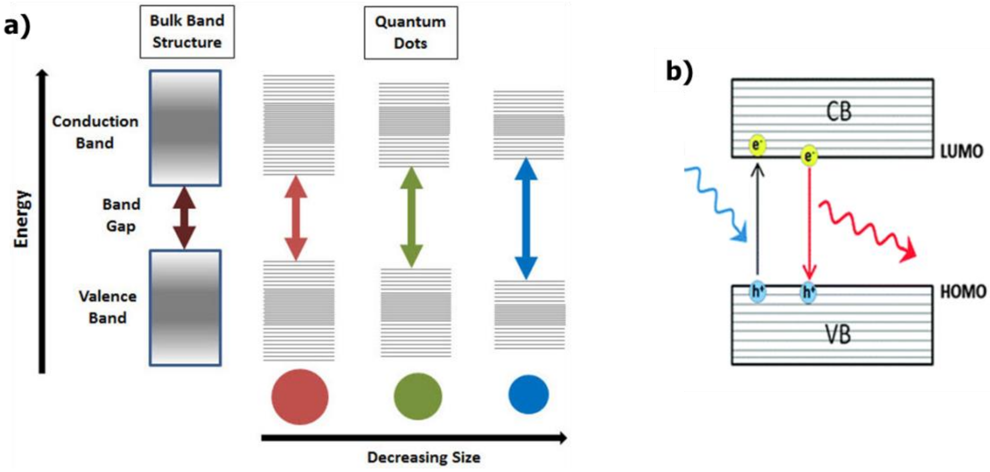

Figure 2. 17 (a) Splitting of energy levels in semiconductor quantum dots (QDs) due to the quantum confinement effect. Band gap of QDs increases with the decrease in size of QDs. (b) Photoluminescence mechanism in QDs.
Reproduced from Cayuela *et al.*[101], Copyright The Royal Society of Chemistry 2016.

Origins of photoluminescence (PL) in carbon dots (CDs) are different than in QDs. PL emission in CDs can occur when trap states are present in the bandgap (due to surface defects, impurities and functional groups).[101] The photoexcited electron (and/or hole) can be trapped and their following recombination will lead to a radiative emission of lower energy (higher wavelength) photon (**Figure 2. 18 a**). This observed PL emission is not a unique mechanism but a combination of two mechanisms from different sources. One source is the core of CDs, with its intrinsic quantization effects, and the other source is the surface of CDs, the properties of which are determined by the surface functional groups and surface defects (surface trap states). As mentioned previously, CDs can show excitation-dependent PL emission and/or excitation-independent PL emission.

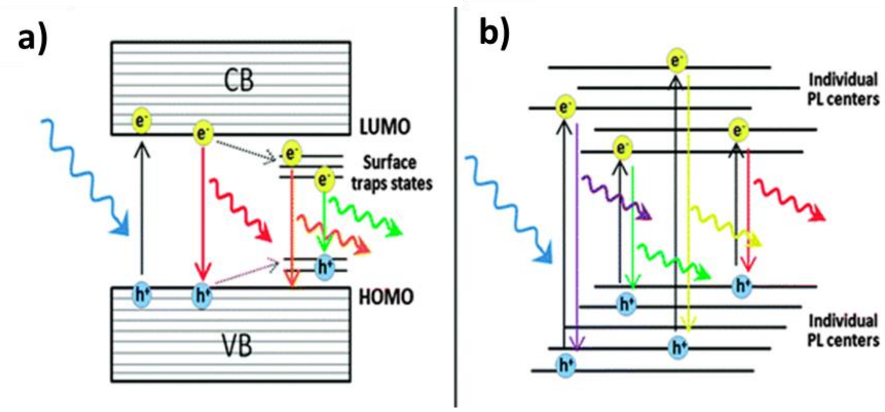

Figure 2. 18 Scheme of the different photoluminescence mechanisms in CDs: (a) when trap states are present and (b) when individual emitters are present.
Reproduced from Cayuela *et al.*[101], Copyright The Royal Society of Chemistry 2016.

Also, PL of CDs can result from the superposition of emissions of individual emitters (emitter functional groups located on the surface of CDs, or fluorophore molecules) (**Figure 2. 18 b**).[101] In this specific case there is no quantum confinement or a collective excitonic effect. CDs which are synthesized by bottom-up synthesis methods at low temperatures usually show PL emission *via* this mechanism. These CDs show broad emission bands due to the superposition of several emission centers. As mentioned previously, Krysmann *et al.*[54] have reported that carbogenic cores in CDs start forming at temperatures greater than 230 °C, and that the corresponding PL emission is due to the presence of both carbogenic cores and molecular fluorophores. When there is no formation of carbogenic core in the CDs, the PL emission is determined by surface trap states. There is no strong correlation between the PL emission bands of CDs and the particle size of CDs. PL emission in CDs also strongly depends on the synthesis method used, synthesis conditions and functionalisation of the surface of CDs. These factors influence the competition between the intrinsic state PL emission and the trap state PL emission in CDs.

2.4. Applications of Carbon Dots

Majority of the interest in carbon dots (CDs) is related to their vast potential in medical and biological applications.[102,103,104] CDs possess high photostability and resistance to photobleaching even exceeding that of organic dyes like rhodamine B or fluorescin.[105] CDs show excellent colloidal stability and water solubility when using appropriate surface functionalization or surface passivation.[102] Another advantage of CDs is their low toxicity and biocompatibility when compared to currently available colloidal semiconductor quantum dots (QDs) based on Cd (CdS, CdSe, etc.). *In vivo* toxicity and cytotoxicity of CDs have been tested and have shown to be very low.[103,80] CDs are mostly used in imaging technologies for cell imaging [72,41], in vivo imaging[103,106] and targeted cell imaging [107]. Majority of the *in vivo* imaging studies which used CDs have used standard down-conversion photoluminescence (PL) rather than up-conversion photoluminescence (UCPL; when a sample is excited with a certain wavelength λ it emits light with shorter wavelength). It shows that CDs are bright enough to provide enough contrast in tissue samples even when excited by visible light.

Another application of CDs is as fluorescent biosensors for measuring pH or detecting metal ions.[38,108] CDs also show potential as photocatalysts in visible-light CO_2 conversion and H_2 generation from water.[109] It has been demonstrated that CDs with surface passivation by amino or certain other molecules are capable of being visible-light photocatalyst for CO_2 reduction in aqueous solution.[110,111] There has been extensive effort in the development of potent visible-light photocatalysts for solar H_2 production. Since CDs show absorption spectra extending into the visible region, they have been explored as photocatalysts for H_2 generation from water-splitting.[112,113]

Light emission and high PL QY of CDs have also been utilized in optoelectronic devices like in electrically driven CD-based light emitting diodes (LEDs). CDs in LEDs showed efficient conversion of blue light to white light [114,38] and CDs were also used as blue-emitting components in highly efficient RGB white-light-emitting diodes [115]. In a pioneering work Zhang *et al.*[116] have reported multicolour electroluminescence from CD-LEDs which were operated at different voltages. Authors have been able to obtain blue, cyan, magenta and white light emission.

Up till now, there have been a limited number of publications focusing on the application of CDs as sensitizers for nanostructured solar cells. In a pioneering work from 2012, Mirtchev *et al.*[117] have presented solution phase synthesis of water soluble carbon quantum dots (CQDs) *via* the dehydration of γ-butyrolactone with concentrated sulphuric acid, and have used CQDs as sensitizers for TiO_2 solar cells. Authors have obtained solar cell with short circuit current density (J_{sc}) of 0.53 mA cm^{-2}, an open circuit voltage (V_{oc}) of 0.38 V and fill factor (FF) of 0.64. Power conversion efficiency of as-fabricated solar cells was 0.13 %.

Zhang *et al.*[118] have reported N-doped carbon quantum dots (NCQDs) combined with TiO_2 to form NCQDs/TiO_2 hierarchical microspheres assembled by nanorods. Hydrothermal synthesis method at 100 °C was used to make NCQDs/TiO_2 hierarchical microspheres assembled by nanorods. Authors have fabricated NCQDs-sensitized TiO_2-based solar cell with short circuit current density (J_{sc}) of 0.69 mA cm^{-2}, an open circuit voltage (V_{oc}) of 0.46 V and fill factor (FF) of 0.43. Overall power conversion efficiency (PCE) of solar cell was 0.13 %.

Margraf *et al.*[119] have used carbon nanodots (CNDs) as sensitizers in mesoscopic solar cells (TiO_2-based solar cells) where CNDs were synthesized using a one-step, bottom-up microwave approach from citric acid, urea and formic acid. They have fabricated the solar cell with short circuit current density (J_{sc}) of 0.99 mA cm^{-2}, an open circuit voltage (V_{oc}) of 0.49 V and fill factor (FF) of 0.50. As-fabricated solar cell showed the power conversion efficiency (PCE) of 0.24 %. Authors have also concluded that extending the light absorption of CDs towards longer wavelengths does not necessarily improve the performance of solar cells, since these additional low energy (high wavelength) excited states do not inject electrons into TiO_2 efficiently.

In our pioneering work, Marinovic *et al.*[120] have synthesized biomass-derived CDs and used them as sensitizers for ZnO-nanorod-based solid-state solar cells. CDs were synthesized *via* hydrothermal method from chitosan, chitin and glucose precursors. As-fabricated champion solar cell devices showed short circuit current density (J_{sc}) of 0.674 mA cm^{-2}, an open circuit voltage (V_{oc}) of 0.265 V and fill factor (FF) of 0.43. Best power conversion efficiency (PCE) of solar cell devices was 0.077 %.

Following that previous research, Marinovic *et al.* have also used CDs as sensitizers for TiO_2-based nanostructured solar cells with liquid electrolyte (work submitted for publication). CDs were synthesized *via* hydrothermal synthesis from monosaccharide (D-glucose), polysaccharides (chitosan and chitin) and amino acids (L-arginine and L-cysteine). Best performing solar cells were based on L-arginine CDs as sensitizers for TiO_2 and have shown short circuit current density (J_{sc}) of (0.97 ± 0.05) mA cm^{-2}, an open circuit voltage (V_{oc}) of (0.660 ± 0.003) V and fill factor (FF) of (0.57 ± 0.02). These solar cells had the highest power conversion efficiency (PCE) of (0.362 ± 0.007) %.

2.5. Solar Photovoltaics Technologies

Solar photovoltaics (PV) are the fastest growing energy technology in the world today and are a leading candidate for carbon-free, terawatt-scale electricity generation. Photovoltaic solar cells are usually classified as first, second and third generation devices.

Today, the most commonly used solar cell devices are based on single crystalline or multicrystalline p-n junction silicon solar cells. They are the first generation solar cell devices. Crystalline silicon (c-Si) - based solar cells are profiting from the materials availability and experience in the development, and currently offer the best possibilities for large-scale manufacturing, good efficiency and relatively low-cost production. The best confirmed power conversion efficiency (PCE) of crystalline silicon solar cells today is 25.6 % (143.7 cm^2 area) produced by Panasonic.[121]

Second generation PV solar cells are based on thin film technologies which are deposited between transparent conductive substrate and a counter electrode. They are mostly based on GaAs, CdTe, $CuInS_2$, $CuInSe_2$, $CuInGaSe_2$ (CIGS), and also amorphous and nanocrystalline silicon. The best confirmed solar cell efficiency for GaAs thin film solar cells is 28.8 % (0.993 cm^2 area) and for CIGS solar cells it is 21.0% (0.993 cm^2 area).[121] Amorphous silicon thin film solar cells have the confirmed efficiency of 10.2 % (1.001 cm^2 area).[121] Shockley-Queisser limit, which is the thermodynamic limit for the light to electric conversion efficiency of a single-junction PV solar cell under AM 1.5G spectrum illumination, has the value of 32.9 %.[22,23] It means that the photons with energies below the energy band gap of a solar cell material are not absorbed, while the photons with energies greater than the band gap release the additional energy mostly as heat.

The main focus of the third generation PV solar cells is to reduce the production costs and obtain the efficiencies greater than the Shockley-Queisser [22,23] limit. Third generation PVs are trying to accomplish this by utilizing advanced photovoltaic concepts such as multiexciton generation, multijunction solar cells and hot electron injection.[122] Third generation PVs include organic photovoltaics (OPV) [123,124], perovskite solar cells [125,126], dye-sensitized solar cells (DSSC) [127], semiconductor quantum dot sensitized solar cells (QDSSC) [128] and carbon dot sensitized solar cells (CDSSC) [120,117,118]. DSSCs, OPVs and QDSSCs / CDSSCs all hold the promise for high power conversion efficiency, and low-cost and flexible solar cell devices. Organic thin-film solar cells have reached confirmed efficiency of 11 % [121] while perovskite thin-film solar cells have confirmed efficiency of 20.1 %.[121] The best confirmed solar cell efficiency for dye-sensitized solar cells is 11.9 % (1.005 cm^2 area) and for a submodule dye-sensitized solar cell it is 8.8 % (398.8 cm^2 area), both produced by Sharp.[121] The highest PCE for dye-sensitized solar cells reported in the literature is 14 %.[129]

Quantum dot sensitized solar cells (QDSSCs) today still show moderate power conversion efficiency (PCE) of about 8 % [130,131,132,133] which is primarily limited by the charge recombination [134]. The highest certified efficiency of QDSSCs is 11.3 % [135]. Currently, QDSSCs are mainly fabricated by using highly toxic cadmium (Cd) and lead (Pb) elements.[128,136,134] This makes application of QDSSCs problematic because of the health and environmental issues. This is the reason why the development of Cd- and Pb-free solar cell devices is extremely important. One of the attractive alternatives to toxic Cd- and Pb-based quantum dot solar cells are $CuInS_2$ quantum dot solar cells which have good absorption spectra and optimal band gap of 1.5 eV.[137,138,139] One of the best certified efficiencies for the core/shell $CuInS_2/ZnS$ quantum dot solar cells was reported to be 6.66 % [137]. Slightly lower certified efficiency of 5.13 % was obtained for the CuInSeS quantum dot solar cells but passivated with CdS [140]. As we can see, these efficiencies are still lagging behind those obtained by Cd- and Pb-containing quantum dot solar cells which are around 8 % today [141,142]. Also, indium is scarce and expensive.

Another alternative to the toxic Cd- and Pb-containing quantum dot solar cells are carbon dot (CD) sensitized solar cells. Power conversion efficiencies for CD sensitized solar cells are still below 1 % [117,118,120], with the best reported efficiency in the literature of 0.79 % for the solar cell containing TiO_2 sensitized with nitrogen-doped carbon dots.[143]

Solar PV technologies can be ranked by different classifications such as by power conversion efficiency (PCE), material abundance, module cost or any other performance metric. Most widely used classification today focuses on module efficiency and area cost (**Figure 2. 19**). As mentioned previously, three distinct generations of PV solar cells are: first generation (G1) which includes wafer-based solar cells of c-Si and GaAs ; second generation (G2) technologies which include thin-film solar cells of a-Si:H, CdTe and CIGS ; third generation (G3) technologies which include novel thin-film solar cells like dye-sensitized solar cells, organic solar cells perovskite solar cells and quantum dot/carbon dot solar cells. Three generations of solar cell technologies are represented as shaded regions on the **Figure 2. 19**, and module performance trends for commercial PV technologies from 2009-2013 are given on the same graph [18]. As solar cell efficiencies rise and costs fall, all technologies tend to move to the upper-left corner of the plot with time. All current G1 and G2 technologies are close to zone designated G2. No third generation technology has yet reached the zone marked G3.

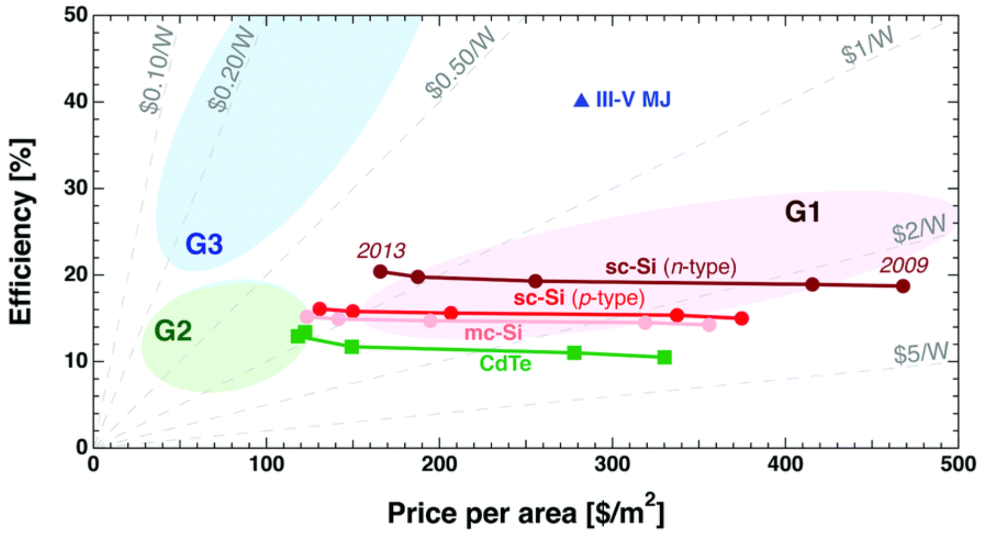

Figure 2. 19 Average module efficiencies and price per area from 2009-2013 are shown for commercial PV technologies in three conventional generations (G1 in red, G2 in green and G3 in blue). The single G3 data point corresponds to performance projections for a III-V MJ module (multijunction module).

Reproduced from Jean *et al.*[18], Copyright 2015 The Royal Society of Chemistry.

2.6. Solar Cell Basics

Fundamental functional unit of a solar cell is a *pn*-junction diode [144,18]. It is formed at the interface between the two semiconductors. One semiconductor is doped with an excess of electron-donating impurities (*n-type* semiconductor) and another semiconductor is doped with an excess of hole-donating impurities (*p-type* semiconductor). **Figure 2. 20** shows the fundamentals of the *pn*-junction diode.

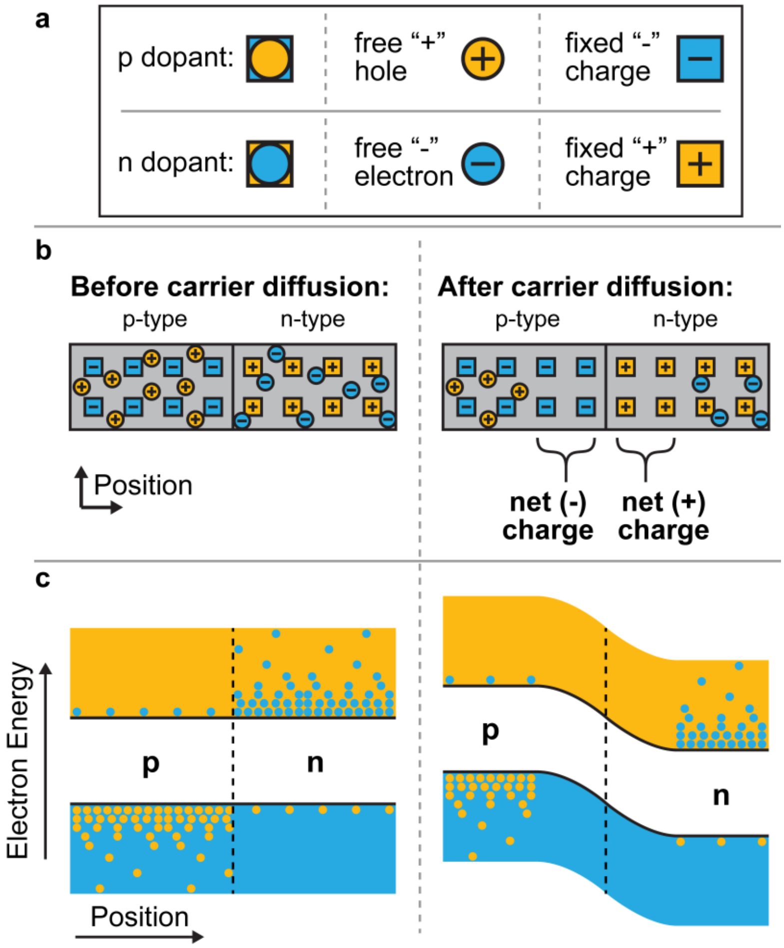

Figure 2. 20 Structure and electric properties of a *pn*-junction diode before and after diffusion of charge carriers across the junction interface.

Reproduced from Jean *et al.*[18], Copyright 2015 The Royal Society of Chemistry.

When an *n*-type and *p*-type material are put in contact, free electrons from the *n*-type side and free holes from the *p*-type side diffuse across the interface, recombining with each other. This recombination of the free carriers near the interface uncovers the fixed charges of the dopants that originally balanced the charge of the free electrons and holes (**Figure 2. 20 b**). This way a built-in electric field is generated in the interface region and it prevents further diffusion of charges. This electric field corresponds to a built-in voltage between the *n*-type and *p*-type sides of the junction.

If a positive voltage is applied to the *p*-type side of the junction (forward bias), the built-in field is reduced, and large numbers of carriers can diffuse across the interface, generating a large current. If a negative voltage is applied to the *p*-type side (reverse bias), the built-in field is strengthened, the diffusion is low, and the current remains low (**Figure 2. 21**).

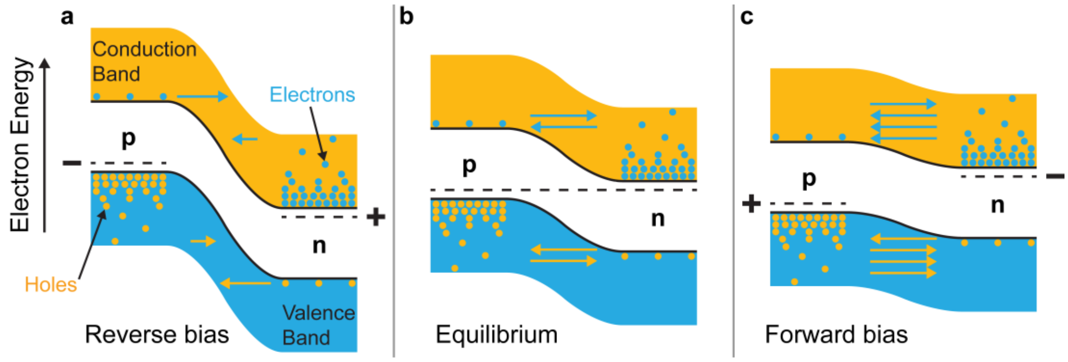

Figure 2. 21 Energy band diagrams during operation of a *pn*-junction diode in the dark showing: (a) reverse bias, (b) equilibrium, and (c) forward bias conditions. Blue and orange arrows represent flux of electrons and holes, respectively.

Reproduced from Jean *et al.*[18], Copyright 2015 The Royal Society of Chemistry.

The current flow in a diode at different applied voltage levels is shown by the curve labelled “dark” in **Figure 2. 22**. The current increases exponentially under positive voltage but remains small under negative voltage.

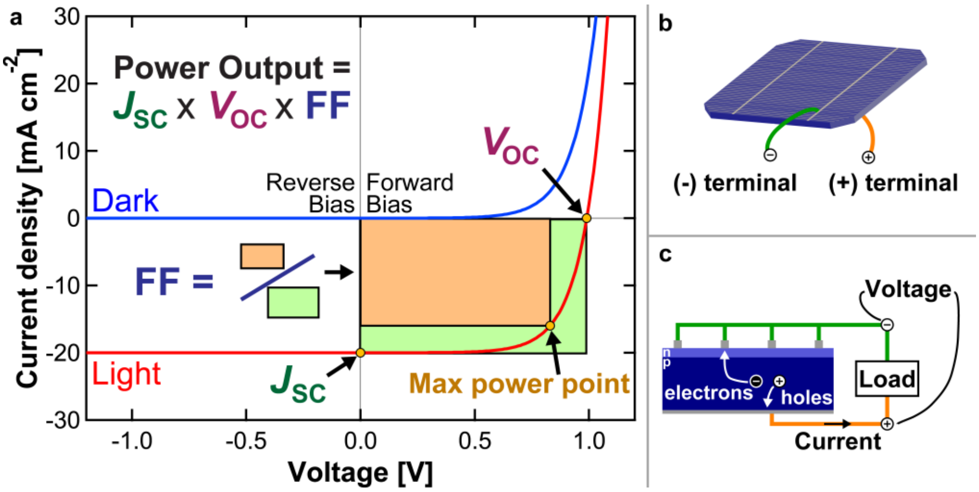

Figure 2. 22 (a) Current-voltage (J-V) characteristics of a solar cell in the dark (blue curve) and under illumination (red curve). The short-circuit current density (J_{SC}), open-circuit voltage (V_{OC}), and fill factor (*FF*) are indicated on the graph. Since the current output of an illuminated solar cell is proportional to its illuminated surface area, the current density (*J* ; current divided by area) is normalized for different cell sizes. (b, c) Current and voltage are measured between the positive and negative terminals of the solar cell.

Reproduced from Jean *et al.*[18], Copyright 2015 The Royal Society of Chemistry.

Solar cell is simply a diode that can generate free electrons and holes through the absorption of photons of light, as shown in **Figure 2. 23**.

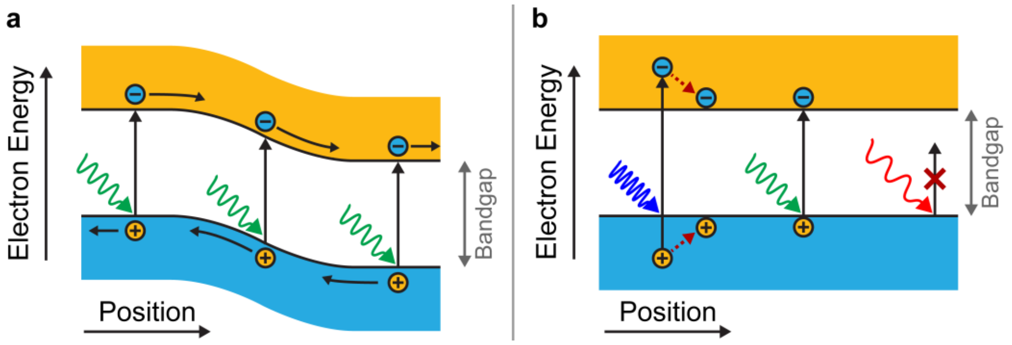

Figure 2. 23 Operation of a solar cell under illumination and interaction of photons with semiconductor material.

(a) Operation of a solar cell under illumination showing excitation of electrons and holes by photons of light, followed by charge carrier separation under the built-in electric field. Conduction band and holes are shown in orange and the valence band and electrons are shown in blue. (b) Interaction of photons of light of various wavelengths with a light-absorbing semiconductor material. Photons of energy higher than the bandgap (blue wavy arrows) generate excited electron-hole pairs with net energy greater than the bandgap. But the electron and hole quickly lose their excess energy and “relax” to the bottom of the conduction band (for electrons) and top of the valence band (for holes). Photons of energy lower than the bandgap (red wavy arrows) are not absorbed and do not generate free electron-hole pairs. Reproduced from Jean *et al.*[18], Copyright 2015 The Royal Society of Chemistry.

These free charge carriers are separated under the built-in electric field of the diode and they generate the photocurrent. The “light” curve in the **Figure 2. 22** is vertically offset by a constant value from the “dark” curve because the generation of photocurrent is roughly independent of the voltage across the solar cell. The current is correlated with the number of carriers generated, which depends on the absorption properties of the material and its efficiency in turning absorbed photons into extractable charge carriers. Since the solar cell is generating power, the convention is to invert the current density axis (so the current density shows positive values). The voltage is correlated with the strength of the built-in electric field of the diode.

As mentioned previously, **Figure 2. 22** shows the current-voltage characteristics (J-V) of a representative solar cell both in the dark (blue curve, acting as a simple diode) and under illumination (red curve). If the two terminals of an illuminated solar cell are left open (not connected to each other by a conductive path) and no current is allowed to flow, the voltage measured between them is the *open-circuit voltage* (V_{OC}). If the two terminals of a solar cell are short-connected together by a conductive pathway (*e.g.* a copper wire) and thus held at the same voltage, the current flowing through that pathway divided by the solar cell area is called the *short-circuit current density* (J_{SC}).

The voltage of an operating solar cell can range between zero and V_{OC}. The current output stays roughly constant over much of this range until the voltage approaches roughly the value of V_{OC}. The power output at a given voltage is equal to the product of the current and the voltage. Power output reaches a maximum value (P_{MAX}) near the apparent "shoulder" in the current-voltage curve (orange square in the **Figure 2. 22**).

The ratio between the power output per area at this maximum power point and the product of the J_{SC} and V_{OC} , is the fill factor (*FF*). FF corresponds to the "squareness" of the illuminated current-voltage curve.

The power conversion efficiency (PCE) is equal to the product of the short-circuit current density (J_{SC}), open-circuit voltage (V_{OC}), and fill factor (*FF*), divided by the power per area of the incident light source (light source is used under standard AM 1.5G illumination conditions of 1000 W/m^2). More mathematical details about the operational parameters of solar cells will be given in the **Chapter 2.7**.

Optimization of the current and voltage output of a solar cell cannot be done simultaneously. Solar cell can only absorb photons with energy equal or greater than the bandgap, so reducing the bandgap generally will increase the current. However, electrons excited by photons with energy greater than the bandgap quickly dissipate their excess energy as wasted heat and ultimately settle at energy equal to the bandgap (**Figure 2. 23**). The bandgap energy is the maximum energy that can be extracted as electrical energy from each photon absorbed by the solar cell. Reducing the bandgap will lead to smaller voltages, which will counteract the benefits of increased current. Since the sun has broad emission spectrum this limits our ability to harvest both the maximum number of photons and the maximum energy from each photon.

Resistive effects in solar cells reduce the efficiency of the solar cell by dissipating power in the resistances. The most common parasitic resistances are *series resistance* (R_S) and *shunt resistance* (R_{SH}). In most cases the key impact of parasitic resistance is to reduce the fill factor (*FF*). Since the value of resistance will depend on the area of the solar cell, when comparing the series resistance of solar cells which may have different areas, a common unit for resistance is Ωcm^2.

The series resistance (R_S) can be estimated by the inverse of the slope near the open circuit potential point (V_{OC}) (**Figure 2. 24**). Ideally, the series resistance would be zero. However, resistances of metal contacts or bulk substrate lead to an additional voltage drop within the cell. As a result, the slope of the curve near V_{OC} decreases with increasing R_S. That's why both the area under the curve and the power maximum decrease. Open circuit voltage (V_{OC}) is not affected by R_S because the current flow is zero. The short circuit current (J_{SC}) is also unaffected by R_S. Only very large values of R_S can lead to a reduction of J_{SC}.

The shunt resistance (R_{SH}) can be estimated by the inverse slope near the short circuit current point (**Figure 2. 24**). In the ideal case, this resistance is infinite so that no additional current path exists. The lower the R_{SH} the more the slope of the *J*-*V* curve increases near the short circuit current. This also leads to a smaller open circuit voltage (V_{OC}). R_{SH} is mainly caused by the leakage current through the cell caused by impurities or defects in the manufacturing process. Power maximum, fill factor, and efficiency of a solar cell are all negatively affected by small shunt resistances.

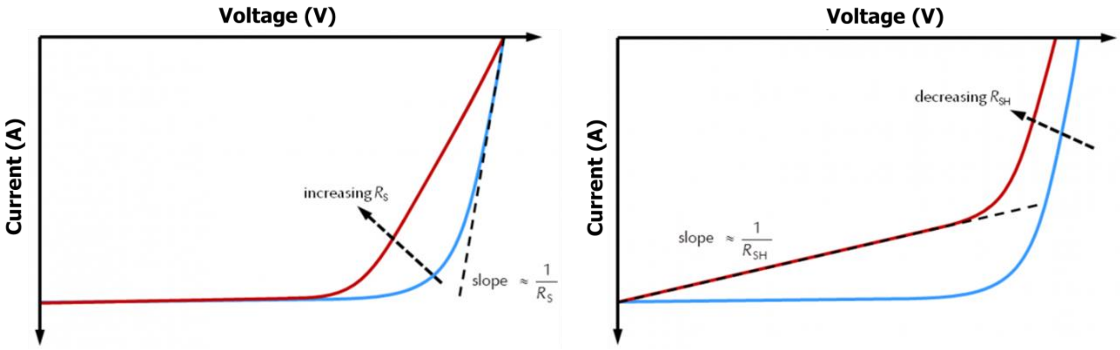

Figure 2. 24 Effects of the series resistance (R_S) and shunt resistance (R_{SH}) on the shape of an *I-V* curve.

2.7. Basic Working Principles of Carbon Dot Solar Cells

Carbon dot sensitized solar cells (CDSSCs) show a lot of similarities with dye sensitized solar cells (DSSCs). Briefly, DSSCs consist of a dye-sensitized photoanode, a counter electrode and an electrolyte (mostly iodide, polysulfide redox couple or solid-state electrolyte) (see **Figure 2. 25**).[145,146] The photoanode is composed of a mesoporous wide band-gap semiconductor (TiO_2, ZnO) which is highly stable under visible light illumination. TiO_2 colloidal solution is coated onto a transparent conductive oxide (TCO) substrate which is usually indium tin oxide (ITO) or fluorine doped tin oxide

(FTO). The resultant film is usually 10 μm thick and has a nanoporous structure that increases dye adsorption to the TiO_2 film. The dye sensitizer (usually an organic Ru complex) is adsorbed onto the TiO_2 surface which leads to absorption of photons and injection of electrons. The electrolyte, I^- / I_3^- redox couple, is used to transfer electrons between the TiO_2 and the counter electrode (Pt or earth-abundant alternatives). Tri-iodide ions (I_3^-), which are created by the reduction of the dye cations with I^- ion, are then reduced to I^- ions at the counter electrode. Pt-based materials, carbon-based materials or earth-abundant alternatives coated on the TCO substrate are usually used as the counter electrode. Physically blocked FTO - electrolyte interface prevents the injected electrons in the FTO to recombine with the redox couple in the electrolyte.

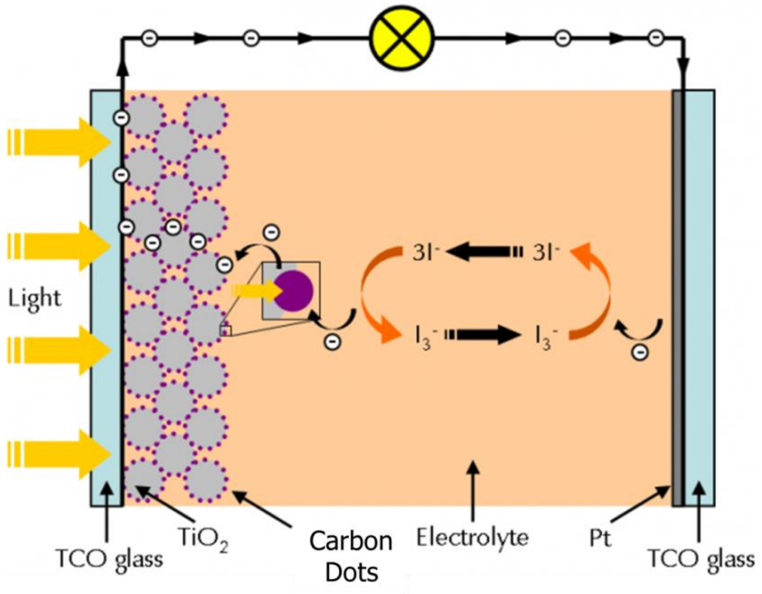

Figure 2. 25 Schematic representation of dye sensitized solar cell (DSSC).

Nanocrystalline semiconductor oxide (TiO_2) can be prepared with a hydrothermal method.[147] Average size of the nanoparticles is around 20 nm. A short sintering process is usually applied to ensure that the particles are electronically interconnected. To enhance the light-harvesting capacity of the dye-sensitized film in the red or NIR region, larger particles of 200-400 nm radius are mixed in the film or printed as an overlayer on top of the smaller particles. Apart from providing nanostructured, porous surface to enhance light harvesting by the adsorbed sensitizer, the role of the nanocrystalline TiO_2 film is also to serve as an electron collector and conductor. The conduction band of the semiconductor oxide (TiO_2) accepts the electrons from the electronically excited sensitizer. The electrons injected into the TiO_2 percolate very rapidly across the TiO_2 layer (for crossing a TiO_2 film of 10 μm thickness the time is 10 ms).

Figure 2. 26 illustrates the injection and recombination processes in a dye sensitized solar cell. The initial events of electron injection and dye regeneration leading to photoinduced charge separation occur on a femtosecond to nanosecond or microsecond time scale. The redox capture of the electron by the oxidized relay and the electron migration across the nanocrystalline film take place within milliseconds or even seconds[145].

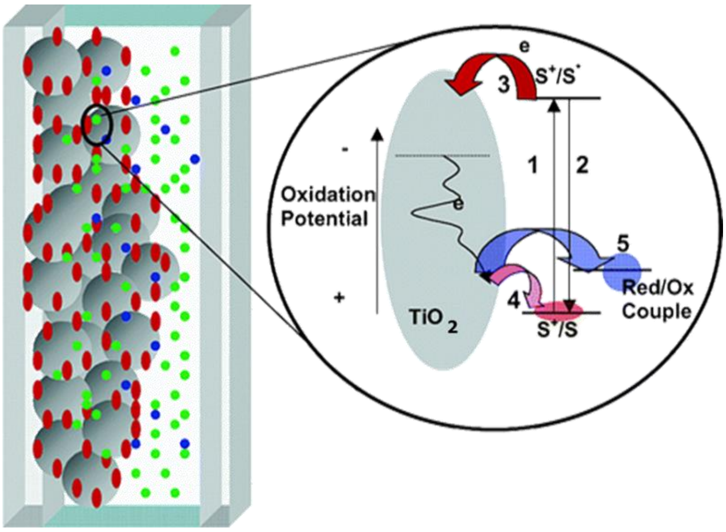

Figure 2. 26 Photoinduced processes occurring during the photovoltaic energy conversion at the surface of the nanocrystalline TiO_2.
(1) sensitizer (S) excitation by light; (2) radiative and nonradiative deactivation of the sensitizer; (3) electron injection in the conduction band of TiO_2 followed by electron trapping and diffusion to the particle surface; (4) recapture of the conduction band electron by the oxidized sensitizer (S^+); (5) recapture of the conduction band electrons by the oxidized form of the redox couple regenerating the sensitizer and transporting the positive charge (hole) to the counter electrode. Gray spheres are titania nanoparticles, red dots are sensitizer, green and blue dots are oxidized and reduced forms of the redox couple. Reproduced from Grätzel [145], Copyright 2005 American Chemical Society.

The only difference between the DSSCs and the CDSSCs is the sensitizing material. In CDSSCs carbon dots (CDs) are used as light-harvesting units to replace the dyes used in DSSCs. Light absorption produces excitons (electron-hole pairs) in the

CDs. Upon illumination, electrons from the conduction band (CB) of CDs are injected into CB of TiO_2 resulting in the oxidation of the photosensitizer (**Figure 2. 27**).

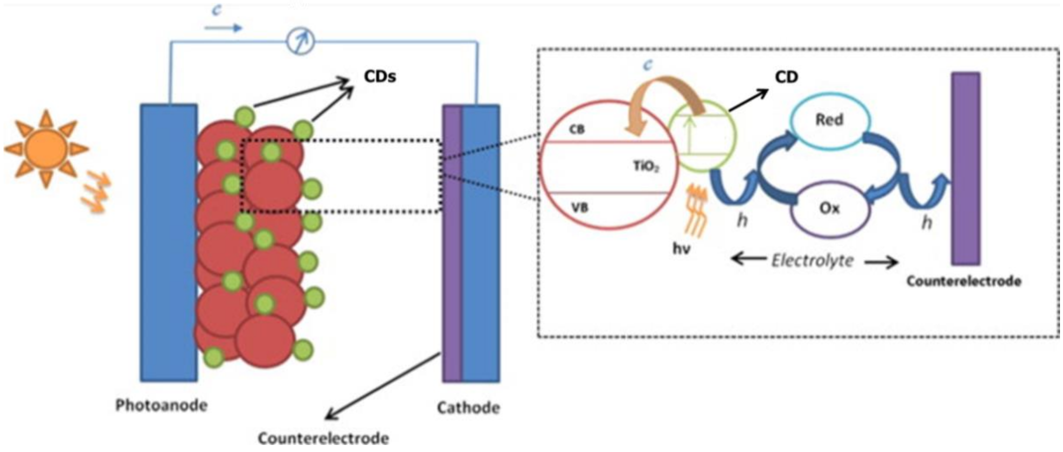

Figure 2. 27 Operating principle of a typical carbon dot sensitized solar cell (CDSSC). Reproduced from Kouhnavard *et al.*[148], Copyright 2014 Elsevier Ltd.

The ground state of CDs is regenerated through electron donation from the electrolyte (organic solvent containing a redox couple, usually iodide/triiodide couple). Another oxidation then occurs at the photoanode-electrolyte interface in the electrolyte. The iodide is regenerated by the reduction of triiodide at the counter electrode, with the circuit being completed *via* electron migration through the external load. The voltage generated under illumination corresponds to the difference between the Fermi level of the electron in the solid (electron in the photoelectrode) and the redox potential of the electrolyte. As a result, CDSSC device generates electrical power by using sunlight and the power conversion efficiency (PCE or η) of the solar cell is given by the equation:

$$\eta = \frac{J_{sc} * V_{oc} * FF}{P_{in}}$$

Eq. 1

, where J_{SC} is the short circuit current density (mA/cm^2), V_{OC} is the open circuit voltage (V), FF is the fill factor and P_{in} is the incident power (1000 W/m^2 under standard solar spectrum AM 1.5 G). More details about these solar cell operating parameters can be found in **Chapter 2.6**. J_{SC} and V_{OC} are directly measured from the current-voltage (J-V) curve of a solar cell (**Figure 2. 22**). J_{SC} is dependent on the light intensity, light absorption and electron injection efficiency, while V_{OC} is dependent on both the Fermi level of the semiconductor oxide and the level of dark current. Maximum value of the V_{OC} is determined by the difference between the Fermi level of the semiconductor oxide and the redox potential of the hole conductor.

The ideality of the solar cell is determined by the fill factor (FF) which is given by the following equation:

$$FF = \frac{J_m * V_m}{J_{SC} * V_{OC}}$$

Eq. 2

, where J_m is the maximum current density and V_m is the maximum voltage, both at the point of maximum power (**Figure 2. 22**). Assuming that the FF is equal to one, the *J*-*V* curve of a solar cell would reach the outer rectangular area.

The incident photon to current conversion efficiency (IPCE), also referred to as "external quantum efficiency" (EQE), corresponds to the number of electrons measured as photocurrent in the external circuit divided by the monochromatic photon flux that strikes the solar cell. IPCE can be expressed by the following equation:

$$IPCE\ (\lambda) = \frac{1240 * J_{SC}(\frac{A}{cm^2})}{\lambda(nm) * I_{inc}(\frac{W}{cm^2})}$$

Eq. 3

, where I_{inc} is the incident light power and J_{SC} is measured at various excitation wavelengths (λ).

For cell illumination, a standard solar spectrum of AM 1.5G (air mass global) is used. This spectrum is derived from the path length the light needs to travel through the atmosphere and reach the surface of the Earth. The spectrum is normalized so that the integrated irradiance is 1000 W/m^2 (100 mW/cm^2).

Chapter 3 | Structural and Optical Properties of Carbon Dots

3.1. Introduction

Structural and optical properties of carbon dots have gained huge attention in the research community in the last 12 years since their first discovery.[29, 37, 40, 38] In this chapter, several characterization techniques such as transmission electron microscopy (TEM), elemental analysis, Fourier transform infrared spectroscopy (FTIR), X-ray photoelectron spectroscopy (XPS), Raman, X-ray diffraction (XRD), UV-Vis absorption and photoluminescence spectroscopy, have been used to understand the correlations between formation mechanism, structure and optical properties of carbon dots.

The chapter opens with the study of morphology of carbon dots and carbon microspheres synthesized by hydrothermal method (HTC) using different precursors. After the HTC synthesis, the obtained yellow/brown liquid phase contained fluorescent carbon dots. After the HTC synthesis of certain precursors, the solid black/brown precipitate was also obtained at the bottom of the reaction vessel together with the upper liquid phase, and the black precipitate was named carbon microspheres.

This is followed by studies of chemical composition and structural features of carbon dots and carbon microspheres. The idea was to gain further insights into the presence and chemical environment of different functional groups on the surface, and to probe crystalline/amorphous character of as-synthesized carbon nanoparticles.

Moving on, the optical properties of carbon dots were extensively studied, while carbon microspheres didn’t show any photoluminescence properties. The focus was to fully characterize absorption, excitation and photoluminescence spectra of carbon dots, which enabled conclusions about origins of photoluminescence in carbon dots.

Finally this chapter will close with the description of a possible formation mechanism of carbon dots and carbon microspheres.

The precursors used for the synthesis of carbon dots were as follows: chitosan, chitin, D-glucose, L-arginine, L-cysteine and lobster shells. The idea was to use low-cost and highly abundant biomass-derived or food waste precursors for the synthesis of fluorescent carbon nanoparticles by hydrothermal synthesis under mild conditions.

Glucose was used as a model precursor for the synthesis of fluorescent carbon dots. Since glucose only contains C, O and H atoms, the as-synthesized carbon dots were considered “undoped”. Glucose is a sugar with molecular formula $C_6H_{12}O_6$. It is a monosaccharide and a hexose sugar (6 carbon atoms). The D-isomer (D-glucose) is also known as dextrose and occurs widely in nature. Glucose may exist in the form of five different isomers where one of the isomers represents an open-chain form and the other four are cyclic forms.

In its open-chain form, the glucose molecule has an open and unbranched backbone of six carbon atoms, C-1 to C-6 (**Figure 3. 1**). C-1 carbon atom is a part of an aldehyde group -(C=O)H and each of the other five carbon atoms connects to one hydroxyl group (-OH). The remaining bonds of the backbone carbon atoms are connected to hydrogen atoms (-H). In D-glucose, hydroxyls connected to C-2, C-4 and C-5 must be on the right side, while that connected to C-3 must be on the left side.

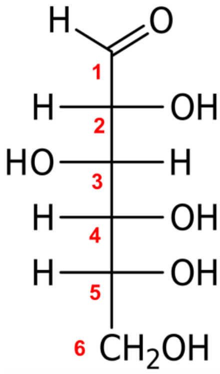

Figure 3. 1 Structure of D-glucose in its open-chain form.

In solutions, the open-chain form of glucose exists in equilibrium with several cyclic isomers which contain a ring of carbon atoms closed by one oxygen atom. The ring structure arises from the open-chain form by chemical reaction between the aldehyde group -(C=O)H at position C-1 and the hydroxyl group (-OH) at position C-4 or C-5. The reaction between C-1 and C-5 creates a molecule with a six-membered ring called pyranose, and the much rarer reaction between C-1 and C-4 creates a molecule with a five-membered ring called furanose. The open-chain isomer D-glucose gives rise to four cyclic isomers: α-D-glucopyranose, β-D-glucopyranose, α-D-glucofuranose, and β-D-glucofuranose (**Figure 3. 2**). The designation "α" means that the hydroxyl group attached to C-1 and the -CH_2OH group at C-5 lay on the opposite sides of the ring's plane, while "β" means that they are on the same side of the ring’s plane.

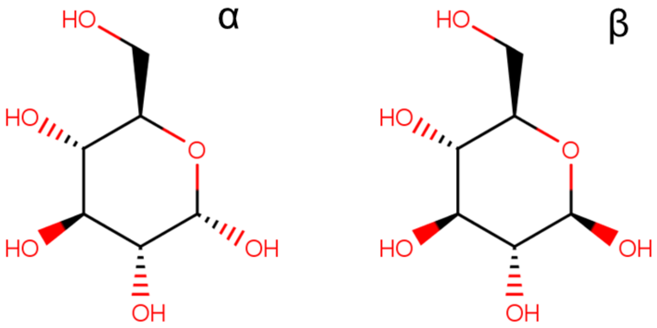

Figure 3. 2 Structure of α-D-glucopyranose and β-D-glucopyranose isomers.

Chitosan and chitin precursors were used as nitrogen source for the synthesis of fluorescent carbon dots. The idea was to synthesize nitrogen “doped” carbon dots and to compare their structural and optical properties with non-nitrogen containing carbon dots. Chitosan contains nitrogen in the form of amine group while chitin contains nitrogen in the form of amide group.

Chitin and chitosan are natural polysaccharides with unique structures. They have interesting properties such as biocompatibility, biodegradability and non-toxicity. Chitin is a structural biopolymer and has a role analogous to that of cellulose in plants. Cellulose is produced in cell walls of plants and chitin is produced by insects and crustaceans in their shells. Chitin occurs in nature as crystalline microfibrils which are structural components of exoskeleton of arthropods, crustaceans (lobsters, crabs, shrimps, prawns) and cell walls of fungi. Chitin is a poly (β-(1→4)-N-acetyl-D-glucosamine) and is the second most abundant natural polymer in the world after cellulose (**Figure 3. 3**).[149, 150] The degree of acetylation in chitin is typically 0.9 which indicates the presence of some amino groups.

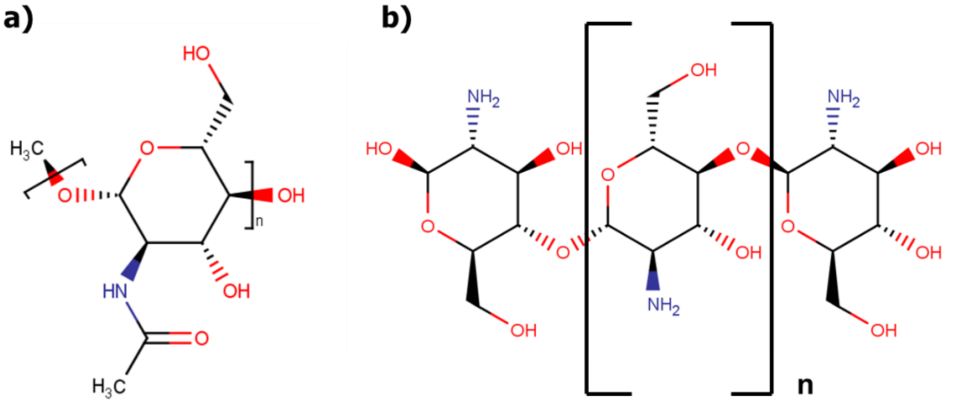

Figure 3. 3 Structure of chitin (a) and chitosan (b).

Chitosan is the N-deacetylated derivative of chitin with a typical degree of acetylation of less than 0.35 (**Figure 3. 3**).[151] Chitosan is a copolymer composed of glucosamine and N-acetylglucosamine. Crustacean shells (lobsters, shrimps, prawns, crabs) which can be considered food waste, are commercially used for the production of chitin and chitosan.

L-arginine and L-cysteine amino acids were used for the synthesis of carbon dots with the idea of synthesizing sulphur and nitrogen “doped” carbon dots, and to compare their structural and optical properties with monosaccharide and polysaccharide derived carbon dots.

Arginine (2-amino-5-guanidinopentanoic acid) is a semi essential amino acid. It contains α-amino group, α-carboxylic acid group, and a 3-carbon aliphatic straight chain capped by guanidinium (**Figure 3. 4**).[152] Arginine is found in a wide variety of foods from animal sources (beef, pork, poultry, cheese, milk) and plant sources (oatmeal, peanuts, nuts, seeds).

L-cysteine, 2-amino-3-sulfhydrylpropanoic acid, is a semi essential amino acid with the thiol side chain. (**Figure 3. 4**).[153] L-cysteine is found in most high protein foods from animal sources and plant sources. Industrially produced L-cysteine is obtained by hydrolysis of animal materials like poultry feathers or hog hair.

Real lobster shells were chosen as a final precursor for the synthesis of fluorescent carbon dots. The idea was to use real food waste to synthesize carbon dots and to compare their optical properties with carbon dots synthesized from commercially available precursors (monosaccharides, polysaccharides and amino acids).

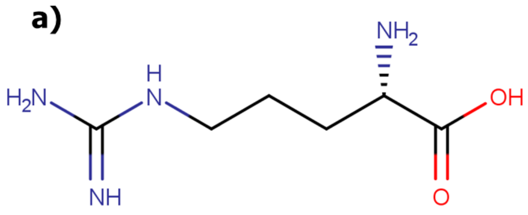

Figure 3. 4 Structure of L-arginine (a) and L-cysteine (b).

3.2. Morphology of Carbon Dots

Transmission electron microscopy (TEM) characterization was performed to examine the structures and morphologies of all luminescent carbon dots (CDs). Carbon dots represented the nanometer sized nucleation clusters dispersed in the aqueous phase, resulting from hydrothermal treatment of starting precursors. **Figure 3. 5** shows TEM images of the as-synthesized carbon dots taken at accelerating voltage of 200 kV, together with the corresponding particle size distributions.

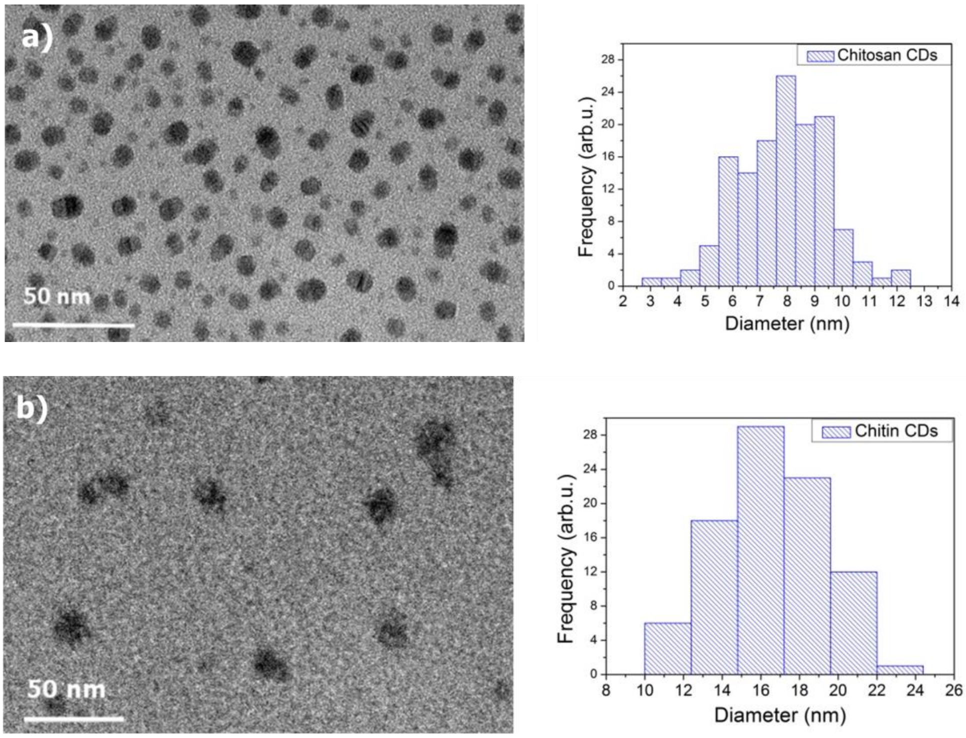

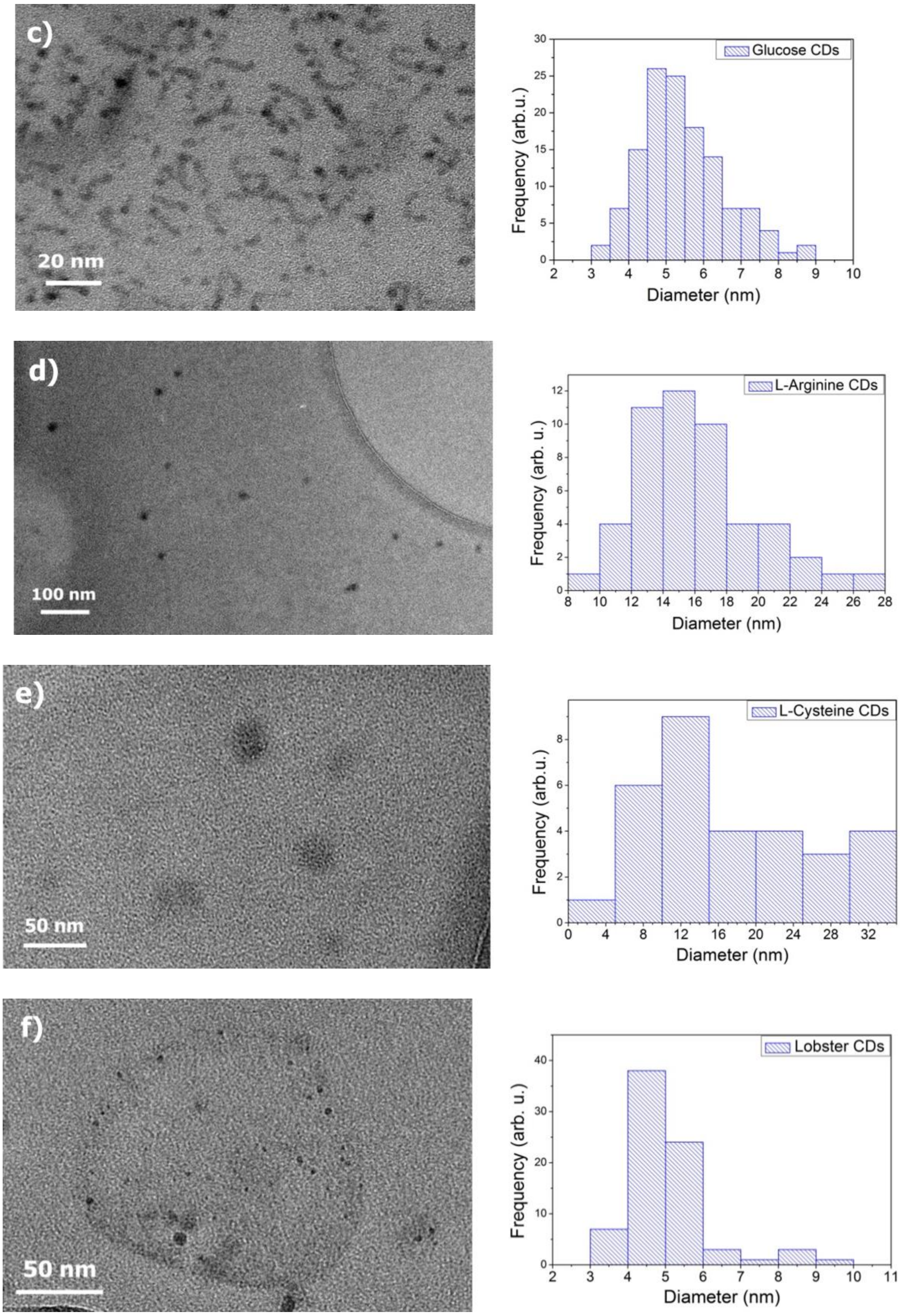

Figure 3. 5 TEM images at 200 kV and corresponding size histograms of as-synthesized carbon dots derived from: a) chitosan, b) chitin, c) D-glucose, d) L-arginine, e) L-cysteine and f) lobster.

All carbon dots showed a quasi-spherical morphology and polydispersity. As it can be seen from **Figure 3. 5 c**, glucose carbon dots showed long strips of material connected to the spherical cores. The origin of these long strips of material is still unclear and needs further investigation. One possible explanation is that these long strips show amorphous carbon nature, while spherical carbon cores can show crystalline nature. This is similar to the observation by Xu *et al.*[58], who showed the presence of amorphous sp^3 surface regions in CDs together with the crystalline sp^2 carbon core. The particle size distribution of carbon dots was measured from TEM images by using ImageJ software. For glucose carbon dots' particle sizes, only quasi-spherical cores were considered, not the long strips connected to them. Particle size histograms of all carbon dots are shown in **Figure 3. 5**, from which the average particle size and standard deviation were calculated. Average particle size and standard deviation were based on the statistics of about 100 particles of each precursor in several TEM images. Size distribution measurements showed that the average diameters of as-synthesized carbon dots were as follows: chitosan (7.91 ± 1.64) nm, chitin (16.54 ± 3.40) nm, glucose (5.15 ± 0.83) nm, L-arginine (15.0 ± 2.5) nm, L-cysteine (11.4 ± 3.0) nm and lobster (4.80 ± 0.67) nm.

It is very challenging to synthesize monodispersed and narrow size distribution carbon dots by using hydrothermal / solvothermal synthesis methods. One elegant solution was presented by Kwon *et al.*[154, 155] who have developed size-controlled synthesis of carbon dots by using reverse micelles as nanoreactors. They used "water-in-oil" emulsion as a self-assembled soft template, and they regulated the size of the micelles by the water-surfactant molar ratio. This enabled them to offer precise size tunability and narrow size distribution of synthesized carbon dots.

It was interesting to notice how the choice of molecular precursor has a clear influence on the carbon dots' average size under the same hydrothermal synthesis conditions. Chitosan and chitin precursors, which are nitrogen-containing polysaccharides, gave carbon dots with bigger average sizes than D-glucose precursor, which is a monosaccharide. The difference in average size of carbon dots between chitosan/chitin and D-glucose carbon dots can be attributed to a different reaction mechanism during the hydrothermal carbonization (HTC) process. Briefly, during the hydrothermal carbonization of chitosan and chitin as starting precursors, the formation of carbon dots involves Maillard reactions between the resulting 5-hydroxymethylfurfural (HMF) and the nitrogen compounds which were formed during the HTC treatment (**Chapter 3.3, Scheme 3. 2**).[156] D-glucose as a precursor formed carbon dots involving only a single molecular species (HMF), which resulted in a smaller average particle size (**Chapter 3.3, Scheme 3. 1**).

Lobster carbon dots which were obtained from real lobster shells (see **Chapter 6**), had similar chemical composition as chitin precursor, but as it can be seen from **Figure 3. 5** the average particle size of lobster carbon dots was much smaller than the chitin carbon dots. The possible reason for that is still unclear.

Both L-arginine and L-cysteine, as precursors for the synthesis of carbon dots, are nitrogen-containing amino acids and L-cysteine also contains sulphur. Carbon dots obtained from L-arginine and L-cysteine, together with chitin carbon dots, showed the biggest particle sizes compared to all other carbon dots. This points out to a potentially different formation mechanism as discussed at the end of **Chapter 3.3**.

The TEM images for a rather small number of chitosan-derived carbon dots showed graphitic crystalline structure with a repeating distance between the crystalline planes of (0.325 ± 0.007) nm, determined using ImageJ software (**Figure 3. 6**). Electron diffraction image showed that the as-prepared chitosan carbon dots were crystalline showing lattice fringes spaced at (0.318 ± 0.002) nm.

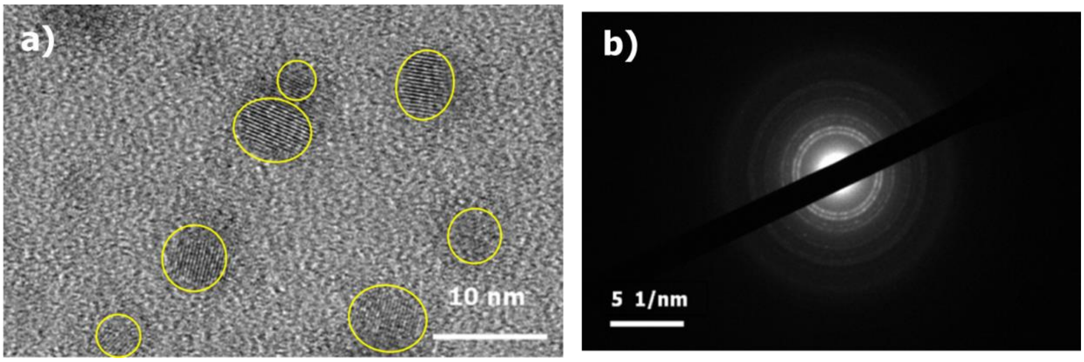

Figure 3. 6 a) High resolution TEM image at 200 kV of chitosan carbon dots and b) electron diffraction image of chitosan carbon dots.

The appearance of these lattice fringes in the CDs synthesized by hydrothermal method under mild-synthesis conditions (200 °C for 6 hours), is still a point of big debate among researchers. There is a possibility that these lattice fringes could have origin in the effect of annealing the sample by an electron beam. A lot of published data[157,34,158,159,77] in the literature had reported crystalline structures for the hydrothermally synthesized carbon dots from biomass-derived precursors. It may also be that graphitic structures form during the hydrothermal carbonization and co-exist with the amorphous structures (see Raman and XRD data in **Chapter 3.4.**).

After the hydrothermal carbonization of certain starting precursors, solid precipitate was formed at the bottom of the HTC reactor together with the upper liquid phase. As mentioned previously, the upper liquid phase contained nanometer sized carbon dots. The solid precipitate at the bottom of the HTC reactor was named carbon microspheres due to their micron size. Chitosan-, chitin- and glucose-derived microspheres are used as a model for further discussion.

Figure 3. 7 shows SEM images of chitosan-, chitin- and glucose-derived HTC carbon microspheres collected at the bottom of the reaction vessel. One possible hypothesis was that the carbon microspheres were possibly produced upon aggregation/growth of the carbon dots.

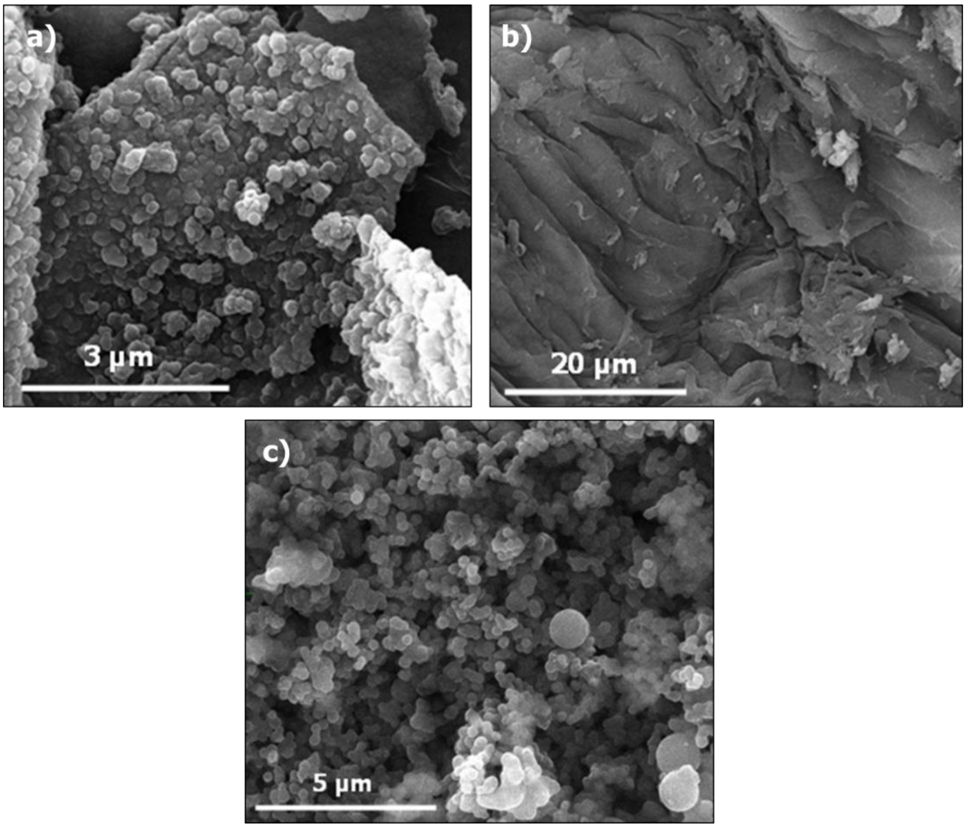

Figure 3. 7 SEM images of: a) chitosan microspheres, b) chitin microspheres and c) glucose microspheres.

It was observed that glucose microspheres were spherical particles with a rather homogenous size and an average diameter of around 0.4 µm (**Figure 3. 7 c**). In the case of chitosan, the resulting microspheres had a rather heterogeneous morphology and were formed out of smaller particles aggregated together (**Figure 3. 7 a**). Chitin hydrothermal carbons had a smooth surface and were made out of continuous flakes (**Figure 3. 7 b**).

The reaction mechanism is even more complex in the case of the amine-containing carbohydrates, especially given the fact that chitosan and chitin are polysaccharides similar to cellulose which needs to be firstly hydrolysed into glucosamine, and after decomposed into 5-hydroxymethylfurfural (HMF) and ammonia. In the case of chitin the hydrolysis is even more complicated than for chitosan due to the acetyl groups. Therefore the different morphology of the HTC carbon microspheres derived from chitin was due to the presence of a high fraction of unreacted chitin in the solid precipitate.

This was also confirmed by the lower carbon content of chitin-derived carbonaceous microspheres, which was lower than for glucose microspheres (46 wt% *vs*. 67 wt%, see **Chapter 3.4, Table 3. 2**). Also, this was confirmed by the FTIR spectrum which showed lot of features corresponding to pure chitin, as will be discussed in the following chapters. Chitosan-derived microspheres also contained a fraction of unconverted chitosan molecule, however in a smaller percentage compared to chitin microspheres.

In order to obtain further insights into the possible formation of the large carbon microspheres from the nanometer carbon dots, cross-section TEM micrographs were performed for the materials obtained from glucose. A selection of some microtommed TEM micrographs are shown in **Figure 3. 8**. It was difficult to say if the particles were formed from small carbon dots merged together or not. However, considering the fact that the particles were very smooth, a possible growth mechanism according to the classical nucleation theory was suggested.

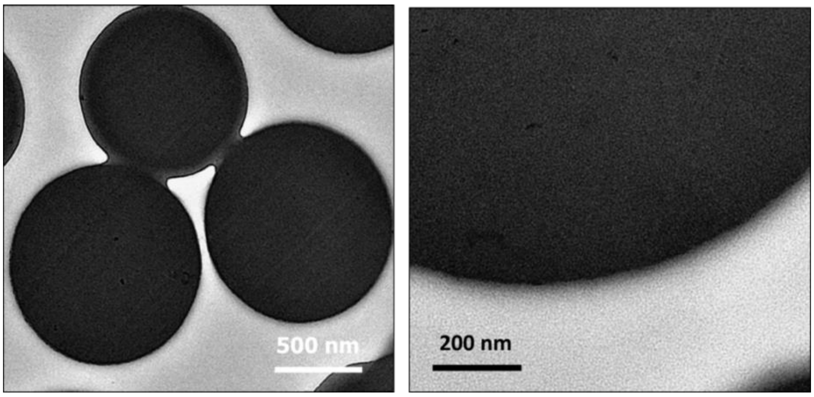

Figure 3. 8 TEM microtommed micrography of glucose microspheres at different magnifications.

This possible growth mechanism was further confirmed by the complete lack of porosity detected in all HTC carbons using both N_2 and CO_2 adsorption, as was previously reported by Titirici research group.[160] If the carbon microspheres were formed by the agglomeration of the small carbon dots, some intrinsic porosity would have been detected within the micropore range. However, the CO_2 adsorption isotherms for chitosan and chitin microspheres (**Figure 3. 9**) clearly followed the trend of a typical vapour-liquid equilibrium curve. This indicated that there is no presence of any micropores in chitosan and chitin microspheres. Glucose microspheres showed a slightly different CO_2 uptake throughout the range of pressure studied (**Figure 3. 9**). The analysis of the narrow micropore volume using the Dubinin-Radushkevich equation confirmed that this sample contained extremely low volume of micropores (0.016 g/cm^3). This was probably due to the fact that the morphology of glucose-derived microspheres was far more homogenous than the chitin and chitosan microspheres which contained higher amounts of unreacted precursors.

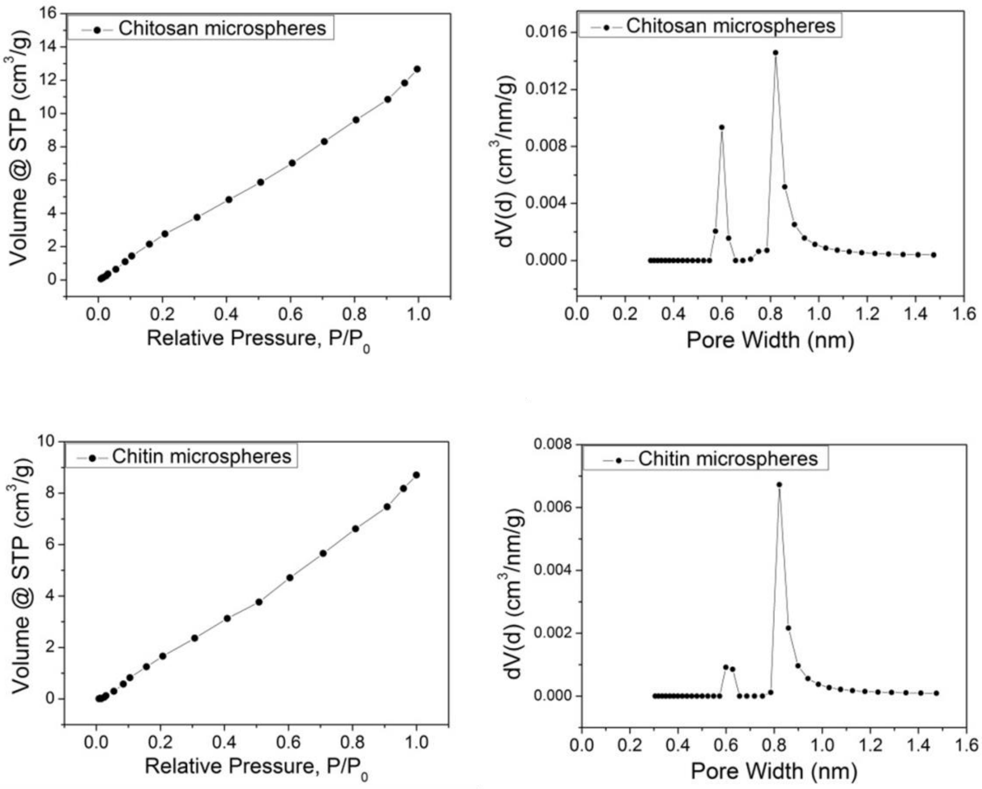

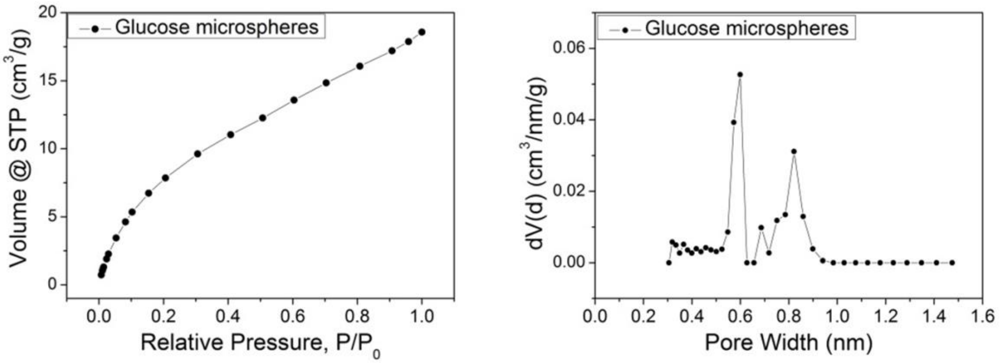

Figure 3. 9 CO_2 adsorption isotherms (273 K) and pore size distributions (calculated using CO_2 adsorption data *via* the NLDFT kernel assuming carbon slit pores) of chitosan-, chitin- and glucose microspheres (continued from previous page).

Upon the hydrothermal treatment of glucose, carbon dots were firstly formed upon complex hydroxymethylfurfural (HMF) reactions. These carbon dots were about 5 nm in diameter and possibly further grew into carbon microspheres with spherically shaped morphology and diameters of 0.5-1 µm (see **Chapter 3.3** for more details about the potential formation mechanism). After 6 h of hydrothermal reaction at 200 °C, both the carbon dots and the carbon microspheres were found to coexist with mass yield and concentration given in **Table 3. 1**.

The concentration of carbon dots was calculated from the freeze-dried liquid phase, and the synthesis mass yield of carbon microspheres was calculated as the mass ratio of the final solid product to the starting precursor. For precursors like L-arginine, L-cysteine and lobster, no solid product was obtained at the bottom of the reaction vessel after hydrothermal reaction.

Table 3. 1 Concentration of carbon dots and synthesis mass yield of carbon microspheres, all after 6 h of HTC reaction at 200 °C.

Precursor	**Concentration of carbon dots [mg/mL]**	**Synthesis mass yield of carbon microspheres [%]**
Chitosan	1.5 ± 0.2	47.1 ± 0.3
Chitin	0.6 ± 0.1	78.7 ± 0.6
D-glucose	56.3 ± 1.0	33.1 ± 0.3
L-arginine	35.3 ± 0.6	-
L-cysteine	9.8 ± 0.9	-
Lobster	1.8 ± 0.6	-

The situation was more complex for chitosan/chitin precursors, which are nitrogen-containing polysaccharides in the form of free amines in chitosan or as protected acetylated amides in chitin.

Upon hydrothermal treatment at 200 °C for 6 h, parts of chitosan/chitin were hydrolysed to glucosamine which then decomposed further to hydroxymethylfurfural (HMF) and ammonia forming the carbon dots in a solution (see **Chapter 3.3** for more details about the potential formation mechanism). Some of these carbon dots continued to grow, but *via* heterogeneous nucleation mechanisms on some of the unreacted initial precursor, leading to a more complex morphology. A very low concentration of carbon dots was obtained for chitosan- and chitin-derived carbon dots. The concentration of chitosan carbon dots after 6 h of hydrothermal synthesis was (1.5 ± 0.2) mg/mL, while for chitin carbon dots it was (0.6 ± 0.1) mg/mL (**Table 3. 1**). The respective mass yield of chitosan microspheres was (47.1 ± 0.3) % and for chitin microspheres it was (78.7 ± 0.6) % (**Table 3. 1**). The highest concentration of as-synthesized carbon dots was obtained for D-glucose CDs (56.3 ± 1.0) mg/mL, and for L-arginine CDs (35.3 ± 0.6) mg/mL.

3.3. Potential Formation Mechanism of Chitosan -, Chitin- and Glucose-derived Carbon Dots and Microspheres

During hydrothermal carbonization (HTC) under subcritical regime, glucose is first isomerised to fructose followed by the elimination of three water molecules to form hydroxymethylfurfural (HMF). HMF can be hydrolysed to further produce levulinic acid (4-oxopentanoic acid) and formic acid in a ratio 1:1. (**Scheme 3. 1 a**).[161]

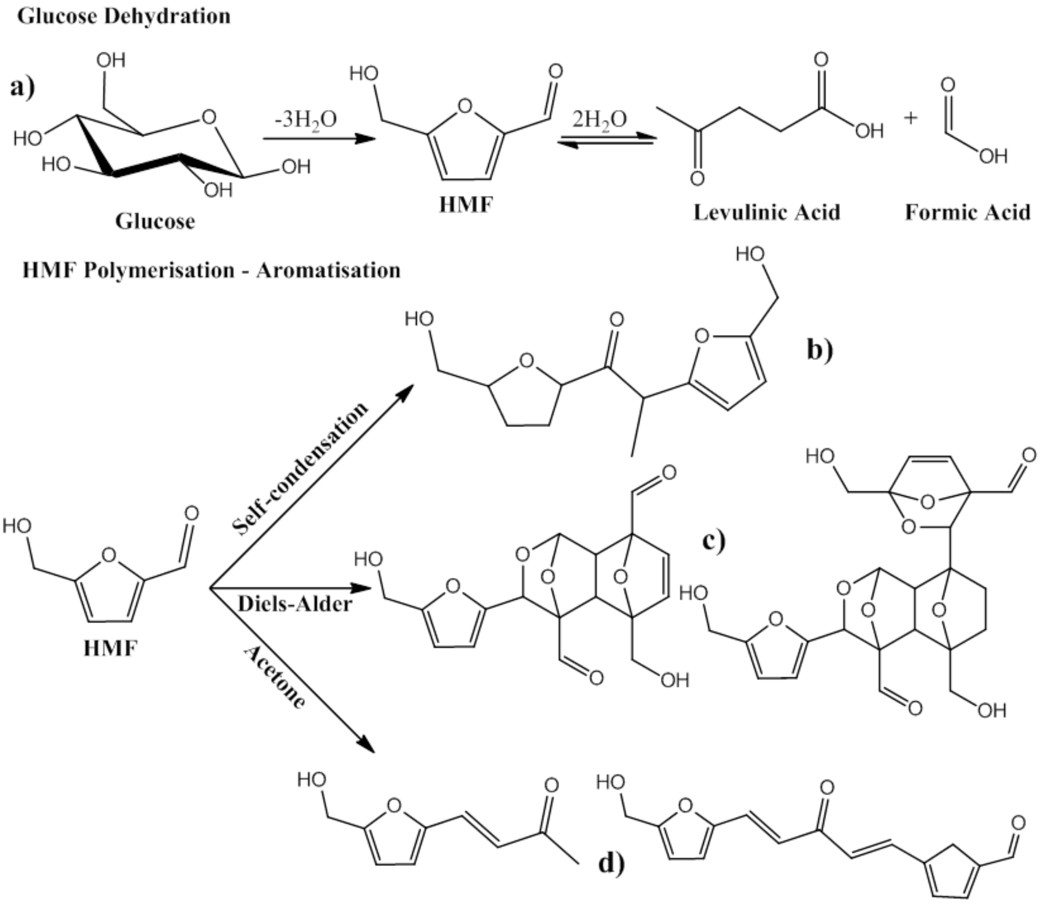

Scheme 3. 1 Potential chemical reactions involved in the formation of carbon dots and carbon microspheres formed by hydrothermal carbonization of glucose: a) dehydration of glucose to HMF and potentially to levulinic and formic acid; b) self-condensation reaction of HMF; c) Diels-Alder condensation of HMF; d) reaction of acetone with HMF.

HMF, which is in equilibrium with levulinic acid in water, can undergo further complex reactions with other products resulting in the formation of new carbon-carbon bonds. For example, HMF can undergo condensation reaction of aromatic aldehydes known as benzoin condensation. Self-benzoin condensation of HMF forms a coupled product called furoin (**Scheme 3. 1 b**).

Another possible reaction route is the Diels–Alder reaction, where there is the linking of two or more HMF units together by C–C bond formation. A typical Diels–Alder reaction is a 4πs + 2πs reaction involving a diene and a dienophile in which all atoms participating in the reaction are unsaturated carbons [162] (**Scheme 3. 1 c**). Diels–Alder reaction also ensures rate acceleration and enhanced selectivity in aqueous solution at elevated temperatures, which were the exact conditions in carbon dots' system. This is attributed to the combined effects of hydrogen bonding of water and enforced hydrophobic interactions. Successive condensations of more than two units of HMF are also possible, giving five and six carbon chains.

Also, HMF can undergo cross condensation with acetone and other aldehydes and ketones, with at least an acidic α-proton known to be also formed during the glucose hydrothermal treatment degradation reaction (**Scheme 3. 1 d**). The cross-aldol condensation route was demonstrated by Dumesic *et al*.[163]

Along with the formation of new C-C bonds, a growth in the molecular weight of the forming products occurs. Therefore new "carbonaceous" species are formed within the aqueous phase. This is when the nucleation process occurs as a new phase has been formed leading to the thermodynamic instability. The small nuclei formed at this stage represent the fluorescent carbon dots, which were previously reported via the HTC process.[120] These small nucleation clusters further grow into micrometre sized carbon spheres upon continuation of complex reactions mentioned above. Size dispersion of the carbon microspheres depends on the heterogeneity of the system (*i.e*. the complexity of the reactions), while their size can be controlled by time of reaction and concentration. It is not yet clear how the growth of the small nucleation clusters in HTC occurs. Two different mechanisms have been proposed in the literature. One suggested agglomeration of the small nuclei to form porous carbon spheres with a raspberry-like structure. [164] The other HTC formation mechanism suggested a growth according to the classical La Mer model [165], where the resulting nuclei grew uniformly and isotropically by diffusion of solutes towards the particle surface until the final size was attained.[166] Results of this PhD research project support the second mechanism based on nucleation of growth and considering the complete lack of porosity after the HTC process (previously demonstrated by Titirici research group).[160]

The reaction pathway is even more complex in the case of chitosan- and chitin-derived carbon dots and microspheres. Firstly chitosan/chitin precursors need to be hydrolysed to glucosamine (**Scheme 3. 2 a**), which is then decomposed to HMF (**Scheme 3. 2 b**) and ammonia, and then can initiate ring opening of furfurals to form aminopentanals (**Scheme 3. 2 c**).

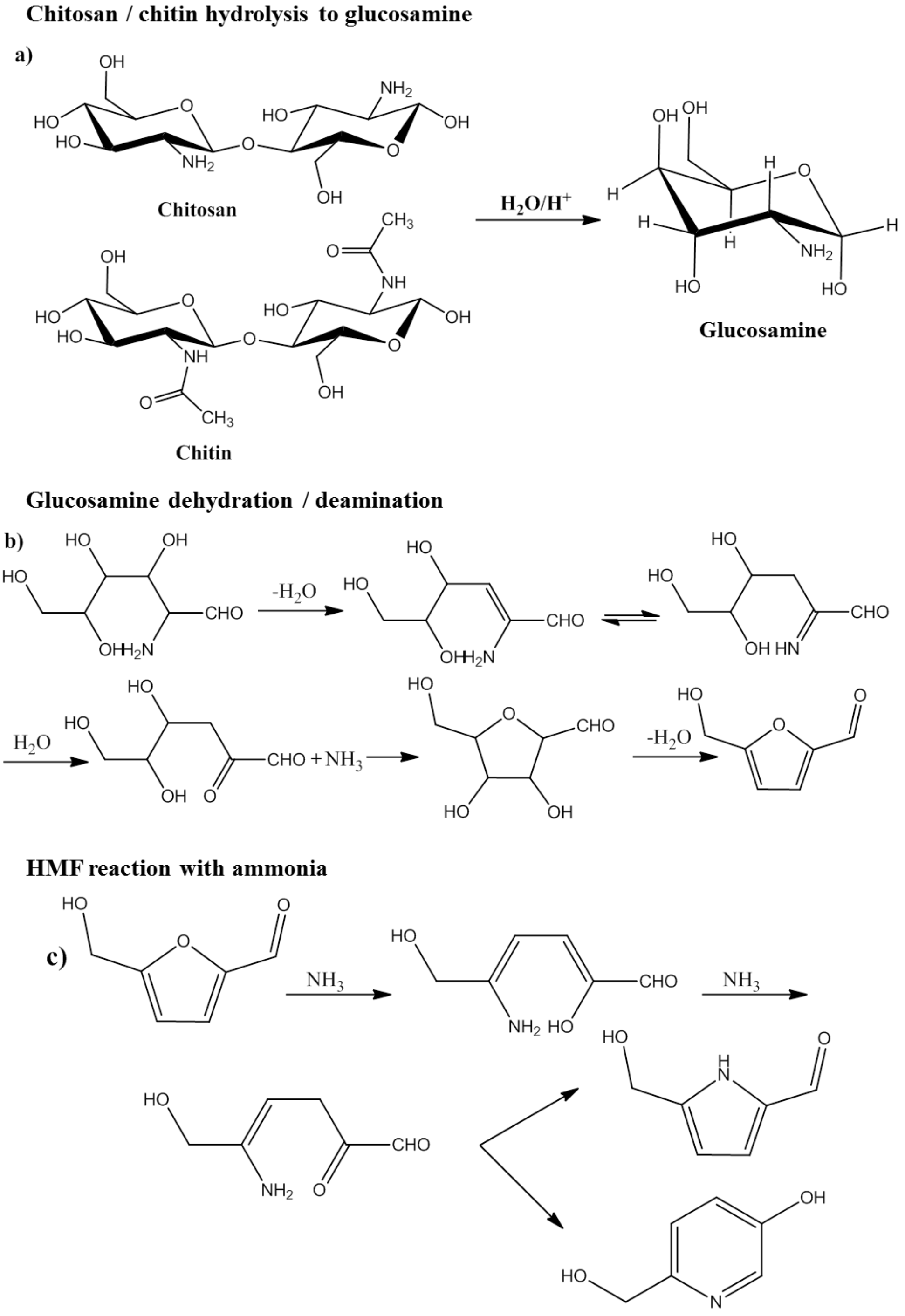

Scheme 3. 2 Potential chemical reactions involved in the formation of carbon dots from chitosan/chitin precursors: a) hydrolysis of chitosan/chitin to glucosamine; b) glucosamine dehydration / deamination to HMF and ammonia; c) reaction of HMF with ammonia.

Intramolecular condensation occurring in these intermediates between the amino groups and the aldehyde, leads to the formation of pyridines. Similar condensation between the amino group and keto group leads to the formation of pyrroles, with some amines remaining free (**Scheme 3. 2 c**).[167] All these functionalities were clearly identified in both the carbon dots and the carbon microspheres from chitosan and chitin. This more complex mechanism explains the polydispersity of carbon dots obtained from chitosan/chitin compared with glucose.

The formation of carbonaceous materials via HTC is a very complex process. The reactions provided in **Scheme 3. 1** and **Scheme 3. 2** are by far a simplified version of what is actually happening inside the reactor during HTC process, and should only be used as a tentative guidance. HTC materials' chemical structure is also complicated containing sp^2 and sp^3 carbon atoms and various oxygenated functional groups on the surface (hydroxyl, lactones, ketones, aldehydes and carboxylic groups). In the case of chitosan/chitin HTC derived carbonaceous materials, they also contain free amines along with pyridinic and pyrrolic nitrogen groups.

Structures shown in the **Scheme 3. 3** were drawn based on the potential chemical reactions discussed above. They do not necessarily reflect the real HTC carbonaceous materials' structure which is hard to precisely visualize. Previous solid state NMR studies from Titirici group on the carbon microspheres derived from glucose[8] and glucosamine[156], supported such a complex chemical structure.

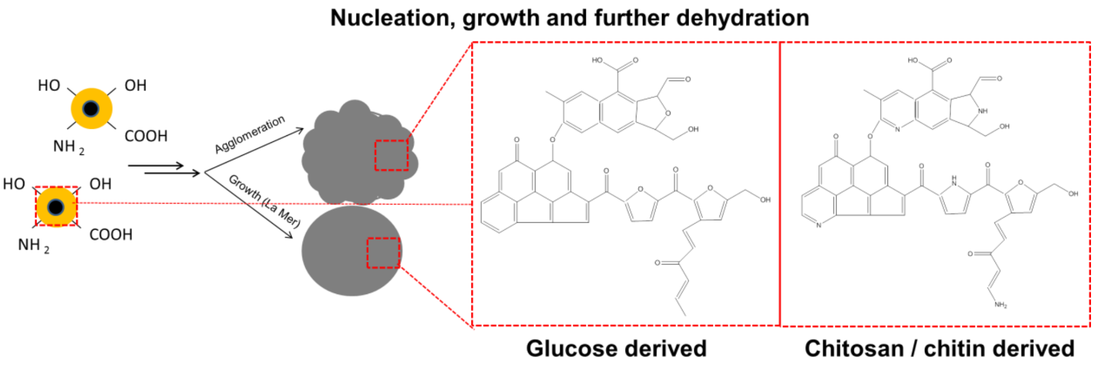

Scheme 3. 3 Possible formation of carbon dots and their further growth into carbon microspheres, along with a schematic of their chemical structure when produced from glucose or chitosan/chitin precursors.

There have only been a small number of published research papers in the literature which tried to explain the formation mechanism in carbogenic nanoparticles and graphene quantum dots. Qu *et al.*[74] have synthesized N-doped graphene quantum dots (GQDs) with hydrothermal method by using citric acid and urea. Citric acid was used as the carbon source and urea as the N source (in the form of amine group). They concluded that the formation of N-doped GQDs involved two steps. In the first step amine group worked as a base to facilitate dehydrolysis reaction. Citric acid molecules self-assembled into sheet structures and dehydrolyzed to form graphene framework, and also amide molecules were formed in reaction between citric acid and amines. Through the second step of intramolecular dehydrolysis, amides reacted with carboxylic groups and formed pyrrolic N. They concluded that N atoms entered graphene framework through the intramolecular dehydrolysis between amide and -COOH. Photoluminescence quantum yield exhibited significant improvement when pyrrolic N was formed.

Sahu *et al.*[52] have also proposed a very simplified explanation for the formation mechanism of hydrothermally synthesized CDs. These authors have synthesized green-fluorescence CDs by one step hydrothermal treatment of orange juice at low temperature (120 °C for 150 min). Authors have concluded that the dehydration and decomposition of fructose/glucose gave rise to different soluble products like furfural compounds (5-hydroxymethyl furfural, furfural, 5-methyl furfural, etc.), several organic acids (acetic, lactic, propionic, levulinic and formic acids), aldehydes and phenols. Hydronium ion formed from these acids acted as a catalyst in subsequent decomposition reaction stages. Due to the presence of weak acids like citric acid and ascorbic acid in orange juice, the dehydration and decomposition reaction proceeded in a controlled manner. The polymerisation and condensation of these products gave rise to soluble polymers. Aromatization and formation of aromatic clusters took place *via* aldol condensation, cycloaddition and hydroxymethyl-mediated furan resin condensation.[168] When the concentration of aromatic clusters reached a critical supersaturation point, a burst nucleation took place and carbon dots were formed.

Considering the formation mechanism of hydrothermally synthesized CDs from amino acid precursors, as far as the author of this PhD thesis is aware, there have been no publications explaining the formation mechanism. For example, Dong *et al.*[62] have used citric acid and L-cysteine to synthesize nitrogen and sulphur co-doped CDs (N,S-CDs) by using one-step hydrothermal treatment. Authors have characterized the CDs and provided possible explanation for the photoluminescence properties, but the authors didn’t provide any explanation for the formation mechanism of CDs. Similarly, Xu *et al.*[58] have synthesized nitrogen-doped carbon dots by using L-arginine as starting precursor. The authors have carbonized L-arginine by heating in air at 400 °C for 2 h, followed by extraction of CDs by using DMF (N,N-dimethylformamide) as solvent. Again, authors have provided detailed characterization of CDs and explanation of photoluminescence properties, but they didn’t provide any possible formation mechanism of as-synthesized CDs. Here, potential self-condensation reactions with branching might be possible. This needs to be studied in depth by liquid chromatography-mass spectrometry (LC-MS) analytical technique.

Although, it has to be mentioned that Kasprzyk *et al.*[63] have offered a simplified explanation of the formation mechanism during the reaction of citric acid and L-cysteine. Authors have studied the possible origin of luminescent properties of biodegradable photoluminescent polyesters (BPLPs). They have identified the compound named TPA (5-oxo-2,3-dihydro-5H-[1,3]thiazolo[3,2-a]pyridine-3,7-dicarboxylic acid) as the possible moiety responsible for the luminescence properties of BPLPs. The synthesis was straightforward: combining citric acid and L-cysteine followed by heating the mixture at 100 °C for 40 min (solvent free). The obtained product was purified and only the luminescent fraction was collected. Authors have assumed the formation of cysteine imide and condensation of the thiol group with the carbonyl moiety of citric acid (**Figure 3. 10**).

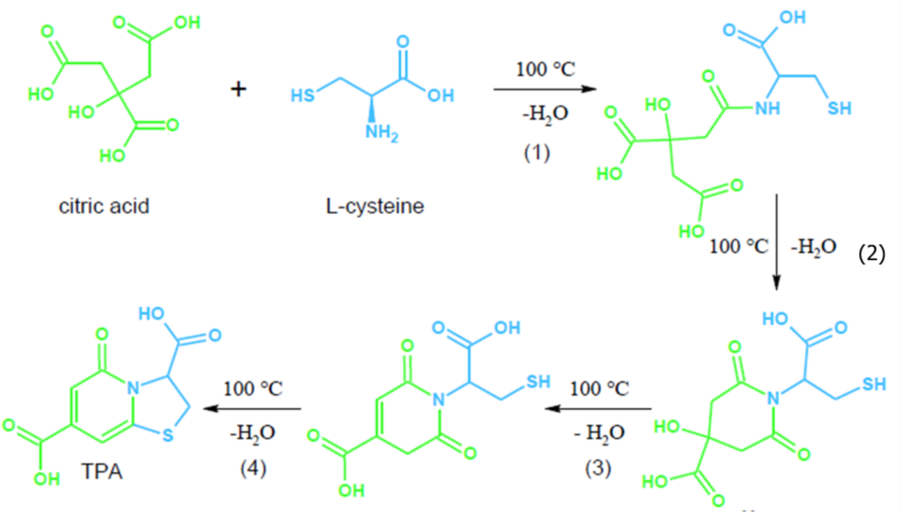

Figure 3. 10 The proposed mechanism of TPA formation: (1) amide formation, (2) imide formation, (3) dehydration and (4) intramolecular condensation.

Reproduced from Kasprzyk *et al.*[63], Copyright 2013 The Royal Society of Chemistry.

The work of Kasprzyk *et al.*[63] has been based on the previous work of Yang *et al.*[169] who have also synthesized biodegradable photoluminescent polymers. But, Yang *et al.*[169] have extended the synthesis by using citric acid and 20 different amino acids, not just L-cysteine.

The formation mechanism of hydrothermally synthesized CDs from different precursors still remains mainly unexplained. This should be the priority and focus of future research efforts in the field of hydrothermally synthesized CDs.

3.4. Chemical Composition and Structural Features of Carbon Dots

Elemental analysis data for the as-synthesized carbon dots (CDs) and selected model examples for the carbon microspheres, is provided in **Table 3. 2**. As it can be seen, chitosan, D-glucose and L-arginine derived carbon dots showed similar percentage of C at around 50 wt%. Chitin CDs contained the lowest amount of C (40.88 wt%) while L-cysteine CDs and lobster CDs contained around 47 wt% of C. Nitrogen containing functionalities from the starting precursors were well preserved into the final product of carbon dots after hydrothermal carbonization. The highest N content was observed in L-arginine CDs (20.05 wt %). Also, high N content was present in all other carbon dots. D-Glucose is a non-nitrogen containing precursor so D-glucose CDs had no nitrogen functionalities.

Regardless of the precursor used, all the as-synthesized carbon dots contained oxygenated functionalities. The amount of oxygen in carbon dots was calculated by difference to the other existing elements. The highest oxygen content was present in chitin CDs at 43.03 wt %. The oxygen content in D-glucose CDs and lobster CDs was around 40 wt %, in chitosan CDs it was 34.38 wt %, and the lowest value was for L-arginine CDs at 19.23 wt %. Recently, some authors have correlated the content of oxygen functionalities on the surface of carbon dots with the energy band gap between HOMO and LUMO molecular energy levels, and thus controlled the emission spectra of carbon dots.[73,170] During the course of this PhD research, these theory/effects were not investigated. L-cysteine CDs also showed the presence of small amount of sulphur (0.63 wt %), which originated from the sulphur functionalities in L-cysteine starting precursor.

Table 3. 2 Elemental composition of the as-synthesized carbon dots (CDs) and the selected examples of carbon microspheres.

Name	N [wt %]	H [wt %]	C [wt %]	O [wt %]	S [wt %]	C/N
Chitosan CDs	8.24	6.15	50.63	34.38	-	6.14
Chitin CDs	10.26	5.83	40.88	43.03	-	3.98
D-glucose CDs	-	5.54	53.75	40.71	-	-
L-arginine CDs	20.05	7.18	53.54	19.23	-	2.67
L-cysteine CDs	11.19	8.92	47.02	32.24	0.63	4.20
Lobster CDs	7.69	6.08	46.60	39.63	-	6.06
Chitosan microspheres	8.65	5.55	59.66	26.14	-	6.89
Chitin microspheres	6.63	6.19	46.49	40.69	-	7.01
Glucose microspheres	-	4.49	66.79	28.72	-	-

Glucose-derived carbon microspheres contained 66.79 wt% C due to the high solubilisation of glucose under hydrothermal conditions, and the formation of carbonaceous materials *via* the hydrothermal carbonization route. Chitosan microspheres had 59.66 wt% C, while the microspheres from chitin had the lowest carbon content of 46.49 wt%. This was in a good correlation with the different morphology of chitin-derived microspheres, which suggested that they contained a higher fraction of raw chitin. Nitrogen functionalities were also observed in the carbon microspheres up to 6.63 wt% in chitin and 8.65 wt% in chitosan. Carbon microspheres contained lower oxygenated functionalities compared with the corresponding carbon dots. As expected, chitin-derived microspheres contained the highest percentage of oxygen (40.69 wt%) in comparison with glucose microspheres (28.72 wt%).

Structural and chemical information about carbon dots and selected examples of carbon microspheres, have also been obtained from the corresponding FTIR analysis. FTIR spectra of all as-synthesized carbon dots (CDs) and selected examples of carbon microspheres are shown in **Figure 3. 11**.

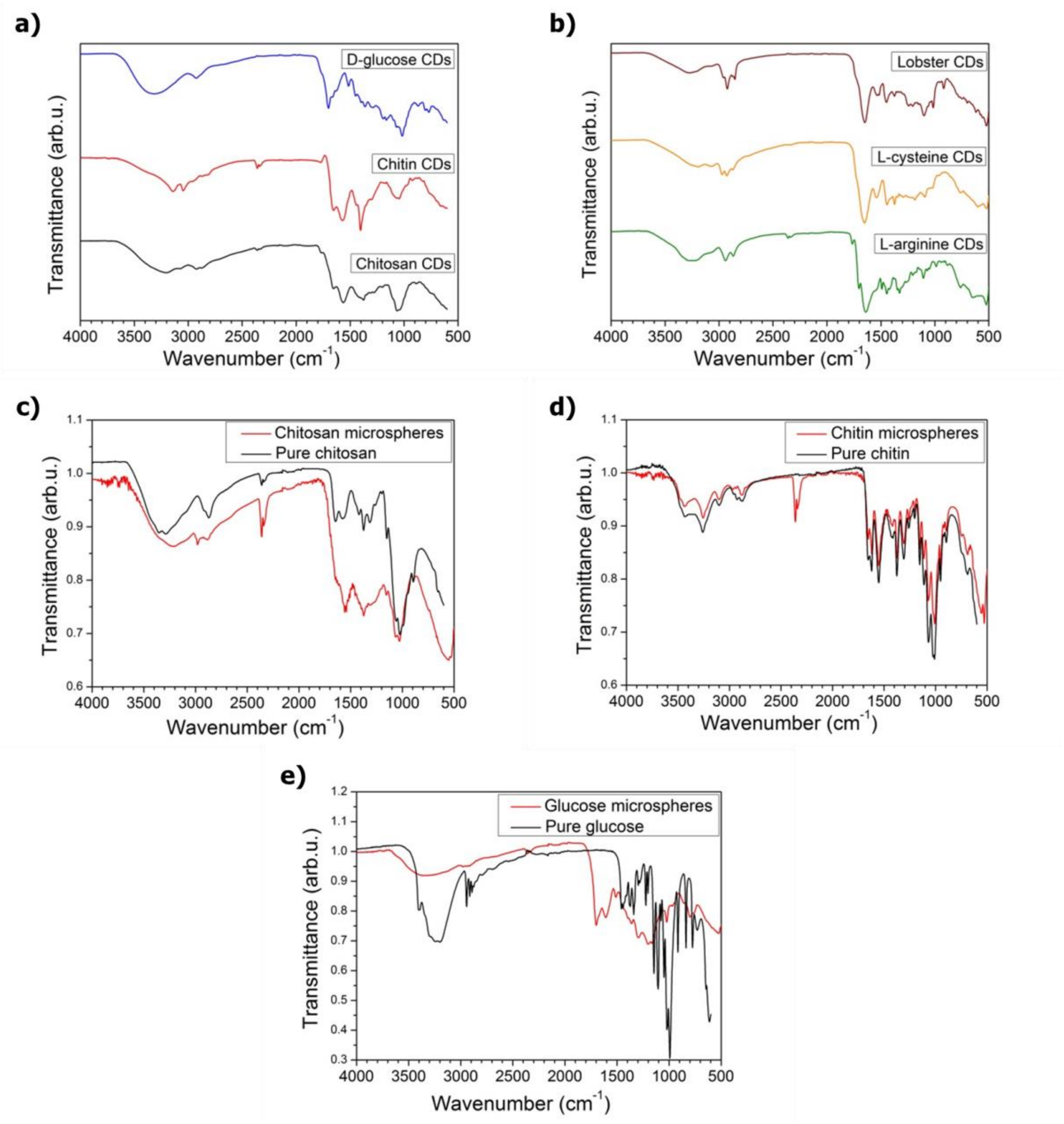

Figure 3. 11 FTIR spectra of: (a,b) carbon dots and (c, d, e) carbon microspheres.

Table 3. 3 shows a detailed overview of the FTIR results for the as-synthesized carbon dots.

Table 3. 3 Summary of FTIR results for as-synthesized carbon dots (CDs).

	Chitosan CDs [171,150]	Chitin CDs [150]	D-Glucose CDs [172,173]	L-arginine CDs [152]	L-cysteine CDs [153]	Lobster CDs
O-H stretching [cm^{-1}]	3500-3100	3400-3100	3600-3200	3400-3100	3400-3140	3500-3100
N-H stretching [cm^{-1}]	3500-3100 1570	3400-3100		3400-3100	3400-3140	3500-3100
C-H stretching [cm^{-1}]	2915 2870		2920	2940 2867	2970 2923	2921
C=O stretching [cm^{-1}]			1695	1695	1652	1650
-NH_2 bending [cm^{-1}]	1656			1645	1650 -1590	
Amide I band [cm^{-1}]		1652 1620				1652
Amide II band [cm^{-1}]		1570				1545
O-C-H and C-O-H deformation [cm^{-1}]			1525-1350			
CH_2 deformation [cm^{-1}]		1400				1450
C-H deformation [cm^{-1}]	1380			1445	1442	
O-H bending [cm^{-1}]				1325		
In plane C-H and O-H deformation [cm^{-1}]			1170			
C-C-C stretching [cm^{-1}]				1110		
C-C and C-O stretching [cm^{-1}]	1050		1191-995			1097
S-H bending [cm^{-1}]					962	
Aromatic C-H bending [cm^{-1}]			875-750			

FTIR spectra of chitosan carbon dots (**Figure 3. 11 a** and **Table 3. 3**) exhibited characteristic absorption bands of O-H stretching overlapping N-H stretching vibrations of amine group in the region of 3500-3100 cm^{-1}, -NH_2 bending at 1656 cm^{-1} and N-H stretching at 1570 cm^{-1}. [171,150] Chitosan microspheres exhibited similar features suggesting a mixture of raw chitosan and nitrogen doped carbonaceous material (**Figure 3. 11 c**).

Chitin carbon dots showed amide bands located at 1652 cm^{-1}, 1620 cm^{-1} and 1570 cm^{-1}, along with -OH groups and N-H stretching (**Figure 3. 11 a** and **Table 3. 3**). [150]

The FTIR spectrum of chitin-derived microspheres is very similar to the FTIR spectrum of pure chitin (**Figure 3. 11 d**). The large similarities between raw chitin and chitin microspheres' FTIR spectra were in a good agreement with elemental analysis data which showed the lowest percentage of carbon and the highest percentage of oxygen (**Table 3. 2**) compared to other carbon microspheres.

The FTIR spectra of glucose carbon dots (**Figure 3. 11 a** and **Table 3. 3**) showed the presence of O-H stretching vibrations (3600 – 3200 cm^{-1}) along with C=O stretching at 1695 cm^{-1}. Combination bands of O-C-H and C-O-H deformation were in the region of 1525 – 1350 cm^{-1}. In plane C-H and O-H deformation was observed at 1170 cm^{-1} and a band of C-O and C-C stretching was assigned from 1191 cm^{-1} to 995 cm^{-1}. [172,173] Similarly, for glucose microspheres the following strong absorption bands were observed: O-H stretching at 3367 cm^{-1}, C-H stretching at 2930 cm^{-1}, C=O stretching at 1695 cm^{-1}, C-O stretching at 1150 cm^{-1} and 1000 cm^{-1}, and C-H stretching at 845 cm^{-1}.

L-arginine and L-cysteine carbon dots showed strong absorption bands of O-H stretching overlapping with N-H stretching (3400-3100 cm^{-1}), C-H stretching at around 2900 cm^{-1}, C=O stretching at 1695-1650 cm^{-1} and -NH_2 bending at 1650 -1590 cm^{-1}. [152, 153] L-cysteine carbon dots also showed absorption band of S-H bending at 962 cm^{-1}. (**Figure 3. 11 b** and **Table 3. 3**)

Lobster carbon dots showed similar absorption bands to chitin carbon dots, such as O-H stretching overlapping with N-H stretching (3500-3100 cm^{-1}), C-H stretching at 2921 cm^{-1}, C=O stretching at 1650 cm^{-1} and amide bands at 1652-1545 cm^{-1}. (**Figure 3. 11 b** and **Table 3. 3)**

As a summary of FTIR results, from **Table 3. 3** and **Figure 3. 11**, it can be seen that O-H stretching vibrations in the region of 3600-3100 cm^{-1} were present in all CDs. N-H stretching band (3500-3100 cm^{-1} and at 1570 cm^{-1}), which was overlapping with

O-H stretching band, was observed for all CDs, except for D-glucose CDs (since D-glucose is a non-nitrogen containing precursor). C-H stretching vibrations in the region of 2970-2870 cm^{-1} were observed for all CDs, except for chitin CDs. CDs from D-glucose, L-arginine, L-cysteine, and lobster all showed the presence of C=O stretching band in the region of 1695-1650 cm^{-1}. NH_2 bending vibrations (1656-1590 cm^{-1}) were observed for chitosan CDs, L-arginine CDs and L-cysteine CDs. Amide I band (1652 cm^{-1} and 1620 cm^{-1}) and amide II band (1570 cm^{-1} and 1545 cm^{-1}) were all observed for chitin CDs and lobster CDs. Characteristic O-C-H and C-O-H vibrations (1525-1350 cm^{-1}) were observed for D-glucose CDs. Chitin CDs and lobster CDs showed the presence of CH_2 deformation (1400 cm^{-1} and 1450 cm^{-1}), while C-H deformation (1445-1380 cm^{-1}) was observed for chitosan CDs, L-arginine CDs and L-cysteine CDs. S-H bending vibrations (962 cm^{-1}) were only present for L-cysteine CDs.

X-ray photoelectron spectroscopy (XPS) was performed on all carbon dots and selected examples of carbon microspheres, in order to gain further information into the chemical environment of functional groups. Summary of general XPS data of carbon dots and carbon microspheres is given in **Table 3. 4**, confirming the presence of oxygen, carbon and nitrogen. **Figure 3. 12** shows C 1s and N 1s deconvoluted XPS spectra of carbon dots, and also includes S 2p deconvoluted peak of L-cysteine carbon dots. **Table 3. 5** shows the summary of XPS peak positions found for all carbon dots.

Table 3. 4 The summary of general XPS data of carbon dots and carbon microspheres.

	O 1s [at%]	**C 1s [at%]**	**N 1s [at%]**	**S 2p [at%]**
Chitosan CDs	27.65	66.30	6.05	-
Chitin CDs	20.36	63.01	6.10	-
D-glucose CDs	21.69	71.18	-	-
L-arginine CDs	19.82	73.10	7.08	-
L-cysteine CDs	11.08	73.63	7.58	7.71
Lobster CDs	48.76	47.12	4.12	-
Chitosan microspheres	19.67	74.72	5.61	-
Chitin microspheres	27.64	66.17	6.18	-
Glucose microspheres	20.55	79.45	-	-

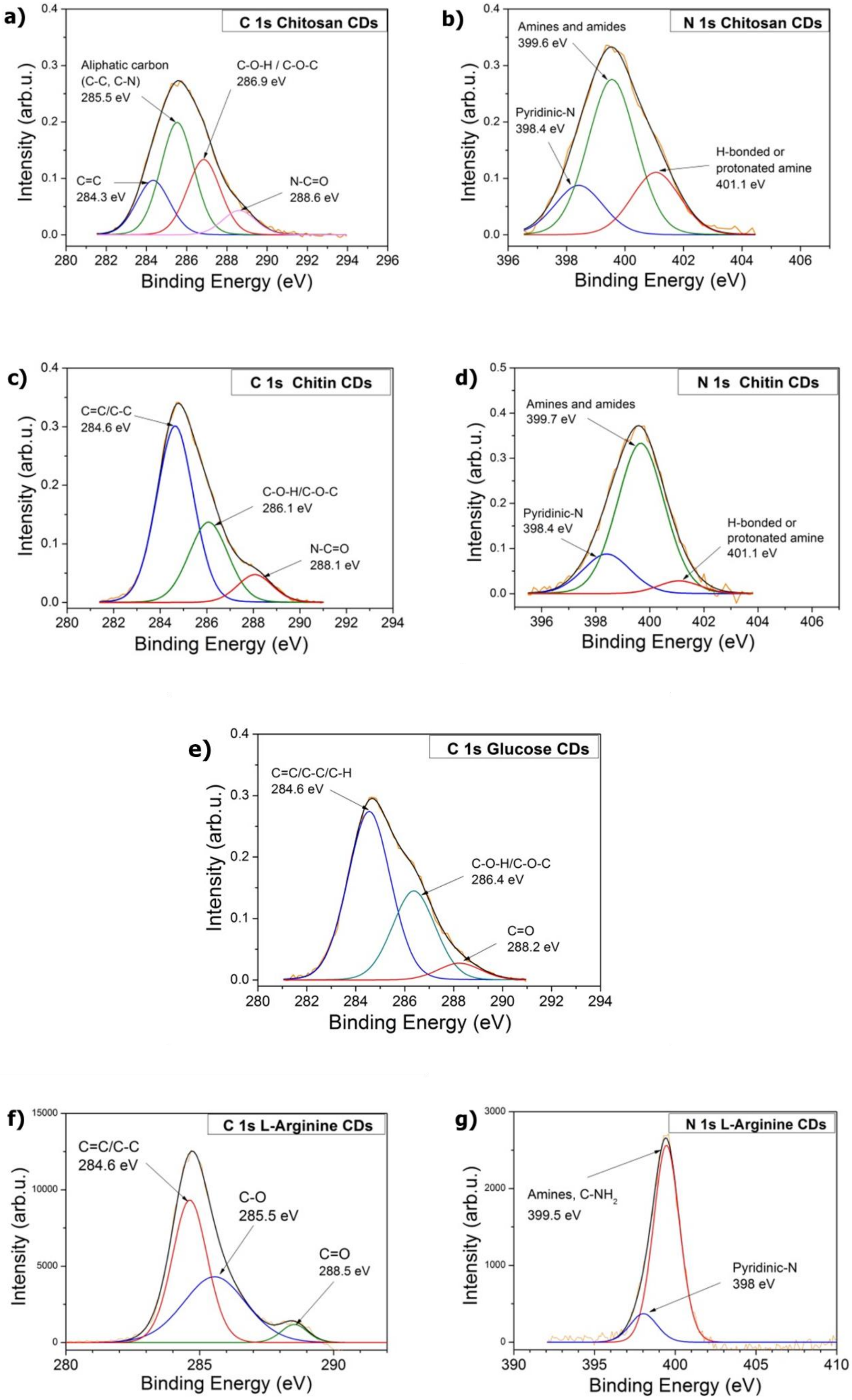
a)
C 1s Chitosan CDs
Aliphatic carbon (C-C, C-N) 285.5 eV
C-O-H / C-O-C 286.9 eV
C=C 284.3 eV
N-C=O 288.6 eV
Intensity (arb.u.)
Binding Energy (eV)
b)
N 1s Chitosan CDs
Amines and amides 399.6 eV
Pyridinic-N 398.4 eV
H-bonded or protonated amine 401.1 eV
Intensity (arb.u.)
Binding Energy (eV)
c)
C 1s Chitin CDs
C=C/C-C 284.6 eV
C-O-H/C-O-C 286.1 eV
N-C=O 288.1 eV
Intensity (arb.u.)
Binding Energy (eV)
d)
N 1s Chitin CDs
Amines and amides 399.7 eV
Pyridinic-N 398.4 eV
H-bonded or protonated amine 401.1 eV
Intensity (arb.u.)
Binding Energy (eV)
e)
C 1s Glucose CDs
C=C/C-C/C-H 284.6 eV
C-O-H/C-O-C 286.4 eV
C=O 288.2 eV
Intensity (arb.u.)
Binding Energy (eV)
f)
C 1s L-Arginine CDs
C=C/C-C 284.6 eV
C-O 285.5 eV
C=O 288.5 eV
Intensity (arb.u.)
Binding Energy (eV)
g)
N 1s L-Arginine CDs
Amines, C-NH2 399.5 eV
Pyridinic-N 398 eV
Intensity (arb.u.)
Binding Energy (eV)

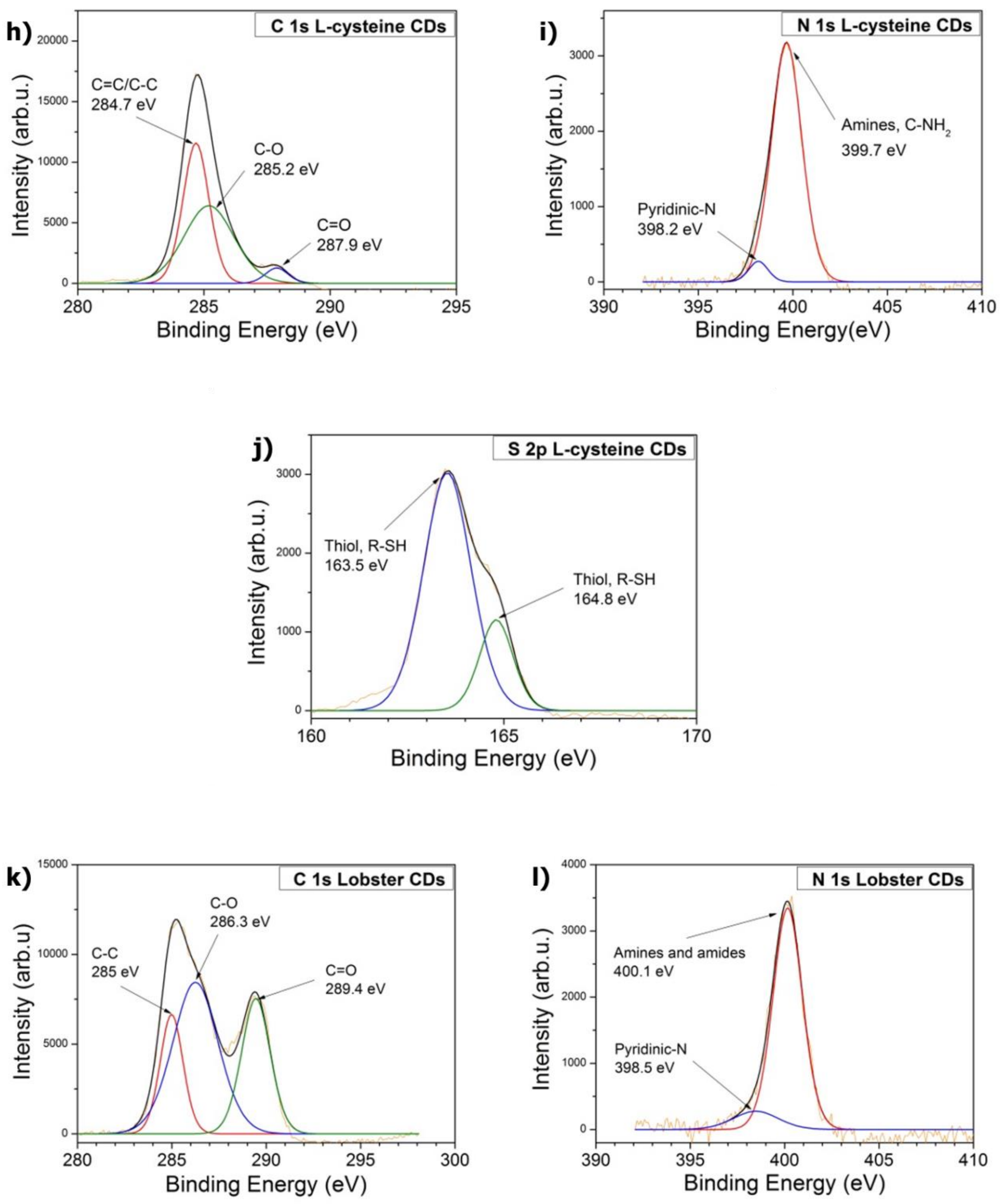

Figure 3. 12 Deconvoluted C 1s and N 1s peaks of: (a, b) chitosan CDs, (c, d) chitin CDs, (e) glucose CDs, (f, g) L-arginine CDs, (h, i, j) L-cysteine CDs and (k, l) lobster CDs.

C 1s peak of chitosan CDs was deconvoluted into the following peaks (**Figure 3. 12 a**): sp^2 carbon (C=C) at 284.3 eV; aliphatic carbon from C-N and C-C at 285.5 eV; C-O-H / C-O-C at 286.9 eV; and amide carbonyl (N-C=O) at 288.6 eV.[174]

Chitin CDs showed three single peaks in C 1s spectrum (**Figure 3. 12 c**): sp^2 / sp^3 carbon (C=C / C-C) at 284.6 eV; C-O-H / C-O-C at 286.1 eV; and amide (N-C=O) at 288.1 eV. Deconvoluted C 1s peak of glucose CDs (**Figure 3. 12 e**) confirmed the presence of -OH groups and C-O-C linkages, which was evident by the peaks at 284.6 eV and 286.4 eV.

Chitosan CDs showed dominant peak of amines and/or amides (C-NH / N-C=O) in N 1s spectra at 399.6 eV (**Figure 3. 12 b**). Based on the strong contribution in C 1s peak at 285.5 eV of chitosan CDs (**Figure 3. 12 a**), the N 1s peak at 399.6 eV (**Figure 3. 12 b**) was mainly attributed to amines. Also, the absence of this C 1s peak at 285.5 eV in chitin CDs (**Figure 3. 12 c**) suggested that the N 1s peak at 399.7 eV in chitin CDs (**Figure 3. 12 d**) was predominantly amides. This was also supported by the very small contribution from H-bonded or protonated amine at 401.1 eV in N 1s peak of chitin CDs, which is much larger for chitosan CDs. Also, pyridinic-N was confirmed in N 1s peak of chitosan CDs at 398.4 eV and H-bonded or protonated amine at 401.1 eV (**Figure 3. 12 b**).[174]

C 1s peak of L-arginine CDs (**Figure 3. 12 f**) was deconvoluted into 3 peaks which corresponded to: sp^2/sp^3 carbon (284.6 eV), C-O (285.5 eV) and C=O (288.5 eV).

Similarly, the C 1s peak of L-cysteine CDs (**Figure 3. 12 h**) was deconvoluted into: sp^2/sp^3 carbon (284.7 eV), C-O (285.2 eV) and C=O (287.9 eV). S 2p peak of L-cysteine CDs showed the presence of thiol group (R-SH) at 163.5 eV.

The N 1s peak of L-arginine CDs and L-cysteine CDs showed predominantly the presence of amines at 399.5 eV and 399.7 eV, respectively (**Figure 3. 12 g, i**).

C 1s peak of lobster CDs (**Figure 3. 12 k**) showed the presence of sp^3 carbon (285 eV), C-O (286.3 eV) and C=O (289.4 eV), while N 1s peak (**Figure 3. 12 l**) showed predominantly amines (400.1 eV) and a small fraction of pyridinic-N (398.5 eV).

The presence of the graphitic structure was confirmed by the sp^2/sp^3 carbon fraction observed in C 1s peak in the region of 284.3 - 285 eV for all carbon dots (**Figure 3. 12**). It was not possible to fully resolve the peaks corresponding to sp^2 and sp^3 bonded carbon due to the close proximity of these peaks (~284.0 eV and ~284.5 eV, respectively). XPS broadening further indicated significant dispersion in bonding energies suggesting disordered samples.

Table 3. 5 Summary of XPS peak positions found for all CDs.

	Chitosan CDs [174]	Chitin CDs [174]	D-glucose CDs	L-arginine CDs	L-cysteine CDs	Lobster CDs
Thiol (R-SH) [eV]					163.5	
sp^2 carbon (C=C) [eV]	284.3					
sp^2 / sp^3 carbon (C=C / C-C) [eV]		284.6	284.6	284.6	284.7	285
C-O [eV]				285.5	285.2	286.3
Aliphatic carbon (C-N and C-C) [eV]	285.5					
C-O-H / C-O-C [eV]	286.9	286.1	286.4			
Amide carbonyl (N-C=O) or C=O [eV]	288.6	288.1	288.2	288.5	287.9	289.4
Pyridinic-N [eV]	398.4	398.4		398	398.2	398.5
Amines and/or amides (C-NH / N-C=O) [eV]	399.6	399.7		399.5	399.7	400.1
H-bonded or protonated amine [eV]	401.1	401.1				

Figure 3. 13 shows C 1s and N 1s deconvoluted XPS spectra of chitosan-, chitin- and glucose-derived microspheres. Since D-glucose is non-nitrogen containing precursor, only C 1s spectra is shown.

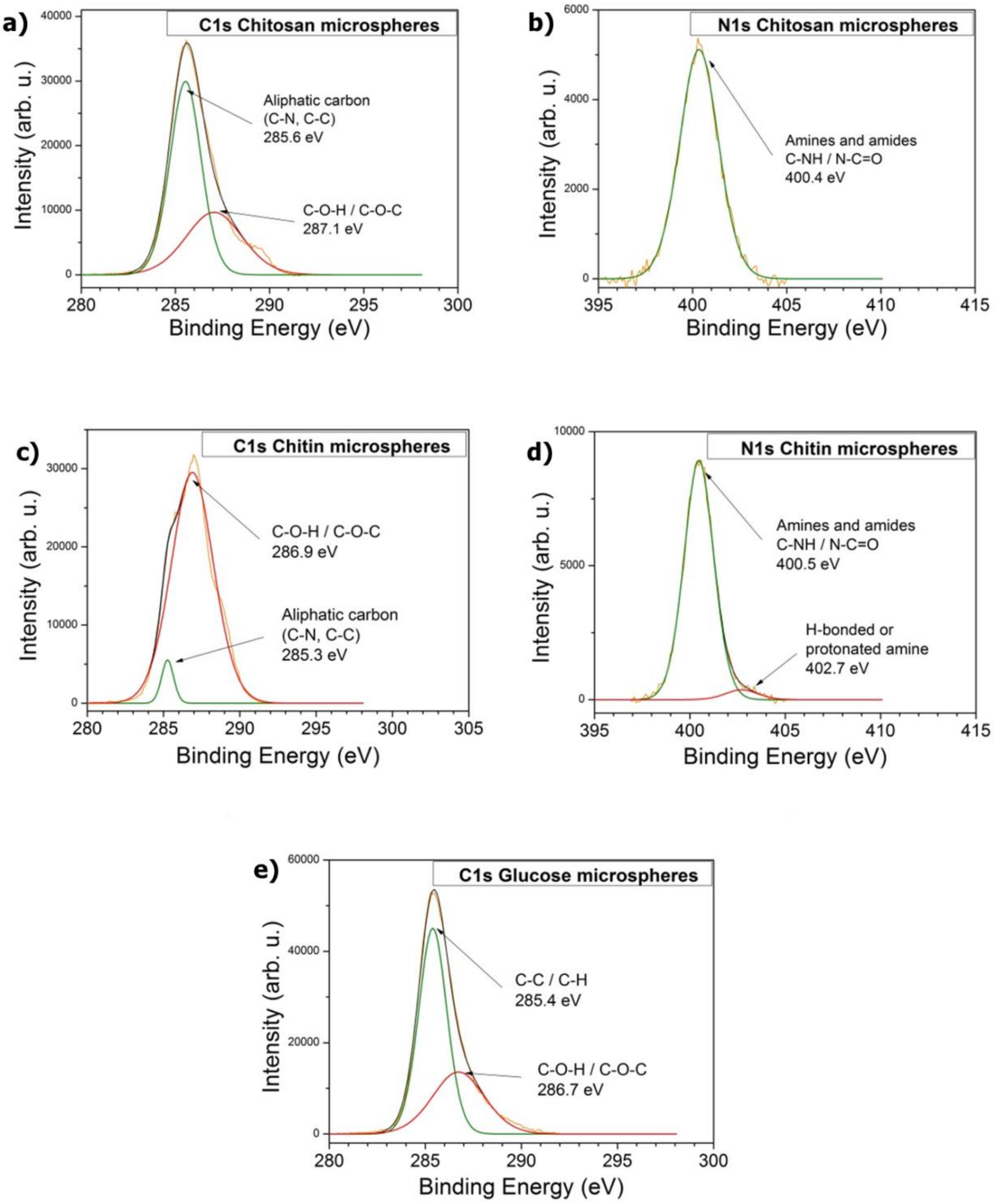

Figure 3. 13 Deconvoluted C 1s and N 1s peaks of: (a, b) chitosan microspheres, (c, d) chitin microspheres and (e) glucose microspheres.

The C 1s peak of chitosan microspheres showed predominantly aliphatic carbon (C-N, C-C) at 285.6 eV, while C 1s peak of chitin microspheres showed C-O-H / C-O-C linkages at 286.9 eV. C1 s peak of glucose microspheres showed strong contribution of C-C / C-H at 285.4 eV and the presence of -OH groups and C-O-C linkages at 286.7 eV (**Figure 3. 13 a, c, e**).

The N 1s peak of chitosan and chitin microspheres showed the presence of amines and amides (C-NH / N-C=O) at 400.5 eV (**Figure 3. 13 b, d**).

As a summary of XPS results, from **Table 3. 4** and **Table 3. 5**, we can see that oxygen and carbon functionalities were present in all CDs. Nitrogen functionalities were present in all CDs except from D-glucose CDs (since D-glucose is a non-nitrogen containing precursor), and sulphur functionalities were only present in L-cysteine CDs. The highest nitrogen content was observed in L-cysteine CDs (7.58 at%) and the lowest in lobster CDs (4.12 at%). L-cysteine CDs showed the highest carbon content (73.63 at%), while the lobster CDs showed the lowest carbon content (47.12 at%). Oxygen functionalities were the highest in lobster CDs (48.76 at%), while the lowest value was observed for L-cysteine CDs (11.08 at%). Chitosan, chitin and glucose microspheres all showed the presence of carbon and oxygen functionalities, while nitrogen functionalities were present in chitosan microspheres and chitin microspheres.

Going a bit more into details, it can be seen that sp^2 / sp^3 carbon was detected in all CDs in the region of 284.3 eV - 285 eV. Amide carbonyl (N-C=O) or C=O groups were also present in all CDs in the region of 287.9 eV - 289.4 eV. C-O groups were present for L-arginine CDs, L-cysteine CDs and lobster CDs in the region of 285.2 eV - 286.3 eV. Pyridinic-N was present in the region of 398 eV - 398.5 eV for all CDs, except for D-glucose CDs (D-glucose is a non-nitrogen containing precursor). Amines and/or amides (C-NH / N-C=O) were present in the region of 399.5 eV - 400.1 eV for all CDs, except for D-glucose CDs. Sulphur functionalities in the form of thiol group at 163.5 eV were present only in L-cysteine CDs.

TEM micrographs and the corresponding electron diffraction image of small number of chitosan CDs (**Figure 3. 6**) showed some lattice fringes suggesting an increased degree of order within the chitosan CDs. To further verify crystalline/amorphous nature of as-synthesized carbon dots and carbon microspheres, Raman and X-ray diffraction (XRD) measurements were carried out.

Raman can provide a wealth of additional structural information in low dimensional carbon systems.[175] The Raman data for carbon dots are shown in **Figure 3. 14** and all the Raman analysis results are summarised in **Table 3. 6**.

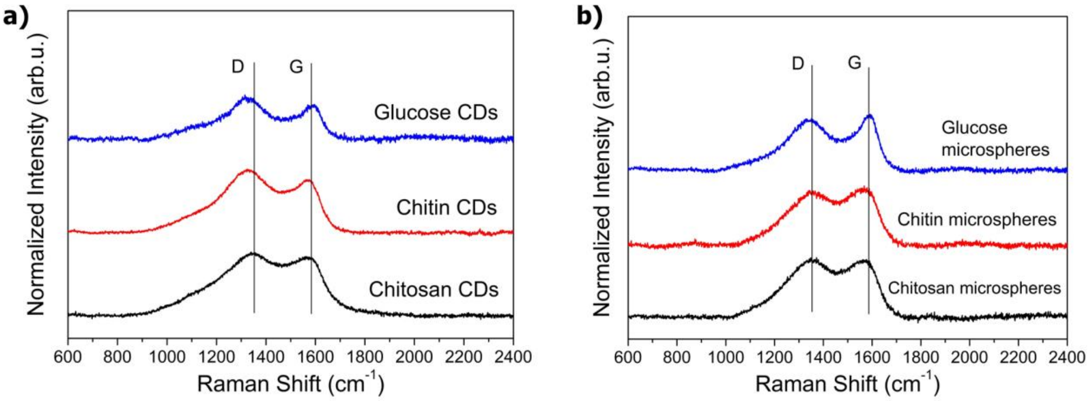

Figure 3. 14 Raman spectra of: a) carbon dots and b) carbon microspheres.

Table 3. 6 Summary of Raman analysis data for carbon dots and carbon microspheres. Data fitting has been carried out using Lorentzian peaks. The last column shows the ratio of D to G band intensity.

	Size [nm]	**D band [cm^{-1}] Position/FWHM**	**G band [cm^{-1}] Position/FWHM**	I_D/I_G
Graphene	-	-	1586/10 [176]	-
Graphite	-	-	1582/12 [68]	-
Chitosan CDs	7.91 ± 1.64	1337/318	1567/130	1.08
Chitin CDs	16.54 ± 3.40	1325/265	1563/99	1.18
Glucose CDs	5.15 ± 0.83	1322/225	1582/82	1.29
Chitosan microspheres	-	1348/220	1559/119	1.02
Chitin microspheres	-	1352/217	1559/121	0.95
Glucose microspheres	-	1343/220	1581/85	0.87

From the Raman spectra the following features can be usually observed for graphite and graphene [177,178] : D band (at around 1350 cm^{-1}) corresponding to A_{1g} vibration mode (this mode is forbidden in the case of graphene single crystals and it only appears for polycrystalline materials) ; G band (at around 1580 cm^{-1}) is attributed to the E_{2g} mode ; D' band (at around 1620 cm^{-1}) is related to the D band ; 2D band (at around 2700 cm^{-1}) which is an overtone of the D band and is related to the stacking order of the material. The G band for graphene can be found at 1586 cm^{-1} and for graphite at 1582 cm^{-1}.[176, 68]

The intensity ratio between D and G bands (I_D/I_G) reflects the level of disorder and clustering, while the position of the G band can provide information about the average cluster size [179].

For L-arginine CDs, L-cysteine CDs and lobster CDs, no obvious D and G bands were detected in the Raman spectra. High fluorescence of these carbon dots can disturb the Raman characterization, as it was also reported by Zhu *et al* .[33] On the other hand, TEM images of L-arginine CDs, L-cysteine CDs and lobster CDs (**Figure 3. 5**) showed amorphous carbon particles without any crystalline lattices.

As it can be seen from **Table 3. 6** and **Figure 3. 14**, one of the most obvious differences in the Raman spectra of carbon dots and carbon microspheres was the change in I_D/I_G ratio. Increase in the I_D/I_G ratio for carbon dots reflected the reduction in the average cluster size and was consistent with TEM data. But only in the case of glucose-derived CDs the absolute value of I_D/I_G ratio was consistent with the observed carbon dot size.[178] In the case of chitosan CDs and chitin CDs, the corresponding I_D/I_G values were higher than expected for ordered graphite (or aromatic oligomer) clusters.[179, 178] This suggested significant influence of clustering in chitosan- and chitin-derived CDs, where larger carbon dots consisted of clusters (*e.g.* aromatic units) of smaller or similar size than that in glucose-derived CDs. However, smaller unit size should also result in upshift of the G band as compared to the graphite value of 1582 cm^{-1}. This was not observed in chitosan CDs and chitin CDs, which showed downshift in the G band value. Such a downshift was an indication of structural disorder (*i.e.* loss of the carbon ring symmetry and amorphous-like behaviour) and suggested higher structural disorder in chitosan CDs and chitin CDs compared to glucose CDs.

The drop in the I_D/I_G ratio observed in the carbon microspheres (**Table 3. 6**) reflected stronger amorphous-like character of samples of carbon dots as compared to carbon microspheres. The position of the G band in carbon microspheres clearly suggested that the size effects were the strongest in the glucose-derived microspheres. Significant broadening of the D and G bands, which were observed in the Raman spectra for all samples, were due to the cluster size distribution.[180]

Decrease of full-width-at half-maximum (FWHM) of G band from 130/99 cm^{-1} for chitosan/chitin CDs to 82 cm^{-1} for glucose CDs, suggested better in-plane crystallisation and a lower degree of disorder in glucose CDs. This tendency was also observed in carbon microspheres where FWHM of G band decreased from 119/121 cm^{-1} for chitosan/chitin microspheres to 85 cm^{-1} for glucose microspheres. Since glucose as a precursor is a monosaccharide (single molecular precursor), it was more likely that it would produce a less disordered and a more homogenous carbonaceous structures compared to chitosan/chitin as precursors (polysaccharides).

The XRD measurements for carbon dots (CDs) and carbon microspheres were performed in order to probe the average sample structure directly. XRD data are shown in **Figure 3. 15** and had confirmed significant level of topological disorder in all samples. In the case of carbon dots, the interlayer spacing didn't change from sample to sample. The broad 002 peak at about 2θ=21° corresponded to a set of sp^2 carbons-graphitic carbons with stacking faults known as turbostratic carbons.[69] No peak for hexagonal graphite was detected at 2θ=12°. The XRD pattern of lobster-derived carbon dots showed all the features characteristic to the pure lobster powder (not shown here), which was consistent with the observation that only a small fraction of pure lobster powder was soluble during the HTC reaction. No other peaks were detected in the XRD spectrum which confirmed the amorphous nature of the as-synthesized carbon dots.

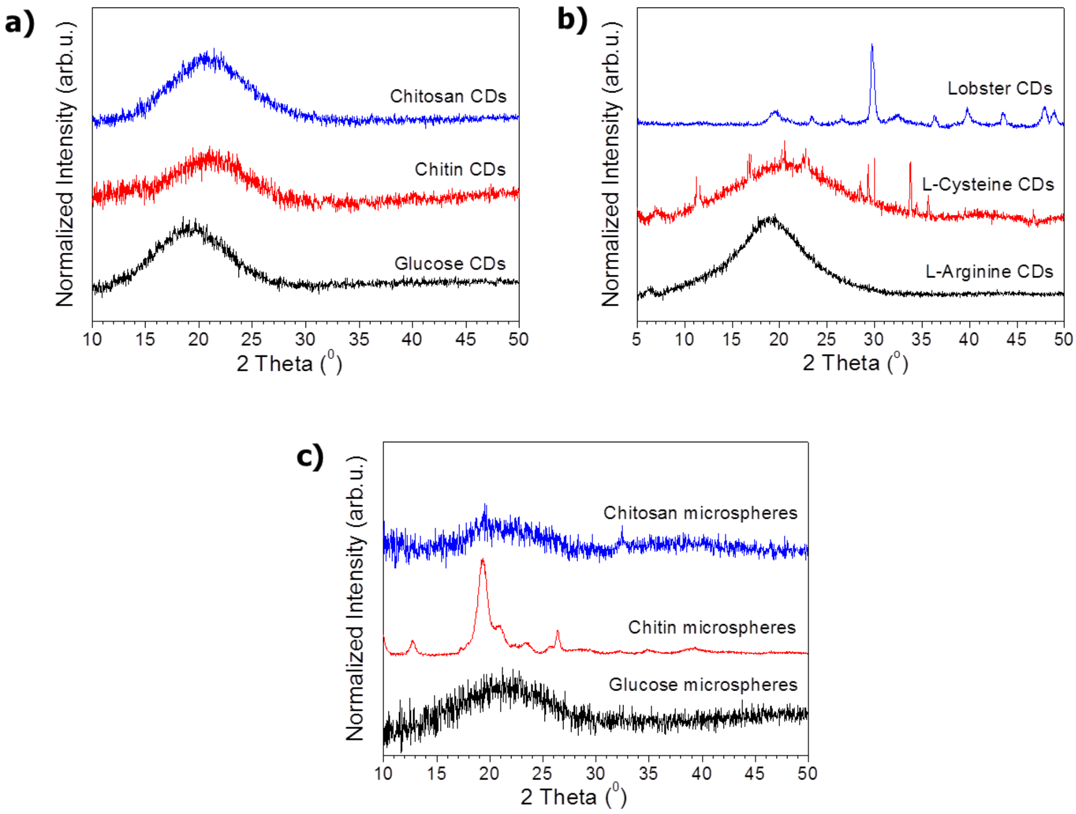

Figure 3. 15 XRD profiles for: (a, b) carbon dots and c) carbon microspheres.

The XRD patterns for chitosan and glucose microspheres (**Figure 3. 15 c**) were similar showing broad 002 peaks (2θ=22°) as a proof of their disordered structure. Interestingly, XRD pattern of chitin-derived microspheres showed all the features characteristic to pure chitin (XRD of pure chitin not shown here), which was in a good agreement with SEM, FTIR and elemental analysis data. As mentioned previously, only a small fraction of chitin was soluble during the HTC process leading to the formation of chitin CDs (XRD spectrum of chitin CDs is similar to glucose CDs and chitosan CDs showing amorphous carbon features). Chitin microspheres were mostly formed of unreacted chitin.

To conclude this section, it can be said that hydrothermal carbonization of chitosan, chitin, D-glucose, L-arginine, L-cysteine and lobster precursors, led to the formation of two different carbonaceous morphologies, named carbon dots and carbon microspheres. In the case of L-arginine, L-cysteine and lobster precursors, no carbon microspheres were obtained after hydrothermal synthesis. Chitosan and glucose carbonaceous morphologies (carbon dots and carbon microspheres) had similar physical properties in terms of functional groups, chemical composition and level of crystalline order. The only major difference was associated with their morphology. Chitin-derived materials were very different from carbon dots to carbon microspheres. Chitin CDs showed typical amorphous carbon features with amine and oxygenated functionalities, while chitin microspheres were mostly unreacted chitin precursor. Chitin microspheres had the highest mass yield (78.7 %) compared to chitosan and glucose microspheres which had 47.1 % and 33.1 % mass yield, respectively (**Table 3. 1**).

Nanoscale of such a complex carbonaceous systems with a large degree of dispersion of structural units, conjugated C=C domains and various functional groups on the surface, can show interesting optical properties which will be discussed in the following section.

3.5. The Optical Properties of Carbon Dots

In this section, the optical properties of as-synthesized carbon dots are discussed. Since the carbon microspheres didn’t show photoluminescence emission spectra, their optical properties were not studied.

Images of as-synthesized carbon dots under daylight and under UV light (excitation at 365 nm) are shown in **Figure 3. 16**. Undiluted solutions of carbon dots under daylight showed colours ranging from almost transparent (lobster CDs), through yellowish colour (chitin CDs and L-arginine CDs), to brown colour (chitosan CDs, D-glucose CDs and L-cysteine CDs). The diluted solutions of all carbon dots appeared transparent under daylight and showed strong blue-green photoluminescence emission under UV light excitation.

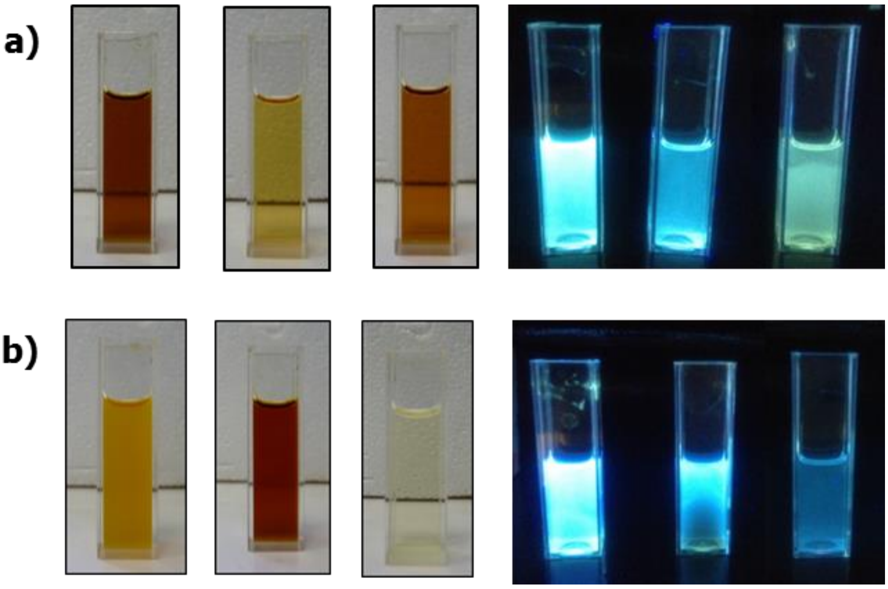

Figure 3. 16 Carbon dots under daylight (undiluted) and under UV excitation of 365 nm (diluted solutions). Row (a) from left to right: chitosan CDs, chitin CDs and D-glucose CDs. Row (b) from left to right: L-arginine CDs, L-cysteine CDs and lobster CDs.

The UV-Vis absorption spectra of as-synthesized carbon dots are shown in **Figure 3. 17**. It can clearly be seen that D-glucose CDs showed different shape of the absorption spectra compared to all other carbon dots. D-glucose CDs showed a sharp absorption peak at 280 nm (4.4 eV) and an absorption "shoulder" at 218 nm (5.7 eV). Chitosan CDs and chitin CDs showed only absorption "shoulder" at around 270 nm (4.6 eV) and 280 nm (4.4 eV), respectively. L-arginine CDs showed a sharp absorption peak at 281 nm (4.4 eV) and a weak absorption "shoulder" at 340 nm (3.7 eV). L-cysteine CDs had two absorption "shoulders" at 268 nm (4.6 eV) and at 380 nm (3.3 eV), while lobster CDs showed a featureless absorption curve with strong absorption in the range 200 - 350 nm. All carbon dots showed no absorption of light for wavelengths higher than 450 nm.

Carbon dots typically show strong absorption bands in the UV region at 220 - 360 nm. High energy UV absorption band at 220 - 260 nm is assigned to the $\pi \rightarrow \pi^*$ transitions of aromatic C-C bonds for the carbon core. Low energy UV absorption band at 300 - 360 nm is assigned to n→π^* transitions by non-bonding orbitals such as C=O bonds, or other connected surface functional groups.[83, 33, 181, 71]

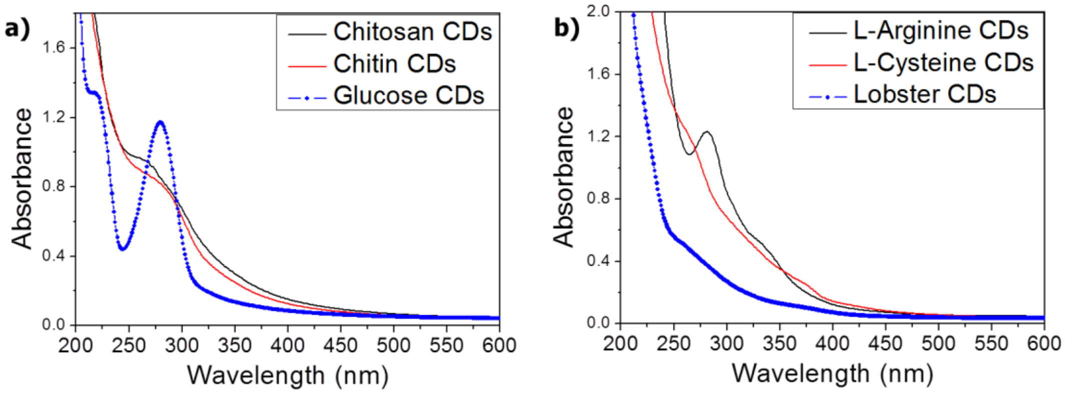

Figure 3. 17 UV-Vis absorption spectra of as-synthesized carbon dots.

The photoluminescence spectra (PL) and emission wavelength *vs.* excitation wavelength, for all the carbon dots, are shown in **Figure 3. 18**. When measuring the PL of the carbon dots, the excitation wavelength was increased from 200 nm to 480 nm in 20 nm increments and the corresponding fluorescence emission spectra was recorded. For the sake of clear PL emission spectra, the PL emission graphs were divided into two parts; one part represented excitation from 200 - 340 nm and the other part represented excitation from 340 - 480 nm (for example **Figure 3. 18 a, b**).

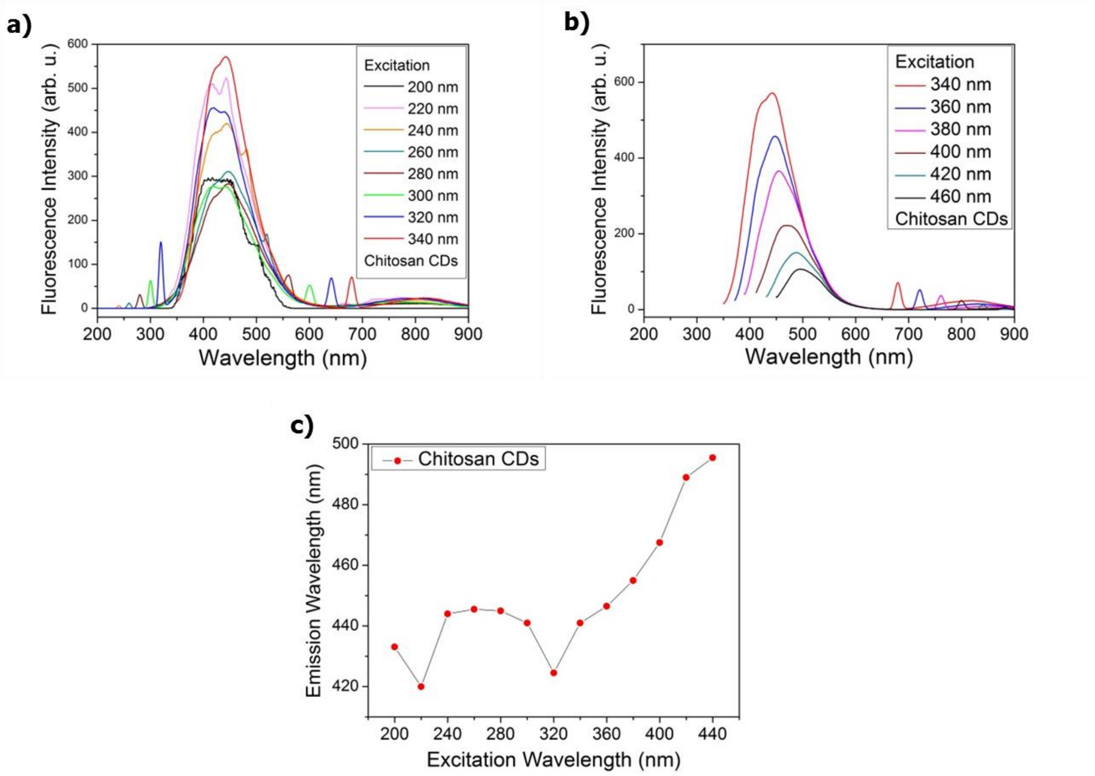

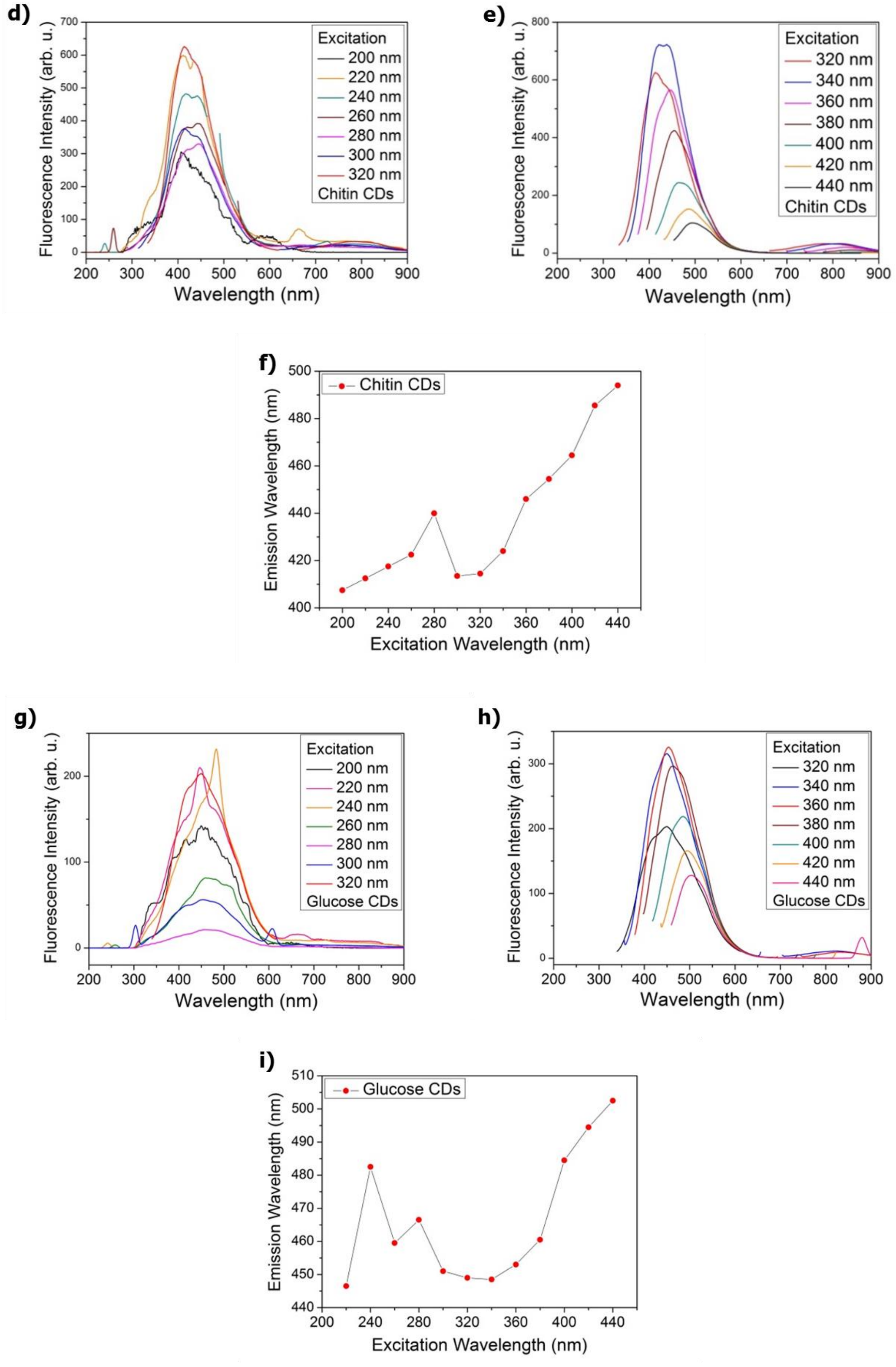
d)
Fluorescence Intensity (arb. u.)
Wavelength (nm)
Excitation
200 nm
220 nm
240 nm
260 nm
280 nm
300 nm
320 nm
Chitin CDs
e)
Fluorescence Intensity (arb. u.)
Wavelength (nm)
Excitation
320 nm
340 nm
360 nm
380 nm
400 nm
420 nm
440 nm
Chitin CDs
f)
Chitin CDs
Emission Wavelength (nm)
Excitation Wavelength (nm)
g)
Fluorescence Intensity (arb. u.)
Wavelength (nm)
Excitation
200 nm
220 nm
240 nm
260 nm
280 nm
300 nm
320 nm
Glucose CDs
h)
Fluorescence Intensity (arb. u.)
Wavelength (nm)
Excitation
320 nm
340 nm
360 nm
380 nm
400 nm
420 nm
440 nm
Glucose CDs
i)
Glucose CDs
Emission Wavelength (nm)
Excitation Wavelength (nm)

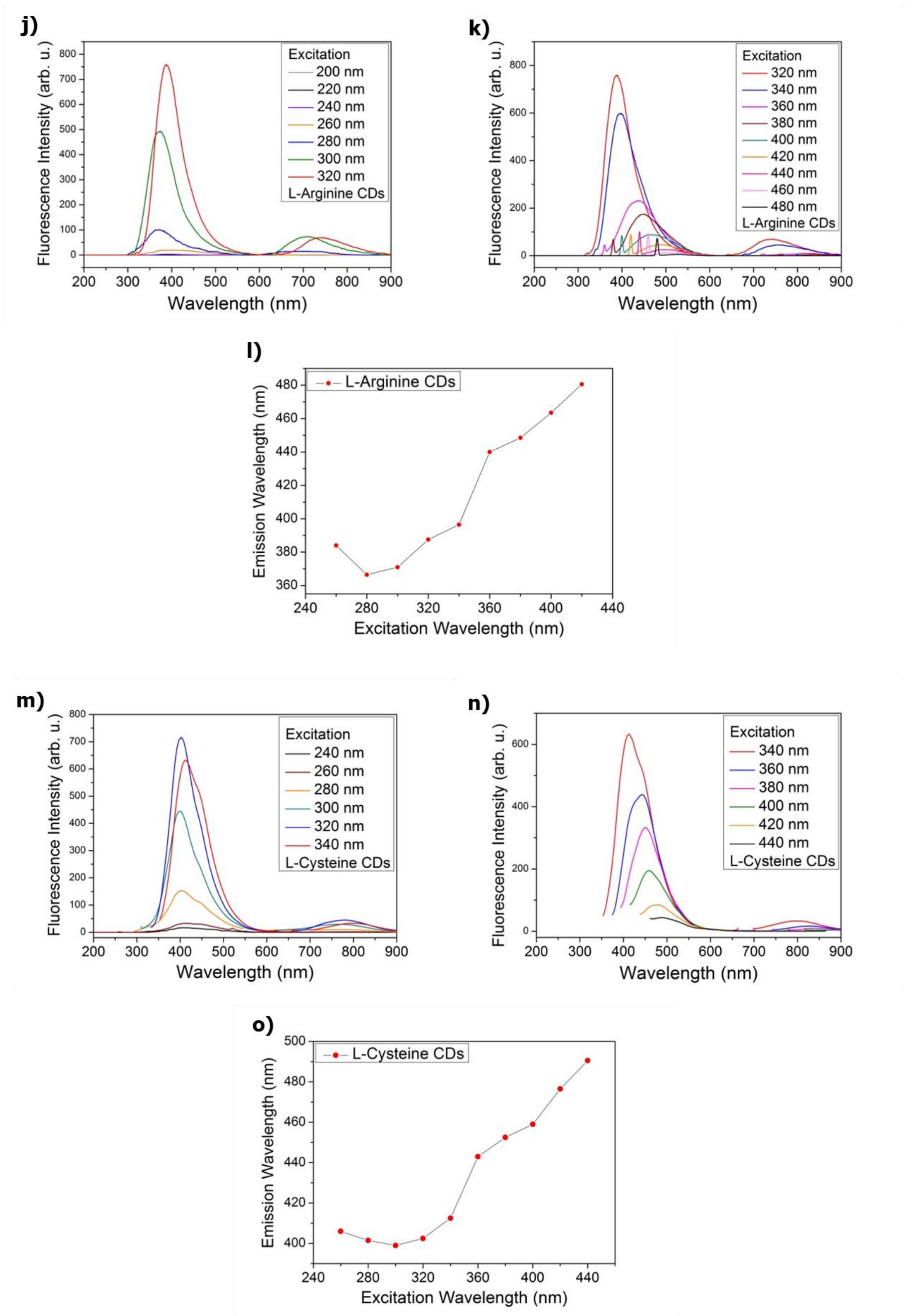
j)
Fluorescence Intensity (arb. u.)
Wavelength (nm)
Excitation
200 nm
220 nm
240 nm
260 nm
280 nm
300 nm
320 nm
L-Arginine CDs
k)
Fluorescence Intensity (arb. u.)
Wavelength (nm)
Excitation
320 nm
340 nm
360 nm
380 nm
400 nm
420 nm
440 nm
460 nm
480 nm
L-Arginine CDs
l)
L-Arginine CDs
Emission Wavelength (nm)
Excitation Wavelength (nm)
m)
Fluorescence Intensity (arb. u.)
Wavelength (nm)
Excitation
240 nm
260 nm
280 nm
300 nm
320 nm
340 nm
L-Cysteine CDs
n)
Fluorescence Intensity (arb. u.)
Wavelength (nm)
Excitation
340 nm
360 nm
380 nm
400 nm
420 nm
440 nm
L-Cysteine CDs
o)
L-Cysteine CDs
Emission Wavelength (nm)
Excitation Wavelength (nm)

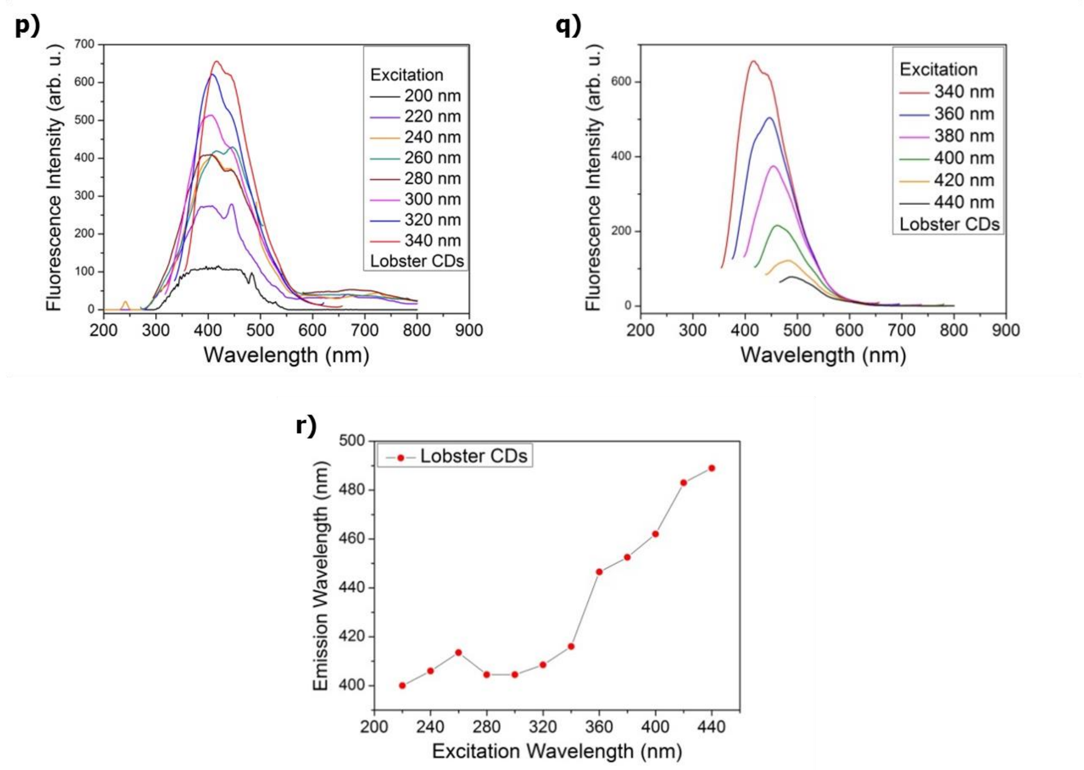

Figure 3. 18 Photoluminescence spectra and excitation-independent/dependent emission plots of the as-synthesized carbon dots (continued from previous pages): chitosan CDs (a, b, c); chitin CDs (d, e, f); glucose CDs (g, h, i); L-arginine CDs (j, k, l); L-cysteine CDs (m, n, o) and lobster CDs (p, q, r).

As it can be seen from **Figure 3. 18**, all the carbon dots showed strong PL emission in the blue-green region of the visible light spectrum (violet/blue colour: 380-495 nm; green colour: 495-570 nm) depending on the excitation wavelength. Also, all the carbon dots showed excitation-dependent photoluminescence (**Figure 3. 18 c, f, i, l, o, r**) which is a typical property of hydrothermally synthesized carbon dots.[182, 171, 183, 184] As the excitation wavelength was increased from 200 nm to 480 nm, the emission wavelength was red-shifted and the PL emission intensity was decreased, for all carbon dots. It is interesting to notice that all the carbon dots showed a much more pronounced excitation-dependent PL emission starting from an excitation wavelength of around 320 nm and going to higher excitation wavelengths. For certain carbon dots, the excitation-independent PL emission had been observed (**Figure 3. 18 c, o, r**) for the excitation wavelengths in the range 200 - 320 nm.

Normalized absorption, photoluminescence excitation (PLE) and photoluminescence (PL) spectra for all carbon dots are shown in **Figure 3. 19**. For the PL spectra, the strongest emission peak for each of the carbon dots was chosen and the corresponding excitation wavelength is given in brackets on each of the graphs. PLE peak positions were extracted from the emission intensity *vs.* excitation wavelength plots.

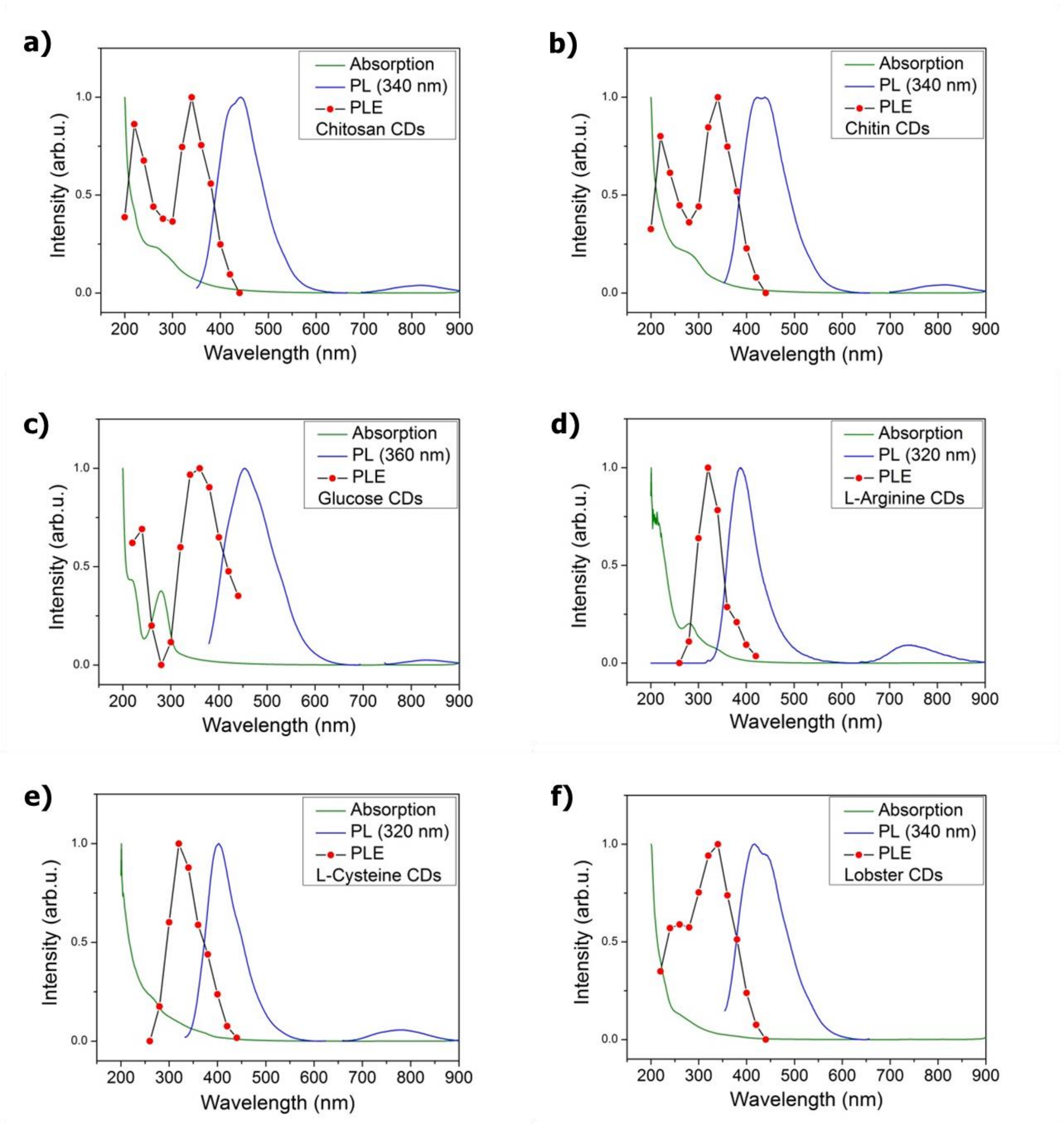

Figure 3. 19 Normalized absorption, photoluminescence excitation (PLE) and photoluminescence (PL) emission plots for all carbon dots (PL excitation wavelength is given in brackets): a) chitosan CDs, b) chitin CDs, c) D-glucose CDs, d) L-arginine CDs, e) L-cysteine CDs and f) lobster CDs.

The strongest PL emission in each of the carbon dots was located in the blue region of the visible spectrum (at around 450 nm). Looking at the PLE data from **Figure 3. 19** it can be seen that for chitosan CDs, chitin CDs, glucose CDs and lobster CDs, there are two distinctive excitation peaks and the one at around 340 nm is the dominant one. For L-arginine CDs and L-cysteine CDs there was only one dominant excitation peak, again at around 340 nm. These results indicate that the blue emission in all the carbon dots originate from energy levels located at around 340 nm (3.65 eV). These levels most likely correspond to HOMO-LUMO energy levels (*e.g.* σ-σ* and π-π* transitions) in sp^2 bound carbon clusters. A partial overlap of absorption spectra and PLE spectra was observed for chitosan CDs, chitin CDs, glucose CDs and lobster CDs. Other carbon dots showed small degree of overlap of PLE with the onset of absorption spectra.

Table 3. 7 shows the fluorescence quantum yield (QY) values for the solutions of carbon dots together with the position of excitation peak and PL emission peak, and the full-width-at half-maximum (FWHM) of maximum PL emission peak. The fluorescence QY values were calculated as described in **Chapter 6.7**.

It was interesting to notice that the highest fluorescence QY came from the amino-acid-derived L-arginine CDs followed by the polysaccharide-derived chitosan CDs, which was also evident from the strong fluorescence emission of these carbon dots under UV excitation (**Figure 3. 16**). The lowest fluorescence QY was observed for D-glucose CDs.

It has to be noted here that the fluorescence QY values given in **Table 3. 7** were not calculated correctly. As mentioned in the **Chapter 6.7**, the fluorescence QY values were calculated by plotting the integrated fluorescence intensity (excited at 340 nm) *vs.* absorbency values (less than 0.1 at 340 nm) for CDs and Quinine Sulphate (reference). The slope of the curves was determined, and by using the equation **Eq. 4** (**Chapter 6.7**) the fluorescence QY of CDs was calculated. But, absorbency values shouldn't be measured at 340 nm for all CDs. Absorbency values (kept at less than 0.1) should be measured at maximum absorption wavelength separately for each type of CDs. For example, absorbency values for D-glucose CDs should be measured at 280 nm because D-glucose CDs showed a strong absorption peak at 280 nm (**Figure 3. 17**). Also, fluorescence excitation wavelength of 340 nm shouldn't be used for all CDs. Each type of CDs should be excited at their specific excitation wavelength which gives the maximum fluorescence intensity. For example, D-glucose CDs should be excited with the wavelength of 360 nm (**Figure 3. 18 h** and **Figure 3. 19 c**).

Glucose CDs and lobster CDs showed the widest PL emission peak, while L-arginine CDs and L-cysteine CDs showed the narrowest PL emission peak, as evident by FWHM values in **Table 3. 7**. The narrow PL emission peak is highly desirable for carbon dots in applications like LED lighting and displays, and also shows the precise tunability of PL emission colour.

Table 3. 7 Position of the maximum excitation peaks, PL emission peaks, FWHM of maximum PL emission and fluorescence QY values, for all carbon dots.

	1st Excitation peak [nm]	2nd Excitation peak [nm]	1st PL emission peak [nm]	2nd PL emission peak [nm]	FWHM of max emission [nm]	Fluorescence QY [%]
Chitosan CDs	220	340	420	441	102.5	35.3 ± 3.9
Chitin CDs	220	340	412.5	414.5	104	9.7 ± 1.7
Glucose CDs	240	360	482.5	453	116	2.2 ± 0.2
Arginine CDs	320	-	387.5	-	69.5	43.3 ± 2.1
Cysteine CDs	320	-	402.5	-	79	9.1 ± 0.9
Lobster CDs	260	340	413.5	416	111	12.7 ± 0.8

When considered collectively, the structural data, optical absorption and excitation-emission data, pointed to HOMO-LUMO transitions as the origin of the excitation-independent PL light emission (**Figure 3. 20**).

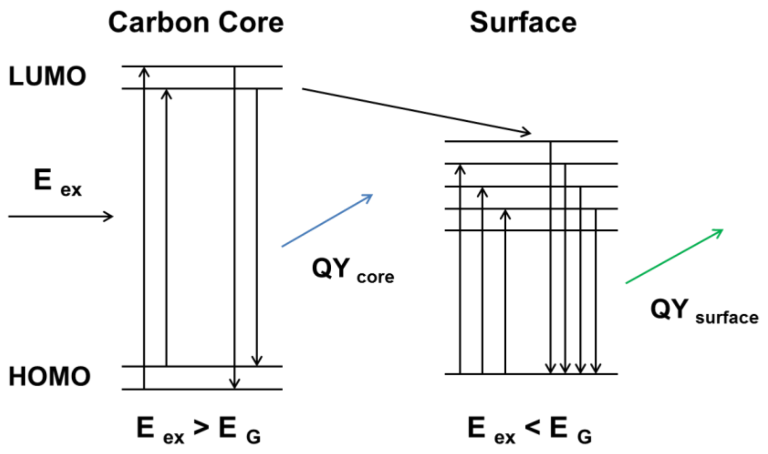

Figure 3. 20 Schematic diagram of energy levels of carbon dots' core and surface states. Highest occupied molecular orbital (HOMO), lowest unoccupied molecular orbital (LUMO), excitation energy (E_{ex}), energy band-gap (E_G), and quantum yield (QY).

Excitation-dependent PL emission was most likely due to the HOMO-LUMO gap states (**Figure 3. 20**). The exact nature of these gap states is still unclear. Considering XPS data, which showed that all the samples contained similar fractions of sp^2 and sp^3 bonded carbon, it was reasonable to suggest that the origin of light emission must be governed by the interplay between absorption due to the carbon-based cores and the surface functional groups (hydroxyl, carboxyl, amines and amides).

This picture was consistent with the fluorescence QY data, under the assumption that quantum yield due to the carbon core states (sp^2) was higher than that due to the surface states. In that case, the lowest fluorescence QY of (2.2 ± 0.2) % for glucose CDs, which were the smallest carbon dots, was explained by the increase in the surface-to-volume ratio which led to the increased contribution to PL emission due to the low yielding surface states.

Still today there is a lot of debate in the literature about the origins of photoluminescence (PL) emission in carbon dots.[82, 93, 73, 60] More detailed information about the different theories proposed in the literature for PL origin in CDs, is given in **Chapter 2.3.**

Just briefly, the mechanism of PL in CDs still remains poorly understood even though there have been several attempts to clarify it. The heterogeneity of the as-synthesized CDs makes experimental investigations problematic because it is difficult to isolate individual factors that may influence the PL. These individual factors are: the particles' crystallinity, the sizes and shapes of the particles and their cores, and the particles' surface/edge characteristics. More systematic studies are needed that can separate and distinguish between different types of CDs. Single-particle characterization techniques will be required to achieve this goal.

The PL mechanism of CDs has been mainly attributed to both aromatic-like PL arising from sp^2 domains and to surface functional groups/surface defects-related PL. Also, PL properties of CDs are highly sensitive to the synthesis method used, to structural properties of CDs, and to sample heterogeneity.

3.6. Summary

In this chapter, fluorescent carbon dots were synthesized from biomass-derived precursors under mild synthetic conditions using the hydrothermal synthesis method. The idea was to use specific biomass-derived precursors to obtain "undoped" and N, S "doped" carbon dots, and to characterize and explain their structural and optical properties. Carbon dots (as nanometre sized nucleation clusters dispersed in the liquid phase) and carbon microspheres (as solid black/brown precipitate at the bottom of the reaction vessel) were distinguished and their synthesis was explained.

The as-synthesized carbon dots showed quasi-spherical morphology and polydispersity. Narrow particle size distributions were obtained using certain precursors, but generally carbon dots synthesized with hydrothermal method showed a polydisperse particle size distribution. The smallest carbon dots were obtained from glucose (5.15 ± 0.83) nm, while the biggest carbon dots were obtained from chitin (16.54 ± 3.40) nm. The choice of molecular precursor had a clear influence on the carbon dots' size and on the particle size distribution.

A small number of chitosan carbon dots showed graphitic crystalline structure. There is a possibility that these crystalline lattice fringes can have origin in the effect of annealing the sample by the electron beam. Also, there is a possibility that graphitic structures form and co-exist with amorphous structures in carbon dots synthesized at these mild synthesis conditions (hydrothermal carbonization at 200 °C for 6 h).

A potential formation mechanism of chitosan-, chitin- and glucose-derived carbon dots and carbon microspheres was discussed, and simplified chemical reactions were provided as a tentative guidance.

Elemental analysis data for carbon dots showed the presence of C (40% - 54%), O (19% - 43%) and N (8% - 20%). Carbon microspheres also confirmed the presence of C, O and N elements. Different functional groups on the surface of carbon dots and carbon microspheres were confirmed by FTIR and XPS analysis. Carbon dots showed the presence of stretching vibrations of O-H, N-H, C-H, C=O, amide and amine groups, while carbon microspheres showed similar chemical features as the pure starting precursors. The XPS analysis was performed to gain further information into the chemical environment of different functional groups. Carbon dots showed the presence of sp^2/sp^3 carbons (C=C / C-C), C-O, C=O, pyridinic-N and amines and/or amides (C-NH / N-C=O). The presence of sulphur functionalities (thiols) was detected for L-arginine carbon dots. Carbon microspheres showed similar chemical environment of functional groups as carbon dots.

Considered collectively, elemental analysis, FTIR and XPS all confirmed the successful synthesis of “undoped” carbon dots from glucose, and N and S “doped” carbon dots from other precursors.

Raman and XRD measurements were performed to verify crystalline/amorphous nature of carbon dots and carbon microspheres. Raman analysis confirmed the structural disorder and amorphous-like character for all carbon dots and carbon microspheres. XRD patterns of carbon dots and carbon microspheres showed significant level of topological disorder in all samples, and the observed peak at about $2\theta=22°$ corresponded to a set of sp^2 carbons-graphitic carbons with stacking faults (turbostratic carbons).

The diluted solutions of all carbon dots were transparent under daylight and showed a strong blue-green photoluminescence emission under UV excitation. Strong absorption bands in the UV region at 220-360 nm were observed for all carbon dots, and no absorption was present for wavelengths larger than 450 nm. All the carbon dots showed excitation-dependent photoluminescence emission which was more pronounced for the excitation wavelengths larger than 320 nm. As the excitation wavelength was increased, the emission wavelength was red-shifted and the photoluminescence (PL) emission intensity was decreased. Chitosan CDs, L-cysteine CDs and lobster CDs showed excitation-independent PL emission for the excitation wavelengths in the range 200 - 320 nm. The absorption spectra, PL excitation and PL emission spectra, all suggested that the blue emission in all carbon dots originated from energy levels located at around 340 nm. These levels most likely corresponded to HOMO-LUMO energy levels in sp^2 bound carbon clusters. Arginine CDs showed the highest fluorescence quantum yield (QY) of (43.3 ± 2.1) %, while glucose CDs had the lowest QY of (2.2 ± 0.2) %. The quality of as-synthesized carbon dots is closely connected to fluorescence QY, so the tendency is to reach the QY value of 100 %. Full-width-half-maximum (FWHM) value of PL emission peaks of carbon dots was around 100 nm, with the exception of L-arginine CDs and L-cysteine CDs which showed narrow PL emission of 70-80 nm.

Finally, optical characterizations (UV-Vis absorption, photoluminescence excitation, and photoluminescence emission) of carbon dots confirmed that HOMO-LUMO transitions were the origin of the excitation-independent PL light emission, while excitation-dependent PL light emission was most likely due to the HOMO-LUMO gap states.

Chapter 4 | Carbon Dot Sensitized Solar Cells

4.1. Introduction

In order to address the challenge of pushing forward sustainable energy technologies to achieve low-cost solar cell devices derived from abundant materials, it is necessary to explore new types of materials to find those with desirable properties that meet these criteria. Biomass and particularly waste materials offer a huge, largely untapped resource of chemical precursors. The big challenge in materials research is to develop new, advanced materials with good optical and electrical properties that will enable us to develop highly efficient, flexible, mass-producible and inexpensive photovoltaics (PVs). In order to achieve this, the use of expensive and rare elements should be avoided,[185] in addition to avoiding toxic materials that could be harmful if released into the environment.

The third generation PVs aim to reduce the production costs, and to obtain power conversion efficiencies greater than the Shockley-Queisser [22] limit (32.9 % efficiency) by utilizing advanced photovoltaic concepts such as multijunction solar cells, hot electron injection and multiexciton generation.[122] Technologies that aim for lower production cost include dye-sensitized solar cells (DSSC)[127], organic photovoltaics (OPV)[123,124], perovskite solar cells[125,126], quantum dot sensitized solar cells (QDSSC)[128] and carbon dot sensitized solar cells (CDSSC)[120,117,118]. QDSSCs are currently mainly fabricated by using highly toxic cadmium (Cd) and lead (Pb) chalcogenide elements[128,134,136], which makes their implementation problematic because of the health and environmental issues (similar problem also currently shared by perovskite solar cells). An alternative class of material that has been investigated as a sensitizer in mesostructured solar cells is carbon dots (CDs), sometimes referred in the literature as carbon quantum dots (CQDs).[37,38] CDs are cheap and easy to synthesize and possess low toxicity. To date relatively few carbon dot sensitized solar cells (CDSSCs) have been reported, with efficiency remaining below 1% [117,118,120,143].

This chapter opens with the fabrication of ZnO-nanorod-based solid state solar cells sensitized with different types of biomass-derived carbon dots. Carbon dots were synthesized from polysaccharides (chitosan and chitin) and monosaccharide (D-glucose), and all have successfully sensitized ZnO-nanorod-based solar cells. Optical properties and operational parameters of as-fabricated solar cells were measured, and correlations between structural and optical properties of carbon dots and performance parameters of solar cells have been discussed.

This is followed by the fabrication of TiO_2-based solar cells with liquid electrolyte and using carbon dots as sensitizers. The main idea was to further increase the efficiency of solar cell devices by using mesoporous TiO_2 scaffold which had a much greater surface area than the previously used ZnO-nanorods. This allowed for a greater loading of carbon dots onto the surface of TiO_2. The carbon dots were synthesized from polysaccharides (chitosan and chitin), monosaccharide (D-glucose), amino acids (L-arginine and L-cysteine) and real food waste (lobster shells), and all were successfully used as sensitizers for TiO_2-based solar cells. The operational parameters and optical properties of as-fabricated TiO_2-based solar cells were measured, and increased efficiency was obtained compared to previously fabricated ZnO-nanorod-based solar cells.

Finally, this chapter closes with the discussion about future directions in the development of carbon dot sensitized nanostructured solar cells.

4.2. Carbon Dots as Sensitizers for ZnO-based Solid State Nanostructured Solar Cells

Three different types of carbon dots (CDs) with and without nitrogen functionalities (chitosan-, chitin- and glucose-derived CDs) were used as sensitizers for ZnO-nanorod-based solid state nanostructured solar cells. As explained in experimental section (**Chapter 6**), these carbon dots were synthesized *via* simple one step hydrothermal carbonization of chitosan, chitin and D-glucose precursors. These abundant and renewable precursors are present in most of the lignocellulosic biomass and food waste. ZnO nanorods were synthesized using a low-temperature aqueous method (see **Chapter 6**). **Scheme 4. 1** shows the synthesis of carbon dots together with the chemical growth of ZnO nanorods, and their combination into the solid state nanostructured solar cell.

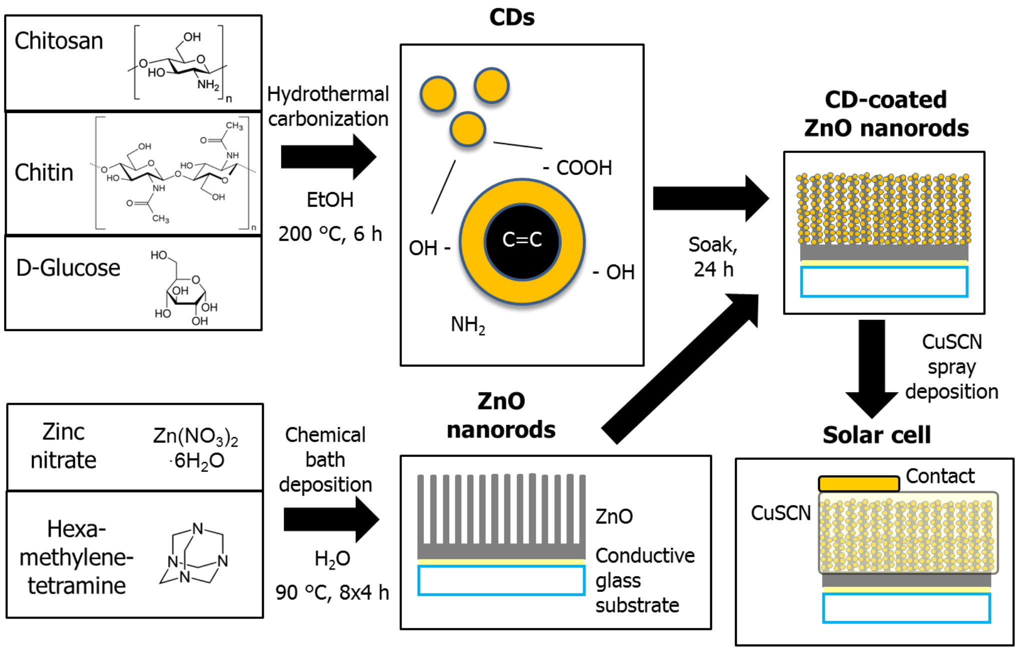

Scheme 4. 1 Preparation of carbon dot sensitized nanostructured solar cells by hydrothermal carbonization of biomass-derived precursors, and combination with chemically grown ZnO nanorods.

This approach combined the inexpensive inorganic materials, ZnO and copper (I) thiocyanate (CuSCN), as electron and hole conductor, with carbon dots synthesized from biomass-derived precursors. The solid state hole conductor (CuSCN) was used to overcome the instability issues associated with liquid electrolytes and their potential reactions with the CDs. CuSCN allowed the full infiltration of the high aspect ratio ZnO nanorods which was not possible with organic alternatives such as spiro-OMeTAD (2,2',7,7'-Tetrakis[N,N-di(4-methoxyphenyl)amino]-9,9'-spirobifluorene). Also, spiro-OMeTAD is considerably more expensive than CuSCN. Thus, the entire nanostructured solar-cell device was produced simply and inexpensively.

The as-synthesized ZnO nanorods were soaked in undiluted carbon dots' solutions for 24 h (concentration of carbon dots is given in **Chapter 3**, **Table 3. 1**). This process enabled the carbon dots to adhere to the ZnO nanorod surface as it can be seen in **Figure 4. 1**, appearing as the roughening of the nominally smooth ZnO surface.

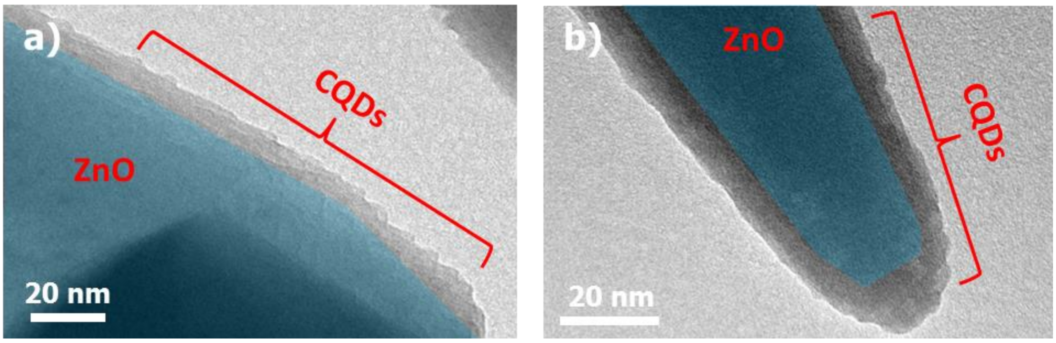

Figure 4. 1 TEM images of ZnO nanorods coated with carbon dots: a) single coating of glucose CDs and b) four layers of chitosan CDs + glucose CDs. Clear texturing on the smooth crystalline ZnO surface indicated the coverage of ZnO nanorods with carbon dots (highlighted by the blue area to show the interface between the ZnO and CDs).

The analysis of the average carbon content of the ZnO nanorod + carbon dot samples from the wide-area SEM-EDX scans, showed that the carbon content increased from around 5% for uncoated ZnO nanorods (origin of this was in synthesis-related and atmospheric impurities) up to 10-11% for chitosan CDs and glucose CDs coated ZnO nanorods, and to 7% for chitin CDs coated ZnO nanorods. Presence of additional carbon had supported TEM images (**Figure 4. 1**) and showed that the ZnO nanorods had been successfully coated with carbon dots. It also implied that the chitosan CDs and glucose CDs coated the ZnO nanorods more densely than the chitin CDs.

As it can be seen from **Figure 4. 2**, the UV/Vis transmission spectra showed that the transmission of chitosan CDs- and glucose CDs-coated ZnO nanorods was decreased in the range of 400-500 nm. This indicated that the carbon dots had successfully sensitized ZnO nanorods to visible light through the absorption tails extending into the visible light region.

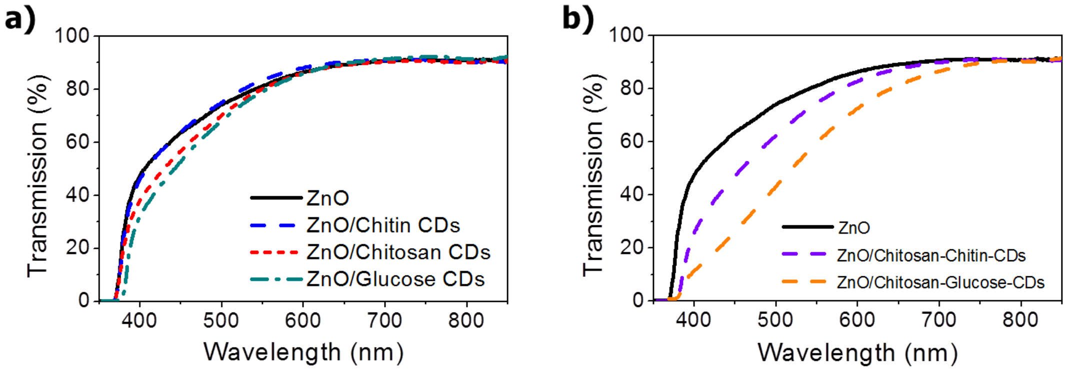

Figure 4. 2 UV/Vis transmission spectra for ZnO nanorods coated with carbon dots using single layer of carbon dots (a), and 4-layer layer-by-layer (LbL) coating (b).

The transmission spectra of chitin CDs-coated ZnO nanorods varied little compared with the uncoated ZnO nanorods (**Figure 4. 2 a**) which reflected the low level of carbon detected in this sample. This was in a good agreement with the FTIR and XPS results (**Chapter 3.4**), which showed the presence of amine groups in the case of chitosan CDs facilitating their binding onto the ZnO nanorod surface via electrostatic interactions. The presence of amide group on chitin CDs hindered their binding onto the ZnO nanorod surface.

Solar cell current-voltage curves (J-V) are shown in **Figure 4. 3** and the associated solar cell operational parameters are given in **Table 4. 1**. All the carbon dot coatings had improved the efficiency of as-fabricated solar cells compared to the uncoated solar cell devices (ZnO/CuSCN).

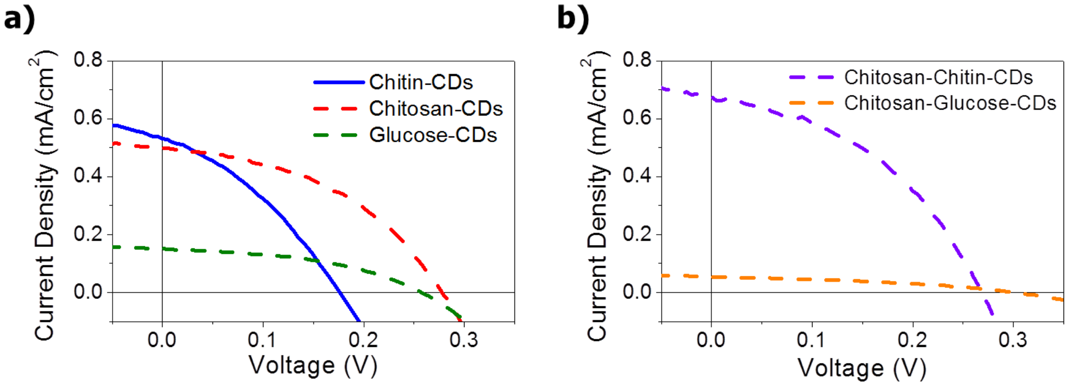

Figure 4. 3 Illuminated current-voltage plots for ZnO/CDs/CuSCN solar cells using single layer of carbon dots (a), and 4-layer layer-by-layer (LbL) coating (b).

Table 4. 1 Solar cell parameters for CDs-sensitized ZnO nanorod solar cells, obtained from J-V curves in **Figure 4. 3**.

Sample	J_{sc} **[mA cm^{-2}]**	V_{oc} **[mV]**	**FF**	**PCE [%]**	R_s **[kΩ]**	R_{sh} **[kΩ]**
Uncoated	0.083	15	0.34	0.0004	0.27	0.30
Chitin	0.530	175	0.35	0.032	0.98	4.11
Chitosan	0.500	275	0.44	0.061	1.13	15.90
Glucose	0.153	255	0.44	0.017	3.05	40.00
Chitosan-chitin	0.674	265	0.43	0.077	0.85	9.18
Chitosan-glucose	0.054	300	0.38	0.006	14.10	66.10

The chitosan-CDs-sensitized solar cell device had the highest power conversion efficiency (PCE) due to the combination of relatively high open-circuit voltage (V_{oc}) and short-circuit current (J_{sc}), associated with the low series resistance (R_s) and high shunt resistance (R_{sh}). The glucose-CDs-sensitized solar cell device had the highest light absorption (**Figure 4. 2 a**), but had the lowest J_{sc} value providing a low efficiency due to high R_s. The chitin-CDs-sensitized device also had lower efficiency which was associated with low R_{sh} value and therefore low fill factor (*FF*) and V_{oc}.

The low correlation between light absorption and J_{sc} and large variability in the internal resistance (R_s and R_{sh}), suggested that the solar cell performance was determined more by the structural nature of the coating than its light harvesting ability. The thicker glucose CDs layer on ZnO nanorods enabled high light absorption, but had limited collection of photogenerated carriers due to the internal recombination.[186, 187, 188] On the other hand, the low density of chitin CDs on the ZnO-nanorod surface was not sufficient to reduce the interfacial recombination leading to a low R_{sh}. This situation demonstrated the strong dependence of the performance of solar cells on the type of carbon dot precursors used, and the subsequent functionalization of the carbon dot surface. It was likely that the functionalization had determined the binding of the carbon dots to the ZnO-nanorod surface and the nature of the charge transport in the layer, which impacted the solar cell performance.

The efficiency of 0.061 % for the chitosan-CDs-sensitized solar cell device was lower than the TiO_2-based carbon quantum dot (CQD) solar cell fabricated by Mirtchev *et al.* which had efficiency of 0.13 %.[117] The best reported efficiency in the literature for the solar cells based on TiO_2 sensitized with nitrogen-doped carbon dots is 0.79 %.[143] In order to increase the light absorption while altering the composition of the coating layer, layer-by-layer (LbL) methods [189,190] were investigated by soaking the ZnO nanorods in four alternating layers of either chitosan- and chitin-CDs or chitosan- and glucose-CDs to utilise the opposite charges of the amine and hydroxyl groups in solution. This method led to a clear increase in the optical absorption compared to the single CDs samples (**Figure 4. 2 b**), and the coatings can be seen in the TEM images (**Figure 4. 1 b**). The increased light absorption of the chitosan-glucose-CDs device did not lead to increased efficiency. The device had a very low J_{sc} associated with very high R_s (**Table 4. 1**). This has supported the hypothesis that the glucose-derived CDs led to high levels of recombination within the carbon dot layer, which was intensified in the thicker LbL film. The combination of chitosan- and chitin-CDs as sensitizers using the LbL method, had produced solar cell with increased efficiency of 0.077 %. This efficiency was achieved because the use of alternate layers of carbon dots led to an increased loading on the ZnO-nanorod surface and therefore higher light absorption, but the effect of the functional groups of the two types of carbon dots on the transport properties of the film were complementary enabling high J_{sc} without increasing R_s or reducing FF and V_{oc}.

The efficiency of the solar cell devices was largely limited by the light harvesting efficiency (LHE) of the carbon dots. The average value of LHE of solar cell devices was calculated in the range 400-850 nm, from the absorption data given in **Figure 4. 2**, in order to separate the contribution from the light harvesting and internal efficiency to the PCE. For the chitosan-chitin-CDs solar cell devices LHE was around 5.7 %, whereas it was only 2 % for the solar cell device using chitosan-CDs only. Dividing PCE by LHE gives the average internal efficiency of these solar cell devices. Chitosan-chitin-CDs solar cell devices showed average internal efficiency of 1.4 % while chitosan-CDs solar cell devices showed 3.0 % internal efficiency. This result showed that although chitosan-chitin-CDs solar cell device had marginally higher light absorption compared with chitosan-CDs only device, it was at the expense of internal efficiency. If the carbon dots could be engineered with close to 100 % light absorption in the range 300-800 nm, it would be possible to achieve overall PCE value larger than 1%.

It has been shown here that the carbon dots can be synthesized simply and cheaply from biomass-derived precursors (chitosan, chitin and D-glucose) which can be sourced from food waste materials. The as-synthesized carbon dots, which were functionalized with the surface groups found in the starting precursors, were used to sensitize ZnO nanorods to visible light and were used in solid state nanostructured solar cells. The performance of the as-fabricated solar cell devices was dependent on the functional groups present on the carbon dots. Solar cell devices with the highest PCE of 0.077 % were produced by combining chitosan- and chitin-derived CDs as sensitizers for ZnO nanorods in layer-by-layer structure. Although the solar cell devices were fabricated simply and inexpensively using solution methods their PCE values require further improvement to become a useful alternative to current emerging solar cell technologies. Some possible solutions would be to increase the light absorption of carbon dots themselves by composition control, or to improve the light harvesting efficiency of fabricated solar cell devices by coating multiple thicker layers of carbon dots without increasing the series resistance (R_s).

4.3. Carbon Dots as Sensitizers for TiO_2-based Nanostructured Solar Cells

In this chapter, the performance of carbon dots (CDs) derived from a wide range of biomaterials obtained from different biomass sources were compared as sensitizers for TiO_2-based nanostructured solar cells. Polysaccharides (chitosan and chitin), monosaccharide (D-glucose), amino acids (L-arginine and L-cysteine) and raw lobster shells were all used to synthesize carbon dots via hydrothermal carbonisation. Detailed synthesis procedure for carbon dots and fabrication method for TiO_2-based nanostructured solar cells are given in **Chapter 6**.

In the previous section (**Chapter 4.2**) it has been shown that carbon dots derived from the hydrothermal carbonisation of biomass-derived precursors can be used as sensitizers in solar cells, producing a solid-state solar cell based on ZnO nanorods and CuSCN. However, it was found that the light absorption was a clear limiting factor, and could not be increased by building up thicker layers of the CDs, similar to conventional dye-sensitized solar cells (DSSCs). Therefore here the sensitisation of mesoporous TiO_2 layers was investigated, which had a much greater available surface area, and their use in liquid-state solar cells was demonstrated. As well as using mono/polysaccharide precursors, including those with nitrogen functionality as in previous chapter (chitosan, chitin and glucose), here also amino acids L-arginine and L-cysteine were investigated. L-cysteine precursor also included sulphur functionality in the form of a thiol group (see Error! Reference source not found.). Furthermore, CDs can be produced from actual food waste in the form of lobster shells, which were purified, followed by equivalent hydrothermal carbonisation to the other precursors.

Although the main portion of the absorption spectra of CDs was in the UV region with the small tail extending into the visible (**Chapter 3, Figure 3. 17**), and fluorescence spectra that spans a part of the visible range from 400-500 nm (**Chapter 3, Figure 3. 18**), all indicated that visible transitions do exist and warrant further investigation. Therefore, each type of CDs was coated onto a mesoporous TiO_2 (P25) scaffold, and combined with an I_3^-/I^- redox couple and Pt counter electrode to produce a carbon dot sensitized solar cell (CDSSC). **Figure 4. 4** shows the schematic overview of the TiO_2-based nanostructured solar cell sensitized with carbon dots. Details of the fabrication process are given in **Chapter 6**.

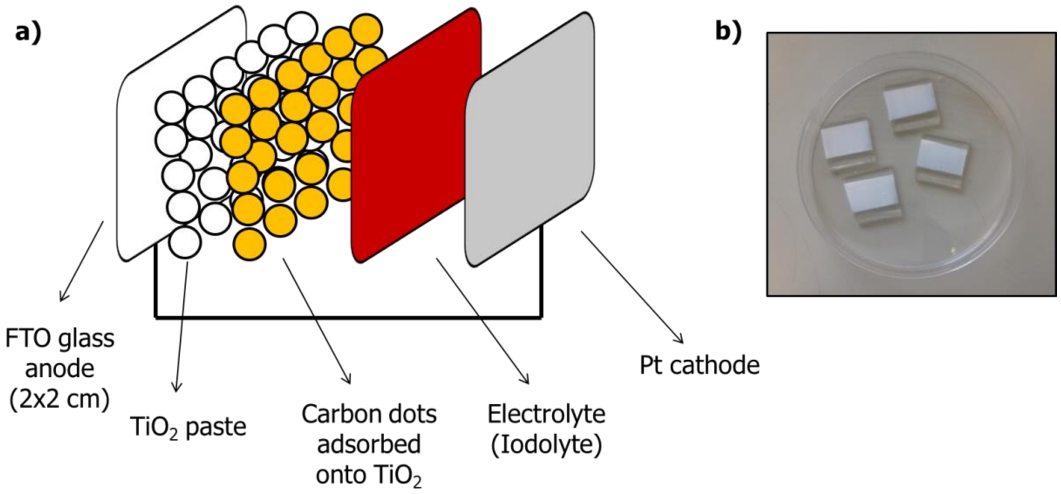

Figure 4. 4 (a) Schematic overview of the TiO_2-based nanostructured solar cell sensitized with carbon dots, and (b) non-sensitized photoanodes consisting of TiO_2 paste coated onto FTO glass substrate.

Looking at the optical absorption of the CD-sensitized TiO_2 (P25), it can be seen that the CDs had clearly increased the TiO_2 absorption across the 400-800 nm visible range, and particularly 400-600 nm, compared to non-sensitized TiO_2 (P25) (**Figure 4. 5**).

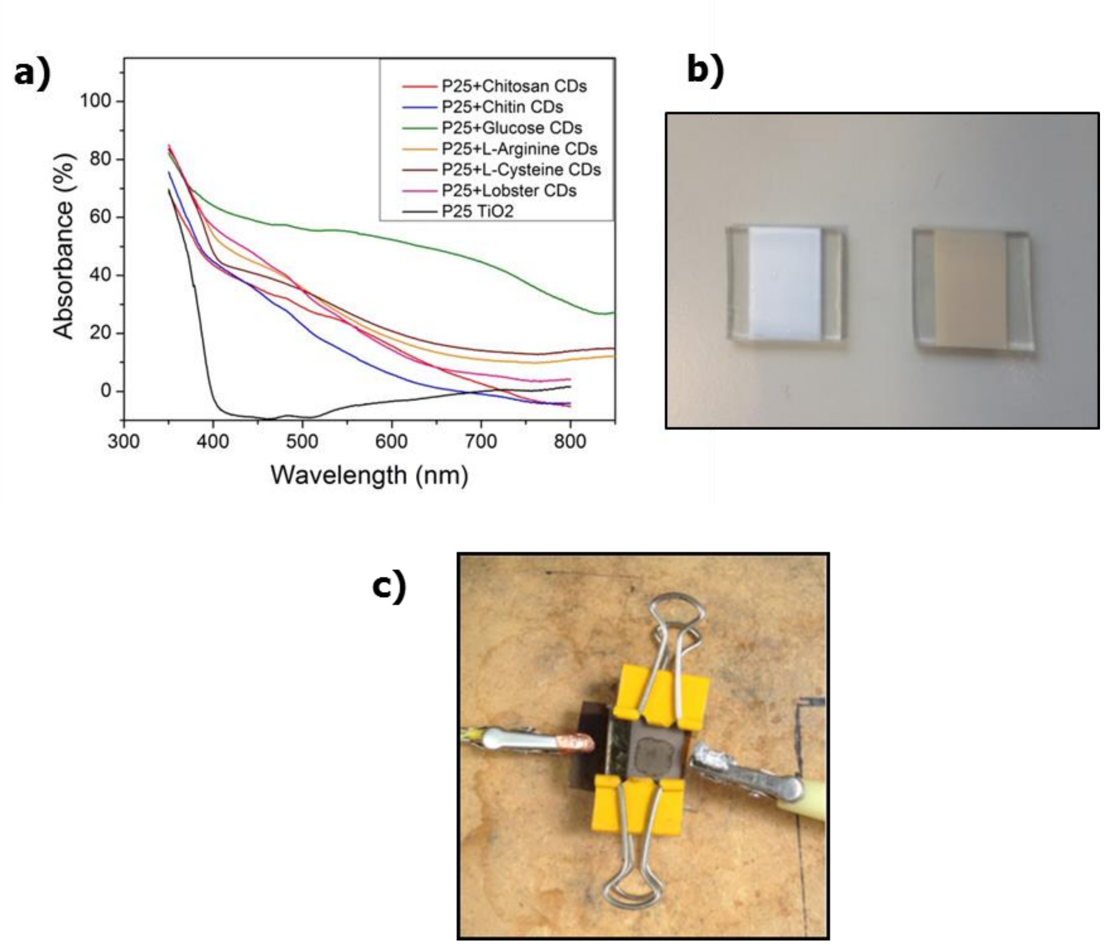

Figure 4. 5 (a) Absorption spectra of TiO_2 (P25) sensitized with different carbon dots. (b) Images of non-sensitized TiO_2 (P25) photoanode (left) and sensitized TiO_2 (P25) photoanode with carbon dots (right). (c) As-fabricated complete nanostructured solar cell (2x2 cm) held together by paper clips (yellow) and consisting of: FTO / TiO_2 (P25) / CDs / electrolyte / Pt electrode.

The strongest absorption of light was observed with D-glucose CDs as sensitizers and the lowest light absorption was observed for chitin CDs as sensitizers. This was in a good agreement with the previous findings from **Chapter 4.2** where it was suggested that the high level of -OH and potentially carboxylic acid groups on glucose CDs allowed a high loading on the TiO_2 (P25) surface, whereas the amide groups on chitin CDs prevented good loading. However, this may also reflect the fact that there was a different concentration of CDs in the soaking solutions. The quantity of starting precursor was kept constant not adjusting the final CDs concentration, so that 'as-synthesized' CD solutions were used reflecting the yield of the process. As mentioned in **Chapter 3** (**Table 3. 1**), the concentrations of CD dispersions were found to be: chitosan (1.5 ± 0.2) mg/mL, chitin (0.6 ± 0.1) mg/mL, glucose (56.3 ± 1.0) mg/mL, L-arginine (35.3 ± 0.6) mg/mL, L-cysteine (9.8 ± 0.9) mg/mL and lobster (1.8 ± 0.6) mg/mL. Thus the extremely high concentration of glucose CDs might have accounted for the high light absorption of this sample. However, there was clearly not a direct correlation between concentration and light absorption, as chitosan, L-cysteine, L-arginine, and lobster CDs all showed similar light absorption levels on TiO_2 (P25) despite a wide range of concentrations. As the TiO_2 (P25) was allowed to soak for a long time in the CD solutions (12 h), it was expected that the surface adsorption would be able to saturate, and thus not be limited by concentration.[119] Therefore it was expected that the nature of the functional groups and potentially also the size of the CDs will have the dominant effect on CD loading, and therefore light absorption. As glucose and lobster had produced the smallest CDs, this suggested that size may also be an important factor in CD loading, as lobster CD-sensitized TiO_2 (P25) showed relatively high light absorption despite low concentration of the CDs and the presence of amide groups on the surface. The CD size may influence the CD loading on TiO_2 (P25), as the CD size was on the order of the pore size of the TiO_2 (P25) found by BET analysis (see **Figure 4. 10** which showed the majority of the pores to be below 5 nm in diameter. The complex interplay between size, functionalisation and concentration of CDs would therefore benefit from more in-depth investigation in future studies.

Solar cell current-voltage (J-V) curves are shown in **Figure 4. 6**, and the corresponding solar cell operational parameters are shown in **Table 4. 2** and as box plots in **Figure 4. 7**. To confirm the consistency in the fabrication of solar cell devices, 3 solar cell devices per each of the carbon dots as sensitizers were produced in parallel, and current under light was measured 3 times. This has also allowed the verification of the solar cell performance parameters more accurately, and has confirmed the stability and consistency of the fabrication procedure.

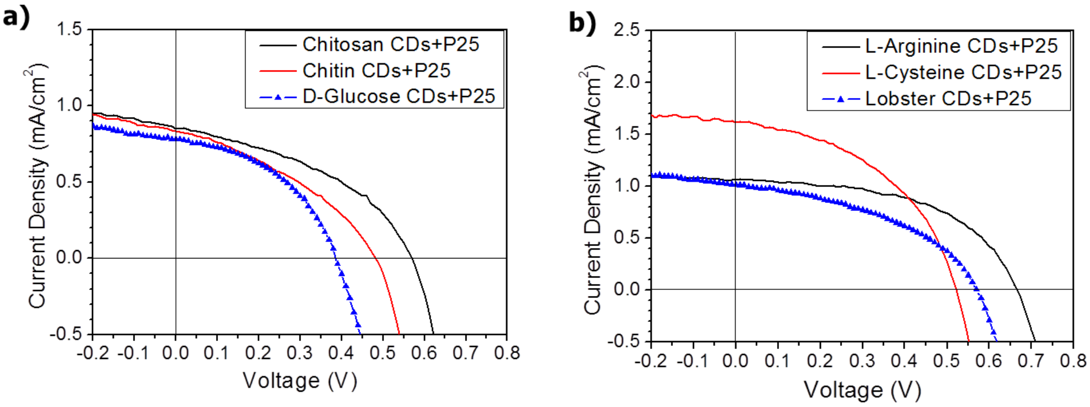

Figure 4. 6 Illuminated current-voltage (J-V) data for solar cells composed of FTO / TiO_2 (P25) / CDs / (I_3^-/I^-) electrolyte / Pt electrode : a) chitosan CDs+P25, chitin CDs+P25 and D-glucose CDs+P25 ; b) L-arginine CDs+P25, L-cysteine CDs+P25 and lobster CDs+P25. Data is shown for the best solar cell devices of each type.

Table 4. 2 Solar cell operational parameters for carbon dot sensitized TiO_2 (P25) solar cells. Averages and errors are taken from three devices per type and three measurements per device.

Sample	J_{SC} **[mA/cm^2]**	V_{OC} **[V]**	**FF**	**PCE [%]**	R_S **[kΩ]**	R_{SH} **[kΩ]**
Non-sensitized TiO_2 (P25)	0.024 ± 0.003	0.493 ± 0.009	0.326 ± 0.004	0.004 ± 0.001	34.7 ± 0.4	113.4 ± 0.9
Chitosan CDs+P25	0.80 ± 0.03	0.550 ± 0.003	0.38 ± 0.01	0.167 ± 0.008	0.80 ± 0.01	7.5 ± 0.2
Chitin CDs+P25	0.83 ± 0.01	0.469 ± 0.002	0.357 ± 0.004	0.139 ± 0.002	0.88 ± 0.03	6.8 ± 0.2
D-Glucose CDs+P25	0.68 ± 0.05	0.410 ± 0.008	0.38 ± 0.02	0.103 ± 0.008	0.94 ± 0.05	4.4 ± 0.2
L-Arginine CDs+P25	0.97 ± 0.05	0.660 ± 0.003	0.57 ± 0.02	0.362 ± 0.007	0.43 ± 0.02	24.3 ± 1.9
L-Cysteine CDs+P25	1.43 ± 0.06	0.509 ± 0.005	0.461 ± 0.006	0.34 ± 0.01	0.30 ± 0.02	8.2 ± 0.6
Lobster CDs+P25	1.05 ± 0.01	0.554 ± 0.003	0.37 ± 0.01	0.216 ± 0.008	0.48 ± 0.03	7.8 ± 0.2

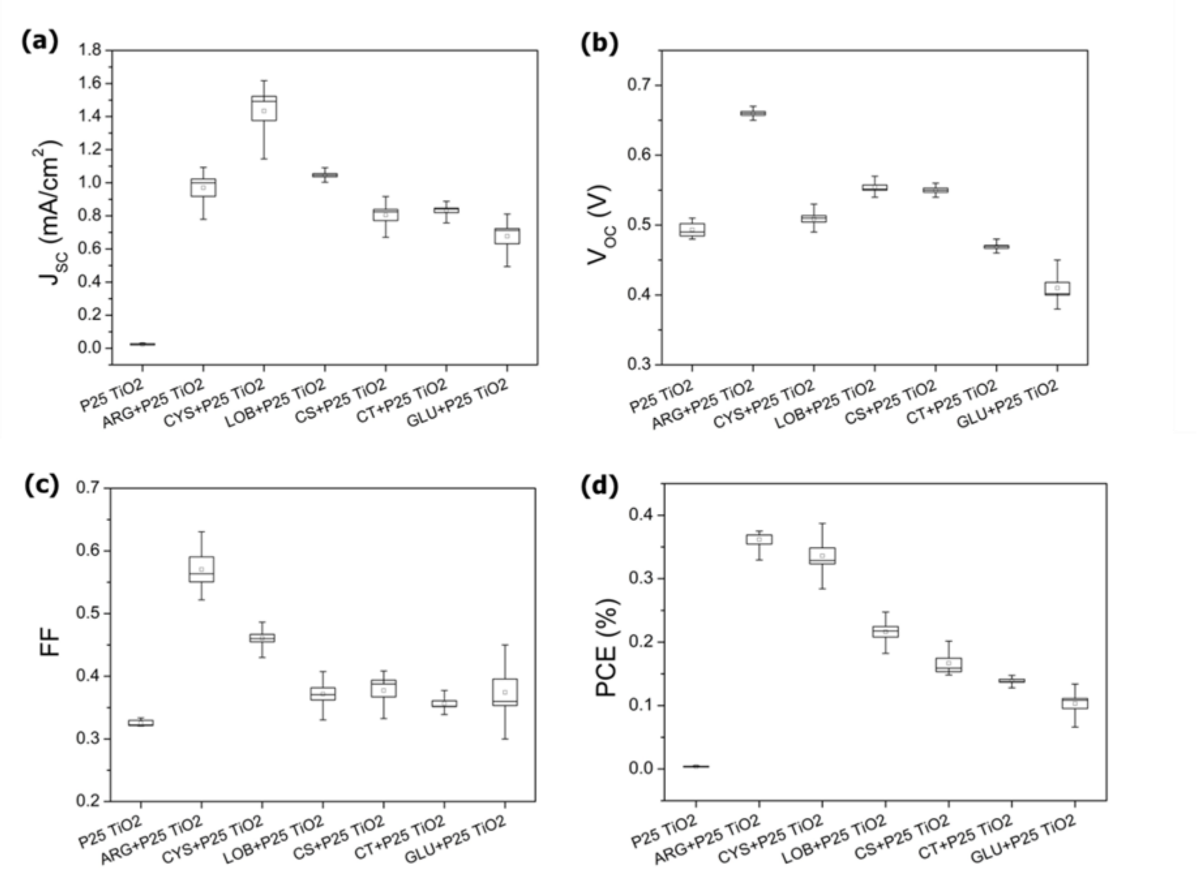

Figure 4. 7 Box plots of solar cell parameters using carbon dots derived from L-arginine (ARG), L-cysteine (CYS), lobster shells (LOB), chitosan (CS), chitin (CT) and glucose (GLU): (a) short-circuit current density (J_{sc}); (b) open-circuit voltage (V_{oc}); (c) fill factor (*FF*); (d) power conversion efficiency (*PCE*). Height of box plot represents standard error while whiskers represent min-max value.

The highest PCE of all CD-sensitized solar cells were produced by the amino-acid-derived CDs, with L-arginine giving efficiency of (0.362 ± 0.007) % and L-cysteine giving (0.34 ± 0.01) %. These efficiencies resulted from a combination of high J_{sc} values (up to (1.43 ± 0.06) mA/cm^2 for L-cysteine), with good V_{oc} and *FF* values. These can partially be attributed to the high R_{sh}, particularly for L-Arginine (**Table 4. 2**). The high value of J_{sc} likely resulted from a combination of high light absorption of L-arginine CDs and L-cysteine CDs as sensitizers, and their low R_s values (**Figure 4. 5 a** and **Table 4. 2**). The next best PCE value was obtained by lobster-derived CDs, with efficiency of (0.216 ± 0.008) % as a result of high J_{sc} of (1.05 ± 0.01) mA/cm^2 and high V_{oc}, coupled with low R_s of (0.48 ± 0.03) kΩ and moderate R_{sh} of (7.8 ± 0.2) kΩ. Finally, chitosan, chitin, and D-glucose CDs gave PCEs of (0.167 ± 0.008) %, (0.139 ± 0.002) % and (0.103 ± 0.008) %, respectively. This correlated well with increasing R_s

and decreasing R_{sh}, the former potentially explaining the low J_{sc} for D-glucose-based solar cells despite high light absorption.

Looking at the data from **Figure 4. 5** and **Table 4. 2,** it can be seen that there is a low correlation between the light absorption of CDs as sensitizers for TiO_2 (P25) and the solar cell performance parameters, particularly J_{sc}. It would be expected for J_{sc} to correlate well with the light absorption, with all else being equal. This suggested that the variation in performance of solar cell devices (J_{sc}, V_{oc}, FF and PCE) was influenced by more factors than just the ability to harvest light. Therefore the structural properties and nature of the sensitizers used, as determined by the functional groups present on the surface of CDs, may also influence other factors like efficiency of charge collection. Binding of carbon dots to the surface of TiO_2 (P25) and the nature of charge transport and charge recombination in the solar cell devices, were determined by the functionalization of as-synthesized carbon dots.

Therefore, mean value of light harvesting efficiency (LHE) of solar cell devices (**Table 4. 3**) was calculated in the range of 400-800 nm from the absorption data given in **Figure 4. 5**, in order to separate the contribution from the light harvesting efficiency and internal efficiency to the PCE. Dividing PCE by LHE gave the average internal efficiency of solar cell devices.

Table 4. 3 Light harvesting efficiency (LHE), power conversion efficiency (PCE) and average internal efficiency of as-fabricated solar cells with commercial TiO_2 (P25).

Sample	LHE [%]	PCE [%]	Average internal efficiency [%]
Chitosan CDs+P25	16.3	0.167 ± 0.008	1.02 ± 0.05
Chitin CDs+P25	11.6	0.139 ± 0.002	1.20 ± 0.02
D-Glucose CDs+P25	50.0	0.103 ± 0.008	0.20 ± 0.02
L-Arginine CDs+P25	23.6	0.362 ± 0.007	1.53 ± 0.03
L-Cysteine CDs+P25	24.5	0.34 ± 0.01	1.39 ± 0.04
Lobster CDs+P25	20.8	0.216 ± 0.008	1.04 ± 0.04

These calculations demonstrated that the high PCE of amino-acid- and lobster-derived CDs resulted from a combination of good light harvesting efficiency and good internal efficiency. Although glucose CDs as sensitizers showed the highest LHE, their average internal efficiency was the lowest of all solar cell devices, leading to the lowest value of PCE of all solar cell devices. On the other hand, chitin CDs had the lowest LHE, but showed high average internal efficiency, which led to a moderate PCE. This indicated that a precursor which leads to CDs with both good light harvesting properties and high internal efficiency in the solar cell device (low internal and interfacial losses, good charge transfer, etc.) will lead to the highest solar cell efficiency (PCE). Looking at this sample set it can be seen that amino-acid derived CDs had the best combination of these properties, which might be related to the high proportion of amine groups present on their surface. The presence of thiol groups in the case of L-cysteine CDs seems to have made little difference to the solar cell performance.

Relating the functional groups present on the surface of CDs with the differences in light harvesting efficiency and internal efficiency, a possible theory was developed on how the CDs interact with the TiO_2 surface, and how this affects the efficiency of solar cells. As it was shown, the UV-Vis absorption and LHE indicated that glucose CDs adsorb most strongly to the TiO_2 surface. The high concentration of alcohol and carboxylic acid functional groups on the surface of these CDs led to strong bonding to the TiO_2 surface through bidentate-bridging and H-bonding, as is the case for common molecular dyes like N719.[191] However, as the proportion of these groups was so high, the inter-molecular bonding was also promoted between the CDs, as found with TEM analysis (**Chapter 3.2**), and it likely led to CD clusters on the TiO_2 surface. This would explain the significantly higher light absorption of glucose CDs sensitized TiO_2 compared to other CD sensitizers, but also the low internal efficiency (as shown for clusters of dye molecules in DSSCs [188]) where the clusters of CDs on the surface of TiO_2 would hinder charge transfer and increase charge recombination.

In the case of amino acid-derived CDs (L-arginine and L-cysteine), these were shown to have a high proportion of amine groups present of the surface (**Chapter 3.4**), which might lead to the high efficiency. However, chitosan CDs also had amine groups present, and had only demonstrated slightly higher efficiency compared with the amide-containing chitin. However, structural studies showed (**Chapter 3.4**) that amino-acid-derived CDs retained the carboxylic acid functions due to the presence of both -OH and C=O groups, which is commonly used in traditional dye molecules like N719 to anchor the molecule to the surface.[191,192] Although it may be possible for the CDs to bond to the TiO_2 surface via hydrogen bonding of the amine group, it is much more likely to bond via -OH group or carboxylic acid groups where these are present, as shown in studies of dopamine bonding to the TiO_2 surface.[193] The presence of the amine groups in this case may be beneficial to reduce cluster formation compared to glucose CDs, rather than for bonding to the TiO_2 surface, as hydrogen bonding in amines is less efficient than for -OH containing molecules. Considering this, inter-molecular bonding leading to cluster formation would be further reduced in amide-containing CDs, leading to a higher internal efficiency due to reduced recombination and increased charge transfer. This is in agreement with the high internal efficiency of solar cells made with chitin CDs, which contained amides. However, in the case of chitin CDs, there was no carboxylic acid group, thus the binding to the TiO_2 surface was poor and therefore LHE was low. It was interesting to notice that lobster CDs demonstrated a similar internal efficiency to chitin CDs and chitosan CDs, but a LHE closer to the amino acids. XPS data for lobster CDs confirmed that they contain a high level of C=O groups compared to other CDs including chitin (**Chapter 3.4**), even though the purified lobster should largely resemble chitin. This functionalisation may assist in the binding to the TiO_2 surface, leading to the higher LHE for lobster CDs.

Combining these explanations, it was hypothesised that the most beneficial functional groups in CDs for optimum solar cell efficiency was a combination of carboxylic acid groups to encourage binding to the TiO_2 surface, coupled with groups which prevent cluster formation, such as amines. In the set of precursor materials used here, amino acids had the optimum combination of this functionalisation, which led to the best combination of light harvesting efficiency and internal efficiency. It was further hypothesised that precursors which led to functionalisation of CDs with both carboxylic acid groups and amines, or other groups that prevented cluster formation, would display higher solar cell efficiency.

However, in order to further increase the efficiency of solar cell devices, full understanding of the relationship between functional groups on the surface of CDs, light absorption and internal efficiency of solar cell devices, all require further detailed study. Full understanding of the origin of light absorption in hydrothermally synthesized CDs, and understanding how both light absorption and charge carrier dynamics depend on the functional groups present on the surface of CDs, will lead to specifically engineered carbon dots with LHE close to 100 % in a given wavelength range (*e.g.* 400-900 nm) together with a high internal efficiency. For carbon dot sensitized solar cells it is imperative to improve their non-trap related absorption and also chemical surface modifications. This will be a promising way to improve charge injection and regeneration kinetics. All this will contribute to the development of carbon dot sensitized solar cells with efficiencies well above 1 %.

Since light harvesting efficiency was the limiting factor in as-fabricated solar cells, it has been attempted to further increase the light harvesting by synthesizing new TiO_2 powder using a block copolymer to increase the porosity and therefore surface area[194] (see **Chapter 6.4**). This TiO_2 powder, named QM-TiO_2, was used to build solar cells with the same procedure as described in the previous section for the commercial TiO_2 (P25) (for more details about the fabrication of photovoltaic devices see **Chapter 6.5**). L-Arginine CDs and chitosan CDs were used as sensitizers for QM-TiO_2, representing the highest efficiency amino-acid- and polysaccharide-derived CDs from the TiO_2 (P25) devices. In order to ensure the consistency in fabrication of solar cell devices and reliability of measured photovoltaic performance, 3 solar cell devices were fabricated in parallel per each of the carbon dot precursors, and photovoltaic performance was measured under same standard conditions (AM 1.5 G spectrum, 100 mW/cm^2).

Figure 4. 8 shows TEM images of the as-synthesized QM-TiO_2 powder together with the corresponding electron diffraction patterns. Well-defined polycrystalline structure with aggregated particles having a diameter of around 15 nm, and containing well-ordered nanometre size openings/channels, was observed. As a comparison, TEM images and the corresponding diffraction image of the commercial TiO_2 (P25) powder are given in **Figure 4. 9**. TiO_2 (P25) powder showed well-defined crystalline structure. Also, well-ordered nanometre channels arranged in hexagonal arrays were observed. TiO_2 (P25) consisted of aggregated primary particles which had a diameter of around 20 nm.

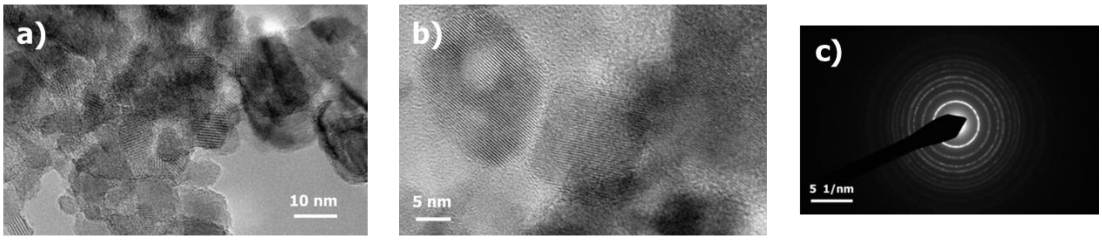

Figure 4. 8 (a, b) TEM images of QM-TiO_2 powder, and (c) corresponding electron diffraction image.

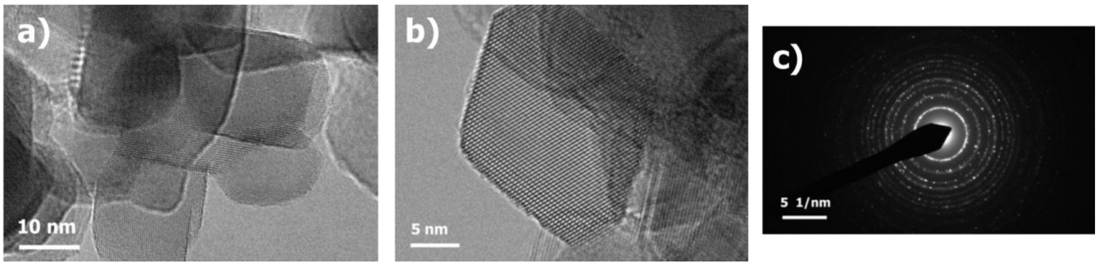

Figure 4. 9 (a, b) TEM images of commercial TiO_2 (P25) powder, and (c) corresponding electron diffraction image.

The surface area and porosity measurements of QM-TiO_2 and TiO_2 (P25) powders were performed to probe the pore size distribution (**Figure 4. 10**). The surface area of QM-TiO_2 was calculated to be 98 m^2/g which was much higher than the commercial TiO_2 (P25) powder (51 m^2/g). The pore size distribution of QM-TiO_2 showed that the majority of the pores were around 6 nm in diameter, while in the case of commercial TiO_2 (P25) the majority of the pores were around 3 nm in diameter (**Figure 4. 10 b**). QM-TiO_2 also had bigger pore volume (0.31 cm^3/g) compared to the pore volume of commercial (P25) TiO_2 (0.13 cm^3/g).

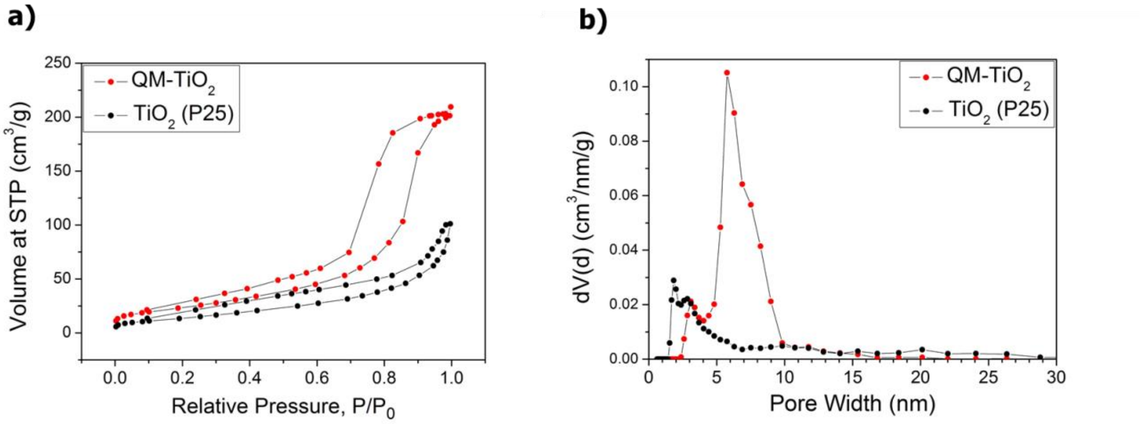

Figure 4. 10 (a) Nitrogen adsorption-desorption isotherms and (b) pore size distribution plots for TiO_2 (P25) and QM-TiO_2 powders. Surface area was determined by applying the BET theory and the pore size distribution was obtained by fitting the isotherm to QSDFT adsorption kernel implemented in the NovaWin software.

The XRD measurements of the commercial TiO_2 (P25) and QM-TiO_2 powders were carried out as shown in **Figure 4. 11**. XRD pattern of TiO_2 (P25) exhibited strong diffraction peaks at 25.4°, 37.8°, 48° and around 55°, which corresponded to TiO_2 in the anatase phase. Diffraction peaks at 27.5°, 36° and around 55° corresponded to TiO_2 in the rutile phase.[195] As seen from the XRD data, the commercial TiO_2 (P25) powder was mostly composed of anatase phase. The anatase structure is preferred over the other TiO_2 phases because of the lower recombination rate of electron-hole pairs and higher energy of the conduction band edge.[196] The XRD pattern of QM-TiO_2 (**Figure 4. 11**) exhibited strong diffraction peaks at 25.3°, 37.8°, 48.2° and around 55°, which corresponded to TiO_2 in the anatase phase, [195] differing from TiO_2 (P25) which was a mixture of anatase and rutile phases.

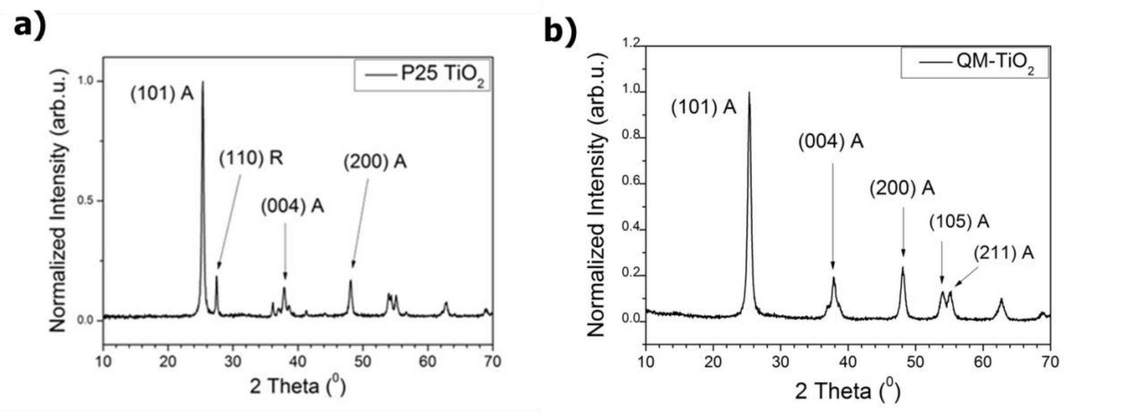

Figure 4. 11 XRD plots for the as-synthesized TiO_2 (P25) powder (a) and QM-TiO_2 powder (b). (A=anatase, R=rutile).

The absorption spectra of QM-TiO_2 sensitized with L-Arginine CDs and chitosan CDs are shown in **Figure 4. 12 a**. When QM-TiO_2 was sensitized with L-Arginine CDs and chitosan CDs, drastically increased absorption of light in the whole visible spectrum was observed. Both L-Arginine CDs and chitosan CDs as sensitizers showed similar absorption curves for the whole visible spectrum, with slightly more absorption for chitosan CDs for wavelengths higher than 600 nm.

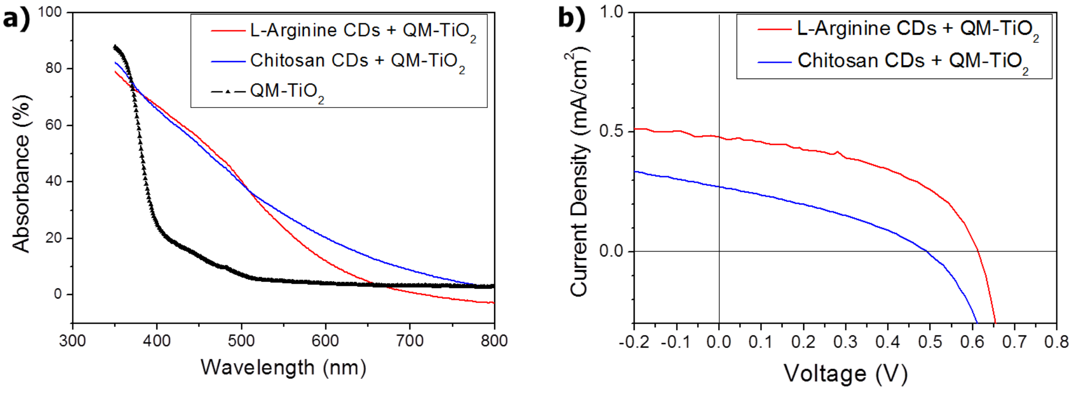

Figure 4. 12 (a) Absorption spectra of QM-TiO_2 sensitized with carbon dots. (b) Illuminated current-voltage (J-V) curves for solar cells made from QM-TiO_2 sensitized with L-Arginine CDs and chitosan CDs.

Current-voltage (J-V) curves of solar cell devices are shown in **Figure 4. 12 b**, and the corresponding solar cell parameters are shown in **Table 4. 4**. As with the TiO_2 (P25)-based solar cells, higher PCE was obtained by using L-Arginine CDs as sensitizers (0.114 ± 0.009) %, while chitosan CDs as sensitizers showed low PCE of only (0.038 ± 0.003) %. This was the lowest PCE obtained compared to all of the other carbon dots used as sensitizers in this work. Solar cells made with chitosan CDs as sensitizers for QM-TiO_2 showed high series resistance (R_S) which was the reason for low PCE value.

Table 4. 4 Solar-cell operational parameters for solar cells fabricated from QM-TiO_2 sensitized with L-Arginine CDs and chitosan CDs. Averages and errors are taken from three devices per type and three measurements per device.

Sample	**J_{SC} [mA/cm^2]**	**V_{OC} [V]**	**FF**	**PCE [%]**	**R_S [kΩ]**	**R_{SH} [kΩ]**
Non-sensitized QM-TiO_2	0.0586 ± 0.0001	0.377 ± 0.007	0.38 ± 0.02	0.008 ± 0.001	15.8 ± 0.6	54.1 ± 1.1
L-Arginine CDs + QM-TiO_2	0.39 ± 0.04	0.61 ± 0.01	0.487 ± 0.008	0.114 ± 0.009	0.54 ± 0.03	21.0 ± 1.8
Chitosan CDs + QM-TiO_2	0.22 ± 0.02	0.486 ± 0.005	0.357 ± 0.007	0.038 ± 0.003	2.7 ± 0.1	12.1 ± 0.3

Unfortunately, with both types of CDs, PCE values were lower than when using TiO_2 (P25) as a scaffold despite the higher surface area of the QM-TiO_2. In both cases J_{sc} was considerably lower for the QM-TiO_2 devices, which for chitosan QDs was partly attributed to high R_s value.

To look in more detail at the contributing factors to the PCE, light harvesting efficiency (LHE) for these devices was calculated in the range of 400-800 nm from the absorption data given in **Figure 4. 12 a** and internal efficiency was also calculated, as shown in **Table 4. 5**. Dividing PCE values by LHE values gave the average internal efficiency of solar cell devices.

Table 4. 5 Light harvesting efficiency (LHE), power conversion efficiency (PCE) and average internal efficiency of as-fabricated solar cells with QM-TiO_2 sensitized with L-arginine CDs and chitosan CDs.

Sample	LHE [%]	PCE [%]	Average Internal Efficiency [%]
L-Arginine CDs + QM-TiO_2	20.9	0.114 ± 0.009	0.55 ± 0.04
Chitosan CDs + QM-TiO_2	25.2	0.038 ± 0.003	0.15 ± 0.01

Comparing **Table 4. 5** and **Table 4. 3**, the light harvesting efficiency (LHE) of solar cells with L-Arginine CDs as sensitizers for QM-TiO_2 was lower (20.9 %) than the value obtained with L-arginine CDs as sensitizers for commercial P25 TiO_2 (23.6 %). On the other hand, solar cells with chitosan CDs as sensitizers for the QM-TiO_2 showed higher LHE (25.2 %) compared to chitosan CDs as sensitizers for commercial P25 TiO_2 (16.3 %). In both cases average internal efficiency of solar cells made with QM-TiO_2 was much lower than the values obtained when using commercial TiO_2 (P25). This indicated that there is a difference in the tendency for each type of CDs to bond to the QM-TiO_2 surface compared to the TiO_2 (P25) surface. This might be related to the different range of functional groups found on each of CDs, and indicates that the optimum functional groups may differ for different TiO_2 surfaces. This factor should be taken into consideration in future optimisation of solar cell devices.

4.4. Summary

The main focus of this chapter was to use the as-synthesized carbon dots (CDs) as sensitizers for ZnO-based and TiO_2-based nanostructured solar cells, and to measure the photovoltaic performance of as-fabricated solar cell devices. Also, it was important to make correlations between structural and optical properties of carbon dots, and photovoltaic performance of fabricated solar cell devices.

In the first part of this chapter, ZnO-nanorod-based solid state solar cells were fabricated by using three types of carbon dots as sensitizers, and their photovoltaic performance was measured. Carbon dots derived from polysaccharides and containing nitrogen functionalities (chitosan CDs and chitin CDs) and monosaccharide-derived carbon dots without nitrogen functionalities (D-glucose CDs), were all used as sensitizers for ZnO-nanorod-based solid state solar cells. The carbon dots were synthesized *via* simple one step hydrothermal carbonization method and the ZnO nanorods were synthesized using a low-temperature aqueous method (for more details see **Chapter 6**). The fabricated solar cell devices consisted of: ZnO nanorods grown on fluorine-doped tin oxide (FTO) substrates and sensitized with carbon dots (photoanode), copper (I) thiocyanate (CuSCN) as a hole conductor, and Au contacts. TEM images and UV/Vis transmission spectra confirmed that carbon dots have successfully sensitized ZnO nanorods to visible light. The photovoltaic current-voltage (J-V) measurements confirmed that all the carbon dot coatings improved the efficiency of as-fabricated solar cells compared to the uncoated solar cell devices (ZnO/CuSCN). Using a single layer coating, chitosan-CDs-sensitized solar cell device had the highest power conversion efficiency (PCE) of 0.061 %, while glucose-CDs-sensitized solar cells had the lowest PCE value of 0.017 %. The layer-by-layer (LbL) method of coating carbon dots onto ZnO nanorods was used in order to increase the light absorption of solar cell devices. The combination of chitosan CDs and chitin CDs as sensitizers using the LbL method produced solar cells with the highest efficiency of 0.077 %. This efficiency was achieved because of the increased loading of carbon dots on the ZnO-nanorod surface and therefore higher light absorption. Also, the effect of the functional groups of the two types of carbon dots on the charge transport properties of the film were complementary, enabling high value of short circuit current (J_{sc}) in these solar cells. The efficiency of solar cell devices was largely limited by the low value of light harvesting efficiency (LHE) in the range of 400-850 nm. The chitosan-chitin-CDs solar cell devices had LHE of around 5.7 %, whereas LHE was only 2 % for the solar cell devices using chitosan-CDs only.

In the second part of this chapter, carbon dots (CDs) derived from a wide range of biomaterials were used as sensitizers for TiO_2-based nanostructured solar cells. The carbon dots were synthesized *via* the hydrothermal carbonization of: polysaccharides (chitosan and chitin), monosaccharide (D-glucose), amino acids (L-arginine and L-cysteine) and raw lobster shells. As mentioned previously, when using carbon dots as sensitizers for ZnO-nanorod-based solar cells it was found that the light absorption was the limiting factor and could not be increased by building up thicker layers of CDs on ZnO nanorods. Therefore, carbon dots were used as sensitizers for TiO_2-based solar cells with liquid electrolyte, because TiO_2 had much greater available surface area for adsorbing carbon dots and increasing light absorption of solar cell devices. The as-fabricated solar cell devices consisted of: photoanode composed of TiO_2 sensitized with carbon dots and coated onto fluorine-doped tin oxide (FTO) glass substrate, liquid electrolyte, and Pt counter electrode. Two types of mesoporous TiO_2 scaffold were used: commercial TiO_2 (P25) and TiO_2 synthesized by using block copolymer (named QM-TiO_2).

TiO_2 (P25) sensitized with carbon dots had an increased absorption across the 400-800 nm visible range compared to non-sensitized TiO_2 (P25). The photoanode with D-glucose as sensitizers for TiO_2 (P25) showed the strongest light absorption, while the lowest light absorption was obtained when using chitin CDs as sensitizers. The nature of the functional groups on the surface of CDs and potentially also the size of the CDs, had a dominant effect on CD loading on TiO_2 (P25) and therefore light absorption. Photovoltaic current-voltage (J-V) measurements of solar cells showed that the highest power conversion efficiency (PCE) was obtained by using amino-acid-derived CDs as sensitizers, with L-arginine giving efficiency of (0.362 ± 0.007) % and L-cysteine giving (0.34 ± 0.01) %. The next best PCE value was obtained by lobster-derived CDs as sensitizers, with efficiency of (0.216 ± 0.008) %. There was a low correlation between the light absorption of CDs as sensitizers for TiO_2 (P25) and the solar cell performance parameters, particularly short circuit current (J_{sc}). This demonstrated that the solar cell performance parameters (J_{sc}, V_{oc}, FF and PCE) strongly depended on the precursors used for the synthesis of CDs, and therefore on the functional groups present on CDs. Functionalization of carbon dots had determined the binding of CDs to the TiO_2 (P25) surface, and charge transport and recombination in fabricated solar cell devices. Calculated light harvesting efficiency (LHE) in the range of 400-800 nm showed that D-glucose-CDs sensitized TiO_2 (P25) had the highest LHE of 50 %, followed by L-cysteine CDs (24.5 %) and L-arginine CDs (23.6 %) as sensitizers. Although D-glucose CDs as sensitizers showed the highest LHE, their internal efficiency was the lowest, leading to the lowest value of PCE of all solar cell devices. The amino-acid-derived CDs showed the best combination of light harvesting efficiency and internal efficiency which led to the highest value of PCE of all solar cell devices.

In order to increase the light harvesting efficiency of fabricated solar cell devices, new TiO_2 powder (named QM-TiO_2) was synthesized from block copolymer to obtain high surface area and high porosity TiO_2. L-arginine CDs and chitosan CDs were used as sensitizers for QM-TiO_2 but unfortunately as-fabricated solar cell devices didn’t show any significant increase in the light harvesting efficiency, and PCE values were much lower than values obtained when using commercial TiO_2 (P25). This indicated that there was a difference in tendency for carbon dots to bond to TiO_2 (P25) surface compared to QM-TiO_2 surface. It also confirmed that optimum functional groups are needed on the surface of carbon dots to bond carbon dots to different TiO_2 surfaces.

All the solar cell devices were produced simply and cheaply from biomass-derived precursors by using solution methods. It was demonstrated that sensitizers produced from not only biomass, but specifically from food waste (lobster shells) could potentially be used in nanostructured solar cells. However, PCE values of as-fabricated solar cells need further improvement to be a viable alternative to established and emerging solar cell technologies. To achieve this, the light harvesting efficiency of carbon dots should be increased in the visible and NIR part of solar spectrum, and the charge transfer processes should be improved to increase the internal efficiency of solar cell devices. In addition, further optimisation of the solar cell structure, such as using light-scattering layers, alternative electrolytes and counter electrodes, will also contribute to higher efficiencies of solar cells. With further understanding of the specific role of functional groups in the properties of carbon dots and understanding the process of anchoring carbon dots on the TiO_2 surface, it should be possible to survey the huge range of potential biomass-derived and waste-derived organic materials to identify those with the greatest potential to fabricate nanostructured solar cells with significantly increased device efficiency. Additionally, chemical surface modifications of carbon dots offer a promising way to improve the charge injection and regeneration under device operating conditions. It is important to investigate nanostructured solar cell devices under operating conditions to obtain high performance carbon dot sensitized solar cells.

Chapter 5 | Conclusions and Perspectives

The main objectives of this PhD research were: to synthesize fluorescent carbon dots from biomass-derived precursors using the hydrothermal synthesis method, to characterize and explain structural and optical properties of the as-synthesized carbon dots, and to use carbon dots as sensitizers for nanostructured solar cells.

The motivation for this research was inspired by the need to develop low-cost, non-toxic materials with good optical and electrical properties to be used for the fabrication of inexpensive, mass-producible photovoltaic solar cells with good efficiency.

Carbon dots (CDs) were synthesized from different biomass-derived precursors by using hydrothermal synthesis method (HTC) under mild conditions (200 °C for 6 h). Precursors used for the synthesis of carbon dots were: polysaccharides (chitosan and chitin), monosaccharide (D-glucose), amino acids (L-arginine and L-cysteine) and real food waste in the form of lobster shells. The carbon dots were obtained as nanometre sized nucleation clusters dispersed in the liquid phase for all precursors. Also, for certain precursors, carbon microspheres were also obtained as a solid black/brown precipitate at the bottom of the reaction vessel. A detailed investigation of morphology of carbon dots was firstly developed (**Chapter 3**). The as-synthesized carbon dots showed quasi-spherical morphology and polydispersity. Generally, the carbon dots showed a wide particle size distribution, where only D-glucose CDs and lobster CDs showed relatively narrow particle size distribution. D-glucose CDs showed the smallest particle size of (5.15 ± 0.83) nm, while chitin CDs showed the biggest particle size of (16.54 ± 3.40) nm. The choice of molecular precursor had a clear influence on the average size of carbon dots under the same hydrothermal synthesis conditions. Also, the difference in average size of carbon dots could be attributed to the different reaction mechanism during the hydrothermal synthesis of precursors containing nitrogen compounds and precursors which didn’t contain nitrogen compounds. Although a small number of chitosan CDs showed graphitic crystalline structure in TEM under 200 kV, there is a possibility that crystalline lattice fringes originated from the effect of annealing the sample by the electron beam. Also, it has to be mentioned that it may be that graphitic structures form and co-exist together with amorphous structures in carbon dots synthesized by the hydrothermal carbonization at mild synthesis conditions.

Considering carbon microspheres, they showed formation of spherical particles and/or heterogeneous morphology. Their formation mechanism was confirmed by microtommed TEM micrographs, and by the complete lack of porosity detected by using CO_2 adsorption analysis.

Moving on, chemical composition and structural features of carbon dots were investigated. Elemental analysis of carbon dots confirmed the presence of C (40% - 54%), O (19% - 43%) and N (8% - 20%) elements, which were also detected in carbon microspheres. FTIR and XPS analysis showed the presence of different functional groups on the surface of carbon dots and carbon microspheres, and these functional gups originated from the starting precursors. Stretching vibrations of O-H, N-H, C-H, C=O, amide and amine groups were detected in FTIR spectra of carbon dots, while carbon microspheres showed similar chemical features as the pure starting precursors. XPS analysis for all carbon dots showed the presence of sp^2/sp^3 carbons (C=C / C-C), C-O, C=O, pyridinic-N and amines and/or amides (C-NH / N-C=O), together with the presence of sulphur functionalities (thiols) for L-arginine CDs. Similar chemical environment of functional groups was also observed for carbon microspheres. Considered together, XPS and FTIR results confirmed that the functional groups from the starting precursors were successfully incorporated into the as-synthesized carbon dots.

To further verify the crystalline/amorphous nature of carbon dots and carbon microspheres, Raman and XRD measurements were performed. Raman analysis showed that carbon dots and carbon microspheres possess structural disorder and amorphous-like character. The XRD analysis of carbon dots and carbon microspheres showed a significant level of topological disorder in all samples, and the observed peak at about $2\theta=22°$ corresponded to a set of sp^2 carbons-graphitic carbons with stacking faults (turbostratic carbons).

The photoluminescence (PL) properties of carbon dots were further investigated, while carbon microspheres were disregarded since they didn’t show any photoluminescence properties. Diluted solutions of carbon dots were transparent under daylight and showed strong blue-green photoluminescence emission under UV excitation. All the carbon dots showed a strong absorption in the UV region from 220-360 nm, while no absorption was observed for wavelengths larger than 450 nm. Excitation-dependent PL emission was observed for all carbon dots and it was more pronounced for the excitation wavelengths larger than 320 nm. Excitation-dependent PL property of carbon dots means that as the excitation wavelength was increased, the emission wavelength of carbon dots was red-shifted and the PL emission intensity of carbon dots was decreased. Excitation-independent PL emission was observed for chitosan CDs, L-cysteine CDs and lobster CDs, for the excitation wavelengths in the range 200 - 320 nm. Full-width-at half-maximum (FWHM) value of PL emission peaks of carbon dots was around 100 nm, with the exception of L-arginine CDs and L-cysteine CDs which showed narrow PL emission of 70-80 nm.

Considered collectively, the absorption spectra, PL excitation and PL emission spectra, all suggested that the blue emission in all carbon dots originated from energy levels located at around 340 nm. These levels most likely corresponded to HOMO-LUMO energy levels in sp^2 bound carbon clusters. The highest fluorescence quantum yield (QY) was calculated for L-arginine CDs with the value of (43.3 ± 2.1) %, while glucose CDs had the lowest QY of (2.2 ± 0.2) %. QY value is connected with the ability of carbon dots to absorb a photon of light, excite an electron into excited state, and when this electron relaxes to the ground state, to re-emit a photon of light without losing to much energy of incoming photon as phonon vibrations and heat. Tendency is to have QY values as close as possible to 100 %.

The optical characterizations of carbon dots confirmed that HOMO-LUMO transitions were the origin of the excitation-independent PL light emission, while excitation-dependent PL emission was most likely due to the HOMO-LUMO gap states. The exact nature of these gap states is still unclear. The origin of light emission must be governed by the interplay between absorption due to the carbon-based cores and the surface functional groups.

The main focus of **Chapter 4** was the application of the as-synthesized carbon dots. Carbon dots were used as sensitizers for ZnO-nanorod-based and TiO_2-based nanostructured solar cells. Photovoltaic performance of the as-fabricated solar cells was measured, and correlations between structural and optical properties of carbon dots and performance of solar cells have been explained.

The chapter opens with the fabrication of ZnO-nanorod-based solar cells which were sensitized with three types of carbon dots (chitosan CDs, chitin CDs and D-glucose CDs). Polysaccharide-derived carbon dots (chitosan CDs and chitin CDs) contained nitrogen functionalities in the form of amines and/or amides, while monosaccharide derived carbon dots (D-glucose CDs) had no nitrogen functionalities. ZnO nanorods were synthesized using a low-temperature aqueous method, while carbon dots were synthesized using hydrothermal method (see **Chapter 6**). As-fabricated solar cell devices consisted of the following components: fluorine-doped tin oxide (FTO) coated glass substrate / ZnO nanorods sensitized with carbon dots / copper (I) thiocyanate (CuSCN) as a solid state electrolyte and a hole conductor / Au contacts. ZnO nanorods have been successfully coated with carbon dots, which was confirmed by TEM images. UV/Vis transmission spectra of ZnO nanorods coated with carbon dots showed a decrease of transmission in the region 400-500 nm which confirmed that carbon dots had successfully sensitized ZnO nanorods to visible light. Current-voltage (J-V) measurements of solar cells showed that all the carbon dot coatings had improved the efficiency of the as-fabricated solar cells compared to the uncoated solar cell devices (ZnO/CuSCN). Considering single coating of carbon dots onto ZnO nanorods, chitosan-CDs-sensitized solar cells showed the highest efficiency of 0.061 %, while glucose-CDs-sensitized solar cells showed the lowest efficiency of 0.017 %. When using layer-by-layer (LbL) coating method, it led to the increase of light absorption and efficiency of solar cell devices. Solar cells with combination of chitosan- and chitin-CDs as sensitizers using the LbL method showed the best efficiency of 0.077 %. This increased efficiency was achieved because the use of alternate layers of carbon dots led to an increased loading of carbon dots on the ZnO-nanorod surface, which led to higher light absorption. But also effects of the functional groups at the surface of carbon dots on the charge transport properties of the film were complementary, leading to high short circuit current (J_{sc}) without increasing series resistance (R_s) of solar cell devices. Light harvesting efficiency (LHE) for the chitosan-chitin-CDs solar cell devices was calculated to be around 5.7 %, and for solar cell devices using only chitosan CDs it was around 2 %. Low LHE was one of the limiting factors for high solar cell efficiency.

In the second part of **Chapter 4** carbon dots synthesized from different biomass-derived precursors were used as sensitizers for TiO_2-based nanostructured solar cells. The main idea was to use high surface area, mesoporous, commercial TiO_2 (P25) scaffold to increase the adsorption of carbon dots, and thus increase the light absorption and efficiency of fabricated solar cell devices. Carbon dots were synthesized with hydrothermal method from polysaccharides (chitosan and chitin), monosaccharide (D-glucose), amino acids (L-arginine and L-cysteine) and real food waste in the form of lobster shells. As-fabricated solar cells consisted of the following components: fluorine doped tin oxide (FTO) glass anode / TiO_2 (P25) sensitized with carbon dots / liquid electrolyte (I_3^-/I^- redox couple) / Pt counter electrode. Optical absorption spectra showed clear increase in the absorption across the 400-800 nm visible range for TiO_2 (P25) sensitized with CDs compared to non-sensitized TiO_2 (P25). D-glucose-sensitized TiO_2 (P25) photoanode showed the highest light absorption while the lowest light absorption was observed for chitin-sensitized TiO_2 (P25). It was concluded that the high level of -OH groups and potentially carboxylic acid groups on the surface of D-glucose CDs contributed to high loading on the TiO_2 (P25) surface, while the amide groups on chitin CDs prevented good loading. It was also shown that the size of CDs can potentially have dominant effect on CD loading onto TiO_2 (P25), especially if the carbon dots were on the order of the pore size in TiO_2 (P25). Current-voltage (J-V) measurements of as-fabricated solar cell devices showed that the highest power conversion efficiency (PCE) was obtained by using amino-acid-derived CDs as sensitizers. L-arginine CDs sensitized solar cells showed the highest efficiency of (0.362 ± 0.007) %, and L-cysteine CDs sensitized solar cells showed efficiency of (0.34 ± 0.01) %. L-arginine CDs and L-cysteine CDs as sensitizers showed high light absorption coupled with low series resistance (R_s) and high short circuit current (J_{sc}). The next best PCE value of (0.216 ± 0.008) % was obtained by using lobster-derived CDs as a result of high J_{sc} coupled with low R_s. Low correlation between the light absorption of CDs as sensitizers for TiO_2 (P25) and the solar cell operational parameters (J_{sc}, V_{oc}, FF and PCE) was observed. It was concluded that variation in operational parameters of solar cells was influenced by more factors than just light harvesting ability. Functionalization of as-synthesized carbon dots had determined the binding of carbon dots to the surface of TiO_2 (P25), and the nature of charge transport and charge recombination in the solar cell devices. Calculations of light harvesting efficiency (LHE) showed that the D-glucose CD sensitized solar cells had the highest LHE of 50.0 %, but their internal efficiency was very low leading to low PCE of (0.103 ± 0.008) %. Combination of good LHE and high internal efficiency in L-arginine, L-cysteine and lobster CD sensitized solar cells led to their high PCE values.

A possible theory was developed of how the CDs interact with the TiO_2 surface and how this affects the efficiency of fabricated solar cells. This theory was based on relating the functional groups present on the surface of CDs with the differences in light harvesting efficiency and internal efficiency of fabricated solar cells. It was shown that high concentration of alcohol and carboxylic acid functional groups on the surface of D-glucose CDs led to strong bonding of D-glucose CDs to the TiO_2 surface. However, high concentration of these functional groups also led to inter-molecular bonding between CDs which likely led to formation of CD clusters on the TiO_2 surface. This was the reason why D-glucose CD sensitized solar cells showed low internal efficiency where the clusters of CDs on the surface of TiO_2 had hindered charge transfer and had increased charge recombination. Considering amino-acid-derived CDs (L-arginine and L-cysteine), the presence of the amine groups on their surface was beneficial to reduce the cluster formation of CDs. Also, amino-acid-derived CDs retained carboxylic acid functionalisation due to the presence of both -OH and C=O groups, which was beneficial to anchor CDs to the surface of TiO_2. Lobster CDs contained high level of C=O groups compared to other CDs, which was again beneficial for the binding of lobster CDs to TiO_2 surface and led to high LHE value for lobster CD sensitized solar cells. It was concluded that precursors which led to functionalisation of CDs with both carboxylic acid groups (to increase the binding of CDs to the TiO_2 surface) and amines (or other groups that prevent cluster formation) would lead to CD sensitized solar cell devices with higher efficiency.

In the final part of **Chapter 4**, new TiO_2 powder (named QM-TiO_2) was synthesized from block copolymer to obtain higher surface area and better porosity compared to commercial TiO_2 (P25). The main idea was to anchor even more carbon dots onto surface of QM-TiO_2, and thus increase light harvesting and efficiency of fabricated solar cell devices. L-arginine CDs and chitosan CDs were used as sensitizers for QM-TiO_2. Surface area of QM-TiO_2 was calculated to be 98 m^2/g which was much higher than the commercial TiO_2 (P25) powder (51 m^2/g), and the pore size distribution of QM-TiO_2 showed that the majority of the pores were around 6 nm in diameter, while for TiO_2 (P25) the majority of the pores were around 3 nm in diameter. Unfortunately, as-fabricated solar cell devices with QM-TiO_2 showed much lower PCE than solar cell devices with commercial TiO_2 (P25). L-arginine-CDs sensitized QM-TiO_2 solar cells had efficiency of (0.114 ± 0.009) %, while chitosan-CDs sensitized solar cells had efficiency of (0.038 ± 0.003) %. This had shown that there is a clear difference in the tendency for each type of CDs to anchor to the QM-TiO_2 surface compared to the TiO_2 (P25) surface, leading to variations in operating parameters of solar cells. It also indicated that the optimum functional groups on the surface of CDs may differ for anchoring to different TiO_2 surfaces.

Most research on carbon in recent decades has been focused on low-dimensional carbon allotropes. These carbon allotropes may consist solely of sp^2- or sp^3-hybridized carbon, or be of mixed hybridization. Nanosized carbon allotropes can be functionalized in a wide variety of ways, producing families of carbon nanomaterials with interesting optical properties. The family of carbon nanomaterials includes highly symmetrical and structurally well-defined members (graphene, carbon nanotubes, and fullerene), but it also includes a variety of materials with complex structures many of which have not been fully determined. Comprehensive structural description of these materials, particularly carbon dots (CDs), would provide important insights into their mechanism of photoluminescence (PL). Origin of photoluminescence in CDs still remains only partially understood despite being studied by numerous research groups. It is important to clearly explain the origin of PL in different classes of carbon nanoparticles, especially considering different families of precursors used and different synthesis procedures. PL of semiconductor quantum dots is considered to arise from the nanostructure as a whole, while PL of CDs has been attributed to both sp^2 domains and surface centers. Distinguishing between these two types of PL centers is difficult because typical synthesis procedures for CDs generally produce centers of both kinds.

It is important to introduce clear and unambiguous definitions for different classes of carbon nanoparticles (carbon dots, carbon nanodots, carbon quantum dots, etc.), and to distinguish between dots having different structures and morphologies. Also, it is beneficial to make a clear distinction between carbon nanoparticles with crystalline carbon core, with amorphous carbon core, or a mixture of crystalline core surrounded by amorphous region.

It is of great importance to explain the formation mechanism of hydrothermally synthesized CDs. As mentioned previously in this PhD thesis, there have only been few attempts in the research community to do so. Size-controlled synthesis of CDs and narrow particle size distribution should be the focus of future research in the field of CDs.

Another perspective in the research of fluorescent CDs should be the use of computational modelling. Computational modelling is a powerful tool that can be used to complement experiments, and to relate the electronic and optical properties of CDs to their morphology. However, theoretical scientist should design their studies in a way to make sure to examine appropriate model systems that capture all the phenomena of interest. As a final perspective for CDs, it is important to move from the lab-scale synthesis of CDs to the industrial-scale synthesis for commercial applications.

For carbon dot solar cells to become a competitive solution to already established and to future emerging photovoltaic technologies, certain issues need to be addressed. As mentioned previously, CDs should be synthesized having narrow particle size distribution and well-defined crystalline structure from abundant, biomass-derived precursors. This will enable band gap engineering in CDs and increased light absorption, but also narrow photoluminescence emission of CDs. Carbon dots should be engineered with specific functional groups on the surface to enable better anchoring on TiO_2 or ZnO surface. This will enable better light harvesting efficiency and internal efficiency of fabricated solar cells, which will lead to increased power conversion efficiency of solar cell devices. Further investigations are needed on how the chemical surface modifications of CDs influence charge carrier injection and regeneration under device operating conditions. The main challenge for CD sensitized solar cells is to further improve their efficiency. Device architecture and CD surface should be further optimized, and electrodes and semiconductor oxides should be better structured by using low-cost abundant resources which will enable efficient charge separation, transportation and extraction of electrons and holes. CD films used as sensitizers should be developed with as few as possible charge carrier recombination centers and with high mobilities of electrons and holes. Improvements in charge carrier transport are crucial for the improvements of CD sensitized solar cells.

For the commercial applications of CD sensitized solar cells some other factors also need to be considered in addition to increasing the efficiency of solar cells. It is important to develop scaled-up synthesis of carbon dots from laboratories to industrial manufacturing, which is currently not so trivial. New deposition methods for depositing CDs onto semiconductor oxides should be developed which will enable ink-jet printing and roll-to-roll printing. Stability is another important concern for CD-based solar cells where robust device encapsulation is critical to meet the commercial requirements of stability on a time scale of 10 years.

Overall, the work presented in this PhD research project represents an important contribution to the field of nanostructured photovoltaic solar cells. It highlights the high potential of using cheap biomass-derived precursors for the synthesis of fluorescent carbon dots, and the application of carbon dots as sensitizers for nanostructured solar cells. It also demonstrates the importance of developing future solar photovoltaic technologies based on cheap and abundant resources.

Chapter 6 | Experimental Section

6.1. Synthesis of Carbon Dots

Chitin from shrimp shells (practical grade powder), chitosan (medium molecular weight), D-(+)-Glucose (ACS reagent), L-arginine (reagent grade, assay ≥98%), and L-cysteine (assay ≥97%) were all purchased from Sigma-Aldrich. Lobster was purchased from the food market in London, UK. Ethanol (ACS reagent, assay ≥99.8%) was purchased from Sigma-Aldrich. Hydrochloric acid (assay 36.5-38%) was purchased from VWR Chemicals and sodium hydroxide (pellets, assay ≥98%) was purchased from Sigma-Aldrich. Acrodisc syringe filters (0.2 µm pore size) were purchased from Pall Corporation. Stainless steel autoclaves with Teflon inlets were purchased from Parr Instrument Company. All the chemicals were used without further purification.

Chitosan, chitin, D-glucose, L-arginine, L-cysteine, and lobster powder were all used as precursors for the hydrothermal synthesis of carbon dots. Lobster powder from the real lobster shells was obtained as follows. Lobster was purchased at the food market in London, UK. Then it was cooked in boiling water for 1 h, the meat was consumed, and the shells were preserved. Shells (25 g) were firstly soaked in NaOH (500 mL, 5 wt% compared to the mass of the initial lobster shells) overnight at 70 °C, and then they were soaked in HCl solution (500 mL, 0.1 M) overnight at room temperature. As obtained purified lobster shells were stored in DI water (500 mL) in the fridge at 5 °C for the future use. Prior to their use in hydrothermal reaction, purified lobster shells were dried and milled into the lobster powder. Purification procedure was done to remove the soluble proteins and minerals from the lobster shells, and the procedure was done as described by Nguyen and MacLachlan[197].

Briefly, 0.7 g of precursor was put in 20 mL of ethanol in a glass inlet and placed in a stainless steel autoclave with Teflon inlet (50 mL), which underwent hydrothermal treatment in the oven (Carbolite PN) at 200 °C for 6 hours. After the hydrothermal treatment of certain precursors, two phases were obtained. Solid precipitate was obtained at the bottom of the glass inlet, and the light yellow to dark brown liquid phase was obtained above the solid black precipitate. After the hydrothermal reaction, chitosan, chitin, and D-glucose precursors showed liquid phase and a solid precipitate, while L-arginine, L-cysteine, and lobster precursors only showed liquid phase.

The obtained light yellow to dark brown liquid phase together with the solid precipitate, were centrifuged at 10,000 rpm for 15 min (Thermo Scientific, Heraeus Multifuge X1R) to separate the liquid phase containing fluorescent carbon dots (CDs) from the solid precipitate containing carbon microspheres. The liquid phase containing carbon dots was then filtered through syringe filters (0.2 µm pore size). After the centrifugation and filtration, usually 18-20 mL of liquid phase containing carbon dots was obtained per each of the precursors. As obtained solutions containing carbon dots (~20 mL per each of the precursors) were stored in the fridge at 5 °C for the future use. Also, certain amount (20 mL) of the solutions of carbon dots were freeze dried (-110 °C for 48 h, Scanvac Cool Safe 110-4 Pro) and then vacuum dried (90 °C for 48 h, Thermo Scientific Vacuutherm) to obtain the final powder of carbon dots which was used for further characterization. The masses of the obtained carbon dots' powders (after freeze drying and vacuum drying) were as follows: 0.03 g for chitosan CDs, 0.012 g for chitin CDs, 1.13 g for D-glucose CDs, 0.71 g for L-arginine CDs, 0.2 g for L-cysteine CDs, and 0.036 g for lobster CDs.

The solid precipitate containing carbon microspheres was vacuum dried at 90 °C overnight. The masses (after vacuum drying) of the obtained solid precipitate containing carbon microspheres were as follows: 0.33 g for chitosan precursor, 0.55 g for chitin precursor, and 0.23 g for D-glucose precursor.

More details about the structural features and chemical composition of carbon dots and carbon microspheres are given in **Chapter 3**.

6.2. Synthesis of ZnO Nanorods

Zinc acetate (assay 99.99% trace metals basis), methanol (ACS reagent), hexamethylenetetramine (ACS reagent) and zinc nitrate hexahydrate (reagent grade, 98%) were all purchased from Sigma Aldrich.

ZnO nanorods were grown on fluorine-doped tin oxide (FTO) substrates seeded with ZnO by spray pyrolysis of 0.1 M zinc acetate solution in methanol at 350 °C (modified from Ref.[198]). Seeded substrates were suspended face down in an aqueous solution of 25 mM hexamethylenetetramine (HMT) and 15 mM zinc nitrate, and heated for 4 hours at 90 °C, which was repeated 8 times to increase the length of nanorods.[189,199]

6.3. Fabrication of Photovoltaic Devices Based on ZnO Nanorods Sensitized with Carbon Dots

Ethanol (ACS reagent, assay ≥99.8%), copper (I) thiocyanate (CuSCN), and propyl sulphide (assay 97%) were all purchased from Sigma Aldrich.

ZnO nanorods were coated with carbon dots (CDs) by soaking the substrates in the as-synthesized CDs solution in ethanol for 24 h. Then they were removed from CDs solution (~20 mL) and rinsed with pure ethanol to remove any poorly adhered CDs. This was repeated in subsequent solutions to produce layer-by-layer (LbL) samples.

Photovoltaic devices were completed by spray-coating the CDs-coated ZnO nanorods with a 0.15 M copper (I) thiocyanate (CuSCN) solution in propyl sulphide, while heating at 100 °C on a hotplate until they were completely covered with a compact layer of CuSCN, as reported previously.[200] 150 nm-thick gold (Au) contacts were evaporated to form four ~0.2 cm^2 devices per substrate.

6.4. Synthesis of Homemade TiO_2 Powder (QM-TiO_2)

Titanium (IV) chloride (puriss, ≥99%) was purchased from Fluka Analytical while Pluronic-P123 (PEG-PPG-PEG) and ethanol (ACS reagent, assay ≥99.8%) were purchased from Sigma-Aldrich.

QM-TiO_2 powder was synthesized following the procedure described by Yang *et al.*[194] Briefly, 1g of poly(alkylene oxide) block copolymer (Pluronic P-123) was dissolved in 10 g of ethanol. Then 0.01 mol of $TiCl_4$ was added to this solution with vigorous steering for 30 min. The resulting solution was gelled in an open dish at 40 °C in air for 5 days (Carbolite PN oven). During this time the inorganic precursor ($TiCl_4$) polymerizes and hydrolyses into a metal oxide network. The as-made samples were then calcined at 400 °C in air for 5 hours (Carbolite LHT oven) to remove the block copolymer surfactant. The as-obtained QM-TiO_2 powder (~1 g) was used to fabricate photovoltaic solar cells.

6.5. Fabrication of Photovoltaic Devices Based on TiO_2 Sensitized with Carbon Dots

Acetone (assay ≥ 99.8%) was purchased from Sigma-Aldrich and 2-Propanol (assay ≥ 99.5%) from Fisher Chemical. Titanium (IV) chloride (puriss, ≥99%) was purchased from Fluka Analytical. Titanium (IV) oxide (Aeroxide P25), ethyl cellulose (viscosity 10 cP and 46 cP), lauric acid (assay ≥98%) and α–terpineol (analytical standard) were all purchased from Sigma-Aldrich. Electrolyte solution (Iodolyte HI-30) was purchased from Solaronix.

Nanostructured solar cells based on commercial TiO_2 (Aeroxide P25) sensitized with carbon dots were fabricated as follows. Glass coated with fluorine doped tin oxide (FTO) was purchased from Pilkington and cut into 2x2 cm substrates. The substrates were cleaned by sonicating in acetone for 15 min and then in 2-Propanol for another 15 min. In the meantime, 60 mL of DI water was poured into the glass beaker, and into that 0.22 mL of titanium (IV) chloride was added. The beaker was placed in an ice bath and stirred on electric stirrer for 15 min. Titanium (IV) chloride solution was poured onto the cleaned FTO coated glass slides to fully cover them, and they were put in an electric oven at 60 °C for 30 min (Carbolite LHT oven). After these 30 min in an oven, FTO coated glass slides were taken out and put onto the hot plate at 450 °C for 30 min for the annealing of titanium (IV) chloride.

TiO_2 paste was prepared as follows. 1g of titanium (IV) oxide (Aeroxide P25), 0.25g of ethyl cellulose (viscosity 10 cP), 0.25g of ethyl cellulose (viscosity 46 cP), 0.1g of lauric acid, 10 mL of ethanol and 3.33g of α-terpineol were all mixed together using pestle and mortar for about 30 min until a thick white paste was obtained. This amount of produced TiO_2 paste was enough for coating of about 10 glass substrates (2x2 cm each). Scotch tape or sellotape was used along the two edges of FTO coated glass substrates to act as guides for putting TiO_2 paste onto glass substrates' active area. Using glass slides, TiO_2 paste was uniformly spread onto the active area of FTO coated glass substrates, and left at room temperature for 30 min. Then the FTO coated glass substrates with TiO_2 on them were put in an electrical oven (Carbolite LHT) for the annealing of TiO_2 paste by using the programmed heating rate (0-200 °C at 2 °C /min ; 200-450 °C at 4 °C /min), and the temperature was kept at 450 °C for 30 min. After cooling down to room temperature, glass substrates with TiO_2 coating on them were taken out of the oven and put again into titanium (IV) chloride solution in the oven at 60 °C for 30 min. Then they were taken out of the oven, rinsed with DI water and put on a hot plate at 450 °C for 30 min. Following all this procedure, FTO coated glass substrates with TiO_2 paste on them were obtained, and they were ready to be sensitized with carbon dots.

Sensitization of TiO_2 with carbon dots was done by putting FTO glass substrates coated with TiO_2 into respective carbon dots' solutions (~20 mL) in the fridge at 6 °C for 12 hours. This way, carbon dots were adsorbed onto the TiO_2 mesoporous layers.

Open-type solar cells were made by using platinum (Pt) coated FTO glass substrate as a counter electrode, separated from the TiO_2 photoanode using a spacer, filled with I^-/I_3^- electrolyte solution (Iodolyte HI-30, Solaronix), and clamped shut.

QM-TiO_2 powder was also used to build solar cells with the same procedure as described above for the commercial TiO_2 (P25) powder.

6.6. Current-Voltage Measurements of Solar Cell Devices

Current-voltage measurements of as-fabricated TiO_2-based and ZnO-nanorod-based solar cells sensitized with carbon dots were performed as follows. Keithley 2400 Source Meter SMU Instrument was used as a power supply. Devices were tested with 100 mW/cm^2 illumination (calibrated using a standard Si solar cell) using a Newport Oriel class ABB solar simulator with an AM 1.5 filter, all controlled by Labview software.

Series resistance (R_s) and shunt resistance (R_{sh}) of solar cells were calculated from the current-voltage (I-V) curves. R_s was calculated as the slope of the I-V curve at the point V_{oc} (slope ≈ $1/R_s$), and R_{sh} was calculated as the slope of the I-V curve at the point I_{sc} (slope ≈ $1/R_{sh}$).

For the TiO_2-based solar cells, 3 solar cell devices were fabricated per each of the carbon dot sensitizers, and current under illumination and dark current were measured 3 times to obtain statistically relevant solar cell performance results. Also, this had confirmed the consistency and stability in the fabrication of solar cell devices. For the ZnO nanorod-based solar cells, one solar cell device was fabricated per each of carbon dot sensitizers. Current under illumination and dark current were measured 3 times.

6.7. Structural and Optical Characterisation Methods

Transmission Electron Microscopy (TEM) was performed on JEOL JEM-2010 electron microscope operating at 200 kV to observe the morphologies of the samples. One drop of as-synthesized carbon dots (concentration given in **Chapter 3**, **Table 3.1**), and one drop of carbon microspheres dispersed in ethanol (~1 mg/mL), were applied onto the copper grid coated with lacey carbon film (TAAB, LC 400 Cu) for TEM characterisation. Copper grid was left at room temperature for few minutes to evaporate the ethanol. Then it was put into the sample holder and inserted into the vacuum chamber of TEM microscope.

TEM microtoming for carbon microspheres was realized by first placing the materials into a gelatine capsule followed by embedding in an epoxy resin (L.R. White Resin, Plano, Wetzlar, Germany). After embedding (3-5 days, 60 °C) the sample was cut ultrathin using a diamond knife (Leica E. M. Trim), and the cross section of the materials was examined by TEM JEOL JEM-2010 at 200 kV.

Scanning Electron Microscopy (SEM) images of carbon microspheres were obtained using the FEI Inspect-F electron microscope (accelerating voltage up to 20 kV). Samples were prepared by loading the carbon microspheres powder samples onto the sticky carbon tape and sputtering with gold.

Elemental Analysis data (EA) were obtained by using Vario MICRO Cube elemental analyser system for the detection of C, H, N, S. The wt % of O was calculated.

Freeze dried carbon dots were obtained by using Scanvac Cool Safe 110-4 Pro freeze dryer operating at condenser temperature of -110 °C. Freeze drying process was done for 48 h.

X-ray Photoelectron Spectroscopy (XPS) measurements were performed on Specs spectrometer using Mg Kα (1253.6 eV) radiation from a double anode at 150 W. Freeze dried carbon dots and carbon microspheres powders were used for the XPS measurements. The spectrum was calibrated by setting the C 1s peak at 284.6 eV. For sulphur, the S 2p peak was used for the assignment of binding states. Peak assignments were carried out by using the values reported in the references indicated in the main text.

Fourier Transform Infrared Spectroscopy (FTIR) measurements were recorded by using Bruker Tensor 27 instrument equipped with diamond lens Attenuated Total

Reflectance (ATR) module in the range from 4000 cm^{-1} to 400 cm^{-1}. Freeze dried carbon dots and carbon microspheres powders were used to obtain the FTIR spectra.

Raman spectra were measured by using Renishaw 1000 microspectrometer with an excitation wavelength of 633 nm. Freeze dried carbon dots and carbon microspheres powders were used to obtain the Raman spectra.

X-ray Diffraction (XRD) patterns were recorded using Panalytical Xpert Pro diffractometer equipped with Ni filtered Cu Kα radiation (λ_1=1.5406 Å and λ_2=1.5444 Å), collected in the 2θ range from 5° to 70° using a scan rate of 1° min^{-1}. Freeze dried carbon dots and carbon microspheres powders were used for the XRD measurements.

UV-Vis absorption spectra of carbon dots were recorded by using Perkin Elmer Lambda LS 35 UV-visible spectrometer in the range 200-800 nm. Diluted solutions of carbon dots in ethanol were used for the UV-Vis absorption measurements.

Fluorescence spectra of carbon dots were recorded by using Perkin Elmer LS 55 fluorescence spectrometer in the range 200-900 nm. Slit width of 6 nm, both for excitation and emission spectra, was used when measuring fluorescence emission of solutions of carbon dots in ethanol. The excitation wavelength was increased from 200 nm to 480 nm in 20 nm increments and the corresponding fluorescence emission spectrum was recorded.

Quartz cuvettes (Thor Labs) were used for the measurements of UV-Vis absorption and fluorescence emission spectra. Quartz cuvettes have a 10 mm transmitted path length through the sample and a certified wavelength range from 200 - 3000 nm. Plastic and glass cuvettes show very low transmission below 290 nm, but quartz cuvettes have good transmission spectra all the way down to 200 nm (78% transmission at 200 nm).

Photoluminescence quantum yield (Φ) of carbon dots was determined by using quinine sulphate (QS) as a reference, and following the procedure as described by Sahu *et al.*[52] Quinine sulphate (literature Φ = 54%) was dissolved in 0.1M H_2SO_4 (refractive index η = 1.33), and the carbon dots were dissolved in ethanol (η = 1.36). Five concentrations of each compound were made, all of which had the absorbance at 340 nm less than 0.1 in order to minimize the reabsorption effects in the cuvette. Photoluminescence (PL) emission spectra of all the samples were recorded at an excitation wavelength of 340 nm. The quantum yield (Φ) was calculated using the following equation:

$$\Phi_x = \Phi_{st} \left(\frac{Grad_x}{Grad_{st}}\right) \left(\frac{\eta_x^2}{\eta_{st}^2}\right)$$

Eq. 4

, where the subscript *ST* denotes the standard sample (quinine sulphate) and *X* denotes the test sample. Φ is the fluorescence quantum yield, *Grad* is the gradient from the plot of integrated fluorescence intensity *vs.* absorbance, and η is the refractive index of solvent. By plotting the integrated fluorescence intensity (excited at 340 nm) *vs.* absorbency values (at 340 nm) for the carbon dots and Quinine Sulphate, the slope of the curves were determined, and using that data the fluorescence quantum yield (Φ_x) of carbon dots was calculated.

UV-Vis transmission and absorption spectra of TiO_2 sensitized with carbon dots and ZnO nanorods sensitized with carbon dots were both measured by using Perkin-Elmer Lambda 950 spectrometer fitted with an integrating sphere (in the range 200-850 nm).

N_2 adsorption measurements of TiO_2 powders (P25 TiO_2 and QM-TiO_2) were performed at 77 K using Quantachrome Nova 4200e instrument. Prior to the measurements, the TiO_2 powder samples (0.1 g) were degassed at 150 °C for 24 hours. Surface area was determined by applying the BET theory following the IUPAC procedure and the pore size distribution was obtained by fitting the isotherm to QSDFT adsorption kernel implemented in the NovaWin software provided by Quantachrome Instruments. High purity nitrogen gas was used for all the measurements.

CO_2 sorption measurements of carbon microspheres were performed at 273 K using Quantachrome Nova 4200e instrument. Prior to the measurement, the carbon microspheres powder samples (0.1 g) were degassed at 150 °C for 24 hours. Grand canonical Monte Carlo method was used for CO_2 adsorption. Data evaluation was done using the NovaWin software provided by Quantachrome Instruments. High purity gas was used for all the measurements.

Chapter 7 | Appendix

7.1. List of Publications

1. **Marinovic, A**.; Kiat, L.S.; Dunn, S.; Titirici, M.M.; Briscoe, J. Carbon Dot Solar Cells from Renewable Precursors. *Advanced Functional Materials* (submitted for publication, August 2016)
2. Briscoe, J.*; **Marinovic, A.***; Sevilla, M.; Dunn, S.; Titirici, M. Biomass-Derived Carbon Quantum Dot Sensitizers for Solid-State Nanostructured Solar Cells. *Angew. Chemie Int. Ed.* 2015, 54, 4463–4468. ***equal contribution**
3. Ferrero, G. A.; Preuss, K.; **Marinovic, A**.; Jorge, A. B.; Mansor, N.; Brett, D. J. L.; Fuertes, A. B.; Sevilla, M.; Titirici, M.-M. Fe-N-Doped Carbon Capsules with Outstanding Electrochemical Performance and Stability for the Oxygen Reduction Reaction in Both Acid and Alkaline Conditions. *ACS Nano* 2016, 10, 5922–5932.
4. Preuss, K.; Kannuchamy, V. K.; **Marinovic, A**.; Isaacs, M.; Wilson, K.; Abrahams, I.; Titirici, M.-M. Bio-Inspired Carbon Electro-Catalysts for the Oxygen Reduction Reaction. *J. Energy Chem.* 2016, 25, 228–235.
5. Alatalo, S.-M.; Qiu, K.; Preuss, K.; **Marinovic, A.**; Sevilla, M.; Sillanpää, M.; Guo, X.; Titirici, M.-M. Soy Protein Directed Hydrothermal Synthesis of Porous Carbon Aerogels for Electrocatalytic Oxygen Reduction. *Carbon* 2016, 96, 622–630.
6. **Marinovic, A**.; Pileidis, F. D.; Titirici, M.-M. CHAPTER 5. Hydrothermal Carbonisation (HTC): History, State-of-the-Art and Chemistry. In *Porous Carbon Materials from Sustainable Precursors; The Royal Society of Chemistry*, 2015; pp. 129–155.

7.2. List of International Oral Presentations

1. **Marinovic A**., “Fluorescent Carbon Dots from Biomass-derived Precursors”, World Conference on Carbon (Carbon 2015), Dresden, Germany, June 12-July 17, 2015

2. **Marinovic A**., “Biomass-derived Fluorescent Carbon Quantum Dots”, Green Chemistry Gordon Research Seminar, The Chinese University of Hong Kong, Hong Kong, China, July 26-July 27, 2014

3. **Marinovic A.**, “Biomass-derived Carbon Quantum Dots as Sensitizers for Solid-State ZnO Solar Cells”, Institute of Metal Research, Chinese Academy of Sciences, Shenyang, China, July 2014
4. **Marinovic A.**, “Biomass-derived Fluorescent Carbon Quantum Dots as Solar Cell Sensitizers”, World Conference on Carbon (Carbon 2014), Jeju, South Korea, June 29-July 4, 2014

7.3. List of Poster Presentations

1. **Marinovic A**. and Titirici M. M., “Advanced Carbon Materials from Waste for Renewable Energy Applications”, SET for BRITAIN, Parliamentary and Scientific Committee, House of Commons, London, UK, March 2015
2. **Marinovic A.**, Briscoe J., Dunn S. and Titirici M. M., “Biomass-derived Fluorescent Carbon Quantum Dots as Solar Cell Sensitizers”, Green Chemistry Gordon Research Conference, The Chinese University of Hong Kong, Hong Kong, China, July 27-August 1, 2014
3. **Marinovic A**. and Titirici M. M., “Carbon Quantum Dots and Nitrogen Doped Carbons *via* Hydrothermal Carbonization of Chitosan and Chitin”, International Conference on Carbon for Energy Storage/Conversion and Environment Protection (CESEP 2013), Mülheim an der Ruhr, Germany, September 2013
4. **Marinovic A**. and Titirici M. M., “Carbon Quantum Dots and Nitrogen Doped Carbons *via* Hydrothermal Carbonization of Chitosan and Chitin”, International Conference on Materials Chemistry (MC11), Warwick, UK, July 2013

7.4. Awards and Honours

1. Graduate Research Project Alumni Prize 1st place award (out of more than 100 PhD students), Queen Mary University of London, School of Engineering and Materials Science, UK, October 2015
2. Korean Carbon Society (KCS) Student Award for the best oral presentation (out of more than 200 PhD students), World Conference on Carbon (Carbon 2014), Jeju, South Korea, July 2014

3. Queen Mary University of London Postgraduate Research Fund (£1,850, only 4 awards per year), London, UK, June 2014
4. Journal of Materials Chemistry C 1st place award for the best poster in Environmental Materials category, 11th International Conference on Materials Chemistry (MC11), Warwick, UK, July 2013
5. PhD Studentship Award for the duration of 36 months (£15,560 p.a.) from Queen Mary University of London, UK, January 2013

References

(1) BP Statistical Review of World Energy http://www.bp.com/en/global/corporate/energy-economics/statistical-review-of-world-energy.html (accessed Jul 16, 2016).

(2) Georgakilas, V.; Perman, J. A.; Tucek, J.; Zboril, R. Broad Family of Carbon Nanoallotropes: Classification, Chemistry, and Applications of Fullerenes, Carbon Dots, Nanotubes, Graphene, Nanodiamonds, and Combined Superstructures. *Chem. Rev.* **2015**, *115*, 4744–4822.

(3) Titirici, M. M.; Antonietti, M. Chemistry and Materials Options of Sustainable Carbon Materials Made by Hydrothermal Carbonization. *Chem. Soc. Rev.* **2010**, *39*, 103–116.

(4) Bergius, F. Production of Hydrogen from Water and Coal from Cellulose at High Temperatures and Pressures. *J. Soc. Chem. Ind.* **1913**, *32*, 462–467.

(5) Titirici, M.-M.; Thomas, A.; Antonietti, M. Back in the Black: Hydrothermal Carbonization of Plant Material as an Efficient Chemical Process to Treat the CO2 Problem? *New J. Chem.* **2007**, *31*, 787.

(6) Titirici, M.-M.; White, R. J.; Fellinger, T.-P.; Kubo, S.; Brun, N.; Lozano-Castello, D.; Marco-Lozar, J. P.; Falco, C.; Cazorla-Amoros, D.; Hu, B.; *et al. Sustainable Carbon Materials from Hydrothermal Processes*; Wiley, 2013.

(7) Titirici, M.-M.; White, R. J.; Brun, N.; Budarin, V. L.; Su, D. S.; del Monte, F.; Clark, J. H.; MacLachlan, M. J. Sustainable Carbon Materials. *Chem. Soc. Rev.* **2015**, *44*, 250–290.

(8) Baccile, N.; Laurent, G.; Babonneau, F.; Fayon, F.; Titirici, M.-M.; Antonietti, M. Structural Characterization of Hydrothermal Carbon Spheres by Advanced Solid-State MAS 13 C NMR Investigations. *J. Phys. Chem. C* **2009**, *113*, 9644–9654.

(9) Falco, C.; Perez Caballero, F.; Babonneau, F.; Gervais, C.; Laurent, G.; Titirici, M.-M.; Baccile, N. Hydrothermal Carbon from Biomass: Structural Differences between Hydrothermal and Pyrolyzed Carbons via 13 C Solid State NMR. *Langmuir* **2011**, *27*, 14460–14471.

(10) Zhao, L.; Chen, X.; Wang, X.; Zhang, Y.; Wei, W.; Sun, Y.; Antonietti, M.; Titirici, M.-M. One-Step Solvothermal Synthesis of a Carbon@TiO2 Dyade Structure Effectively Promoting Visible-Light Photocatalysis. *Adv. Mater.* **2010**, *22*, 3317–3321.

(11) J. A. Libra C. Kammann, A. Funke, N. D. Berge, Y. Neubauer, M.-M. Titirici, C. Fuhner, O. Bens, J. Kern and K.-H. Emmerich, K. S. R. Hydrothermal Carbonization of Biomass Residuals : A Comparative Review of the Chemistry, Processes and Applications of Wet and Dry Pyrolysis. *Biofuels* **2011**, *2(1)*, 89–124.

(12) Titirici, M.-M.; Antonietti, M.; Baccile, N. Hydrothermal Carbon from Biomass: A Comparison of the Local Structure from Poly- to Monosaccharides and Pentoses/hexoses. *Green Chem.* **2008**, *10*, 1204.

(13) White, R. J.; Antonietti, M.; Titirici, M.-M. Naturally Inspired Nitrogen Doped Porous Carbon. *J. Mater. Chem.* **2009**, *19*, 8645.

(14) Kubo, S.; White, R. J.; Yoshizawa, N.; Antonietti, M.; Titirici, M. M. Ordered Carbohydrate-Derived Porous Carbons. *Chem. Mater.* **2011**, *23*, 4882–4885.

(15) Kubo, S.; Tan, I.; White, R. J.; Antonietti, M.; Titirici, M. M. Template Synthesis of Carbonaceous Tubular Nanostructures with Tunable Surface Properties. *Chem. Mater.* **2010**, *22*, 6590–6597.

(16) Demir-Cakan, R.; Hu, Y.-S.; Antonietti, M.; Maier, J.; Titirici, M.-M. Facile One-Pot Synthesis of Mesoporous SnO 2 Microspheres via Nanoparticles Assembly and Lithium Storage Properties. *Chem. Mater.* **2008**, *20*, 1227–1229.

(17) Frohlich, C.; Lean, J. Solar Radiative Output and Its Variability: Evidence and Mechanisms. *Astron. Astrophys. Rev.* **2004**, *12*, 273–320.

(18) Jean, J.; Brown, P. R.; Jaffe, R. L.; Buonassisi, T.; Bulović, V. Pathways for Solar Photovoltaics. *Energy Environ. Sci.* **2015**, *8*, 1200–1219.

(19) Jacobson, M. Z.; Delucchi, M. A. Providing All Global Energy with Wind, Water, and Solar Power, Part I: Technologies, Energy Resources, Quantities and Areas of Infrastructure, and Materials. *Energy Policy* **2011**, *39*, 1154–1169.

(20) Beard, M. C.; Luther, J. M.; Semonin, O. E.; Nozik, A. J. Third Generation Photovoltaics Based on Multiple Exciton Generation in Quantum Confined Semiconductors. *Acc. Chem. Res.* **2013**, *46*, 1252–1260.

(21) Beard, M. C.; Luther, J. M.; Nozik, A. J. The Promise and Challenge of Nanostructured Solar Cells. *Nat Nano* **2014**, *9*, 951–954.

(22) Shockley, W.; Queisser, H. J. Detailed Balance Limit of Efficiency of P-N Junction Solar Cells. *J. Appl. Phys.* **1961**, *32*, 510.

(23) Rühle, S. Tabulated Values of the Shockley–Queisser Limit for Single Junction Solar Cells. *Sol. Energy* **2016**, *130*, 139–147.

(24) Burchell, T. D. *Carbon Materials for Advanced Technologies*; Burchell, T. D., Ed.; PERGAMON-ELSEVIER SCIENCE LTD, 1999.

(25) Hirsch, A. The Era of Carbon Allotropes. *Nat. Mater.* **2010**, *9*, 868–871.

(26) Kroto, H. W.; Heath, J. R.; O’Brien, S. C.; Curl, R. F.; Smalley, R. E. C60: Buckminsterfullerene. *Nature* **1985**, *318*, 162–163.

(27) Iijima, S. Helical Microtubules of Graphitic Carbon. *Nature* **1991**, *354*, 56–58.

(28) Novoselov, K. S.; Geim, A. K.; Morozov, S. V.; Jiang, D.; Zhang, Y.; Dubonos, S. V.; Grigorieva, I. V.; Firsov, A. A. Electric Field Effect in Atomically Thin Carbon Films. *Science (80-.).* **2004**, *306*, 666–669.

(29) Xu, X.; Ray, R.; Gu, Y.; Ploehn, H. J.; Gearheart, L.; Raker, K.; Scrivens, W. A. Electrophoretic Analysis and Purification of Fluorescent Single-Walled Carbon Nanotube Fragments. *J. Am. Chem. Soc.* **2004**, *126*, 12736–12737.

(30) Li, L.; Yan, X. Colloidal Graphene Quantum Dots. *J. Phys. Chem. Lett.* **2010**, *1*, 2572–2576.

(31) Shen, J.; Zhu, Y.; Yang, X.; Li, C. Graphene Quantum Dots: Emergent Nanolights for Bioimaging, Sensors, Catalysis and Photovoltaic Devices. *Chem. Commun.* **2012**, *48*, 3686.

(32) Kozák, O.; Sudolská, M.; Pramanik, G.; Cígler, P.; Otyepka, M.; Zbořil, R. Photoluminescent Carbon Nanostructures. *Chem. Mater.* **2016**, *28*, 4085–4128.

(33) Zhu, S.; Meng, Q.; Wang, L.; Zhang, J.; Song, Y.; Jin, H.; Zhang, K.; Sun, H.; Wang, H.; Yang, B. Highly Photoluminescent Carbon Dots for Multicolor Patterning, Sensors, and Bioimaging. *Angew Chem Int Ed Engl* **2013**, *52*, 3953–3957.

(34) Liu, S.; Tian, J.; Wang, L.; Zhang, Y.; Qin, X.; Luo, Y.; Asiri, A. M.; Al-Youbi, A. O.; Sun, X. Hydrothermal Treatment of Grass: A Low-Cost, Green Route to

Nitrogen-Doped, Carbon-Rich, Photoluminescent Polymer Nanodots as an Effective Fluorescent Sensing Platform for Label-Free Detection of Cu(II) Ions. *Adv. Mater.* **2012**, *24*, 2037–2041.

(35) Zhu, S.; Song, Y.; Zhao, X.; Shao, J.; Zhang, J.; Yang, B. The Photoluminescence Mechanism in Carbon Dots (Graphene Quantum Dots, Carbon Nanodots, and Polymer Dots): Current State and Future Perspective. *Nano Res.* **2015**, *8*, 355–381.

(36) Reckmeier, C. J.; Schneider, J.; Susha, A. S.; Rogach, A. L. Luminescent Colloidal Carbon Dots: Optical Properties and Effects of Doping. *Opt. Express* **2016**, *24*, A312.

(37) Lim, S. Y.; Shen, W.; Gao, Z. Carbon Quantum Dots and Their Applications. *Chem. Soc. Rev.* **2015**, *44*, 362–381.

(38) Li, H.; Kang, Z.; Liu, Y.; Lee, S.-T. Carbon Nanodots: Synthesis, Properties and Applications. *J. Mater. Chem.* **2012**, *22*, 24230.

(39) Kargbo, O.; Jin, Y.; Ding, S.-N. Recent Advances in Luminescent Carbon Dots. *Curr. Anal. Chem.* **2014**, *11*, 4–21.

(40) Wang, Y.; Hu, A. Carbon Quantum Dots: Synthesis, Properties and Applications. *J. Mater. Chem. C* **2014**, *2*, 6921.

(41) Sun, Y.-P.; Zhou, B.; Lin, Y.; Wang, W.; Fernando, K. A. S.; Pathak, P.; Meziani, M. J.; Harruff, B. A.; Wang, X.; Wang, H.; *et al.* Quantum-Sized Carbon Dots for Bright and Colorful Photoluminescence. *J. Am. Chem. Soc.* **2006**, *128*, 7756–7757.

(42) Bao, L.; Zhang, Z.-L.; Tian, Z.-Q.; Zhang, L.; Liu, C.; Lin, Y.; Qi, B.; Pang, D.-W. Electrochemical Tuning of Luminescent Carbon Nanodots: From Preparation to Luminescence Mechanism. *Adv. Mater.* **2011**, *23*, 5801–5806.

(43) Liu, H.; Ye, T.; Mao, C. Fluorescent Carbon Nanoparticles Derived from Candle Soot. *Angew. Chemie Int. Ed.* **2007**, *46*, 6473–6475.

(44) Bourlinos, A. B.; Stassinopoulos, A.; Anglos, D.; Zboril, R.; Karakassides, M.; Giannelis, E. P. Surface Functionalized Carbogenic Quantum Dots. *Small* **2008**, *4*, 455–458.

(45) Jiang, K.; Sun, S.; Zhang, L.; Lu, Y.; Wu, A.; Cai, C.; Lin, H. Red, Green, and Blue Luminescence by Carbon Dots: Full-Color Emission Tuning and Multicolor

Cellular Imaging. *Angew. Chemie Int. Ed.* **2015**, *54*, 5360–5363.

(46) Mitra, S.; Chandra, S.; Kundu, T.; Banerjee, R.; Pramanik, P.; Goswami, A. Rapid Microwave Synthesis of Fluorescent Hydrophobic Carbon Dots. *RSC Adv.* **2012**, *2*, 12129.

(47) Zhai, X.; Zhang, P.; Liu, C.; Bai, T.; Li, W.; Dai, L.; Liu, W. Highly Luminescent Carbon Nanodots by Microwave-Assisted Pyrolysis. *Chem. Commun.* **2012**, *48*, 7955.

(48) Bourlinos, A. B.; Stassinopoulos, A.; Anglos, D.; Zboril, R.; Georgakilas, V.; Giannelis, E. P. Photoluminescent Carbogenic Dots. *Chem. Mater.* **2008**, *20*, 4539–4541.

(49) Hu, S.-L.; Niu, K.-Y.; Sun, J.; Yang, J.; Zhao, N.-Q.; Du, X.-W. One-Step Synthesis of Fluorescent Carbon Nanoparticles by Laser Irradiation. *J. Mater. Chem.* **2009**, *19*, 484–488.

(50) Hu, S.; Liu, J.; Yang, J.; Wang, Y.; Cao, S. Laser Synthesis and Size Tailor of Carbon Quantum Dots. *J. Nanoparticle Res.* **2011**, *13*, 7247–7252.

(51) Zhou, J.; Booker, C.; Li, R.; Zhou, X.; Sham, T.-K.; Sun, X.; Ding, Z. An Electrochemical Avenue to Blue Luminescent Nanocrystals from Multiwalled Carbon Nanotubes (MWCNTs). *J. Am. Chem. Soc.* **2007**, *129*, 744–745.

(52) Sahu, S.; Behera, B.; Maiti, T. K.; Mohapatra, S. Simple One-Step Synthesis of Highly Luminescent Carbon Dots from Orange Juice: Application as Excellent Bio-Imaging Agents. *Chem. Commun.* **2012**, *48*, 8835.

(53) Schwenke, A. M.; Hoeppener, S.; Schubert, U. S. Synthesis and Modification of Carbon Nanomaterials Utilizing Microwave Heating. *Adv. Mater.* **2015**, *27*, 4113–4141.

(54) Krysmann, M. J.; Kelarakis, A.; Dallas, P.; Giannelis, E. P. Formation Mechanism of Carbogenic Nanoparticles with Dual Photoluminescence Emission. *J. Am. Chem. Soc.* **2012**, *134*, 747–750.

(55) Zhu, C. Z.; Zhai, J. F.; Dong, S. J. Bifunctional Fluorescent Carbon Nanodots: Green Synthesis via Soy Milk and Application as Metal-Free Electrocatalysts for Oxygen Reduction. *Chem. Commun.* **2012**, *48*, 9367–9369.

(56) Hu, Q.; Paau, M. C.; Zhang, Y.; Gong, X.; Zhang, L.; Lu, D.; Liu, Y.; Liu, Q.; Yao, J.; Choi, M. M. F. Green Synthesis of Fluorescent Nitrogen/sulfur-Doped

Carbon Dots and Investigation of Their Properties by HPLC Coupled with Mass Spectrometry. *RSC Adv.* **2014**, *4*, 18065.

(57) Hsu, P.-C.; Shih, Z.-Y.; Lee, C.-H.; Chang, H.-T. Synthesis and Analytical Applications of Photoluminescent Carbon Nanodots. *Green Chem.* **2012**, *14*, 917.

(58) Xu, Y.; Wu, M.; Liu, Y.; Feng, X.-Z.; Yin, X.-B.; He, X.-W.; Zhang, Y.-K. Nitrogen-Doped Carbon Dots: A Facile and General Preparation Method, Photoluminescence Investigation, and Imaging Applications. *Chem. - A Eur. J.* **2013**, *19*, 2276–2283.

(59) Yang, Z.; Xu, M.; Liu, Y.; He, F.; Gao, F.; Su, Y.; Wei, H.; Zhang, Y. Nitrogen-Doped, Carbon-Rich, Highly Photoluminescent Carbon Dots from Ammonium Citrate. *Nanoscale* **2014**, *6*, 1890–1895.

(60) Wang, L.; Zhu, S.-J.; Wang, H.-Y.; Qu, S.-N.; Zhang, Y.-L.; Zhang, J.-H.; Chen, Q.-D.; Xu, H.-L.; Han, W.; Yang, B.; *et al.* Common Origin of Green Luminescence in Carbon Nanodots and Graphene Quantum Dots. *ACS Nano* **2014**, *8*, 2541–2547.

(61) Ding, H.; Wei, J.-S.; Xiong, H.-M. Nitrogen and Sulfur Co-Doped Carbon Dots with Strong Blue Luminescence. *Nanoscale* **2014**, *6*, 13817–13823.

(62) Dong, Y.; Pang, H.; Yang, H. Bin; Guo, C.; Shao, J.; Chi, Y.; Li, C. M.; Yu, T. Carbon-Based Dots Co-Doped with Nitrogen and Sulfur for High Quantum Yield and Excitation-Independent Emission. *Angew. Chemie Int. Ed.* **2013**, *52*, 7800–7804.

(63) Kasprzyk, W.; Bednarz, S.; Bogdał, D. Luminescence Phenomena of Biodegradable Photoluminescent Poly(diol Citrates). *Chem. Commun.* **2013**, *49*, 6445.

(64) Zhou, J.; Shan, X.; Ma, J.; Gu, Y.; Qian, Z.; Chen, J.; Feng, H. Facile Synthesis of P-Doped Carbon Quantum Dots with Highly Efficient Photoluminescence. *RSC Adv.* **2014**, *4*, 5465.

(65) Shan, X.; Chai, L.; Ma, J.; Qian, Z.; Chen, J.; Feng, H. B-Doped Carbon Quantum Dots as a Sensitive Fluorescence Probe for Hydrogen Peroxide and Glucose Detection. *Analyst* **2014**, *139*, 2322–2325.

(66) Barman, M. K.; Jana, B.; Bhattacharyya, S.; Patra, A. Photophysical Properties of Doped Carbon Dots (N, P, and B) and Their Influence on Electron/Hole Transfer

in Carbon Dots–Nickel (II) Phthalocyanine Conjugates. *J. Phys. Chem. C* **2014**, *118*, 20034–20041.

(67) Fu, M.; Ehrat, F.; Wang, Y.; Milowska, K. Z.; Reckmeier, C.; Rogach, A. L.; Stolarczyk, J. K.; Urban, A. S.; Feldmann, J. Carbon Dots: A Unique Fluorescent Cocktail of Polycyclic Aromatic Hydrocarbons. *Nano Lett.* **2015**, *15*, 6030–6035.

(68) Ferrari, A. C. Raman Spectroscopy of Graphene and Graphite: Disorder, Electron–phonon Coupling, Doping and Nonadiabatic Effects. *Solid State Commun.* **2007**, *143*, 47–57.

(69) Li, Z. Q.; Lu, C. J.; Xia, Z. P.; Zhou, Y.; Luo, Z. X-Ray Diffraction Patterns of Graphite and Turbostratic Carbon. *Carbon N. Y.* **2007**, *45*, 1686–1695.

(70) Dhenadhayalan, N.; Lin, K.-C.; Suresh, R.; Ramamurthy, P. Unravelling the Multiple Emissive States in Citric-Acid-Derived Carbon Dots. *J. Phys. Chem. C* **2016**, *120*, 1252–1261.

(71) Kwon, W.; Do, S.; Kim, J.-H.; Seok Jeong, M.; Rhee, S.-W. Control of Photoluminescence of Carbon Nanodots via Surface Functionalization Using Para-Substituted Anilines. *Sci. Rep.* **2015**, *5*, 12604.

(72) Cao, L.; Wang, X.; Meziani, M. J.; Lu, F.; Wang, H.; Luo, P. G.; Lin, Y.; Harruff, B. A.; Veca, L. M.; Murray, D.; *et al.* Carbon Dots for Multiphoton Bioimaging. *J. Am. Chem. Soc.* **2007**, *129*, 11318–11319.

(73) Ding, H.; Yu, S.-B.; Wei, J.-S.; Xiong, H.-M. Full-Color Light-Emitting Carbon Dots with a Surface-State-Controlled Luminescence Mechanism. *ACS Nano* **2016**, *10*, 484–491.

(74) Qu, D.; Zheng, M.; Zhang, L.; Zhao, H.; Xie, Z.; Jing, X.; Haddad, R. E.; Fan, H.; Sun, Z. Formation Mechanism and Optimization of Highly Luminescent N-Doped Graphene Quantum Dots. *Sci. Rep.* **2014**, *4*, 5294.

(75) Ghosh, S.; Chizhik, A. M.; Karedla, N.; Dekaliuk, M. O.; Gregor, I.; Schuhmann, H.; Seibt, M.; Bodensiek, K.; Schaap, I. A. T.; Schulz, O.; *et al.* Photoluminescence of Carbon Nanodots: Dipole Emission Centers and Electron–Phonon Coupling. *Nano Lett.* **2014**, *14*, 5656–5661.

(76) Vinci, J. C.; Ferrer, I. M.; Seedhouse, S. J.; Bourdon, A. K.; Reynard, J. M.; Foster, B. A.; Bright, F. V.; Colón, L. A. Hidden Properties of Carbon Dots Revealed After HPLC Fractionation. *J. Phys. Chem. Lett.* **2013**, *4*, 239–243.

(77) Yang, Z. C.; Wang, M.; Yong, A. M.; Wong, S. Y.; Zhang, X. H.; Tan, H.; Chang, A. Y.; Li, X.; Wang, J. Intrinsically Fluorescent Carbon Dots with Tunable Emission Derived from Hydrothermal Treatment of Glucose in the Presence of Monopotassium Phosphate. *Chem. Commun.* **2011**, *47*, 11615–11617.

(78) Li, H. T.; He, X. D.; Kang, Z. H.; Huang, H.; Liu, Y.; Liu, J. L.; Lian, S. Y.; Tsang, C. H. A.; Yang, X. B.; Lee, S. T. Water-Soluble Fluorescent Carbon Quantum Dots and Photocatalyst Design. *Angew. Chemie-International Ed.* **2010**, *49*, 4430–4434.

(79) Chestnoy, N.; Harris, T.; Hull, R. Luminescence and Photophysics of CdS Semiconductor Clusters: The Nature of the Emitting Electronic State. *J. Phys. Chem.* **1986**, *90*, 3393–3399.

(80) Zhao, Q.-L.; Zhang, Z.-L.; Huang, B.-H.; Peng, J.; Zhang, M.; Pang, D.-W. Facile Preparation of Low Cytotoxicity Fluorescent Carbon Nanocrystals by Electrooxidation of Graphite. *Chem. Commun. (Camb).* **2008**, 5116.

(81) Fuyuno, N.; Kozawa, D.; Miyauchi, Y.; Mouri, S.; Kitaura, R.; Shinohara, H.; Yasuda, T.; Komatsu, N.; Matsuda, K. Drastic Change in Photoluminescence Properties of Graphene Quantum Dots by Chromatographic Separation. *Adv. Opt. Mater.* **2014**, *2*, 983–989.

(82) Strauss, V.; Margraf, J. T.; Dolle, C.; Butz, B.; Nacken, T. J.; Walter, J.; Bauer, W.; Peukert, W.; Spiecker, E.; Clark, T.; *et al.* Carbon Nanodots: Toward a Comprehensive Understanding of Their Photoluminescence. *J. Am. Chem. Soc.* **2014**, *136*, 17308–17316.

(83) Sudolská, M.; Dubecký, M.; Sarkar, S.; Reckmeier, C. J.; Zbořil, R.; Rogach, A. L.; Otyepka, M. Nature of Absorption Bands in Oxygen-Functionalized Graphitic Carbon Dots. *J. Phys. Chem. C* **2015**, *119*, 13369–13373.

(84) Sarkar, S.; Sudolská, M.; Dubecký, M.; Reckmeier, C. J.; Rogach, A. L.; Zbořil, R.; Otyepka, M. Graphitic Nitrogen Doping in Carbon Dots Causes Red-Shifted Absorption. *J. Phys. Chem. C* **2016**, *120*, 1303–1308.

(85) Reusch, W. UV-Visible Absorption Spectra https://www2.chemistry.msu.edu/faculty/reusch/virttxtjml/Spectrpy/UV-Vis/spectrum.htm#uv3 (accessed Sep 7, 2016).

(86) Margraf, J. T.; Strauss, V.; Guldi, D. M.; Clark, T. The Electronic Structure of Amorphous Carbon Nanodots. *J. Phys. Chem. B* **2015**, *119*, 7258–7265.

(87) Hu, S.; Tian, R.; Dong, Y.; Yang, J.; Liu, J.; Chang, Q. Modulation and Effects of Surface Groups on Photoluminescence and Photocatalytic Activity of Carbon Dots. *Nanoscale* **2013**, *5*, 11665–11671.

(88) Xu, Q.; Zhou, Q.; Hua, Z.; Xue, Q.; Zhang, C.; Wang, X.; Pan, D.; Xiao, M. Single-Particle Spectroscopic Measurements of Fluorescent Graphene Quantum Dots. *ACS Nano* **2013**, *7*, 10654–10661.

(89) Wang, X.; Cao, L.; Yang, S. T.; Lu, F.; Meziani, M. J.; Tian, L.; Sun, K. W.; Bloodgood, M. A.; Sun, Y. P. Bandgap-like Strong Fluorescence in Functionalized Carbon Nanoparticles. *Angew. Chemie - Int. Ed.* **2010**, *49*, 5310–5314.

(90) Zheng, H.; Wang, Q.; Long, Y.; Zhang, H.; Huang, X.; Zhu, R. Enhancing the Luminescence of Carbon Dots with a Reduction Pathway. *Chem. Commun.* **2011**, *47*, 10650.

(91) Ghosh, S.; Chizhik, A. M.; Karedla, N.; Dekaliuk, M. O.; Gregor, I.; Schuhmann, H.; Seibt, M.; Bodensiek, K.; Schaap, I. A. T.; Schulz, O.; *et al.* Photoluminescence of Carbon Nanodots: Dipole Emission Centers and Electron–Phonon Coupling. *Nano Lett.* **2014**, *14*, 5656–5661.

(92) Wang, J.; Zhang, P.; Huang, C.; Liu, G.; Leung, K. C. F.; Wáng, Y. X. J. High Performance Photoluminescent Carbon Dots for in Vitro and in Vivo Bioimaging: Effect of Nitrogen Doping Ratios. *Langmuir* **2015**, *31*, 8063–8073.

(93) Song, Y.; Zhu, S.; Zhang, S.; Fu, Y.; Wang, L.; Zhao, X.; Yang, B. Investigation from Chemical Structure to Photoluminescent Mechanism: A Type of Carbon Dots from the Pyrolysis of Citric Acid and an Amine. *J. Mater. Chem. C* **2015**, *3*, 5976–5984.

(94) Xu, Q.; Liu, Y.; Gao, C.; Wei, J.; Zhou, H.; Chen, Y.; Dong, C.; Sreeprasad, T. S.; Li, N.; Xia, Z. Synthesis, Mechanistic Investigation, and Application of Photoluminescent Sulfur and Nitrogen Co-Doped Carbon Dots. *J. Mater. Chem. C* **2015**, *3*, 9885–9893.

(95) Strauss, V.; Margraf, J. T.; Dirian, K.; Syrgiannis, Z.; Prato, M.; Wessendorf, C.; Hirsch, A.; Clark, T.; Guldi, D. M. Carbon Nanodots: Supramolecular Electron

Donor-Acceptor Hybrids Featuring Perylenediimides. *Angew. Chem. Int. Ed. Engl.* **2015**, *54*, 8292–8297.

(96) Bhunia, S. K.; Pradhan, N.; Jana, N. R. Vitamin B1 Derived Blue and Green Fluorescent Carbon Nanoparticles for Cell-Imaging Application. *ACS Appl. Mater. Interfaces* **2014**, *6*, 7672–7679.

(97) Reed, M.; Randall, J.; Aggarwal, R.; Matyi, R.; Moore, T.; Wetsel, A. Observation of Discrete Electronic States in a Zero-Dimensional Semiconductor Nanostructure. *Phys. Rev. Lett.* **1988**, *60*, 535–537.

(98) Ekimov, A. I.; Onoshchenko, A. A. Quantum Size Effect in Three-Dimensional Microscopic Semiconductor Crystals. *Am. Inst. Phys.* **1982**, *34*, 345.

(99) Onushchenko, A. A.; Ekimov, A. I. Quantum Size Effect in Three Dimensional Microscopic Semiconductor Crystals. *JETP Lett.* **1981**, *34*, 345.

(100) Bawendi, M. G.; Steigerwald, M. L.; Brus, L. E. The Quantum Mechanics of Larger Semiconductor Clusters (“ Quantum Dots”). *Annu. Rev. Phys. Chem.* **1990**, *41*, 477–496.

(101) Cayuela, A.; Soriano, M. L.; Carrillo-Carrión, C.; Valcárcel, M. Semiconductor and Carbon-Based Fluorescent Nanodots: The Need for Consistency. *Chem. Commun.* **2016**, *52*, 1311–1326.

(102) Luo, P. G.; Sahu, S.; Yang, S.-T.; Sonkar, S. K.; Wang, J.; Wang, H.; LeCroy, G. E.; Cao, L.; Sun, Y.-P. Carbon “quantum” dots for Optical Bioimaging. *J. Mater. Chem. B* **2013**, *1*, 2116–2127.

(103) Tao, H.; Yang, K.; Ma, Z.; Wan, J.; Zhang, Y.; Kang, Z.; Liu, Z. In Vivo NIR Fluorescence Imaging, Biodistribution, and Toxicology of Photoluminescent Carbon Dots Produced from Carbon Nanotubes and Graphite. *Small* **2012**, *8*, 281–290.

(104) Esteves da Silva, J. C. G.; Gonçalves, H. M. R. Analytical and Bioanalytical Applications of Carbon Dots. *TrAC Trends Anal. Chem.* **2011**, *30*, 1327–1336.

(105) Yan, H.; Tan, M.; Zhang, D.; Cheng, F.; Wu, H.; Fan, M.; Ma, X.; Wang, J. Development of Multicolor Carbon Nanoparticles for Cell Imaging. *Talanta* **2013**, *108*, 59–65.

(106) Yang, S.-T.; Cao, L.; Luo, P. G.; Lu, F.; Wang, X.; Wang, H.; Meziani, M. J.; Liu, Y.; Qi, G.; Sun, Y.-P. Carbon Dots for Optical Imaging in Vivo. *J. Am.*

Chem. Soc. **2009**, *131*, 11308–11309.

(107) Li, Q.; Ohulchanskyy, T. Y.; Liu, R.; Koynov, K.; Wu, D.; Best, A.; Kumar, R.; Bonoiu, A.; Prasad, P. N. Photoluminescent Carbon Dots as Biocompatible Nanoprobes for Targeting Cancer Cells in Vitro. *J. Phys. Chem. C* **2010**, *114*, 12062–12068.

(108) Zhang, Y.-L.; Wang, L.; Zhang, H.-C.; Liu, Y.; Wang, H.-Y.; Kang, Z.-H.; Lee, S.-T. Graphitic Carbon Quantum Dots as a Fluorescent Sensing Platform for Highly Efficient Detection of Fe3+ Ions. *RSC Adv.* **2013**, *3*, 3733–3738.

(109) Fernando, K. A. S.; Sahu, S.; Liu, Y.; Lewis, W. K.; Guliants, E. A.; Jafariyan, A.; Wang, P.; Bunker, C. E.; Sun, Y.-P. Carbon Quantum Dots and Applications in Photocatalytic Energy Conversion. *ACS Appl. Mater. Interfaces* **2015**, *7*, 8363–8376.

(110) Sahu, S.; Liu, Y.; Wang, P.; Bunker, C. E.; Fernando, K. a S.; Lewis, W. K.; Guliants, E. a; Yang, F.; Wang, J.; Sun, Y.-P. Visible-Light Photoconversion of Carbon Dioxide into Organic Acids in an Aqueous Solution of Carbon Dots. *Langmuir* **2014**, *30*, 8631–8636.

(111) Cao, L.; Sahu, S.; Anilkumar, P.; Bunker, C. E.; Xu, J.; Fernando, K. A. S.; Wang, P.; Guliants, E. A.; Tackett, K. N.; Sun, Y. P. Carbon Nanoparticles as Visible-Light Photocatalysts for Efficient CO 2 Conversion and beyond. *J. Am. Chem. Soc.* **2011**, *133*, 4754–4757.

(112) Zhang, X.; Wang, F.; Huang, H.; Li, H.; Han, X.; Liu, Y.; Kang, Z. Carbon Quantum Dot Sensitized TiO2 Nanotube Arrays for Photoelectrochemical Hydrogen Generation under Visible Light. *Nanoscale* **2013**, *5*, 2274.

(113) Wang, J.; Gao, M.; Ho, G. W. Bidentate-Complex-Derived TiO2/carbon Dot Photocatalysts: In Situ Synthesis, Versatile Heterostructures, and Enhanced H2 Evolution. *J. Mater. Chem. A* **2014**, *2*, 5703.

(114) Wang, F.; Chen, Y.; Liu, C.; Ma, D. White Light-Emitting Devices Based on Carbon Dots' Electroluminescence. *Chem. Commun. (Camb).* **2011**, *47*, 3502–3504.

(115) Wang, Y.; Kalytchuk, S.; Wang, L.; Zhovtiuk, O.; Cepe, K.; Zboril, R.; Rogach, A. L. Carbon Dot Hybrids with Oligomeric Silsesquioxane: Solid-State Luminophores with High Photoluminescence Quantum Yield and Applicability

in White Light Emitting Devices. *Chem. Commun. (Camb).* **2015**, *51*, 2950–2953.

(116) Zhang, X.; Zhang, Y.; Wang, Y.; Kalytchuk, S.; Kershaw, S. V.; Wang, Y.; Wang, P.; Zhang, T.; Zhao, Y.; Zhang, H.; *et al.* Color-Switchable Electroluminescence of Carbon Dot Light-Emitting Diodes. *ACS Nano* **2013**, *7*, 11234–11241.

(117) Mirtchev, P.; Henderson, E. J.; Soheilnia, N.; Yip, C. M.; Ozin, G. A. Solution Phase Synthesis of Carbon Quantum Dots as Sensitizers for Nanocrystalline TiO2 Solar Cells. *J. Mater. Chem.* **2012**, *22*, 1265–1269.

(118) Zhang, Y.-Q. Y.-G.; Ma, D.-K.; Zhang, Y.-Q. Y.-G.; Chen, W.; Huang, S.-M. N-Doped Carbon Quantum Dots for TiO2-Based Photocatalysts and Dye-Sensitized Solar Cells. *Nano Energy* **2013**, *2*, 545–552.

(119) Margraf, J. T.; Lodermeyer, F.; Strauss, V.; Haines, P.; Walter, J.; Peukert, W.; Costa, R. D.; Clark, T.; Guldi, D. M. Using Carbon Nanodots as Inexpensive and Environmentally Friendly Sensitizers in Mesoscopic Solar Cells. *Nanoscale Horiz.* **2016**, *1*, 220–226.

(120) Briscoe, J.; Marinovic, A.; Sevilla, M.; Dunn, S.; Titirici, M. Biomass-Derived Carbon Quantum Dot Sensitizers for Solid-State Nanostructured Solar Cells. *Angew. Chemie Int. Ed.* **2015**, *54*, 4463–4468.

(121) Green, M. A.; Emery, K.; Hishikawa, Y.; Warta, W.; Dunlop, E. D. Solar Cell Efficiency Tables (Version 47). *Prog. Photovoltaics Res. Appl.* **2016**, *24*, 3–11.

(122) Hod, I.; Zaban, A. Materials and Interfaces in Quantum Dot Sensitized Solar Cells: Challenges, Advances and Prospects. *Langmuir* **2014**, *30*, 7264–7273.

(123) Peumans, P.; Yakimov, A.; Forrest, S. R. Small Molecular Weight Organic Thin-Film Photodetectors and Solar Cells. *J. Appl. Phys.* **2003**, *93*, 3693.

(124) Günes, S.; Neugebauer, H.; Sariciftci, N. S. Conjugated Polymer-Based Organic Solar Cells. *Chem. Rev.* **2007**, *107*, 1324–1338.

(125) Noel, N. K.; Stranks, S. D.; Abate, A.; Wehrenfennig, C.; Guarnera, S.; Haghighirad, A.-A.; Sadhanala, A.; Eperon, G. E.; Pathak, S. K.; Johnston, M. B.; *et al.* Lead-Free Organic–inorganic Tin Halide Perovskites for Photovoltaic Applications. *Energy Environ. Sci.* **2014**, *7*, 3061.

(126) Green, M. A.; Ho-Baillie, A.; Snaith, H. J. The Emergence of Perovskite Solar

Cells. *Nat. Photonics* **2014**, *8*, 506–514.

(127) Grätzel, M. Dye-Sensitized Solar Cells. *J. Photochem. Photobiol. C Photochem. Rev.* **2003**, *4*, 145–153.

(128) Kamat, P. V. Quantum Dot Solar Cells. The Next Big Thing in Photovoltaics. *J. Phys. Chem. Lett.* **2013**, *4*, 908–918.

(129) Kakiage, K.; Aoyama, Y.; Yano, T.; Oya, K.; Fujisawa, J.; Hanaya, M. Highly-Efficient Dye-Sensitized Solar Cells with Collaborative Sensitization by Silyl-Anchor and Carboxy-Anchor Dyes. *Chem. Commun.* **2015**, *51*, 15894–15897.

(130) Zhao, K.; Pan, Z.; Mora-Seró, I.; Cánovas, E.; Wang, H.; Song, Y.; Gong, X.; Wang, J.; Bonn, M.; Bisquert, J.; *et al.* Boosting Power Conversion Efficiencies of Quantum-Dot-Sensitized Solar Cells Beyond 8% by Recombination Control. *J. Am. Chem. Soc.* **2015**, *137*, 5602–5609.

(131) Chuang, C.-H. M.; Brown, P. R.; Bulović, V.; Bawendi, M. G. Improved Performance and Stability in Quantum Dot Solar Cells through Band Alignment Engineering. *Nat. Mater.* **2014**, *13*, 796–801.

(132) Jiao, S.; Shen, Q.; Mora-Seró, I.; Wang, J.; Pan, Z.; Zhao, K.; Kuga, Y.; Zhong, X.; Bisquert, J. Band Engineering in Core/Shell ZnTe/CdSe for Photovoltage and Efficiency Enhancement in Exciplex Quantum Dot Sensitized Solar Cells. *ACS Nano* **2015**, *9*, 908–915.

(133) Choi, Y. C.; Lee, D. U.; Noh, J. H.; Kim, E. K.; Seok, S. Il. Highly Improved Sb2S3 Sensitized-Inorganic–Organic Heterojunction Solar Cells and Quantification of Traps by Deep-Level Transient Spectroscopy. *Adv. Funct. Mater.* **2014**, *24*, 3587–3592.

(134) Kramer, I. J.; Sargent, E. H. The Architecture of Colloidal Quantum Dot Solar Cells: Materials to Devices. *Chem. Rev.* **2014**, *114*, 863–882.

(135) NREL. Best Research Cell Efficiencies Chart http://www.nrel.gov/ncpv/images/efficiency_chart.jpg (accessed Jun 15, 2016).

(136) Robel, I.; Subramanian, V.; Kuno, M.; Kamat, P. V. Quantum Dot Solar Cells. Harvesting Light Energy with CdSe Nanocrystals Molecularly Linked to Mesoscopic TiO 2 Films. *J. Am. Chem. Soc.* **2006**, *128*, 2385–2393.

(137) Pan, Z.; Mora-Seró, I.; Shen, Q.; Zhang, H.; Li, Y.; Zhao, K.; Wang, J.; Zhong, X.; Bisquert, J. High-Efficiency “Green” Quantum Dot Solar Cells. *J. Am. Chem.*

Soc. **2014**, *136*, 9203–9210.

(138) Santra, P. K.; Nair, P. V; George Thomas, K.; Kamat, P. V. CuInS2-Sensitized Quantum Dot Solar Cell. Electrophoretic Deposition, Excited-State Dynamics, and Photovoltaic Performance. *J. Phys. Chem. Lett.* **2013**, *4*, 722–729.

(139) McDaniel, H.; Fuke, N.; Pietryga, J. M.; Klimov, V. I. Engineered CuInSe X S 2– X Quantum Dots for Sensitized Solar Cells. *J. Phys. Chem. Lett.* **2013**, *4*, 355–361.

(140) McDaniel, H.; Fuke, N.; Makarov, N. S.; Pietryga, J. M.; Klimov, V. I. An Integrated Approach to Realizing High-Performance Liquid-Junction Quantum Dot Sensitized Solar Cells. *Nat. Commun.* **2013**, *4*.

(141) Ning, Z.; Zhitomirsky, D.; Adinolfi, V.; Sutherland, B.; Xu, J.; Voznyy, O.; Maraghechi, P.; Lan, X.; Hoogland, S.; Ren, Y.; *et al.* Graded Doping for Enhanced Colloidal Quantum Dot Photovoltaics. *Adv. Mater.* **2013**, *25*, 1719–1723.

(142) Wang, J.; Mora-Seró, I.; Pan, Z.; Zhao, K.; Zhang, H.; Feng, Y.; Yang, G.; Zhong, X.; Bisquert, J. Core/Shell Colloidal Quantum Dot Exciplex States for the Development of Highly Efficient Quantum-Dot-Sensitized Solar Cells. *J. Am. Chem. Soc.* **2013**, *135*, 15913–15922.

(143) Wang, H.; Sun, P.; Cong, S.; Wu, J.; Gao, L.; Wang, Y.; Dai, X.; Yi, Q.; Zou, G. Nitrogen-Doped Carbon Dots for "green" Quantum Dot Solar Cells. *Nanoscale Res. Lett.* **2016**, *11*, 27.

(144) Honsberg, C.; Bowden, S. PVeducation.org http://www.pveducation.org/pvcdrom/pn-junction/formation-pn-junction (accessed Jul 13, 2016).

(145) Grätzel, M. Solar Energy Conversion by Dye-Sensitized Photovoltaic Cells. *Inorg. Chem.* **2005**, *44*, 6841–6851.

(146) Gong, J.; Liang, J.; Sumathy, K. Review on Dye-Sensitized Solar Cells (DSSCs): Fundamental Concepts and Novel Materials. *Renewable and Sustainable Energy Reviews*, 2012, *16*, 5848–5860.

(147) Barbé, C. J.; Arendse, F.; Comte, P.; Jirousek, M.; Lenzmann, F.; Shklover, V.; Grätzel, M. Nanocrystalline Titanium Oxide Electrodes for Photovoltaic Applications. *J. Am. Ceram. Soc.* **2005**, *80*, 3157–3171.

(148) Kouhnavard, M.; Ikeda, S.; Ludin, N. A.; Ahmad Khairudin, N. B.; Ghaffari, B. V.; Mat-Teridi, M. A.; Ibrahim, M. A.; Sepeai, S.; Sopian, K. A Review of Semiconductor Materials as Sensitizers for Quantum Dot-Sensitized Solar Cells. *Renew. Sustain. Energy Rev.* **2014**, *37*, 397–407.

(149) Rinaudo, M. Chitin and Chitosan: Properties and Applications. *Prog. Polym. Sci.* **2006**, *31*, 603–632.

(150) Kumirska, J.; Czerwicka, M.; Kaczyński, Z.; Bychowska, A.; Brzozowski, K.; Thöming, J.; Stepnowski, P. Application of Spectroscopic Methods for Structural Analysis of Chitin and Chitosan. *Mar. Drugs* **2010**, *8*, 1567–1636.

(151) Pillai, C. K. S.; Paul, W.; Sharma, C. P. Chitin and Chitosan Polymers: Chemistry, Solubility and Fiber Formation. *Prog. Polym. Sci.* **2009**, *34*, 641–678.

(152) Kumar, S.; Rai, S. B. Spectroscopic Studies of L-Arginine Molecule. *INDIAN J. PURE Appl. Phys.* **2010**, *48*, 251–255.

(153) Pawlukojć, A.; Leciejewicz, J.; Ramirez-Cuesta, A. J.; Nowicka-Scheibe, J. L-Cysteine: Neutron Spectroscopy, Raman, IR and Ab Initio Study. *Spectrochim. Acta Part A Mol. Biomol. Spectrosc.* **2005**, *61*, 2474–2481.

(154) Kwon, W.; Rhee, S.-W. Facile Synthesis of Graphitic Carbon Quantum Dots with Size Tunability and Uniformity Using Reverse Micelles. *Chem. Commun.* **2012**, *48*, 5256.

(155) Kwon, W.; Lee, G.; Do, S.; Joo, T.; Rhee, S.-W. Size-Controlled Soft-Template Synthesis of Carbon Nanodots toward Versatile Photoactive Materials. *Small* **2014**, *10*, 506–513.

(156) Baccile, N.; Laurent, G.; Coelho, C.; Babonneau, F.; Zhao, L.; Titirici, M.-M. Structural Insights on Nitrogen-Containing Hydrothermal Carbon Using Solid-State Magic Angle Spinning 13 C and 15 N Nuclear Magnetic Resonance. *J. Phys. Chem. C* **2011**, *115*, 8976–8982.

(157) Qu, D.; Zheng, M.; Du, P.; Zhou, Y.; Zhang, L.; Li, D.; Tan, H.; Zhao, Z.; Xie, Z.; Sun, Z. Highly Luminescent S, N Co-Doped Graphene Quantum Dots with Broad Visible Absorption Bands for Visible Light Photocatalysts. *Nanoscale* **2013**, *5*, 12272.

(158) Ding, H.; Xiong, H.-M. Exploring the Blue Luminescence Origin of Nitrogen-Doped Carbon Dots by Controlling the Water Amount in Synthesis. *RSC Adv.*

2015, *5*, 66528–66533.

(159) Wu, Z. L.; Zhang, P.; Gao, M. X.; Liu, C. F.; Wang, W.; Leng, F.; Huang, C. Z. One-Pot Hydrothermal Synthesis of Highly Luminescent Nitrogen-Doped Amphoteric Carbon Dots for Bioimaging from Bombyx Mori Silk - Natural Proteins. *J. Mater. Chem. B* **2013**, *1*, 2868–2873.

(160) Yu, L. H.; Falco, C.; Weber, J.; White, R. J.; Howe, J. Y.; Titirici, M. M. Carbohydrate-Derived Hydrothermal Carbons: A Thorough Characterization Study. *Langmuir* **2012**, *28*, 12373–12383.

(161) Horvat, J.; Klaić, B.; Metelko, B.; Šunjić, V. Mechanism of Levulinic Acid Formation. *Tetrahedron Lett.* **1985**, *26*, 2111–2114.

(162) James, O. O.; Maity, S.; Usman, L. A.; Ajanaku, K. O.; Ajani, O. O.; Siyanbola, T. O.; Sahu, S.; Chaubey, R. Towards the Conversion of Carbohydrate Biomass Feedstocks to Biofuels via Hydroxylmethylfurfural. *Energy Environ. Sci.* **2010**, *3*, 1833.

(163) Chheda, J. N.; Dumesic, J. A. An Overview of Dehydration, Aldol-Condensation and Hydrogenation Processes for Production of Liquid Alkanes from Biomass-Derived Carbohydrates. *Catal. TODAY* **2007**, *123*, 59–70.

(164) Yao, C.; Shin, Y.; Wang, L.-Q.; Windisch, C. F.; Samuels, W. D.; Arey, B. W.; Wang, C.; Risen, W. M.; Exarhos, G. J. Hydrothermal Dehydration of Aqueous Fructose Solutions in a Closed System. *J. Phys. Chem. C* **2007**, *111*, 15141–15145.

(165) Mer, V. K. La. Nucleation in Phase Transitions. *Ind. Eng. Chem.* **1952**, *44*, 1270–1277.

(166) Sun, X.; Li, Y. Colloidal Carbon Spheres and Their Core/Shell Structures with Noble-Metal Nanoparticles. *Angew. Chemie Int. Ed.* **2004**, *43*, 597–601.

(167) Shu, C.-K. Degradation Products Formed from Glucosamine in Water. *J. Agric. Food Chem.* **1998**, *46*, 1129–1131.

(168) Sevilla, M.; Fuertes, A. B. The Production of Carbon Materials by Hydrothermal Carbonization of Cellulose. *Carbon N. Y.* **2009**, *47*, 2281–2289.

(169) Yang, J.; Zhang, Y.; Gautam, S.; Liu, L.; Dey, J.; Chen, W.; Mason, R. P.; Serrano, C. A.; Schug, K. A.; Tang, L. Development of Aliphatic Biodegradable Photoluminescent Polymers. *Proc. Natl. Acad. Sci.* **2009**, *106*, 10086–10091.

(170) Xiao, J.; Liu, P.; Li, L.; Yang, G. Fluorescence Origin of Nanodiamonds. *J. Phys. Chem. C* **2015**, *119*, 2239–2248.

(171) Yang, Y. H.; Cui, J. H.; Zheng, M. T.; Hu, C. F.; Tan, S. Z.; Xiao, Y.; Yang, Q.; Liu, Y. L. One-Step Synthesis of Amino-Functionalized Fluorescent Carbon Nanoparticles by Hydrothermal Carbonization of Chitosan. *Chem. Commun.* **2012**, *48*, 380–382.

(172) Sevilla, M.; Fuertes, A. B. Chemical and Structural Properties of Carbonaceous Products Obtained by Hydrothermal Carbonization of Saccharides. *Chem. Eur. J.* **2009**, *15*, 4195–4203.

(173) Ibrahim, M.; Alaam, M.; El-Haes, H.; Jalbout, A. F.; Leon, A. de. Analysis of the Structure and Vibrational Spectra of Glucose and Fructose. *Eclética Química* **2006**, *31*, 15–21.

(174) França, R.; Mbeh, D. A.; Samani, T. D.; Le Tien, C.; Mateescu, M. A.; Yahia, L.; Sacher, E. The Effect of Ethylene Oxide Sterilization on the Surface Chemistry and in Vitro Cytotoxicity of Several Kinds of Chitosan. *J. Biomed. Mater. Res. B. Appl. Biomater.* **2013**, *101*, 1444–1455.

(175) Ferrari, A. C.; Robertson, J. Interpretation of Raman Spectra of Disordered and Amorphous Carbon. *Phys. Rev. B* **2000**, *61*, 14095–14107.

(176) Ferrari, A. C.; Meyer, J. C.; Scardaci, V.; Casiraghi, C.; Lazzeri, M.; Mauri, F.; Piscanec, S.; Jiang, D.; Novoselov, K. S.; Roth, S.; *et al.* Raman Spectrum of Graphene and Graphene Layers. *Phys. Rev. Lett.* **2006**, *97*, 187401.

(177) Tuinstra, F.; Koenig, J. L. Raman Spectrum of Graphite. *J. Chem. Phys.* **1970**, *53*.

(178) Vidano, R. P.; Fischbach, D. B.; Willis, L. J.; Loehr, T. M. Observation of Raman Band Shifting with Excitation Wavelength for Carbons and Graphites. *Solid State Commun.* **1981**, *39*, 341–344.

(179) Nemanich, R. J.; Solin, S. A. First- and Second-Order Raman Scattering from Finite-Size Crystals of Graphite. *Phys. Rev. B* **1979**, *20*, 392–401.

(180) Schwan, J.; Ulrich, S.; Batori, V.; Ehrhardt, H.; Silva, S. R. P. Raman Spectroscopy on Amorphous Carbon Films. *J. Appl. Phys.* **1996**, *80*, 440–447.

(181) Wang, Y.; Kalytchuk, S.; Zhang, Y.; Shi, H.; Kershaw, S. V.; Rogach, A. L. Thickness-Dependent Full-Color Emission Tunability in a Flexible Carbon Dot

Ionogel. *J. Phys. Chem. Lett.* **2014**, *5*, 1412–1420.

(182) Hola, K.; Zhang, Y.; Wang, Y.; Giannelis, E. P.; Zboril, R.; Rogach, A. L. Carbon dots—Emerging Light Emitters for Bioimaging, Cancer Therapy and Optoelectronics. *Nano Today* **2014**, *9*, 590–603.

(183) Li, W.; Zhang, Z.; Kong, B.; Feng, S.; Wang, J.; Wang, L.; Yang, J.; Zhang, F.; Wu, P.; Zhao, D. Simple and Green Synthesis of Nitrogen-Doped Photoluminescent Carbonaceous Nanospheres for Bioimaging. *Angew. Chem. Int. Ed. Engl.* **2013**, *52*, 8151–8155.

(184) Liang, Q.; Ma, W.; Shi, Y.; Li, Z.; Yang, X. Easy Synthesis of Highly Fluorescent Carbon Quantum Dots from Gelatin and Their Luminescent Properties and Applications. *Carbon N. Y.* **2013**, *60*, 421–428.

(185) Briscoe, J.; Dunn, S. The Future of Using Earth-Abundant Elements in Counter Electrodes for Dye-Sensitized Solar Cells. *Adv. Mater.* **2016**, *28*, 3802–3813.

(186) Keis, K.; Bauer, C.; Boschloo, G.; Hagfeldt, A.; Westermark, K.; Rensmo, H.; Siegbahn, H. Nanostructured ZnO Electrodes for Dye-Sensitized Solar Cell Applications. *J. Photochem. Photobiol. A Chem.* **2002**, *148*, 57–64.

(187) Thavasi, V.; Renugopalakrishnan, V.; Jose, R.; Ramakrishna, S. Controlled Electron Injection and Transport at Materials Interfaces in Dye Sensitized Solar Cells. *Mater. Sci. Eng. R Reports* **2009**, *63*, 81–99.

(188) Snaith, H. J.; Schmidt-Mende, L. Advances in Liquid-Electrolyte and Solid-State Dye-Sensitized Solar Cells. *Adv. Mater.* **2007**, *19*, 3187–3200.

(189) Briscoe, J.; Gallardo, D. E.; Hatch, S.; Lesnyak, V.; Gaponik, N.; Dunn, S. Enhanced Quantum Dot Deposition on ZnO Nanorods for Photovoltaics through Layer-by-Layer Processing. *J. Mater. Chem.* **2011**, *21*, 2517.

(190) Ip, A. H.; Thon, S. M.; Hoogland, S.; Voznyy, O.; Zhitomirsky, D.; Debnath, R.; Levina, L.; Rollny, L. R.; Carey, G. H.; Fischer, A.; *et al.* Hybrid Passivated Colloidal Quantum Dot Solids. *Nat Nano* **2012**, *7*, 557–582.

(191) Lee, K. E.; Gomez, M. A.; Elouatik, S.; Demopoulos, G. P. Further Understanding of the Adsorption Mechanism of N719 Sensitizer on Anatase TiO_2 Films for DSSC Applications Using Vibrational Spectroscopy and Confocal Raman Imaging. *Langmuir* **2010**, *26*, 9575–9583.

(192) Wang, H.; Zhang, D.-W.; Li, Z.-T. Hydrogen Bonding for Molecular,

Macromolecular, and Supramolecular Materials. In *Hydrogen Bonded Supramolecular Materials*; Li, Z.-T.; Wu, L.-Z., Eds.; Springer, 2015; pp. 185–231.

(193) Jackman, M. J.; Syres, K. L.; Cant, D. J. H.; Hardman, S. J. O.; Thomas, A. G. Adsorption of Dopamine on Rutile TiO 2 (110): A Photoemission and Near-Edge X-Ray Absorption Fine Structure Study. *Langmuir* **2014**, *30*, 8761–8769.

(194) Yang, P.; Zhao, D.; Margolese, D. I.; Chmelka, B. F.; Stucky, G. D. Generalized Syntheses of Large-Pore Mesoporous Metal Oxides with Semicrystalline Frameworks. *Nature* **1998**, *396*, 152–155.

(195) Thamaphat, K.; Limsuwan, P.; Ngotawornchai, B. Phase Characterization of TiO2 Powder by XRD and TEM\n. *Kasetsart J. Nat. Sci.* **2008**, *42*, 357–361.

(196) Bai, Y.; Mora-Seró, I.; De Angelis, F.; Bisquert, J.; Wang, P. Titanium Dioxide Nanomaterials for Photovoltaic Applications. *Chem. Rev.* **2014**, *114*, 10095–10130.

(197) Nguyen, T.-D.; MacLachlan, M. J. Biomimetic Chiral Nematic Mesoporous Materials from Crab Cuticles. *Adv. Opt. Mater.* **2014**, *2*, 1031–1037.

(198) Bashir, A.; Wöbkenberg, P. H.; Smith, J.; Ball, J. M.; Adamopoulos, G.; Bradley, D. D. C.; Anthopoulos, T. D. High-Performance Zinc Oxide Transistors and Circuits Fabricated by Spray Pyrolysis in Ambient Atmosphere. *Adv. Mater.* **2009**, *21*, 2226–2231.

(199) Leschkies, K. S.; Divakar, R.; Basu, J.; Enache-Pommer, E.; Boercker, J. E.; Carter, C. B.; Kortshagen, U. R.; Norris, D. J.; Aydil, E. S. Photosensitization of ZnO Nanowires with CdSe Quantum Dots for Photovoltaic Devices. *Nano Lett.* **2007**, *7*, 1793–1798.

(200) Hatch, S. M.; Briscoe, J.; Dunn, S. Improved CuSCN–ZnO Diode Performance with Spray Deposited CuSCN. *Thin Solid Films* **2013**, *531*, 404–407.